Design, simulation and fabrication of a vertical microscanner for phase modulation interferometry - Application to optical coherence tomography system for skin imaging

Justine Lullin

HAL Id: tel-01418987

https://tel.archives-ouvertes.fr/tel-01418987

Submitted on 18 Dec 2016

SPIM

Thèse de Doctorat

Design, simulation and fabrication of a vertical microscanner for phase modulation interferometry

Application to optical coherence tomography system for skin imaging

JUSTINE LULLIN

THÈSE présentée par

JUSTINE LULLIN

pour obtenir le

Grade de Docteur de
l'Université Bourgogne Franche-Comté

Spécialité : **Sciences pour l'ingénieur**

Design, simulation and fabrication of a vertical microscanner for phase modulation interferometry

Application to optical coherence tomography system for skin imaging

Soutenue publiquement le 17 décembre 2015 devant le Jury composé de :

HANS ZAPPE	Rapporteur	Professeur à l'Université de Freiburg/IMTEK
ALAIN BOSSEBOEUF	Rapporteur	Directeur de recherche au CNRS
VÉRONIQUE BARDINAL-DELAGNES	Examinateur	Directeur de Recherche au CNRS
MAIK WIEMER	Examinateur	Chef de groupe, Fraunhofer Institut
MICHEL DE LABACHELERIE	Examinateur	Directeur de Recherche au CNRS
CHRISTOPHE GORECKI	Directeur de thèse	Directeur de Recherche au CNRS
SYLWESTER BARGIEL	Co-encadrant	Ingénieur de recherche/Université de Franche-Comté
NICOLAS PASSILLY	Co-encadrant	Chargé de Recherche au CNRS

ACKNOWLEDGEMENTS

Résumé de la thèse en français

Cette thèse décrit le design, la simulation et la fabrication d'une matrice 4x4 de micromiroirs actionnée verticalement et munie d'un capteur de position. Le microscanneur vertical a pour vocation d'être intégré au sein d'un micro-interféromètre de Mirau de type matriciel, réalisé à base de composants micro-optiques fabriqués grâce à des méthodes collectives. Le mouvement du microscanneur génère un signal de référence utilisé pour l'implémentation de l'interférométrie à modulation de phase dans un système de tomographie par cohérence optique (OCT).

La thèse s'inscrit dans le cadre du projet européen FP7 nommé VIAMOS. Sept partenaires européen ont travaillé en collaboration pendant trois ans et mis en commun leurs expertises respectives afin de réaliser un système OCT basé sur un interféromètre de Mirau de type matriciel et intégré verticalement.

De nouveaux systèmes d'imagerie adaptés pour la détection précoce des cancers de la peau sont nécessaires pour répondre aux besoins spécifiques imposés par cette application. En particulier, la profondeur d'imagerie et la résolution sont deux caractéristiques fondamentales. En effet, le diagnostic du cancer de la peau nécessite une profondeur de pénétration d'au moins 500 μm afin de visualiser les tissus jusqu'à la jonction dermo-épidermique. De plus, une résolution autour de 6 μm est nécessaire pour visualiser les cellules de la peau. La technique OCT a l'avantage de répondre à ces deux critères contrairement à d'autres systèmes d'imagerie qui en privilégient un au détriment de l'autre. Enfin, les systèmes OCT existent mais sont très couteux et encombrants ce qui limite leurs accès pour de nombreux hôpitaux. Ainsi, la miniaturisation du système est une solution à ces deux problèmes et est la base de la problématique de cette thèse.
À partir des spécifications données ci-dessus, le design du système OCT basé sur le micro-interféromètre de Mirau est présenté. Le système est un OCT plein champ à source à balayage en longueur d'onde. Cette méthode est basée sur l'acquisition de l'interférogramme spectral (intensité du signal interférométrique en fonction des longueurs d'ondes balayées) auquel on applique ensuite une transformée de Fourier afin de retrouver l'interférogramme spatial (intensité du signal en fonction de la profondeur dans le tissu analysé). De plus, en plein champ, un champ de vue est imagé sur une caméra à chaque acquisition. La combinaison de ces deux méthodes permet

d'augmenter la vitesse d'acquisition d'images par rapport à une méthode classique où l'interférogramme est enregistré point par point et où le miroir de référence est utilisé pour scanner axialement l'échantillon et un autre miroir permet de scanner latéralement le champ de vue. Enfin, l'utilisation de méthode interférométrique à décalage de phase améliore la sensibilité du système en éliminant des termes parasites liés à l'application de la transformée de Fourier. Cette thèse se focalise sur la miniaturisation d'un interféromètre de Mirau et, en particulier, sur le développement d'un microscanneur vertical permettant le décalage de phase au sein de l'interféromètre. L'interféromètre de Mirau a été choisi pour la compatibilité de son architecture verticale avec les techniques d'assemblage de la microfabrication.

Dans un premier temps, l'état de l'art des principes de micro-actionnement illustrés par des exemples issus de la littérature est étudié. Il existe quatre grands groupes de technologies de micro-actionnement: piézoélectrique, thermique, magnétique et électrostatique. L'actionnement électrostatique à base de peignes interdigités est choisi pour actionner et lire la position de la matrice de micromiroirs. En effet, ce type d'actionnement permet de répondre aux exigences d'actionnement imposées par la méthode de modulation sinusoïdale de phase. L'amplitude de déplacement requis est calculée en fonction de la longueur d'onde utilisée et est, dans notre cas, égale à 350 nm. De plus, la fréquence d'actionnement est fixée en fonction des différents paramètres de vitesse du système et est, ici, égale à 500 Hz. Enfin, la technologie de peignes interdigités est relativement simple à adapter à notre design car elle peut être basée uniquement sur du silicium.

Dans un second temps, le développement du microscanneur vertical, c.à.d le design et les simulations ainsi que la fabrication et la caractérisation, est présenté. Le design du microscanneur vertical répond aux spécifications du système optique et en particulier garantie une ouverture transparente autour des micromiroirs. Ce dernier point est lié à la configuration verticale du micro-interféromètre de Mirau, qui a pour conséquence le passage de la lumière des lentilles vers la lame séparatrice en passant par le plan du miroir de référence. Pour obtenir cette configuration atypique, dans laquelle le plan des micromiroirs est transmissif, deux designs sont proposés (Fig. 1).
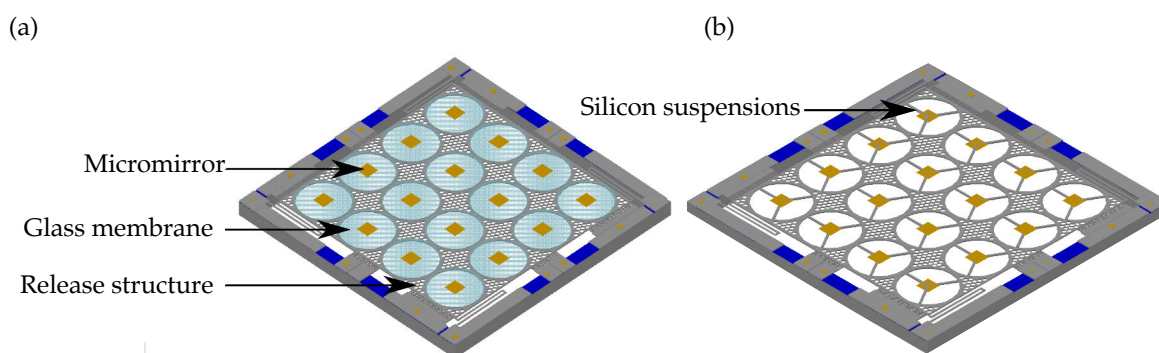
Figure 1: Designs du microscanneur vertical: (a) design basé sur du verre, (b) design basé sur des suspensions en silicium.

Un premier design est basé sur l'intégration d'un support transparent en verre au sein d'une plateforme actionnée en silicium et un deuxième design considère des micromiroirs suspendus par des suspensions courbées en silicium. L'impact des suspensions optiques sur la qualité optique du système est étudié et les résultats montrent que leur impact est négligeable pour une gamme de paramètres de design des suspensions. Une simulation mécanique montre que la déformation verticale de la plateforme actionnée (8 mm x 8 mm) sont négligeables. De plus, des simulations mécaniques et des calculs de raideur permettent d'optimiser les dimensions des suspensions qui maintiennent la plateforme, en fonction du poids des deux designs. Enfin, les résultats des simulations électrostatiques contribuent à définir les paramètres de l'actionneur et du capteur de position (nombre de peignes interdigités, espace entre les peignes,...) (Fig. 2).
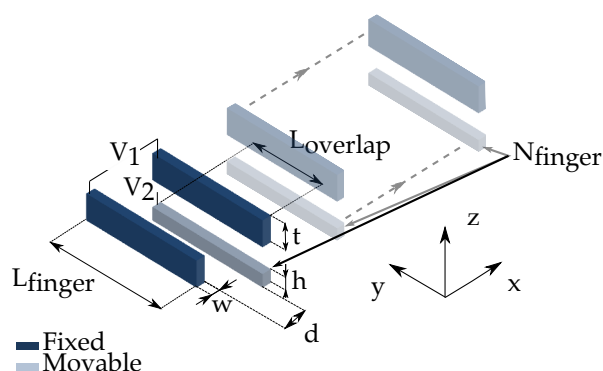
Figure 2: Schéma des peignes interdigités verticaux ainsi que ses paramètres.

Trois technologies de microfabrication sont proposées et réalisées. La première technologie vise à, intégrer d'abord un support en verre sur la plateforme actionnée, puis à utiliser l'enduction par spray et la photolithographie par projection pour patterner la surface non plane du silicium crée par le support en verre. La seconde stratégie est de, d'abord structurer le silicium puis ensuite intégrer le support en verre par thermocompression Au/Au. La couche d'or permet alors de connecter le silicium et le verre mais également

de protéger la couche d'oxyde (BOX) intégré au substrat SOI (Silicon on Insulator) pendant la gravure du verre à l'acide fluorhydrique (HF) liquide. Le première stratégie a été testé avec succès jusqu'à la libération totale du microscanneur qui nécessite l'utilisation de HF, sous forme vapeur, ce qui dégrade la qualité optique du support en verre. La méthode de libération du microscanneur nécessite donc de nouveaux tests et des solutions sont proposées. Le test de la seconde stratégie n'a pas été concluant car la couche d'or n'est pas suffisamment conforme pour protéger le BOX pendant la gravure au HF liquide. Enfin, la troisième stratégie a pour but de créer des suspensions en silicium permettant de soutenir les micromiroirs. Cette statégie a été intégralement testée avec succès et le procédé de fabrication entièrement stabilisé puisque plusieurs wafers ont été réalisés. Le résultat des stratégies 1 et 3 est illustré sur la Fig. 3.
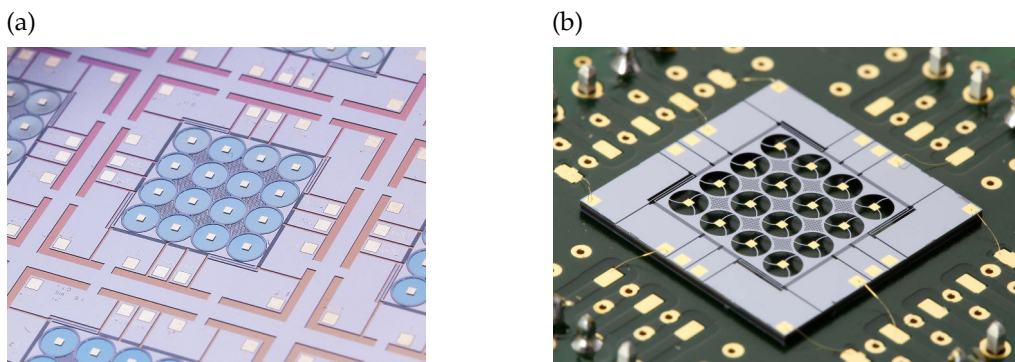
Figure 3: Microscanneur vertical fabriquée: (a) design basé sur du verre, (b) design basé sur des suspensions en silicium.

Les microsystèmes fabriqués sont caractérisés en termes d'actionnement et de détection de position (Fig. 4 et Fig 5, respectively). Les résultats de caractérisation sont cohérents avec ceux des simulations et les fonctions d'actionneurs et de capteurs sont validées. En particulier, la fréquence de résonance est mesurée à 543 Hz et les amplitudes de déplacement sont suffisantes par rapport aux amplitudes requises. Enfin, la mesure de sensibilité du capteur d'environ 27 fF/μm est également conforme aux simulations.
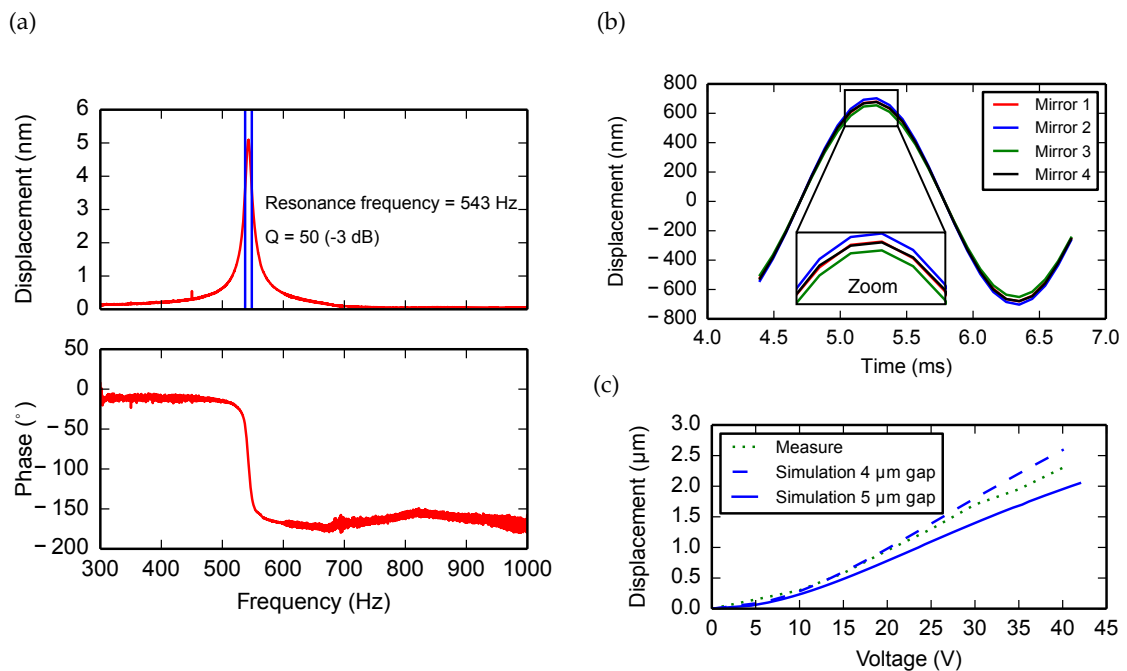
Figure 4: Résultats de caractérisation: (a) réponse spectrale de l'actionneur, (b) déplacement dynamique de la plateforme en quatre points correspondant aux centres de quatre miroirs formant un quart de la plateforme, (c) déplacement statique en fonction de la tension appliqué.
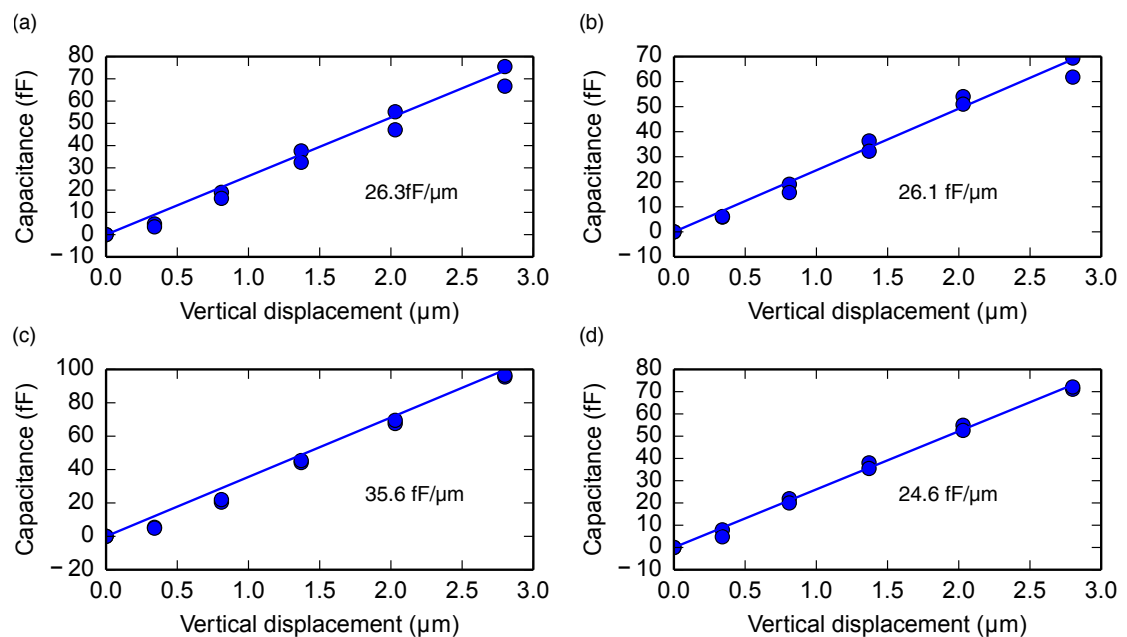
Figure 5: Mesure de la capacité différentielle du capteur en fonction du déplacement vertical statique de la plateforme.

La dernière partie de cette thèse montre l'intégration du microscanneur vertical avec un doublé de microlentilles et une lame séparatrice grâce à des soudures anodiques réalisées

à l'échelle du wafer. Une fois tous les wafers assemblés, d'une épaisseur d'environ 5 mm, il est nécessaire de découper l'ensemble pour obtenir les micro-interféromètres de Mirau individuels. Cependant, les structures à découper ne sont pas complètement hermétiques à cause de tranchées d'isolation nécessaires pour isoler électriquement les actionneurs et les capteurs entre eux. Ainsi, la méthode de découpe à la scie, qui est classiquement utilisée, n'est pas adaptée puisqu'elle nécessite l'utilisation d'un liquide de refroidissement qui pénètre alors dans la cavité du micro-interféromètre de Mirau. Ainsi, la méthode de découpe par laser a été utilisé. Suite à cette découpe, les contacts électriques sont très endommagés car salis par la poussière générée par la découpe. Un nettoyage humide est donc nécessaire. Or, pour les mêmes raisons que celles évoquées ci-avant, l'utilisation de liquide n'est pas possible. Pour y remédier, les tranchées sont alors manuellement remplies unes à unes avec de la colle. Cette méthode est concluante mais reste longue et peu pratique. Ces procédures ont été réalisées par un des partenaires du projet, l'Institut Fraunhofer (ENAS) à Chemnitz. Figure 6 est une image d'un interféromètre de Mirau obtenu et connecté à un circuit imprimé (PCB) par la technique de flip-chip. Le circuit imprimé permet alors de connecter le microscanneur à une source en tension.
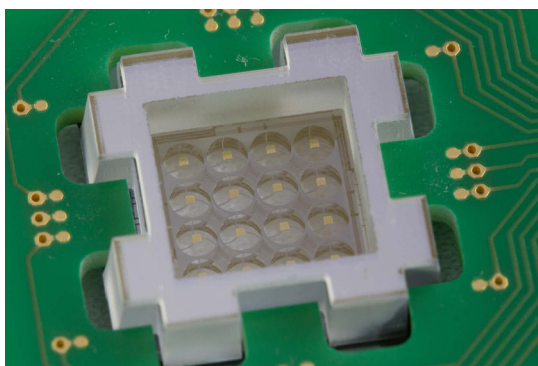
Figure 6: Micro-interféromètre de Mirau.

Une deuxième série de mesures de caractérisation permet d'étudier l'impact de la série de soudure, et de la découpe, sur le microscanneur vertical. Le comportement mécanique du microscanneur ne semble pas impactée par le packaging. En revanche, la qualité optique des micromiroirs est dégradé. Les constatations de dégradation sur les micromiroirs ne sont pas reproductibles et ne permettent pas de comprendre les causes de la dégradation. De nouveaux tests sont donc nécessaires.

Ce manuscrit présente des technologies intéressantes pour le développement d'un microscanneur vertical, muni d'un capteur de position, pour l'interférométrie à décalage de

phase. Des perspectives d'amélioration sont données tout au long de la thèse, comme, par example, un nouveau flow-chart dont le risque total est diminué. Une problématique essentielle est également la protection du microcomposant en verre jusqu'à la libération de la structure. De nouvelle solutions sont proposées mais doivent être testées. Une autre piste d'amélioration est le développement d'un circuit de lecture des capacités pour mesurer en temps réel les capacités différentielles des capteurs et ainsi connaître la position de la plateforme à tout moment. Enfin, une étude systématique de la dégradation de micromiroirs à chaque étape de l'intégration verticale est nécessaire pour comprendre le phénomène.

Les résultats présentés dans cette thèse ouvrent de nouvelles perspectives pour les composants micro-optiques et électro-mécaniques (MOEMS) à haut degré d'intégration. En particulier, la technologie d'intégration du support en verre peut être facilement adaptée pour l'intégration d'autres microcomposants en verre tels que des lentilles en verre ou des réseaux de diffraction. Ce type de composants MOEMS peut alors être utilisé pour des instruments optiques miniaturisés, par exemple un microscope confocale, afin de réaliser un balayage axial ou latéral si des peignes interdigités latéraux sont intégrés.

Le projet européen VIAMOS a permis le développement de nouvelles technologies pour les microsystèmes OCT. Le micro-interféromètre de Mirau est maintenant testé en termes de fonction interférométrique et de modulation de phase. Le système OCT complet est en cours d'assemblage et va être testé cliniquement à l'hôpital de Besançon.

CONTENTS

General introduction

Skin cancer is the most commonly diagnosed type of cancer. Its early diagnosis is critical as it guarantees a more effective treatment. However, the diagnostic tools are limited and the visual examination of the skin followed by a traditional biopsy is still today the reference technique. Nevertheless, biopsy suffers from several drawbacks, such as a long diagnosis time and invasiveness, which is not only affecting the patient but also prevents the follow-up of the diseases. Consequently, non-invasive imaging methods have been developed, including ultrasounds, tomography techniques or confocal imaging. However, the imaging performances of these techniques are limited either by not sufficient resolutions to resolve the morphology of individual cells or by small penetration depths.

Optical Coherence Tomography (OCT) is a recent non-invasive imaging technique based on low coherence interferometry. The resolution can reach 3 μm and the skin penetration depth may reach 1 mm which is enough to image until the dermo-epidermal junction where most developed cutaneous lesions take place. Existing OCT systems allow a fast and non-invasive 3-D reconstruction of tissue morphology. In particular, Fourier domain OCT (FD-OCT) has been recently studied to provide faster and more sensitive imaging. Moreover, the implementation of the phase shifting interferometry (PSI) technique with "active" micro-interferometer allows to further improve the sensitivity and to remove some drawbacks of the FD-OCT technique, such as the presence of artefacts in tomography images. Nevertheless, the commercial systems are bulky, expensive, and hence not sufficiently employed by physicians and dermatologists. The ability to reduce the size of OCT systems, providing a hand-held, low cost and fast OCT devices, is a technological challenge. The miniaturisation of such device is the main motivation for this thesis work.

During my thesis, I have been working in the framework of a European project, called VIAMOS (Vertically Integrated Array-type Mirau-based Oct System), which aims at developing a full-field array-type miniaturised swept-source OCT system. To meet this objective, seven European partners have been working in collaboration during three years to bring together their expertise in different fields (MOEMS, micro-assembly techniques

optical design, camera fabrication, industrial production,...). The targeted system is a swept-source OCT system which is a type of FD-OCT. It is designed as a full-field array-type optical system in order to spatially multiplex the acquisition, to obtain a fast system while imaging a large field-of-view. The latter is important for the targeted application which implies skin lesions as large as few mm^2. In this thesis, the miniaturisation of the micro-interferometer and in particular the reference micromirror scanner, used for the implementation of PSI, will be developed.

The vertical microscanner, used as a phase-shifter, is a micro-opto-electromechanical system (MOEMS) which involves an actuation and a position sensing system to move an array of reference micromirrors. PSI techniques are particularly efficient to remove disturbing interferometric terms specific to Fourier Domain OCT, such as the mirror term, the DC term and the auto-correlation term. Then, this technique leads to an increase of the signal dynamic. The microscanner is a part of a Mirau micro-interferometer which is integrated vertically, at wafer-level, with microfabricated glass lenses, a spacer and a planar beam splitter. The objectives of this thesis is to design, simulate and fabricate a MOEMS device adapted to the vertical architecture of the Mirau microinterferometer, taking into account the optical design but also the assembly processes used for the integration of Mirau microinterferometer. In particular, the design of the vertical microscanner must take into account the optical specifications and the technological limitations. Based on these considerations, two microscanner designs are considered. Their main difference is the way the array of micromirrors is held to let an optical aperture around them. This last point is specific to the Mirau configuration and is critical in this thesis. Finally, electrostatic vertical comb finger are used for both the actuation and the sensing function.

This manuscript is structured in five chapters.

Chapter 1 introduces the framework of this thesis, presenting the motivations to develop such a system as well as introducing the optical coherence tomography techniques and examples of miniaturized systems in the literature. Firstly, the current status of skin cancer and the lack of adapted imaging systems are exposed to show the need for the development of a miniature OCT system to lower its cost and encourage its spreading for the dermatological applications. Then, the theory of the different versions of the OCT technique (time domain and fourier domain OCT) is presented. Finally, examples of miniaturized systems are described and a new solution of miniaturisation for micro-interferometers is shown.

Chapter 2 aims to present the basic principles and the state of the art of vertical microscanners. Piezoelectric, thermal, magnetic and electrostatic actuation principles are

detailed and examples from the literature are given to illustrate the theory. According to this analysis, electrostatic actuation is chosen for both the actuation and the sensing technologies. Then, this actuation principle is considered in details and the different possible designs are analysed in terms of limitations and technological realization.

Then, **Chapter 3** focusses on the design and the simulations of the vertical microscanner. Two designs are presented, one based on the integration of glass support to held the micromirrors and another based on silicon suspensions for the same purpose. The two designs are simulated in terms of mechanical behaviour and the electrostatic actuation capability is also investigated. Finally, an optical simulation is performed to study the impact of the suspensions around the micromirrors on the optical quality of the system.

In the **fourth chapter**, the fabrication of the two designs presented in Ch. 3 is detailed. The elaboration of the flow charts is underlined by analysing the risk factor corresponding to each flow chart. The fabrication results are then presented for three different technologies. The results show the successful realisation of the suspension based design whereas further tests concerning the releasing step are necessary for the glass support design.

Finally, the vertical microscanner chips are characterized in terms of optical quality of the micromirrors, the dynamic and static actuation and the position sensing (**Chapter 5**). The integration of the vertical microscanner within the micro-interferometer is also discussed and a second characterization run is realized.

<div align="right">

1

</div>

FRAMEWORK : MINIATURISATION OF MIRAU INTERFEROMETER FOR OPTICAL COHERENCE TOMOGRAPHY SYSTEM

This chapter describes the framework and the needs that justified this work. The targeted application of the developed device, a high resolution imaging system, is the diagnostic of skin pathologies, in particular, skin cancer. The system design has been strictly constrained by this application. Therefore, the multi-disciplinary interactions between dermatologists and researchers have been the key for the development of a device that meets the specific requirements of skin imaging. To better understand the motivations, the needs of dermatologists in skin imaging are described below. In particular, the potential of OCT systems is shown and compared to other existing imaging technologies. Moreover, the challenges faced for the miniaturization of OCT systems are presented. This description also contributes to define strategies and solutions for the fabrication of a miniature and low cost system using micromachining technologies.

1.1/ MOTIVATIONS : SKIN IMAGING

1.1.1/ SKIN CANCERS

1.1.1.1/ DEFINITIONS

Skin cancer is defined by the Skin Cancer Foundation as *"uncontrolled growth of abnormal skin cells. It occurs when unrepaired DNA damage to skin cells (most often caused by ultraviolet radiation from sunshine or tanning beds) triggers mutations, or genetic defects, that lead the skin*

cells to multiply rapidly and form malignant tumors."

There are two main types of skin cancers: non-melanoma (NMSC) and melanoma (MSC) skin cancers.

NMSC are characterized by a slow superficial evolution in the epidermis. They can be classified in two main types: basal cell carcinoma (BCC), concerning cells at the bottom of the epidermis, and squamous cell carcinoma (SCC) concerning cells at the top of the epidermis. Both forms are highly treatable and survival rates are relatively high. However, because it often occurs in areas easily exposed to the sunlight, i.e. around the neck and the face, it can be disfiguring. Moreover, dermatologists usually prefer to remove a large area around the tumor, whose borders are difficult to localize without appropriate imaging tools. Still, an efficient treatment is possible when an early diagnosis is performed. The risk of developing NMSC increases at lower latitude and with age, and is predominantly linked to a cumulative proportion of sun exposure and to the skin phototype. Basal cell carcinoma represents 70% of the skin cancer. It expands superficially (depth < 500 μm) and rarely metastasises unlike SCC. Consequently, it is usually not life-threatening whereas SCC can lead to death. The ability to diagnose NMSC during its early stages is essential to limit the affected area and then avoid large scares.

Melanoma skin cancers (MSC) are characterized by a transformation of the melanocytes, the cells that are responsible for the skin pigment, and can spread to other organs of the human body. Malignant melanoma is the most serious type of cancer (responsible for 75% of death related to skin cancer) but it is also the less common. MSC is characterized by a prolonged horizontal growth phase, during which the tumor grows within the epidermis but does not spread to the underlying dermis. During the second phase, the tumor expands vertically reaching the dermis and eventually can metastasise. Therefore, it is critical to detect MSC before the vertical growth phase. Although a majority of cutaneous melanomas can be recognized with naked eyes, some lesions that were previously regarded as benign might, thanks to a more careful inspection, be reconsidered as melanomas. Physicians specialized in the evaluation of pigmented lesions have a sensitivity for diagnosing of approximately 80 % and a diagnosis accuracy of 65% [1]. In addition, when it is based on ABCDE criteria [1], lesions that physicians choose to survey are often the visually worse-looking (at skin surface). However, the surface of the lesion is only the top of an iceberg whose bottom is hidden under the skin surface. A screening technique, resolved in depth, would allow a follow-up of a larger number of lesions, including better-looking ones that nevertheless might prove to be more dangerous when depth imaging is performed.

---

[1] ABCDE criteria stands for Asymmetry, Border, Colour, Diameter, Evolving which are the main characteristics that enable the differentiation between benign and malignant cutaneous lesions.

1.1.1.2/ FACTS AND FIGURES

According to the World Health Organisation (WHO), one in every three cancers diagnosed is a skin cancer which makes it the most common of all cancers. Between 2 and 3 million non-melanoma and 132,000 melanoma skin cancers occur each year. A project, named Globocan, supported by the International Agency for Research on Cancer, estimates the "incidence of, mortality and prevalence from major types of cancer, at national level, for 184 countries of the world" [globocan web site]. The figures of incidence and mortality due to melanoma in the world shows that the more concerned countries are mainly developed countries but this must be linked to the reliability of the data provided by the countries (Fig. 1.1 and Fig. 1.2) [2]. It can also be noticed that there are many differences between countries depending on latitude and thus sun exposure and the phototype of patients. According to the Skin cancer foundation, 86 % of melanomas can be attributed to exposure to ultraviolet radiation from the sun. Screening techniques have lead to an increase in the incidence of melanoma that are detected earlier. If NMSC is less dangerous, its high incidence is becoming a burden for the society as explained in [3]. Moreover, a french study reported that, in France in 2011, 10.7% of people, who have been treated for cancers, had a skin cancer [4]. Finally, in terms of number of hospital stay, NMSC is the secondary cause compared to other cancer. These figures show that skin cancer is a national and international health matter.

If the first challenge in the treatment of skin cancer is its early diagnostic, surprisingly the tools developed to help dermatologists in this matter are sparse and still very expensive. This leads to a situation where most dermatologists only have at their disposal dermoscopes and visual inspection to decide if the lesion is worth a histological examination. Histological examination is based on the examination, under microscope, of a suspected tissue that have been removed from the patient. This process is still, today, the gold standard. The dermoscope is widely used but its resolution and imaging depth are limited. Then in case of suspicion, a surgical biopsy is performed. In France, in 2010 , 65,200 patients have been treated for carcinoma but 539,000 biopsy have been performed because of skin cancer suspicion. Then, the percentage of biopsy, that gave positive results with respect to skin cancer, can be approximated to 12%. These figures show the strong need for suitable imaging techniques with the potential to help the diagnosis and reduce the number of unnecessary biopsy. New imaging techniques should be able to provide images close to histopathological views derived from the skin biopsies. Indeed, dermatologist are trained to analyse and interpret this specific type of images to make

Incidence (Age Standardized Ration per 100,000)
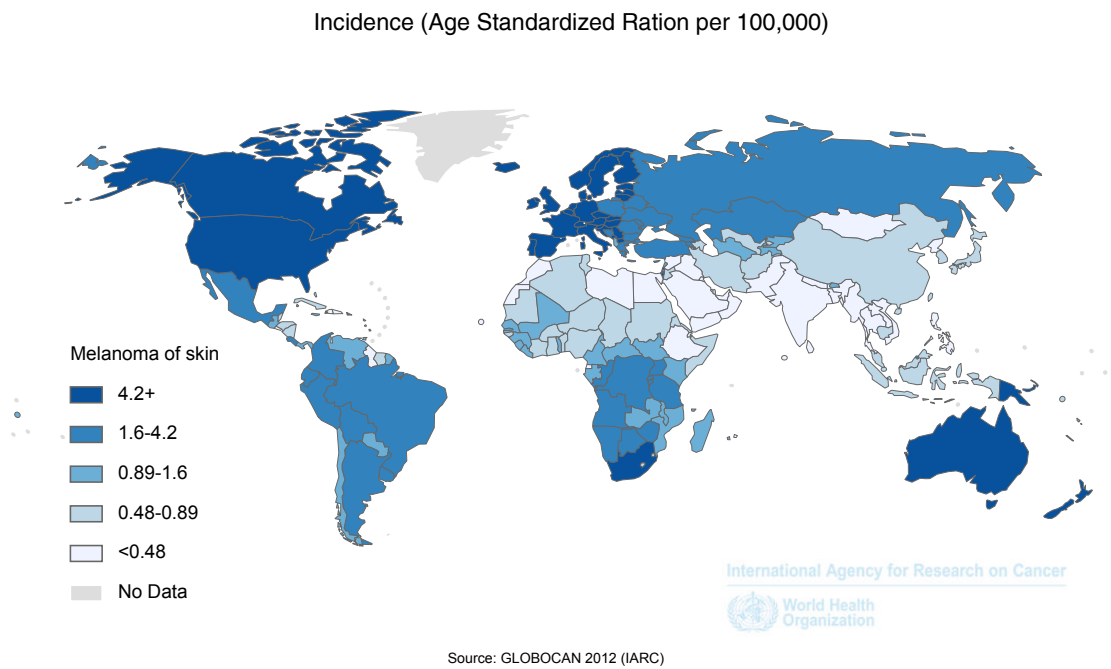
Figure 1.1: Incidence of melanoma skin cancer in the world in 2012 (source: Globocan 2012).

Mortality (Age Standardized Ration per 100,000)
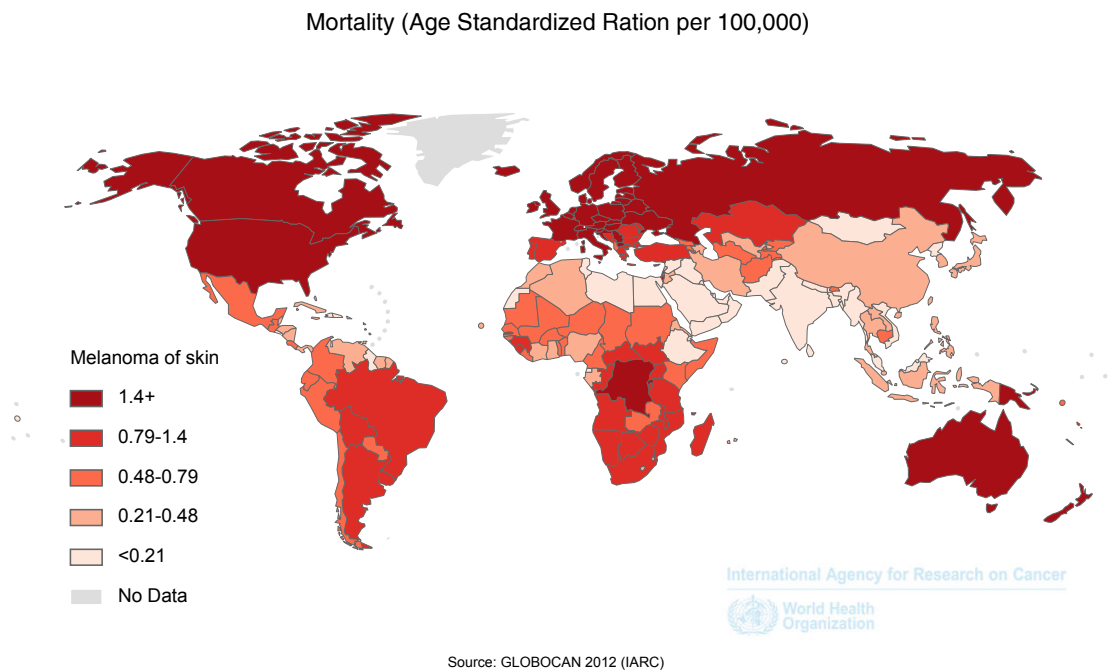
Figure 1.2: Mortality due to melanoma skin cancer in the world in 2012 (source: Globocan 2012).

their diagnosis. These views are characterized by a vertical cross-section, deep enough to see the dermal-epidermal junction (500 μm-1 mm deep), and a high resolution, that is limited by the optics (less than 1 μm), which makes possible the visualisation of cells.

Moreover, the area of exploration is usually around 5 to 8 mm enabling the visualisation of the border of the lesion and limit the surgery to the actual malignant tissues. Current diagnostic methods are based on the identification of some morphological characteristics of the pigmented skin lesions including the overall architecture of the epidermis and the density of atypical cells like mitosis (Fig. 1.3). Also the structural parameters of lesions, such as the epidermal thickness and the depth of dilated blood vessels, can be seen and used to distinguish cancerous skin from normal skin. For non-melanoma diagnosis, the loss of collagen structure and integrity is also characteristic and can be optically detected using its birefringence character. Obviously, the main drawback of the histopathology method is the necessity of a surgery to remove the lesions which consequences are potential bad scares and the impossibility to follow-up the lesions.
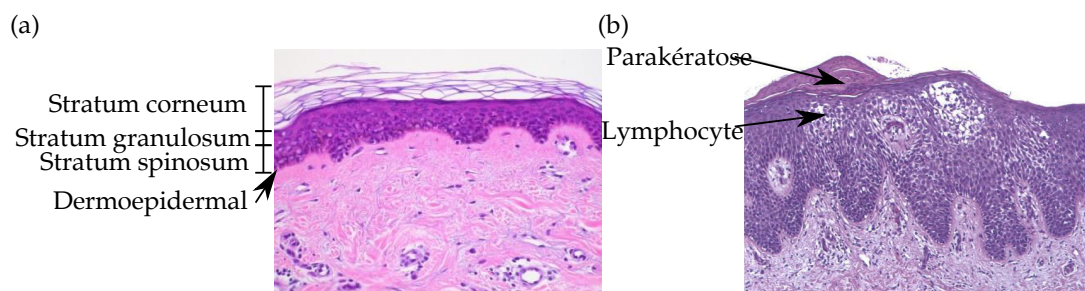
Figure 1.3: Histological images : (a) normal skin, (b) abnormal skin. Source: CHRU Besançon.

1.1.2/ IMAGING TECHNIQUES OVERVIEW

1.1.2.1/ DERMOSCOPY

The examination of skin lesions is usually performed using a dermoscope, also known as dermatoscope and epiluminescent microscope. This instrument magnifies the inspected area in order to help the inspection of a skin lesion. It also allows the visualization of the subsurface of the skin that is not visible with naked eyes. Usually, a liquid is dispensed between the instrument and the skin in order to avoid surface reflections. The optical design of a dermoscope is presented in Fig. 1.4 [5]. The main drawback of this instrument is that all the contributions from the different structures present in the skin are superimposed in a 2D image [6]. In this condition, the identification of the different structures is difficult. To overcome this issue, polarization multi-spectral dermatoscope have been developed [7]. The use of different wavelengths leads to different images specific to different components (melanin, hemoglobin,..). The polarized light enables to preferentially detect light coming from below the surface.
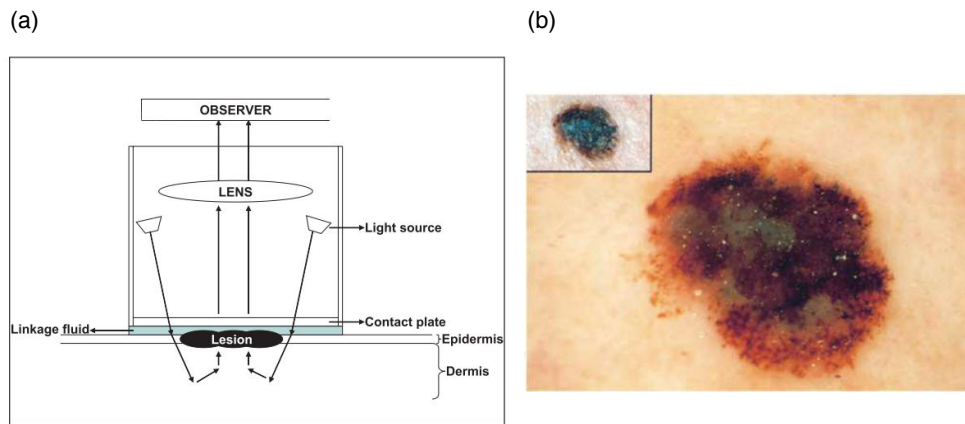
Figure 1.4: Dermoscopy : (a) schematic of the general principle, (b) comparaison of an image with a dermoscope and with naked eyes (inset) [6].

1.1.2.2/ HIGH FREQUENCY ULTRA-SOUND

High frequency ultra-sound (HFUS, 20MHz-100MHz) is used in dermatology for in-vivo measurement and imaging of skin layers. Ultrasound technique is mainly known for its ability to image foetuses. It is based on a sound wave, emitted by a transducer, that is reflected at tissues boundaries generating **echoes**. The echoes are detected back by the transducer and the time of flight allows to determine the positions of the different boundaries. The resolution obtained by this imaging technique is linked to the frequency of the emitted wave. For imaging a foetus, frequencies around 5 MHz are used, which corresponds to a resolution around 0.5 mm. At 100 MHz, the resolutions are limited to 30 μm and 11 μm for lateral and axial direction respectively. The main advantage of this technique is the possibility to image very thick structure, up to 8 mm (Fig. 1.5). The main drawback is its limit in resolution that remains lower than the cell resolution. Finally, the visualization of some tissues that are "echo-poor", like with BCC, is an issue [8].
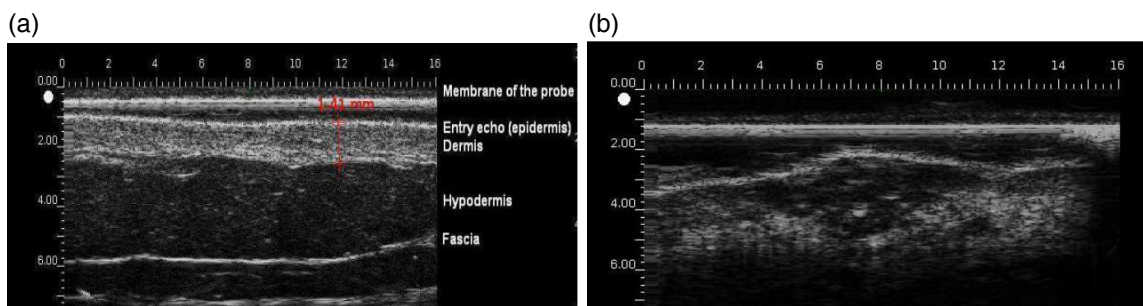
Figure 1.5: HFUS images : (a) normal skin, (b) abnormal skin. Scales are in mm [9].

1.1.2.3/ CONFOCAL MICROSCOPY

If confocal microscopy has been developed and patented in 1995 by M.Minsky, it is only recently that it has been employed in dermatology as only 6 hospitals, in France, in 2012, were equipped with such an instrument. Confocal microscopy enables in-vivo examination of biological tissues and its principle is illustrated in Fig. 1.6. The pin-hole in front of the detector plays the role of a spatial filter which enhances the resolution of the optical system. Confocal microscopy provides 2D horizontal images of the skin by scanning the focal point in the X-Y plane (Fig. 1.7) but 3D images can be reconstructed. 1 μm and 3-5 μm of lateral and axial resolutions, respectively, are reached with a confocal configuration. This leads to a cellular examination [8]. Nevertheless, the maximum penetration depth, limited by the optical penetration and the signal-to-noise ratio, is typically around 200 μm. This depth corresponds to the epidermis and sometimes the upper layer of the dermis, but is usually not sufficient. The latter is the main limit of this imaging technique together with a relatively high cost compared to standard microscopy and dermoscopy.
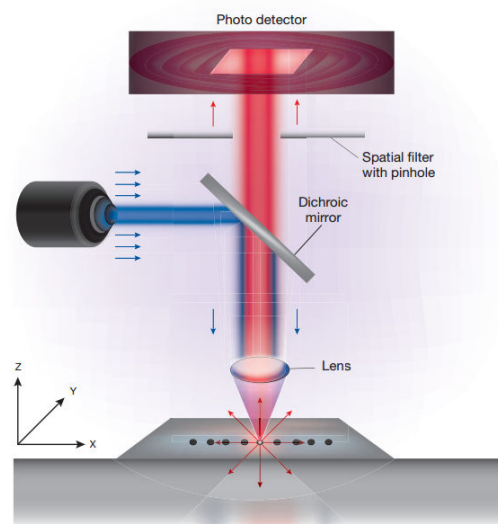
Figure 1.6: Schematic of the general principle of confocal microscopy [10].

1.1.2.4/ OPTICAL COHERENCE TOMOGRAPHY

In 1991, at the Massachussets Institute of Technology (MIT), J. Fujimoto demonstrated the Optical Coherence Tomography (OCT) technique [11]. This technique enables the in-vivo visualization of biological tissues using low coherence interferometry. It is often described as the optical counterpart of ultrasound technique as it is based on the detection of reflected light in function of the depth penetration. However, time delay of the back-reflected light cannot be measured because of the high speed of the light. The max-

(a)   (b)
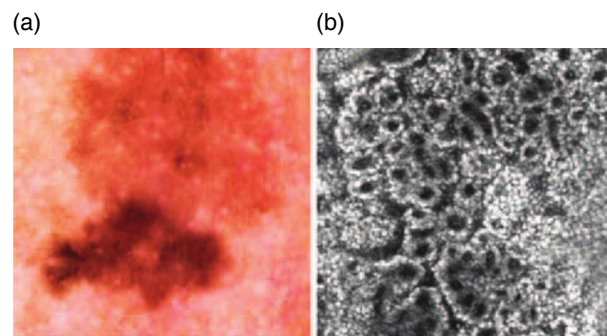
Figure 1.7: Image of a benign naevus: (a) naked eyes, (b) reflectance confocal microscope image [10].

imum penetration depth is limited to few millimetres and the axial and lateral resolution can reach 3-5 μm (cell resolution). Moreover, the cross-sectional views obtained with this technique correspond with the ones obtained from histological analysis, which is comfortable for doctors. These characteristics makes it a great candidate for tissue imaging.

Fig.1.8 summarizes the abilities of the techniques detailed above in terms of resolution and penetration depth. The OCT appears as a compromise between HFUS and confocal microscopy, providing high resolution imaging without limiting too much the penetration depth so that important features of the skin can be investigated. Ultrasounds and confocal microscopy are less adapted to morphological tissue imaging: the first provides a poor resolution and the second one does not enable millimetre penetration depth. For these reasons, OCT has been successfully introduced as an imaging system for various medical applications (ophthalmology, cardiology,...).
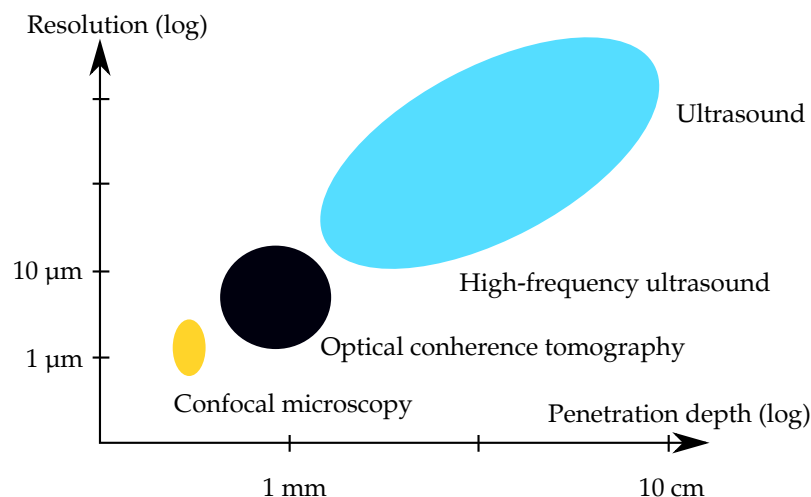
Figure 1.8: Comparison of the performances of skin imaging techniques [8].

1.2/ OPTICAL COHERENCE TOMOGRAPHY TECHNIQUES

OCT can reconstruct a depth-profile of a sample media from which 3D images can be created by scanning the light beam axially and laterally across the sample surface. Starting from the white-light interferometry for in-vivo imaging of the human eye, OCT was investigated by a wide number of groups worldwide. First in-vivo OCT images – displaying retinal structures – were published by Fujimoto group in 1991 [11]. In this first publication, the OCT scanner is defined as *"an extension of previous low-coherence reflectometer systems.(...) The heart of the system is the fibre optic Michelson interferometer, which is illuminated by low-coherence light (830 nm wavelength) from a superluminescent diode (SLD). The tissue is placed in one interferometer arm, and sample reflections are combined with the reflection from the reference mirror. The amplitudes and delays of tissue reflections are measured by scanning the reference mirror position and simultaneously recording the amplitude of the interferometric signal."*. This definition corresponds to a type of OCT called time domain OCT (TD-OCT). More recent implementations of OCT, namely the frequency domain OCT (FD-OCT), provide advantages in sensitivity, and allow faster signal acquisition. The technique has already become established as a standard imaging modality for biological tissue imaging, with numerous commercial instruments on the market. In OCT systems, the lateral resolution is determined by the size of the focal point of light source, whereas the axial resolution depends primarily on the optical bandwidth of the laser source. Thus, OCT systems may combine high axial resolutions with large depths of field. A A-scan corresponds to one axial scan in the z-direction, i.e. in depth, whereas a B-scan correspond to a cross-sectional image in depth in the x-z plane. Today, there are two major categories of OCT instrumentation: time domain OCT and frequency domain OCT, which can be divided in spectral domain OCT (SD-OCT) and swept-source OCT (SS-OCT). The formalism presented below is based on the book "Optical Coherence Tomography" edited by W. Drexler and J. Fujimoto [12].

1.2.1/ PRINCIPLES OF OPTICAL COHERENCE TOMOGRAPHY

1.2.1.1/ LOW COHERENCE INTERFEROMETRY

The principle of OCT technique is based on low-coherence interferometry (LCI). An interferometer is a setup which enables the superposition of two electromagnetic waves that can then **interfere**. Fig. 1.9 illustrates the general principle of a Michelson interferometer. The light is emitted by a source and then splitted in two different arms of the interferometer thanks to a beam splitter. In one arm the light is reflected by a mirror, called the reference mirror, and in the second arm the light is reflected by the sample under test.

The two reflected beams go back to the beam splitter where they are finally superposed. The result of the interference between the two waves depends on their optical path difference (OPD). Two limit cases occur. When there is no optical path difference (OPD=0), constructive interferences are observed, i.e. an intensity peak is measured by the detector (white fringes). The second case corresponds to an optical path difference different from 0 leading to destructive interference, i.e. no intensity is measured by the detector (black fringes).
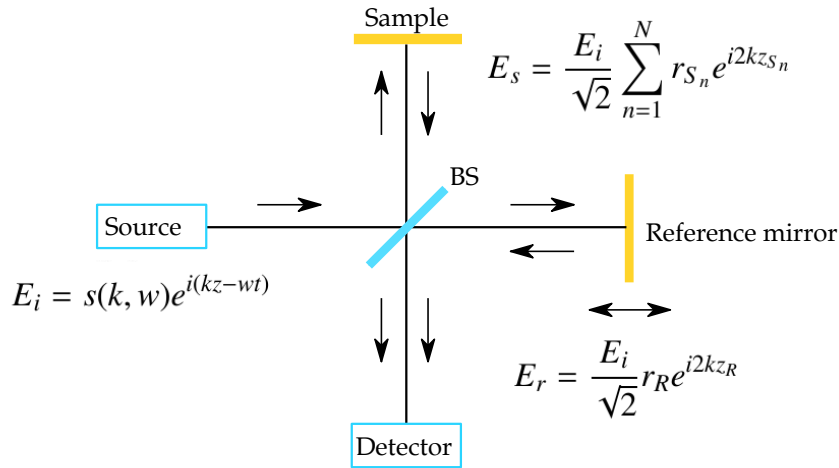
Figure 1.9: Schematic of the Michelson interferometer architecture. BS: Beam splitter of ratio 0.5.

Low-coherence interferences refer to interferences obtained with a low-coherence light source, typically a SLD, which emits a broadband spectrum:

$$E_i = s(k, w)e^{i(kz-wt)} \tag{1.1}$$

with $s(k, w)$ the electric field amplitude of the source depending on the wavenumber k and the angular frequency w. The sample is supposed to be a superposition of different layers of electric field reflectivity r_{S_n}. When low-coherence light is used, the interferences are only observed when the optical path difference between the reference arm and the sample arm, noted ζ, is inferior to the coherence length of the light source, noted l_c.

The autocorrelation function of the source, described as the temporal coherence function, represents the degree of correlation of the light :

$$\Gamma(\zeta) = \langle E_i^*(z)E_i(z+\zeta) \rangle \tag{1.2}$$

where E is the electric field emitted by the source.

This is usually normalized as:

$$\gamma(\zeta) = \frac{\Gamma(\zeta)}{\Gamma(0)} = \frac{\langle E_i^*(z)E_i(z+\zeta)\rangle}{\langle E_i^*(z)E_i(z)\rangle} \tag{1.3}$$

The normalized temporal coherence function is used to define the coherence length l_c, which corresponds to the distance within which the source is said to be coherent. Moreover, the Wiener-Khinchin theorem states that the power spectral density of the source is equal to the Fourier transform of the auto-correlation function :

$$S(k) = \int_{-\infty}^{\infty} \Gamma(\zeta)e^{(-jk\zeta)}d\zeta \tag{1.4}$$

Assuming that the light source has a Gaussian shape, the power spectral density can be written as :

$$S(k) = e^{-[\frac{(k-k_0)}{\Delta k}]^2} \tag{1.5}$$

The coherence length is defined by the full width at half maximum (FWHM) of the auto-correlation function. The autocorrelation is calculated as:

$$\begin{aligned} \Gamma(\zeta) &= \mathfrak{F}^{-1}\left(S(k)\right) \\ &= \frac{\Delta k}{2\sqrt{\pi}}e^{-(\frac{\Delta k}{2}\zeta)^2} \text{ (see Annexe A.1)} \end{aligned} \tag{1.6}$$

where $\mathfrak{F}^{-1}$ is the inverse Fourier transform and Δk is the half width of the gaussian at e^{-1}. Therefore, the coherence length is equal to:

$$\begin{aligned} l_c &= 2\sqrt{ln(2)}\frac{2}{\Delta k} \text{ (see Annexe A.2)} \\ &= \frac{4\sqrt{ln(2)}}{\Delta k} \\ &= \frac{4ln(2)}{\pi}\frac{\lambda_0^2}{\Delta\lambda} \end{aligned} \tag{1.7}$$

where $\Delta k = \frac{\pi}{\sqrt{ln(2)}}\frac{\Delta\lambda}{\lambda_0^2}$ with $\Delta\lambda$ the FWHM of the power spectral density (see Annexe A.3). This assumption is true if the bandwidth of the source is reasonably small.

When $\zeta < l_c$, the signals are strongly correlated whereas when $\zeta > l_c$, the signals are weakly correlated. The two waves interfere if their spatial delay ζ, i.e. the optical path

length difference, is smaller than the coherence length.

In practice, the interference intensity, resulting from the interferometer, is recorded. The total instantaneous field E formed by the superposition of the two fields, i.e. the field coming from the reference arm E_r and the field coming from the sample arm E_s, can be described as follows:

$$E(k) = E_r(k) + E_s(k) \tag{1.8}$$

The interference intensity is then:

$$
\begin{aligned}
I(k, w) &= \langle |E(k)|^2 \rangle \\
&= \langle | \frac{s(k, w)}{\sqrt{(2)}} r_R e^{i(2kz_r - wt)} + \frac{s(k, w)}{\sqrt{(2)}} \sum_{n=1}^{N} r_{S_n} e^{i(2kz_{S_n} - wt)} |^2 \rangle
\end{aligned}
\tag{1.9}
$$

Using the Euler's relation $e^{i\theta} = cos(\theta) + isin(\theta)$, and taking into account that the light angular frequency w is too high to be sensed by a photodetector, the real interferometric intensity signal is retrieved :

$$
\begin{aligned}
I(k) = {} & \frac{S(k)}{2} (R_r + R_{S_1} + R_{S_2} + ... + R_{S_n}) \\
& + S(k) \sum_{n=1}^{N} \sqrt{R_R R_{S_n}} cos(2k(z_R - z_{S_n})) \\
& + \frac{S(k)}{2} \sum_{n \neq m=1}^{N} \sqrt{R_{S_n} R_{S_m}} cos(2k(z_{S_n} - z_{S_m}))
\end{aligned}
\tag{1.10}
$$

where R_R and R_{S_n} are the power reflectivity of the reference and of the different layers in the sample, respectively. This equation is composed of a DC term, a cross-correlation term corresponding to the interference between the two arms and an auto-correlation term corresponding to the correlation between the fields reflected by the different layers of the sample. Moreover, it can be seen that the interferences depend both on the wavenumber k and the position of the reference mirror z_R. When the intensity are recorded as a function of the position of the mirror, we speak about time domain OCT, whereas if the interference are recorded as a function of the wavenumber, we speak about frequency domain OCT.

1.2.1.2/   TIME DOMAIN OPTICAL COHERENCE TOMOGRAPHY

Figure 1.10 shows a scheme of the basic time domain OCT (TD-OCT) architecture. It is based on a Michelson interferometer composed of a reference arm and its reference mirror and of a sample arm in which light is focused into the sample. The interference signal between the reflected reference wave and the backscattered sample wave is then recorded. The mirror is axially scanned and an intensity peak is only detected when the light from the reference and sample arms have travelled the same optical path difference and when the optical path lengths differ by less than the coherence length of the light source. The interference pattern is recorded as a function of time, i.e. for each position of the reference mirror (z_r). By this method, it is possible to reconstruct the tomography of biological tissues. The axial resolution corresponds to the coherent length and the lateral resolution depends on the objective used to illuminate the sample, i.e. the focal spot diameter.

By scanning the mirror longitudinally and laterally, a 2D cross-section can be recovered. However, the acquisition speed is limited by the mirror scanning time.

The intensity measured by the detector is calculated by integrating Eq. 1.10 over k. It results in :

$$I(\zeta) = \frac{S_0}{2}(R_r + R_{S1} + R_{S2} + ... + R_{Sn})$$
$$+ S_0 \sum_{n=1}^{N} \sqrt{R_R R_{Sn}} e^{-\zeta^2 \delta k^2} cos(2k_0\zeta) \tag{1.11}$$

The auto-correlation term equals zero because $z_{Sn} - z_{Sm} > l_c$, then, temporally, the beams reflected by the different layers do not interfere.

(a)   (b)
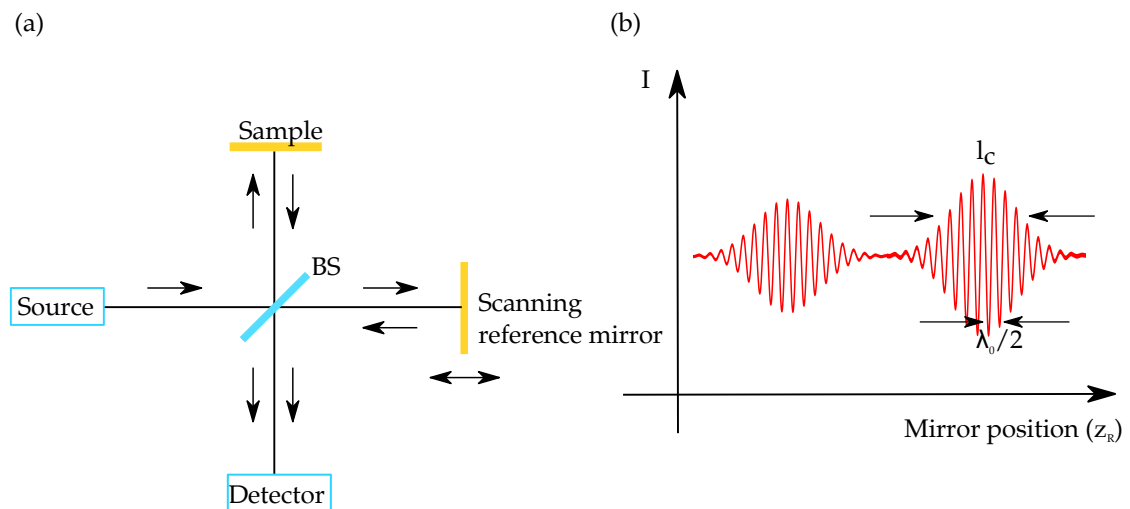
Figure 1.10: TD-OCT: (a) schematic of the general principle, (b) temporal interferogram.

1.2.1.3/   FREQUENCY DOMAIN OPTICAL COHERENCE TOMOGRAPHY

Figure 1.11 (a) shows the basic frequency domain optical coherence tomography (FD-OCT) set-up where most of the components are identical to the set-up of the TD-OCT. The key difference is that for FD-OCT systems the reference arm length is fixed, i.e. the reference mirror does not move. Instead of obtaining the depth information of the sample by scanning the reference arm length, the output light of the interferometer is processed by a spectrometer, i.e. a diffraction grating combined with a line camera (Fig. 1.11 (a)). This type of FD-OCT is called spectral domain OCT (SD-OCT). The numerical Fourier transform (FT) of this spectrum contains the axial A-scan over a scan range which is proportional to the coherence length of the source. The signal, as a function of z, is retrieved by doing the Fourier transform of $I(k)$ and it can be shown that:

$$
\begin{aligned}
I(z) = &\frac{1}{4}[\Gamma(z)(R_r + R_{S1} + R_{S2} + ... + R_{Sn})] \\
&+ \frac{1}{2}[\Gamma(z) \otimes \sum_{n=1}^{N} \sqrt{R_R R_{Sn}}(\delta(z \pm 2(z_R - z_{S_n})))] \\
&+ \frac{1}{4}[\Gamma(z) \otimes \sum_{n=1}^{N} \sqrt{R_{Sn} R_{Sm}}(\delta(z \pm 2(z_{Sn} - z_{Sm})))]
\end{aligned}
\tag{1.12}
$$

where Γ is the auto-correlation function, δ is the Dirac function and $\otimes$ is the convolution operator. $(z_R - z_{S_n})$ and $(z_{Sn} - z_{Sm})$ are optical path differences depending on n_{index}, the refractive index of the medium in the reference arm (usually air) and in the sample. In each term, there is a mirror term coming for the Fourier transform, resulting from the $\pm$ sign. These are artefacts specific to the Fourier transform.

The typical signal obtained in frequency domain OCT (FD-OCT) is presented in Fig. 1.11 (b).

Compared to TD-OCT, the SD-OCT configuration improves imaging speed, while the Fourier transform operation, associated to the acquisition of the signal, improves the signal to noise ratio (SNR) which is inversely proportional to the number of detector pixels. However, the dynamic range is reduced with respect to TD-OCT because of the lower dynamic range of the spectrometer with respect to single photosensitive diodes. Indeed, the line cameras usually have a reduced dynamic range compared to single photodiodes to make the transfer of data faster.

A variant of OCT, called swept-source OCT (SS-OCT), tries to combine some of the advantages of standard TD and SD-OCT. Here, the spectral components are not encoded by their spatial separation but the wavelength scanning is obtained via a frequency-scanned light source or by using a wavelength-tunable Fabry-Perot cavity. The goal is to sweep rapidly through a range of wavelengths, allowing the spectral interferogram to

(a)

(b)
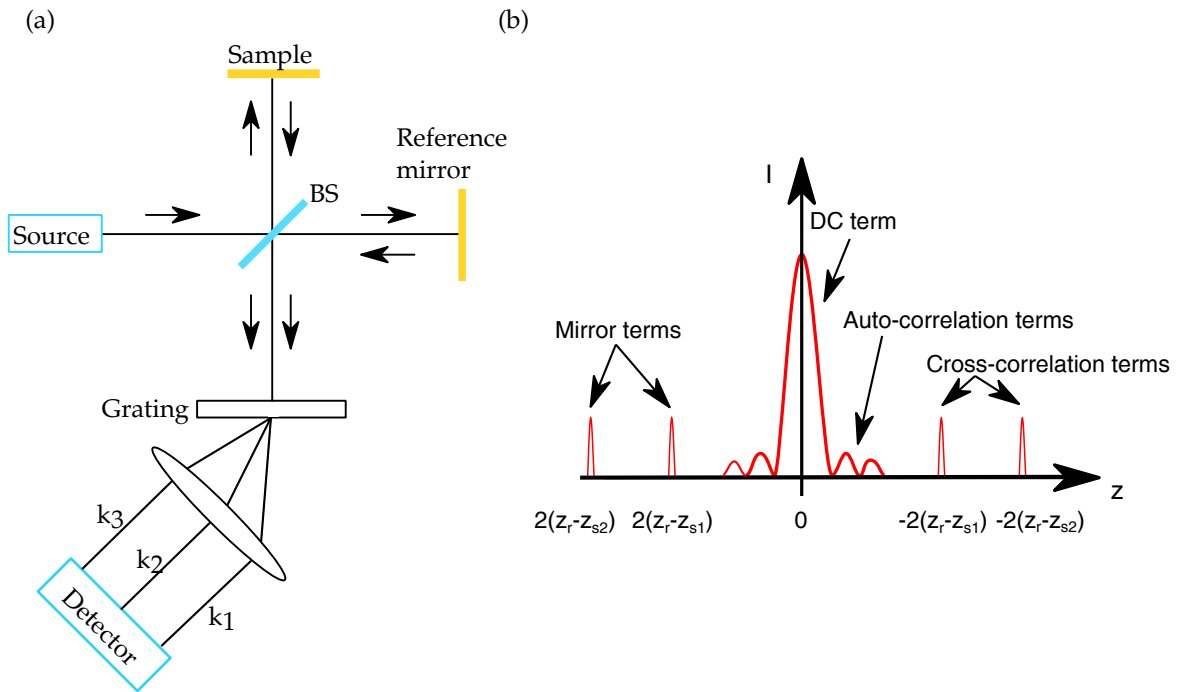
Figure 1.11: SD-OCT: (a) schematic of the general principle, (b) spectral interferogram.

be recorded sequentially. Here, the advantage lies in the proven higher SNR detection of SS-OCT compared to TD-OCT, together with the advantage of using a point detector providing a higher dynamic range compared to FD-OCT. Moreover, a line camera, which has a limiting frame rate, is no more necessary. Indeed, in this configuration, the time to record the spectral interferogram is mostly linked to the sweeping speed of the source since the detector can be a photodiode. Then SS-OCT is usually faster than other OCT. Finally, tremendous developments have recently been achieved in swept laser sources providing fast light source. Table 1.1 summarizes what component of the OCT systems typically limits their speed and their corresponding A-scan rates.

Table 1.1: Comparison of typical limiting frequencies in the different type of OCT systems and their corresponding A-scan rates.

OCT system type	Limiting components	Typical A-scan rate
TD-OCT	Vertically scanning mirror frequency	Few kHz
SD-OCT	Line camera frequency	46 kHz [13]
SS-OCT	Swept-source frequency	350 kHz [14]
FF SS-OCT	Swept-source frequency x Number of pixels	1.5 MHz [15]

1.2.1.4/ FULL-FIELD OPTICAL COHERENCE TOMOGRAPHY

The techniques presented above are based on point-by-point imaging. Hence, a linear scan yields to a 2D data set corresponding to a cross-sectional image (X-Z planes, B scan), and finally 3D images are obtained by 2D scanning (X-Y-Z volumic scan). In 2002, A. Dubois proposed a full-field time domain OCT, based on a spatially incoherent light source [16] and leading to a 3D image. The sample is full-field illuminated and imaged with a CCD[2] camera, so that 2D "en face" images are recorded without requiring a lateral scan anymore. In such a case, Nyquist criteria must be respected, i.e. the lateral resolution in the object plane, must be imaged with at least two pixels in the image space. Then, the magnification of the optical system, in the imaging arm, must be chosen accordingly. In miniaturised systems, the optical design is constrained by the small size and then by relatively short focal lengths. A trade-off between pixel size, resolution and magnification must be found.

1.2.1.5/ RESOLUTION AND SENSITIVITY IN FREQUENCY DOMAIN OPTICAL COHERENCE TOMOGRAPHY

Resolution OCT systems are characterized by their resolution capabilities, their imaging depth and their acquisition speed.

On the first hand, the smaller axial distance between two layers that can be resolved, i.e. the axial resolution, depends on the coherence length. It is equal to l_c and the physical distance noted δz is $l_c/2$:

$$\delta z = \frac{l_c}{2} = \frac{2ln(2)}{\pi} \frac{\lambda_0^2}{\Delta\lambda} \tag{1.13}$$

where λ_0 is the central wavelength and $\Delta\lambda$ is the FWHM of the power spectral density.

However, the geometrical optics can also be taken into account in the axial resolution of the system and a more general expression is obtained [17]:

$$\delta z = [\frac{NA^2}{n\lambda} + \frac{2}{l_c}]^{-1} \tag{1.14}$$

This expression is particularly used for the case of full-field OCT, in which en-face (x-y plane) images are targeted and for which higher numerical aperture objectives can be used. However, in practice, low numerical aperture objectives are used. In this case, the axial resolution only depends on the coherence length (Eq. 1.13) and the contribution from the optics can be neglected.

---

[2]Charge-Coupled Device

The lateral resolution is defined based on the Rayleigh criteria[3]:

$$\delta x = 1.22\lambda\frac{f}{D} \tag{1.15}$$

where f and D are the focal length and the diameter lens of the objective lens and the factor "1.22" corresponds of the first zero of the Bessel function which describes the Airy spot.

The axial field of view, linked to the coherence length of the swept-source, corresponds to the FWHM of the coherence function of the tuned light source. The same calculation, as shown in 1.7, is done and the axial field of view is obtained

$$FOV_{axial-coherent} = l_c = \frac{4ln(2)}{\pi}\frac{\lambda_0^2}{\delta\lambda} \tag{1.16}$$

where $\delta\lambda$ is the source linewidth.

However, the axial field of view can also be limited by the geometrical optics. In optical microscopy, in the paraxial approximation, the axial field of view is defined as [18]:

$$FOV_{axial-geometric} = 1.77\frac{\lambda}{NA^2} \tag{1.17}$$

Figure 1.12 represents the light beam shape and the corresponding axial field of view.

Sensitivity   In OCT systems, the sensitivity is defined as the minimal sample arm reflectivity for which the signal to noise ratio equals 1. The typical noises to be taken into account when dealing with optical detection are the shot noise, the excess noise and the receiver noise. The shot noise is linked to the particle nature of light. The detector counts a number of photons that follows a Poisson distribution. This fluctuation generates the shot noise. The excess noise is the noise linked to the amplification of the signal. Finally, the receiver noise is the sum of the dark noise of the detector and the read noise. The read noise consists of thermal noise called Johnson noise and the electronic noise (mainly coming from the Analog to Digital Converter). The sensitivity will not be calculated here, however [19] gives a full explanation of the noise sources and compare the performances of FD and TD-OCT. It is shown that FD-OCT benefit from a much higher sensitivity, even when it comes to low power levels and high speed detection. Moreover, Choma *et al.* showed that the benefit in terms of sensitivity of SS-OCT and FD-OCT over TD-OCT is typically of 20-30 dB [20].

---

[3]Rayleigh criteria : Two infinitely small points in the object plane can be resolved in the image plane if the maximum of the Airy disk of one point coincides with the minimum of the Airy disk of the other point.
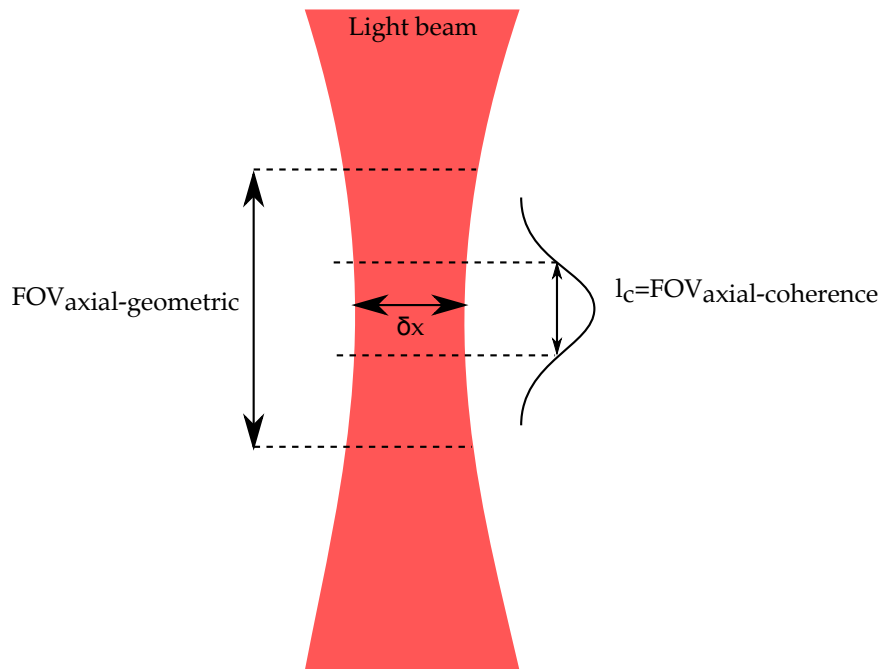
Figure 1.12: Axial field of view axial based on the coherence of the wavelength tunable light source and on the optics.

The sensitivity of the system can be enhanced if the parasitic terms, i.e. the mirror term (complex conjugate term) and the DC term are suppressed. Indeed, the spatial interferogram retrieved in FD-OCT is symmetrical with respect to the zero path difference position. Then, there is an ambiguity between the real sample location signal and its complex conjugate. To avoid this problem, the zero-path difference location is usually chosen to be out of the sample so that the signals coming from the sample layers have always a positive path difference. This solution leads to an imaging depth divided by two compared to the maximum imaging depth. Moreover, the finite sampling generates a sensitivity decrease with depth and the depth corresponding to a decrease of 6 dB can be calculated and equals the coherence length. Therefore, the sensitivity of an OCT system is better if the sample is placed close to the zero-path difference location, i.e. the DC term. To remove the parasitic terms (DC, auto-correlation and mirror terms), phase-shifting interferometry techniques can be used. A comparison of different phase shifting technique is presented in [21].

Phase-shifting   To remove the complex-conjugate term, the auto-correlation term and the DC term, a 4 stepped phase-shifting algorithm can be used. The idea is to create an additional known phase difference 2ϕ between the reference arm and the sample arm. If the phase difference is chosen properly then the terms cancel. To eliminate the DC term and the autocorrelation term, two spectral interferograms with a phase difference

of π radians are subtracted. Finally, two spectral interferograms with a phase difference different from π radians are subtracted to remove the complex conjugate. The use of the four phase-shifted interferogram leads to the following result:

$$I_D(k, 2\phi = 0) - I_D(k, 2\phi = \pi) + j[I_D(k, 2\phi = \pi/2) - I_D(k, 2\phi = 3\pi/2)] =$$

$$[S(k) \sum_{n=1}^{N} \sqrt{R_R R_{S_n}}(cos(2k(z_R - z_{S_n})) - jsin[2k(z_R - z_{S_n})])] \tag{1.18}$$

And in the spatial domain, one obtains:

$$i_D(k, 2\phi = 0) - i_D(k, 2\phi = \pi) + j[i_D(k, 2\phi = \pi/2) - i_D(k, 2\phi = 3\pi/2)] =$$

$$\sum_{n=1}^{N} \sqrt{R_R R_{S_n}}[\gamma(2(z_R - z_{S_n})) + \gamma(-2(z_R - z_{S_n}))$$

$$+ \gamma(2(z_R - z_{S_n})) - \gamma(-2(z_R - z_{S_n}))]$$

$$= \sum_{n=1}^{N} \sqrt{R_R R_{S_n}}\gamma(2(z_R - z_{S_n})) \tag{1.19}$$

The phase difference can be implemented by moving the reference mirror that is usually not moving in FD-OCT. The 4 stepped phase-shifting algorithm is a standard for the elimination of the artefact terms. However, it requires a precise control over the light phase. When an actuated micromirror is used, it means that the displacement of the micromirror must be precisely controlled. Moreover, when actuated dynamically, micromirrors are usually driven by a sinusoidal signal. In this case, the use of the 4 stepped algorithm limits the use of the actuator movement to its linear part to obtain images with a constant phase shift of $\pi/2$ evenly spaced in time.

Another solution has been proposed by Sasaki *et al.* referred to as sinusoidal phase-modulating interferometry [22, 23]. The algorithm is based on the sinusoidal displacement of the reference mirror, taken into account in the interference term by adding the term $Acos(w_a t + \theta)$ to the phase difference $k(z_R - z_{S_n})$ and $k(z_{S_n} - z_{S_m})$ in Eq. 1.10. This gives:

$$I(k) = \frac{S(k)}{2}(R_r + R_{S_1} + R_{S_2} + ... + R_{S_n})$$

$$+ S(k) \sum_{n=1}^{N} \sqrt{R_R R_{S_n}}cos(\phi_{R-n} + Acos(w_a t + \theta))$$

$$+ \frac{S(k)}{2} \sum_{n \neq m=1}^{N} \sqrt{R_{S_n} R_{S_m}}cos(\phi_{n-m} + Acos(w_a t + \theta)) \tag{1.20}$$

where ϕ_{R-n} and ϕ_{n-m} are the phase differences of the correlation and the autocorrelation terms, respectively, w_a is the actuation frequency, and A and θ are the amplitude and the initial phase of the sinusoidal vibration, respectively. By applying a Fourier transform with respect to the time t noted $\mathfrak{F}(I(k,w))$, it is possible to isolate some specific values for $w = w_c$ and $w = 2w_c$. Then, a Fourier transform is finally applied to reconstruct the spatial interferogram which is free of mirror terms (see Annexe A.4).

$$\hat{I}(z) = \sum_{n} \sqrt{R_R R_{S_n}} \Gamma \left(z - (z_R - z_n) \right) \tag{1.21}$$

where Γ is the auto-correlation function.

The formalism is presented in [23].

1.2.2/ OPTICAL COHERENCE TOMOGRAPHY IN DERMATOLOGY

In their first article, in 1991, J. Fujimoto *et al.* had already demonstrated the potential of OCT systems for imaging biological tissues with tests on retina and coronary artery. These two applications have contributed to the success of OCT and are still today the main domains for which commercial OCT systems are developed. In 1992, only one year after the demonstration of the OCT technique, the first OCT system for ophthalmology has been commercialized by Advanced Ophtalmic Devices, now known as Zeiss Meditec. Indeed, OCT has revolutionized the clinical practice of ophthalmology enabling retinal imaging. It has provided a quantitative method to help the diagnostic, evaluate surgical interventions and monitor the effect and the development of a disease with respect to treatments. Cardiology also benefited from OCT technique. In 2010, LightLab commercialized the first OCT system for cardiovascular imaging after it got clearance from the Food and Drug Administration. This technique provides coronary imaging and help for stents appositions and information regarding the stent dissolution with time [24]. The annual growing rate of the OCT market is 45 % and has reached 400 million of dollars in 2013 with 36 companies [25]. More recently, in 2014, an analysis done by Tematys on the OCT technology and market has been released and shows the great potential of this high resolution imaging technique for medical applications. According to this analysis, the market should grow up to 1 billion euros in 2019 with a need for low-cost and compact system for dentist and dermatologist offices. Moreover, it has been observed that better resolution and faster acquisition are of great interest. This should be taken into account by shifting from time domain OCT to frequency domain OCT.

1.2.2.1/ COMMERCIAL OPTICAL COHERENCE TOMOGRAPHY SYSTEMS FOR DERMA-
TOLOGY

Although histopathology is still considered as the gold standard for the morphological
evaluation of the skin, non-invasive OCT imaging techniques are becoming a focus of
interest. Compared with histopathology investigation, they exhibit several advantages:
(1) they are non-invasive allowing a view of the unaltered morphology of structures, (2)
they provide a real-time inspection of the skin which results in a faster diagnosis and
(3) they provide the possibility of the lesion follow-up. Consequently, early diagnosis
and follow-up of cutaneous lesions, which are keys for the success of the treatments, is
possible. Moreover, dermatologists lack of data on the diseases evolution as a function of
time and the possibility of follow-up given by the OCT techniques is a real benefit. Two
OCT systems, applied to dermatology, are now commercially available: "VivoSight" from
Michelson Diagnostics and "Skintell" from Agfa HealthCare, both released in 2011 and
owing a certificate for clinical use. More recently, in 2014, MedLumics released NITID,
a system combining epiluminescence microscopy, i.e. dermoscopy and OCT. They also
expect to release a new device, called BiopsyPen by 2017. However, there is not much
information about these MedLumics' devices. The characteristics of the Skintell and the
Vivosight are summarized in the Tab. 1.2.

Table 1.2: Comparison of the specifications of commercial OCT system and requirements
for the diagnosis of skin cancer [26].

System	Michelson diagnostics	AGFA Healthcare	Specification for skin cancer
Lateral Resolution	$< 7.5 \ \mu m$	$3 \ \mu m$	$\sim 5 \ \mu m$
Axial Resolution	$< 5 \ \mu m$	$3 \ \mu m$	$\sim 5 \ \mu m$
Depth	1.2 to 2.0 mm	1.0 mm	$800 \ \mu m$
Image size	6x6 mm	1.8x1.5 mm	6x6 mm
Wavelength	1305 nm	1300 nm	
A-scan rate	20 kHz	320 kHz	fast
Type	SS-OCT	TD-OCT	
Cost	90 k€	90 k€	low

Michelson Diagnostics' device is based on multi-beam SS-OCT. Four laser beams are used
to maintain high resolution of the system while increasing the axial field of view. Indeed,
each laser is used to image at different depths of penetration maintaining a good resolu-
tion for each of the four acquisitions. AGFA Healthcare device is a TD-OCT where the
coherence gate and the focal plane are maintained at the same depth [27]. This provides

a higher lateral resolution thanks to a high numerical aperture optic while scanning in depth with the reference mirror. There are two main differences between these two systems: the resolution and the image size. From dermatologists' point of view, it is important to have a large field of view in order to visualize the borders of a lesion. An adapted field of view, in the case of imaging skin lesions, is around 8x8 mm^2. Moreover, the ability to have a high resolution image on a specific location is also interesting. Then, the ideal OCT would have the image size of the Vivosight and the resolution of the Skintell. The last column of Tab. 1.2 summarizes the needs expressed by dermatologists. The resolution is set by the cell size. The image size is chosen in order to be able to visualize the entire lesions and help the dermatologists during a surgical biopsy if needed. Finally, the required image depth corresponds to typical depths for early stage tumors, the dermo-epidermal junction being a key feature. If these specifications meet a specific demand for the early diagnosis of skin cancer, one can think that it can be used for many other diseases such as psoriasis and hemangioma or even other applications such as the study of the impact of cosmetics on the skin [28, 29]. Note that other imaging systems are used in dermatology such as the Siascope and Melafind, utilizing multispectral imaging methods and the VivaScope system, utilizing confocal laser scan technology. For this thesis, we consider only the diagnosis of skin cancer using OCT systems which is described in the following.

1.2.2.2/ DIAGNOSIS OF SKIN CANCER USING OPTICAL COHERENCE TOMOGRAPHY

The imaging in depth of the skin requires that the light penetrates in the skin. Therefore, the choice of the light source wavelength is critical to limit absorption and scattering. On the one hand, absorption is minimised for wavelengths between 700 and 1,300 nm . On the other hand, in this window, scattering decreases for higher wavelengths. As a result, 1,300 nm is an appropriate wavelength to obtain higher penetration depth. However, wavelengths around 800 nm lead to better image contrast [30]. In 2006, a study on the optical properties of normal and cancerous human skin showed the difference in absorption and/or scattering between healthy and cancerous skin [31]. Wavelengths ranging from 370 to 1,600 nm were studied. It results that there is a significant decrease in the scattering of normal and cancerous tissues from 1050 to 1400 nm.

Invasive histopathological evaluation is the gold standard for interpreting and monitoring of morphological progress in skin pathologies. Real-time OCT imaging performs tomographic skin tissue imaging which is highly sensitive to the local variations of optical properties. Thus, the multilayer structure of skin depicts different optical properties according to differences in refractive index, relative thickness, and variation in organic/inorganic components (keratin, water, fat, etc ...). Furthermore, due to high resolution and

efficiency to reflect the compositional aspects of the tissue in terms of optical properties, these tomographic images can be correlated with the histopathological images. Figure 1.13 shows a typical OCT image of normal skin and Fig. 1.14 shows the correlation of OCT and histopathological images for normal skin and skin cancer.
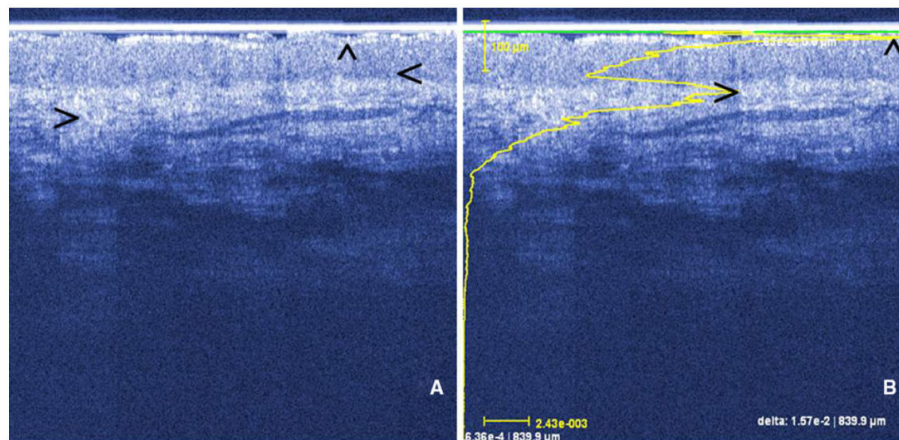
Figure 1.13: OCT image (B-scan) of normal human skin : a) ″cap″ symbol: entrance echo, ″less than″ symbol : epidermis border, ″greater than″ symbol: collagen bundles, b) A-scan with two intensity peaks corresponding to junctions.[30].
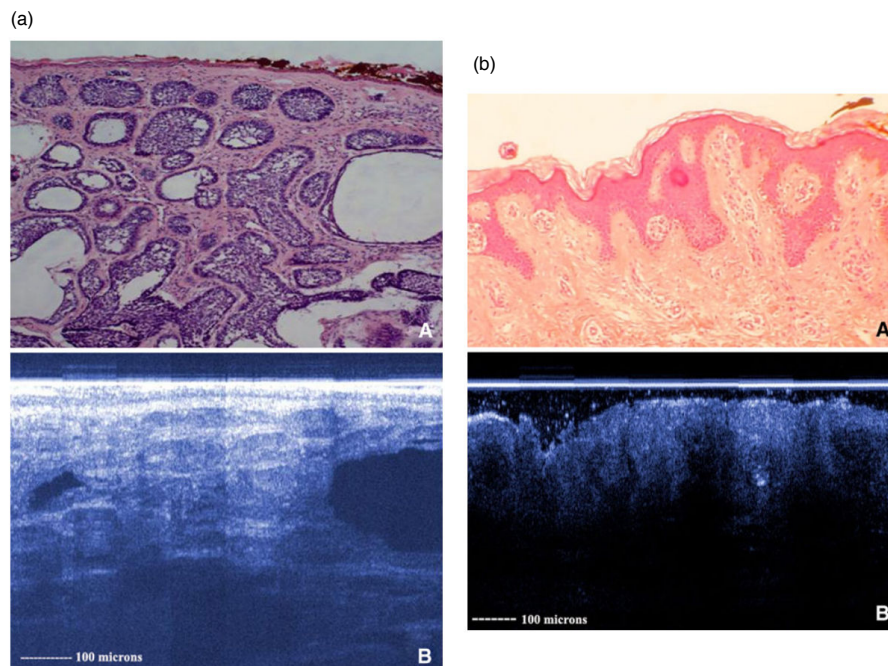
Figure 1.14: Correlation of histological (A) and OCT images (B). (a) basal cell carcinoma with oval tumour nodules, (b) melanocytic naevus with dense naevus cell clusters.[30].

In [32], the specific features of SCC, BCC and melanocytic lesions are described. For BCC, the tumor aggregates and the epidermis appears similarly on OCT images. More-

over, large blood vessels are present in upper part of the dermis, above the tumor. SCC are characterized by a signal reflection at the surface of the tumor and a shadow below due to its strong keratinization. Finally, in the case of benign melanoma, large nests of nevus cells are observed and, in general, for melanoma strong scattering areas are typical. Moreover, in [30], large vertical, icicle-shaped structures are shown to be the most striking feature in OCT image to differentiate benign from malignant melanoma. These studies agree on the potential of OCT for a differential diagnosis between SCC and BCC and studies are progressing for the differentiation of malignant and benign tumors with OCT images. However, systematic studies on the correlation of OCT and histopathological images are still lacking and the interpretation of OCT images is difficult. This can be explained by the difference of the two techniques and in particular the conditions of observation which is in-vivo for the OCT techniques and ex-vivo for the histopathology technique. This implies that the skin shape changes after it has been removed, but the substances used for the colouring of the image also modify the aspect of the skin for a better visualization. Finally, histopathological examination is a direct observation of the structure whereas the refractive index of the skin must be taken into account in the OCT measurements. These different aspects are responsible for a significant distortion between the two types of images.

1.3/ Miniaturization of optical coherence tomography systems

The miniaturization of the OCT makes possible a reduction of its size but also of its cost thanks to batch fabrication. The miniaturization of the system gives the possibility to access any body zones with a maximum of flexibility and leads to multi-functional devices. It also makes possible the fabrication of endoscopic heads for the inspection of tissues inside the body. This section reviews the state of the art of miniaturized OCT systems and more specifically the miniaturization of the interferometer which is the core of the OCT. OCT systems are complex systems composed of many optical components such as a source, an interferometer with a reference mirror that can be actuated, sometimes a lateral scanning mirror, some imaging lenses and an optical detector. The challenge is to miniaturize all these parts and assemble them. The less assembly is required, the higher is the degree of integration of the different optical/mechanical part.

1.3.1/ STATE OF THE ART

1.3.1.1/ FIBER-BASED SYSTEMS

A first degree of miniaturization has been possible thanks to the development of optical fibers. The latter have been widely used for imaging devices and are more particularly interesting for endoscopic systems. The main advantage of optical fibers is that the bulky parts of the optical system can be separated from the endoscopic imaging head. Typically, OCT systems in which the interferometer is deported from the measurement head have been developed. In these systems, the interferometer is realized by coupling of two fibers. In Fig. 1.15, an original architecture of OCT imaging system is presented based on fiber-bundle by Xie *et al.* [33]. The system can achieve a lateral resolution of 12 μm and an axial resolution of 10 μm using a superluminescent diode source. The interest of this system is to eliminate any moving parts within the probe. Instead, the scanning head is located at the entrance of the fiber-bundle which leads to a less bulky probe in contact with the sample. Indeed, only imaging lenses are necessary at the output of the fiber-bundle since the latter maintains the spatial scanning between the entrance and the output of the fiber. Moreover, the interferometer is also based on fibers. The flexibility of design linked to the use of fibers explains that the major part of the OCT systems presented in the literature are fiber-based.
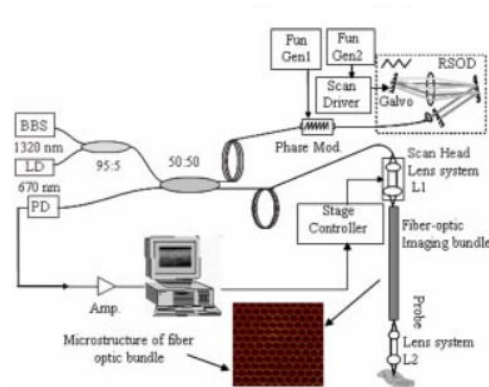
Figure 1.15: Fiber-based OCT system with a fiber-optic imaging bundle used to maintain the spatial scanning between the entrance and the exit of the fiber [33].

1.3.1.2/ MICRO-FABRICATION-BASED SYSTEMS

Research results have shown the great potential of the miniaturisation of OCT imaging systems by incorporating MEMS components and micro-optical components, combined with fiber optics based interferometers. MEMS components show several interests: (1)

MEMS devices are small, (2) MEMS scanners can operate at high speed for real-time imaging, (3) the cost of MEMS devices can be low due to the mass production capability and (4) their power consumption is generally low. Various solutions for the implementation of a lens and of a scanning mechanism in OCT systems have been studied in the literature [34]. In particular MEMS fabrication techniques have been widely used for the realization of scanning mechanisms based on actuated micromirrors. The main reason is that OCT systems used, in the past, galvanometer mirrors to scan the light beam across the sample but this technology is limited to 1D scanning and was quite bulky. Reversely, MEMS micromirrors provide 2D scanning within a small footprint area. Several actuation principles have been experimented such as electrothermal, electromagnetic and piezoelectric [35]. A comparison of these technologies is made in Chapter 2. To name but one, Pan *et al.* reported an electrothermal MEMS OCT scanning head with the interferometer part created by use of two coupled fibers (Fig. 1.16, [36]). The image area scanned is 2.9 mm x 2.8 mm. For skin imaging, this image size limits the visualization of an entire lesion that is essential for an effective surgery.
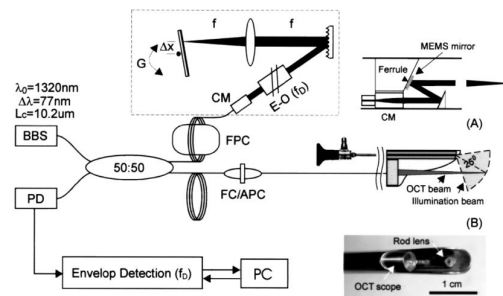
Figure 1.16: Fiber based OCT system with a MEMS scanning based on electrothermal actuation [36].

Very recently, in 2014, Lu *et al.* presented a handheld, ultrahigh speed, swept-source optical coherence tomography instrument using a MEMS scanning mirror dedicated to retinal imaging [14]. The source used is a vertical cavity surface-emitting laser (VCSEL) operating at 1060 nm. 6x6x3 mm^3 volumetric OCT data were generated each 1.4 seconds with an axial resolution of 10 μm in tissue. The handheld system is very compact thanks to the use of fibers that enables the separation of many parts such as the reference arm. Figure 1.17 illustrates the concept. The light goes out the optical fiber, is reflected onto the MEMS scanning mirror and onto another fixed mirror that target the light beam into the eye. Visible light is used to illuminate the iris and an image of the eye is recorded on a camera. A led is also used to see the target point of the SS-OCT with visible light.
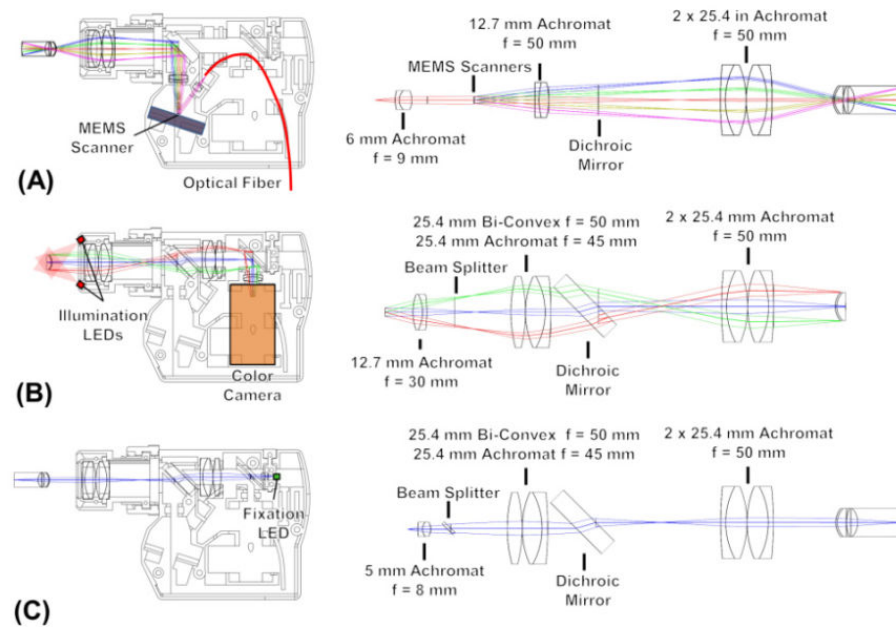
Figure 1.17: Handheld OCT instrument internal optical layout and unfolded optical components showing the (A) OCT 1060 nm optical path, (b) iris camera visible optical path, and (C) fixation target visible optical path [14].

Not only the scanning mirrors have benefited from the microfabrication techniques but other parts of OCT systems have also been investigated in terms of miniaturisation. One of these components is the interferometer. Already in 1997, an original approach was demonstrated by C. Gorecki where a waveguided Mach-Zehnder interferometer is integrated on a silicon substrate [37]. The reference arm integrates a thin film transducer for active sinusoidal phase modulation giving a sensing function to the device. Another example is the realisation of a Fizeau interferometer based on an ultra thin photodiode by the Tohoku University [38]. In 2001, an integrated optical sensor chip in glass has been presented, including eight waveguided interferometers realized on a glass substrate [39] for OCT applications. Finally, Yurtsever *et al.* proposed, in 2008, a Michelson interferometer based on SOI [40, 41] and, in 2014, another photonic integrated interferometer based on Mach-Zehnder configuration [42]. In the latter, the waveguide technology is based on a technology developed by LioniX BV called Triplex, that is based on a high index-contrast waveguide structure including a core in SiO_2 that is surrounded by Si_3N_4 (Fig. 1.18).
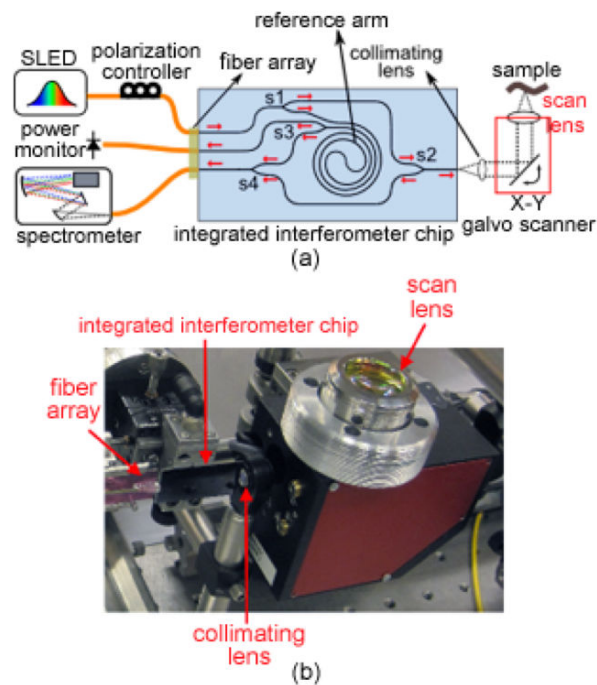
Figure 1.18: Photonic integrated interferometer based on silicon technology: a) schematic of principle, b) photograph of the prototype. [42]

Another component, necessary for FD-OCT, is the spectrometer. R.F. Wolffentbuttel reviews different solutions for the fabrication of MEMS-based microspectrometers in silicon [43]. Moreover, in 2012, Akca *et al.* developed a solution for the implementation of SD-OCT with the integration of a spectrometer based on an array of waveguides made from silicon oxynitride technology (Fig. 1.19) [44].
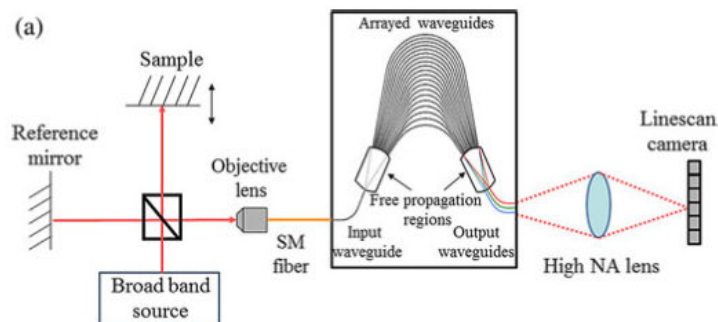
Figure 1.19: Schematic of principle of an integrated spectrometer realized with an array of waveguides based on oxynitride technology [44].

Finally, a very advanced system using micro-optical components is proposed by Aljasem *et al.* [45]. A membrane-based microfluidic tunable microlens is used for the tuning of the beam focus allowing to achieve high resolution over a wider range of depth scan and

an electrostatic 2D scanning micromirror is used for the lateral scan. The measurement head, hosting these microcomponents as well as a microfluidic channel, has a diameter of 4 mm and is then compatible with endoscopes (Fig. 1.20).
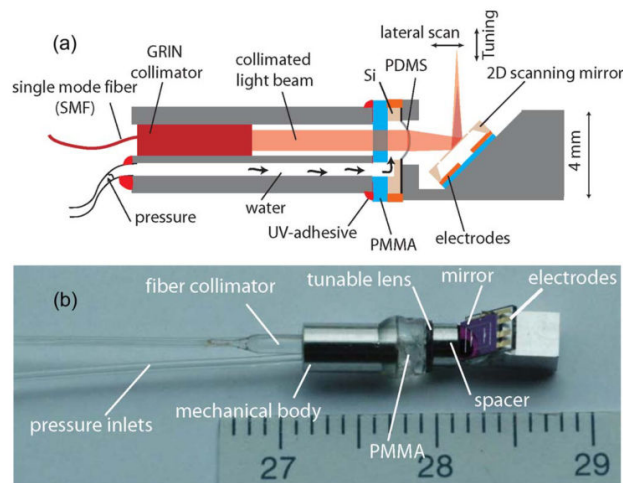
Figure 1.20: Completed measurement head, including the tunable lens arrangement and the scanning micromirror: (a) schematic design and (b) photograph. The relative positions of the GRIN collimator, the tunable lens, the scanning micromirror as well as the optical fiber input and pressure hoses are seen. The outer diameter of the measurement head is 4 mm [45].

Another strategy to achieve a high resolution over a wider range of depth scan is to use Bessel beams. Based on this idea, the same group proposed a system based on three axicons to focus the light in the tissue [46]. The miniaturized axicons are integrated in a silicon bench which enables the fabrication of a very small device (7 mm x 1.5 mm x 1.5 mm).

The presented works testify for the great interest in the size reduction of OCT systems and demonstrate the possibility of integrating interferometers, scanning heads but also spectrometers. However, the integration of all these components together on one chip, or in one integrated system is still a challenge. For this purpose, different approaches have been investigated and are presented in the following.

1.3.1.3/ INTEGRATION STRATEGIES OF MICROFABRICATED COMPONENTS

The miniaturisation of various components of optical systems have been reported above. Once fabricated, these microcomponents must be integrated together, aligned and fixed. The handling of microstructures is not easy and different strategies to manage their assembly have been considered. A first strategy is to assemble the microcomponents on a microbench. In the literature, several demonstrations have been reported to position the

microcomponents in a specific way [47]. The basic principle is to use integrated MEMS micropositioners to move the microcomponents out of the plane in which they are fabricated and align them [48, 49, 50]. Another type of silicon optical bench is proposed based on etched alignment grooves [51]. This design is modular and highly flexible as different optical microcomponents can be adapted. Finally, another solution, reported in 2010, is to use a microgripper to manipulate the microcomponents and place them on a microbench [52]. This solution includes a higher degree of freedom with the possibility to choose/adjust the horizontal distances between the optical microcomponents.
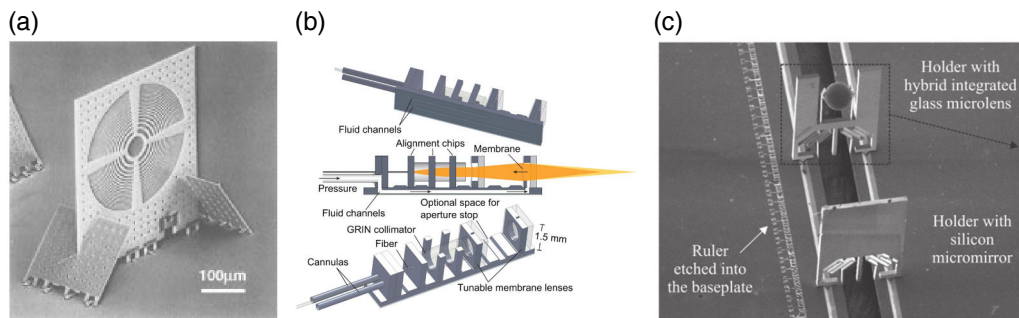
Figure 1.21: Silicon optical microbench: (a) MEMS micropositionners for out-of-plane Fresnel microlens with diameter 280 μm [48, 49] and SEM pictures of two holders assembled onto the rail of the baseplate: (b) modular optical bench [51], (c) two holder carrying a ball microlens of 258 μm diameter and a micromirror [52].

A second strategy is to perform the assembly of microcomponents at wafer level. For this purpose, 3D vertical integration, which is already a major trend in packaging of semiconductor devices, has been developed. In the field of microsensors, it is often used to hybrid an electronic driving/detection circuit with a MEMS sensor. Likewise 3D integration is commonly used in micro-electronics to stack memories [53], processors or mixed signal systems [54] or optoelectronic components [55]. The purpose is to add functionalities and to overcome the limitation of device size reduction while maintaining high performance and low cost. Figure 1.22 illustrates the 3D integration by direct bonding of numerous wafers (up to 6) which was investigated for the fabrication of microturbines [56, 57].
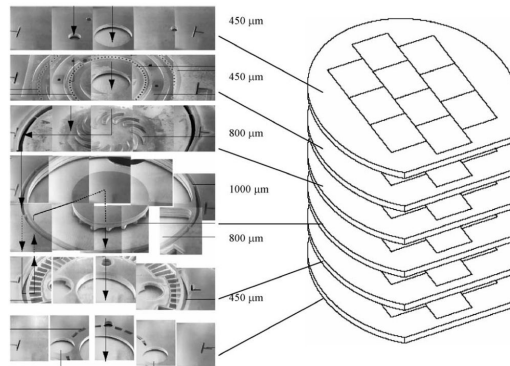
Figure 1.22: An example of the six combustion wafers prior to bonding along with a 3D schematic of the stack [56]

Multi-wafer 3D vertical integration of micro-optical components has different constraints. The main issue is to bond several wafers while controlling the alignment and the geometrical variations between the different microcomponents. Only few investigations were made on vertically integrated optical systems as proposed in this manuscript. One of the first example of a vertical stack of microcomponents reported in the literature aims at the realisation of a confocal microscope [58]. The system integrates a fused silica lens plate with scanning micromirrors realized on a silicon substrate. Two microlens scanner for microconfocal imaging have been successfully stacked to enable 2D raster scanner. Each scanner scans a lateral direction and integrates a polymer microlens. The concept includes the integration of a third out-of-plane scanner for 3D imaging [59, 60, 61]. Finally, a third concept, based on one 2D scanner and one out-of-plane scanner, has also been published [62]. The interest of vertical assembly is that it is compatible with batch-fabrication enabling lower cost and packaging solutions but also the use of alignment machines that guarantees a high alignment precision. In particular, packaging is a critical issue for the protection of the device and is usually complex due to the small size of the microsystem at stake. These three concepts are shown in Fig. 1.23.
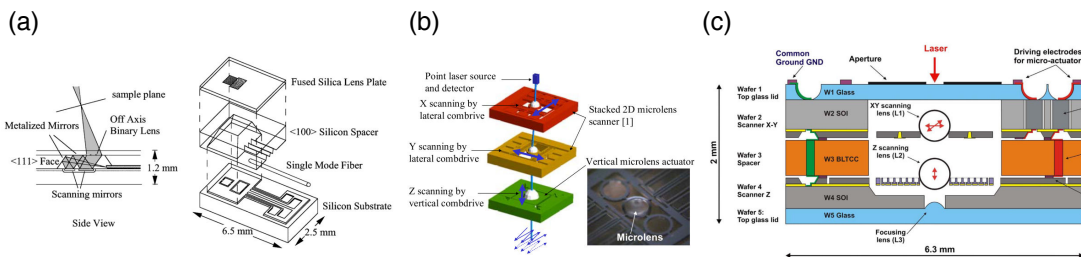
Figure 1.23: Vertically integrated confocal microscope: (a) Fused silica lens with scanning micromirrors [58], (b) three 1D scanners with polymer based microlenses [60], (c) one 2D lateral scanner (XY) assembled with one 1 scanner (Z) [62].

1.3.2/   MINIATURIZATION OF THE INTERFEROMETERS

The miniaturization of interferometers combined with objective lenses is possible with MOEMS technologies. Different types of interferometer configurations have been developed. In this section, a comparison between Mirau, Michelson and Linnik configuration is done in order to evaluate the more suitable configuration for a high degree of integration. Based on this comparison, a review of the integrated Mirau interferometer is presented.

1.3.2.1/   COMPARISON BETWEEN MICHELSON, LINNIK AND MIRAU INTERFEROMETERS

Depending on the optical arrangement, several interferometric configurations exist. Here, we focus on three configurations that are compatible with low coherence interferometry: Michelson, Linnik and Mirau [63]. The Michelson configuration (Fig. 1.24, (a)) generally uses low magnification, up to 5X. The Linnik configuration (Fig. 1.24, (b)) provides very high lateral resolution, with possible high magnifications, up to 200X, since the imaging lens is directly in contact with the sample enabling no limitations on the working distance. However, this configuration suffers from several drawbacks. Because of the presence of two different lenses, one in the reference and the other in the sample arm, Linnik interferometers are bulky, heavy, and also very sensitive to wavefront and misalignment. Mirau type interferometers (Fig. 1.24, (c)) are a compromise in terms of magnification, which ranges usually between 10X and 50X. The Mirau interferometer already benefits, because of its in-line architecture, from a compact construction. The reference mirror is axially centred and placed below the last dioptre of the objective lenses. A semi-transparent plate is positioned between the reference mirror and the specimen. This aspect makes it very interesting for potential miniaturization. Moreover, its vertical configuration is compatible with vertical integration techniques from MEMS technologies reported in the previous section. This specific point of view, based on 3D integration, is different from any other point of view described above where on chip, horizontal interferometers were developed.
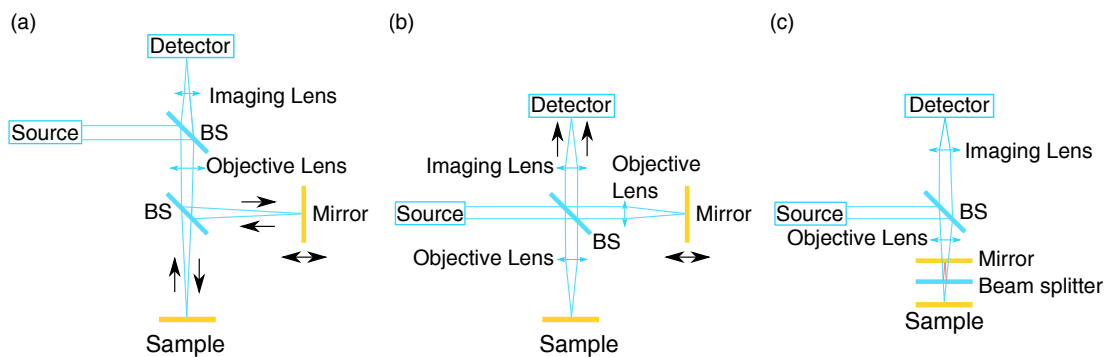
Figure 1.24: Three different configurations of interferometer: (a) Michelson, (b) Linnik, (c) Mirau.

1.3.2.2 / REVIEW OF VERTICALLY INTEGRATED MIRAU MICRO-INTERFEROMETERS

Mirau type interferometers have several advantages linked to their construction that make them interesting for miniaturization. Two different types of Mirau interferometer, presented in the literature, are detailed and a new approach is finally proposed.

Array-type passive Mirau interferometer In 2011, Albero *et al.* presented an array of micromachined Mirau interferometers for low coherence interferometry, dedicated to the parallel inspection of MEMS [64]. It consists in 5x5 passive interferometers combining free-space micro-optical technologies and silicon micro-machining. The array of interferometers is not dense in order to enable the inspection of large wafers.

The technology of the microlenses fabrication is based on a classic polymer UV-molding. A mirror is deposited at the backside of the lens by evaporation with an anti-reflective coating at its backside. Diffractive optical elements are also molded on the backside of the lens to compensate optical aberrations. Finally, the beam splitter is created by deposition of thin dielectric layers. Final assembly is realized with UV-curable adhesive without necessary alignment between the lens wafer and the beam splitter wafer. The concept and first technological results of the Mirau micro-interferometer, integrated into the OCT probe, have been already published in [65].

For OCT systems, the benefit of the frequency domain working principle has been shown previously. Moreover, in this domain, the addition of an active reference micromirror has been proven to be useful for a better dynamic and the discrimination between artefacts and signal of interest. The paper presented above and its related design does not enable to integrate such functionality as the micromirror is deposited on the backside of the microlens.
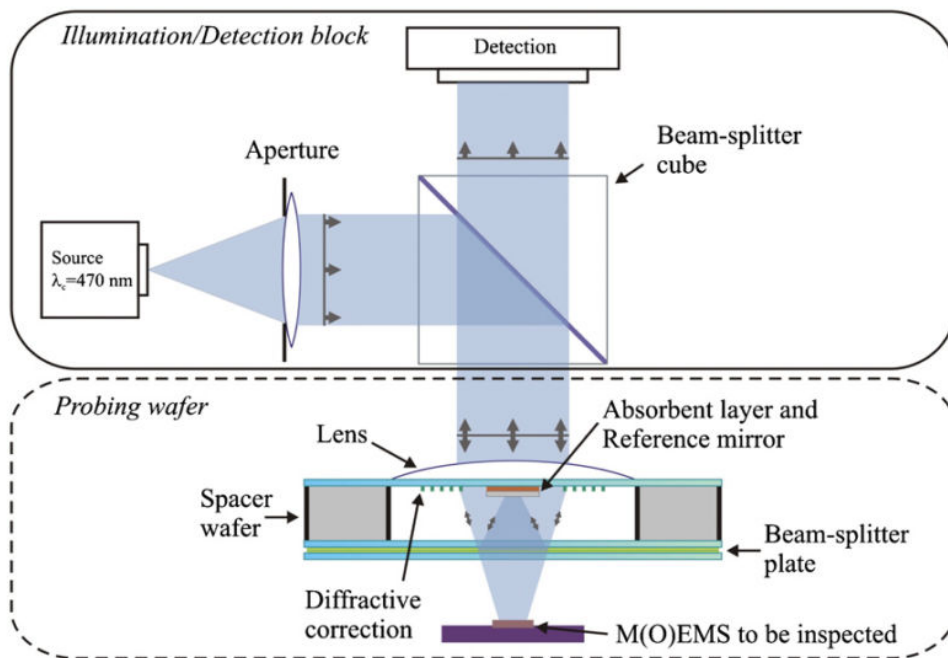
Figure 1.25: Array-type passive Mirau interferometer [64]. Only one channel is drawn out of 25 per wafer.

Individual active Mirau interferometer   During my research work, in 2014, a design, similar to the one exposed in this thesis, is proposed by Xu *et al.* for a 3D single-channel tunable Mirau interferometer. Here, a movable MEMS mirror is integrated on top of a beam splitter [66].

The MEMS vertical microscanner is based on a double SOI wafer used to fabricate an electrostatic vertical comb-drive actuator. It is suggested to assemble the beam splitter and the vertical microscanner by direct bonding. The optical objective is not integrated, then a commercial objective should be used. The proposed design is based on 3D hybrid integration of an out-of plane reference micromirror scanner wafer and an optical beam splitter wafer. The design is presented as well as the complete process flow [67].

These works, based on a Mirau architecture, can be pushed further by implementing an active reference mirror in an array-type Mirau interferometer with both objective lens and beam splitter integrated.
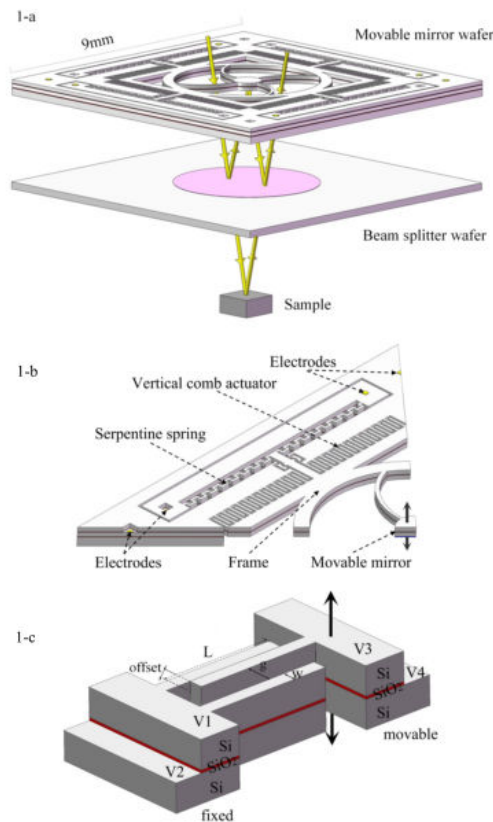
Figure 1.26: Individual active Mirau interferometer [67]

1.3.2.3/ OUR APPROACH: AN ARRAY-TYPE ACTIVE VERTICALLY INTEGRATED MIRAU MICRO-INTERFEROMETER

In the frame of the European project VIAMOS[4] started in 2012, including 7 academic research and industrial partners, we propose to benefit from advanced MOEMS technologies, enabling a new generation of miniature and low-cost instruments, to develop a swept-source OCT (SS-OCT) microsystem based on spectrally tuned Mirau interferometry for the early diagnostic of skin cancer. Each European partner contributes to the development of the system by delivering different building blocks shown in Fig. 1.27. The light comes out from a swept-source realized at VTT institute in Finland and goes through the Mirau interferometer whose microcomponents are fabricated in FEMTO-ST in Besançon and assembled by Fraunhofer institute ENAS in Chemnitz. The light is reflected back in the skin and finally detected by a high speed camera developed by the CSEM in Neuchâtel. The University of Stuttgart (ITO) was responsible for the optical design of the system and the company Statice from Besançon was in charge of the assembly and the packaging of all the components. Clinical tests are planned and realized by the university hospital (CHU) in Besançon. Finally, the industrial partner DermoScan

---

[4]The website of the European project VIAMOS is http://viamos.eu/.

studied and prepared the potential release of the system on the market.
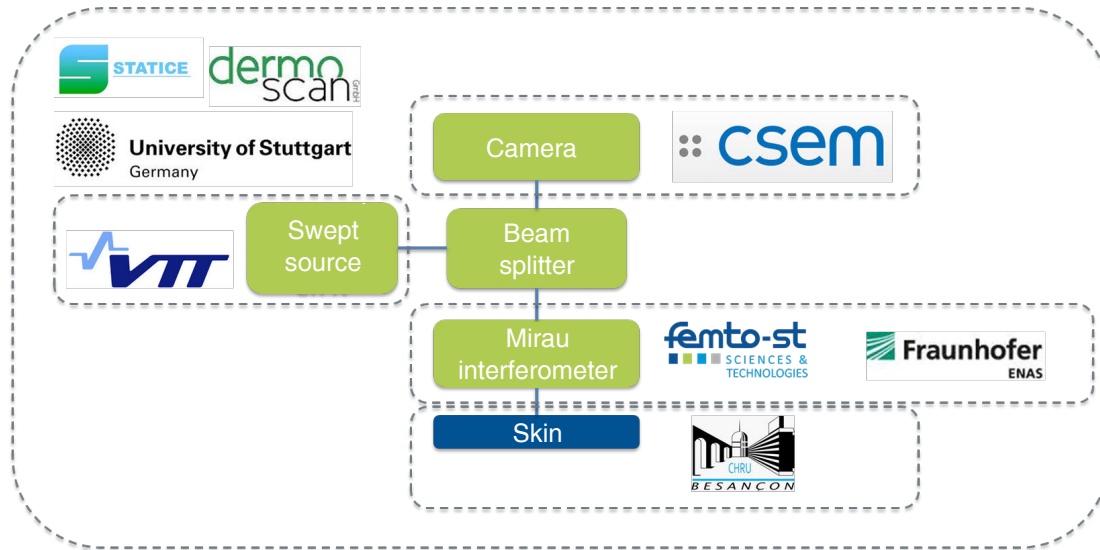
Figure 1.27: Building blocks of the SS-OCT developed in VIAMOS.

The first part of this thesis has reported the need for an integrated OCT system in dermatology that should meet the specifications given in the column 3 of Tab. 1.2. Moreover, the price of the targeted system must be lower than the existing ones. We believe that the high price of the commercial system is the reason that stops its development in the market of skin imaging. To lower the cost, two strategies are employed. Firstly, the miniaturisation of the system, based on collective fabrication techniques, leads to a decrease of the price. Secondly, the light source used in VIAMOS is chosen to be relatively slow compared to the state of the art in order to minimize its cost. To compensate the slowness of the light source, the idea is to spatially parallelize the acquisition using the full-field technique. In addition, to further increase the A-scan speed and to image a large field of view of 8x8 mm^2, a 4x4 array-type micro-interferometer is designed. Indeed, such a field of view cannot be imaged with a full-field acquisition based on microcomponents without an array configuration. The 4x4 array-type micro-interferometer also enables to image a reduced field of view in each channel of the interferometer and then leads to a higher resolution in each channel. The general concept of our vertically integrated Mirau microinterferometer is shown in Fig. 1.28. The Mirau micro-interferometer is composed of a dense matrix of Mirau micro-interferometers, each one composed of a lens, an actuated micromirror and a beamsplitter. The matrix structure is based on the vertical assembly at wafer level of three optically functionalized wafers with the objective lenses, the MEMS vertical microscanners, the beam splitter and the vertical spacers.

The MEMS vertical microscanner is used for the implementation of a phase-shifting algorithm based on the acquisition of 4 images as presented in Sec. 1.2.1.5. It is the core

function of the interferometer and is the subject of this thesis. Its design, fabrication and characterisation will be described in the next chapters.
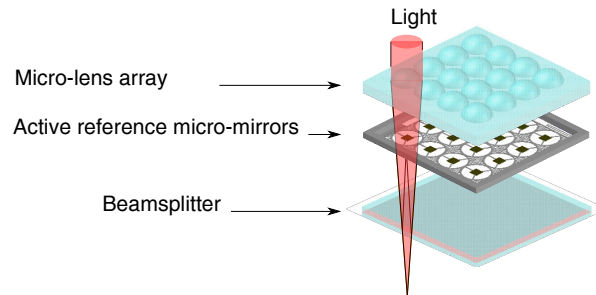
Figure 1.28: Array-type active vertically integrated Mirau micro-interferometer

1.4/ CONCLUSIONS

In this chapter, the status of skin cancer has been described in details. The increase of the number of skin cancers in the world and its consequences such as scares, disfigurement, and potentially deaths, become a global issue that is expected to accentuate in the near future. The first challenge in treating skin cancers is their early diagnosis. Screening techniques, such as self-evaluation based on ABCDE criteria, has shown a limited efficiency since no information resolved in depth can be retrieved. Obviously, the possibility to image skin lesions is a key parameter and enables both early diagnosis, follow-up and monitoring during surgical interventions to perform efficient biopsies. However, nowadays, dermatologists are still lacking of high-resolution imaging systems that allows sufficient depth penetration to obtain a resolved 3D image. Among the possible imaging techniques, OCT systems are a good compromise having both a resolution and a penetration depth suitable for skin imaging. Moreover, the development of a new type of OCT, i.e. frequency domain OCT (FD-OCT), along with the implementation of sweeping optical sources, leads to more sensitive and faster systems. With these features, the OCT system is an ideal candidate for imaging biological tissues. Finally, phase-shifting techniques can be implemented to overcome the presence of artefacts terms linked to the implementation of the FD-OCT technique. However, if OCT systems have revolutionized the ophthalmology, and are more and more used in cardiology, they struggle to become a routine in dermatology where studies show its great potential for the diagnosis of skin diseases and more particularly cancers. One of the reason is that existing systems are very expensive and bulky. Then, the examination of biopsies, i.e. the histopathology, is still the gold standard despite several drawbacks such as invasiveness, delays and deformation of the removed tissue.

Miniaturisation, combined with a high degree of integration, is a solution to these draw-

backs. Developed technologies based on fibers, MEMS and MOEMS already show great promises. However, the specifications required for biomedical imaging of skin detailed in the first chapter are not met yet. In particular, the investigated area is often limited by the MEMS scanning head. If huge progresses have been done in the miniaturization of individual parts of OCT systems, higher degree of integration is still a challenge. Indeed, multi-disciplinary constraints must be taken into account in order to develop successfully miniaturized systems that are completely integrated. In particular, both the optical design and the technological limitations have to be taken into account. Here, we propose a design based on the integration of a Mirau interferometer that is chosen for its compatibility with microfabrication processes. More precisely, the Mirau configuration can be vertically integrated and benefit from optical characteristics suited for our application. The Mirau interferometer is composed of a 4x4 matrix of Mirau micro-interferometers consisting in a matrix of lenses, a matrix of actuated reference micromirrors and a beam splitter. The matrices are both fabricated and vertically assembled at wafer level. This thesis focuses on the design, the fabrication and the characterisation of the array of vertically actuated micromirrors with embedded position sensing function. The goal is to integrate it in a Mirau micro-interferometer, for phase-shifting purposes. Before keeping on with the description of our system, the state of the art of vertical microscanners and position microsensors is discussed in the next chapter.

BASIC PRINCIPLES AND STATE OF THE ART OF VERTICAL MICROSCANNER

In order to introduce the technologies of vertical microscanners, this chapter proposes a brief overview of the micro-actuators according to their different actuation principles. Different mechanisms of MEMS actuation are discussed, illustrating each technology by an example of scanner application. A particular attention is paid to scanners based on the technology of electrostatic vertical comb drive, an architecture that is chosen to achieve the phase modulation of the array-type Mirau micro-interferometer in VIAMOS project. The discussion of the basic fabrication techniques and their limitations is used as a basis to define an adapted electro-mechanical design for the vertical microscanner that is presented in Ch. 3. Finally, the solutions to integrate an embedded displacement sensor are proposed.

2.1 / MEMS ACTUATORS TECHNOLOGIES

There are four main actuation mechanisms employed for generating the scanning function with MEMS mirrors and actuators: piezoelectric, thermal, magnetic and electrostatic.

2.1.1 / PIEZOELECTRIC ACTUATORS

2.1.1.1 / PRINCIPLE

Piezoelectric actuation is based on the deformation of piezoelectric materials. Piezoelectric materials creates an electric field when they are mechanically deformed and reversely, they deform in response to an applied electric field (Fig. 2.1). Piezoelectric materials are crystals and can be natural or man-made. The most commonly used materials in microfabrication processes are Quartz (SiO_2, natural) and Lead Zirconate Titanate (PZT,

man-made). The piezoelectric character of a material is linked to its crystal lattice. The deformation of the crystal lattice changes the polarization, i.e. modifies the electric dipole moment of a unit cell of the crystal. Usually in a crystal, all the domains have a different polarization so that the overall polarization is 0. When a stress is applied, the polarisation of all the domains changes resulting in an overall polarisation equal to 0. In order to see a piezoelectric effect, the polarisation of all the domains needs to be aligned in a one direction. For this purpose, the material is heated up to a temperature higher than the Curie temperature[1] and an external electric field is applied. The dipoles of all the domains will align, reaching a maximum polarization. When the sample is cooled down and the external field is removed, a remanent polarisation remains. After this process, which is called *poling*, the material exhibits a piezoelectric character.

Piezoelectric materials are used to fabricate micro-actuators and microsensors using the direct piezoelectric effect and the reverse one.
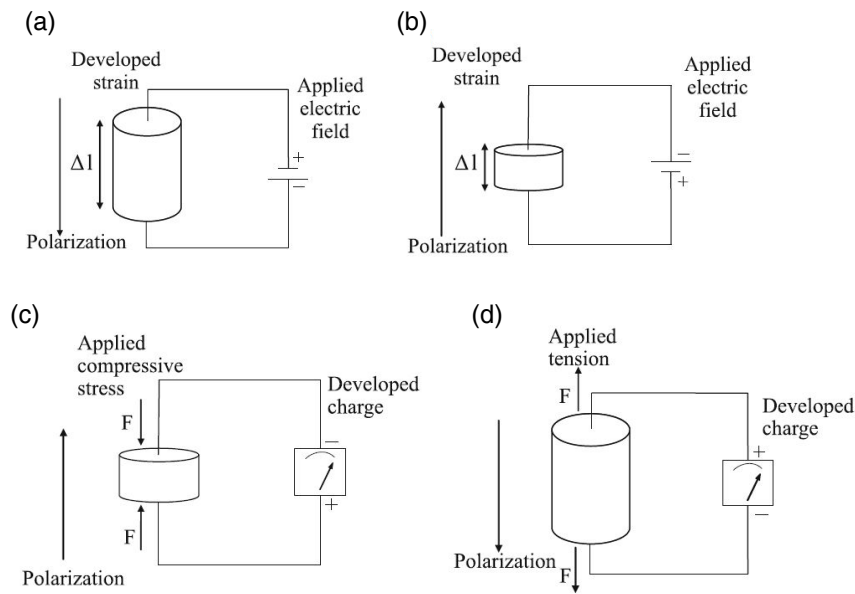
Figure 2.1: Schematic representing the piezoeletric effect: (a)(b) Reverse effect, (c)(d) Direct effect [68]

The relation between the electric displacement D and the mechanical strain S is described by two coupled matrix equations:

$$D = \epsilon^T E + dT$$
$$S = s^E T + d_t E \tag{2.1}$$

where T is the mechanical stress, E the electric field , ϵ^T the permittivity at constant me-

---

[1]The Curie temperature is the temperature above which the natural polarization of a material can be changed

chanical stress, s^E the mechanical compliance at constant electric field and d and d_t are respectively the piezoelectric constant and its transposed tensor. The characteristic coefficients, ϵ^T and d of piezoelectric materials are grouped into tables and the symmetry of the corresponding tensors depends on their crystal lattice [69]. These two constitutive equations are fundamental to describe piezoelectric material and derive piezoelectric actuator design. However, piezoelectric actuators have a main drawback, the electric field-mechanical stress relationship presents hysteresis. The hysteresis effect describes the fact that the response of a system depends on its history. For actuation, this is a problem because it implies that two different displacement value can be obtained for one applied voltage. This effect have been studied and modelled in order to facilitate the use of piezoelectric actuators [70].

2.1.1.2/ EXAMPLES

PZT is the most used piezoelectric material for its great sensitivity, its high operating temperature and its relative easiness to be fabricated. There are three main techniques of microfabrication of PZT films [71] : thick film printing [72], sputtering [73] and sol-gel processing [74, 75]. Another technique is to bond bulk PZT and thinned it by lapping and polishing technique to obtain a thin layer [76]. To apply or sense an electric field, two metal electrodes are usually deposited under and above the PZT film.

The main advantages of piezoelectricity are significant deformations, that can be achieved with a relatively low voltage (typically tens of V), and high actuation frequency in the range of kHz.

A piezoelectric scanning micromirror for endoscopic OCT was presented by Gilchrist *et al.* and Naono *et al.*, respectively in 2009 and 2014 [77, 78]. In the first article PZT is spin coated from metal organic precursors, whereas, in the second one, 13% Nd doped PZT (PNZT) is deposited by RF magnetron sputtering. Moreover, in [78], PNZT sensors were also fabricated and it is shown that doping PZT enables to double the scanning angle (Fig. 2.2). These large angles allowed to achieve 4.6 mm x 3 mm images with a SS-OCT. However, the resolution is limited to 16.7 μm for larger angles and the scanning frequency is 90.3 Hz.
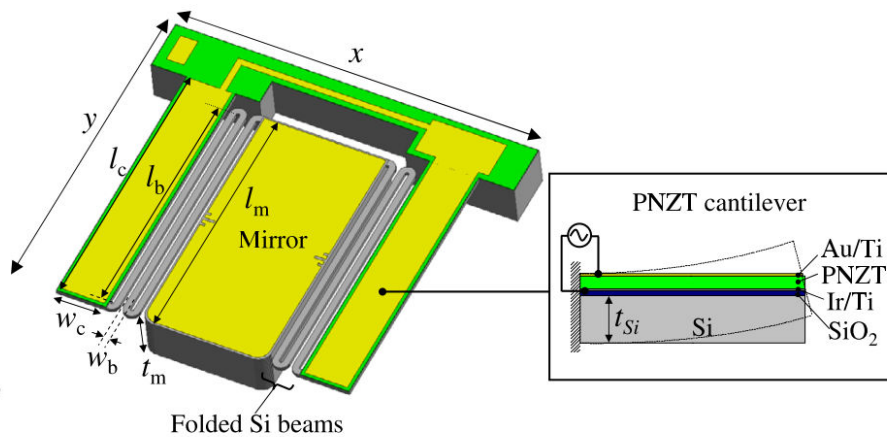
Figure 2.2: PNZT piezoelectric actuator for the implementation of scanning micromirror in an endoscopic OCT [78].

For this thesis, out-of plane actuators are of interest. However, few articles present designs for vertical actuation. Qiu *et al.* proposed in 2010 a vertical translational micro-actuator reaching 80 μm of vertical displacement for 20 V [79]. More recently, a piezoelectric MEMS actuator was presented [80]. The actuator performs piston mode oscillation in resonance with vertical displacements up to $\pm$ 800 μm at 163 Hz with a driving sinusoidal voltage of 25 V.

The easiness of fabrication makes piezoelectric actuation very attractive for MEMS. The main issue with piezoelectric actuation is the hysteresis behaviour and that it is usually incompatible with CMOS process which complicates its implementation.

2.1.2/ THERMAL ACTUATORS

2.1.2.1/ PRINCIPLE

Thermal actuation is based on the mechanical deformation of a material in response to a change in temperature. The change in temperature is usually obtained by applying an electric potential, corresponding to electro-thermal actuation, and in few cases by optical heating with lasers. The electrothermal analysis is based on the study of the dissipation of the heat in the beams [81, 82], which allows to retrieve the mechanical deformation as a function of the applied current [83]. The material properties to take into account are the thermal conductivity and the thermal expansion. The linear expansion can be written as:

$$\Delta L = L\alpha\Delta T \tag{2.2}$$

$$\tag{2.3}$$

where α is the linear expansion coefficient, ΔL and ΔT are respectively the variation of length and temperature.

When a single material is used, specific designs based on a large arm and a thin arm lead respectively to a cold arm and a hot arm resulting from the higher current density obtained in the thin arm. When two materials are used, referred to as bimorph actuators, the mechanical deformation is due to a difference of the thermal expansion coefficients of the two stacked materials leading to the creation of stress. The range of materials used for thermal actuators is wide, including bimetallic actuators using nickel, copper, aluminium, titanium [84, 85] but also polysilicon/silicon dioxyde bimorph structures [86]. Finally, single material actuators are usually based on polysilicon and use specific designs to create stress [87, 83]. Different designs of thermal micro-actuators based on bimorph [88], bent-beam(s) [89] and flexure [90] designs have been implemented [91] (Fig. 2.3). Both in-plane and out-of-plane actuation have been demonstrated [92].
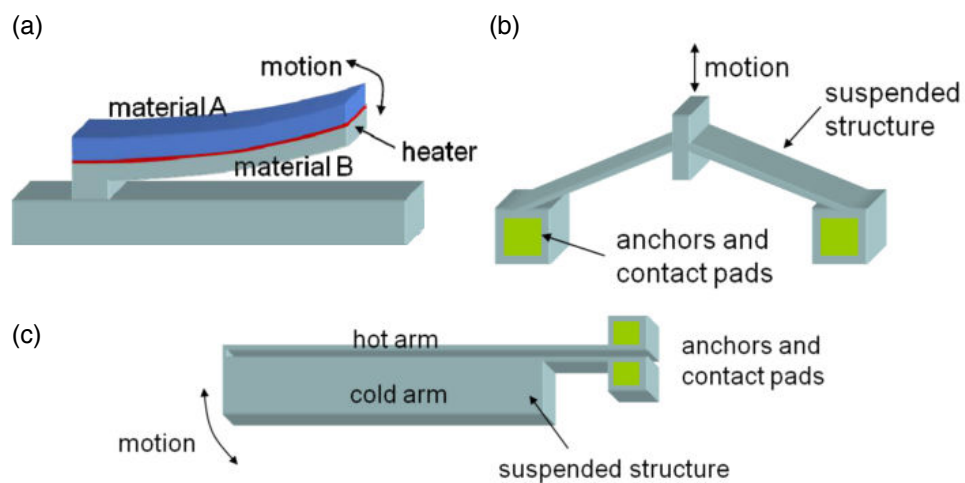
Figure 2.3: Typical designs for thermal actuators: (a) bimorph, (b) bent-beam, (c) flexure [91].

2.1.2.2/ EXAMPLES

The possibility to integrate such actuators in MOEMS has been investigated [93]. In 2005, A. Jain *et al.* presented a large vertical displacement actuator based on thermal actuation compatible with CMOS and suitable for interferometry and in particular OCT systems for biomedical imaging (Fig. 2.4) [86]. The specific design presented allows very large vertical displacement by applying a voltage to both the frame and the mirror. Therefore a relatively low voltage is necessary (200 μm for $V_{frame} = 6$ V and $V_{mirror} = 1.5$ V). However, no dynamic behaviour is presented for the piston mode.
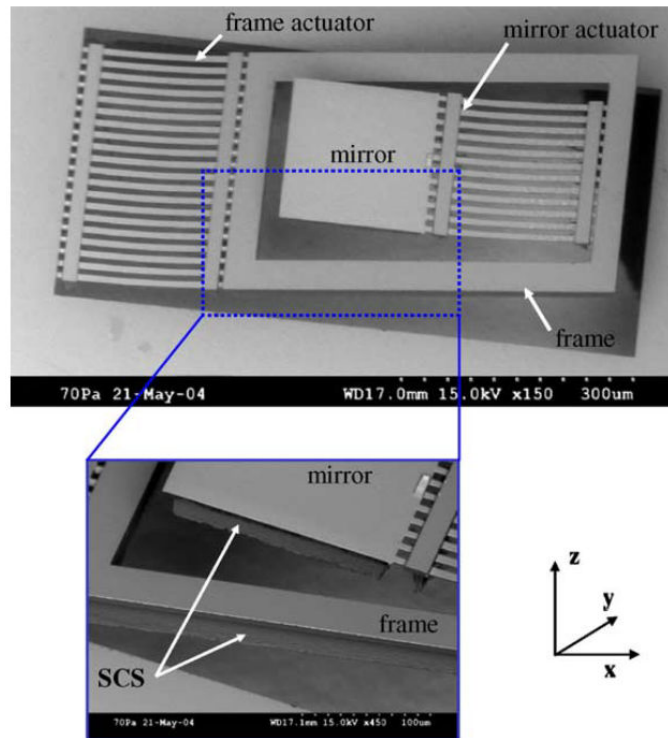
Figure 2.4: Thermal micro-actuator with two embedded mechanical frames for large displacements [86].

More recently in 2014, Liu *et al.* presented a MEMS- based 3D confocal scanning microendoscope [94]. The axial scan is performed thanks to the integration of a lens onto a vertical electrothermal actuator used in piston mode ($f_{resonance} = 24Hz$) whereas the lateral 2D scanning is realized with an actuated micromirror also based on the electrothermal actuation principle. A vertical displacement of 400 μm is measured at only 2 V and a scanning angle of $\pm$ 26 $^\circ$ is obtained at 4.5 V. The footprint of the MEMS devices is 4 mm x 4 mm allowing its use in endoscopic measurement heads.

In general, electro-thermal actuators consume more power than the other actuators and are responsible for an elevation of temperature. This elevation of the temperature is a major constraint for the packaging of the device and in particular when biological imaging is targeted. Finally, another drawback of the electro-thermal actuation is its limitation to low frequencies.

2.1.3/ MAGNETIC ACTUATORS

2.1.3.1/ PRINCIPLE

The magnetic actuators employ two actuation principles. The first principle is based on the fact that under an external applied magnetic field, a magnetic sample experienced a force *F* described as follows:

$$\overrightarrow{F}_{mag} = V_{mag}|\overrightarrow{M} * \overrightarrow{H}| \tag{2.4}$$

where V_{mag} is the volume of the magnetic sample, *M* is the magnetization of the magnetic sample and H is the external applied magnetic field.

Magnetic materials used are permalloys (NiFe) [95, 96] or nickel (Ni) [97] which are easily electroplated on the moving parts, while the electromagnetic field is external to the device. The external electromagnetic field is typically generated with coils or permanent magnets. Another possibility is to use a coil structure on the moving part which generates the electromagnetic force while an external permanent magnet is manually attached to the device [98]. The main drawback of this kind of magnetic actuators is the need of off-chip bulky coils to provide for the external magnetic field. When the coil is integrated, it leads to either large structures, or the use of large current [97]. Finally as piezoelectric actuators, magnetic actuators suffer from the hysteresis effect.

The second actuation principle is based on the Lorentz force law:

$$\overrightarrow{F}_{Lorentz} = l \overrightarrow{I} * \overrightarrow{B} \tag{2.5}$$

where F is the Lorentz force experienced by a conductor across which a current *I* flows and under an applied magnetic field *B*. Using this principle, no magnetic materials must be integrated onto the actuator, and the actuator has no hysteresis effect.

2.1.3.2/ EXAMPLES

Two magnetic actuators, which use the principles mentioned above, are presented below. In [95], permalloy is deposited on the released polysilicon membrane. An external electromagnet provides for the external magnetic field. Very large deflections up to 2 mm have been demonstrated. However, a relatively high biasing magnetic field of 6.10^7 A/m is necessary. In [99], the Lorentz force is used and displacements up to 47 *μm* are measured for relatively low driving voltage (2.4 V). The actuator presented in this article is laterally moving, however it can be easily adapted to vertical actuation by changing the

direction of the magnetic field B. The technology presented, based on silicon standard fabrication processes, is compatible with classical MEMS technology and CMOS circuit implementation.

(a)   (b)
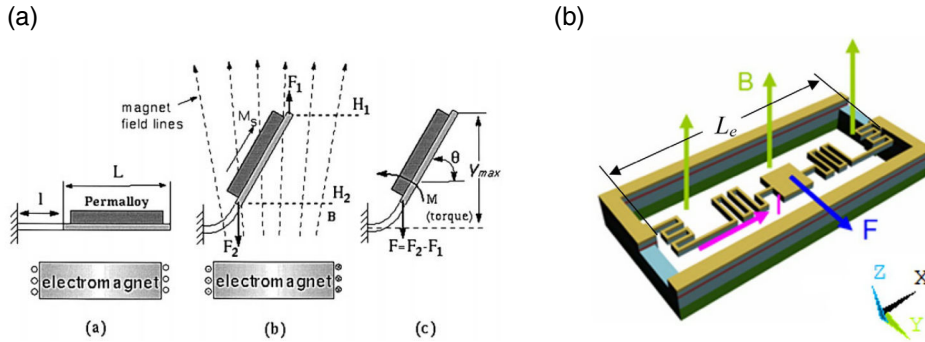
Figure 2.5: (a) Actuation based on magnetic force [95]: permalloy based technology, (b) actuation based on Lorentz force: silicon based technology [99]

2.1.4/   ELECTROSTATIC ACTUATORS

2.1.4.1/   PRINCIPLE

The electrostatic actuators are based on the electrostatic force existing between two opposite charges, which is the Coulomb force. Then, electrostatic actuators are usually composed of two facing structures with opposite charges. Several geometries have been investigated such as the parallel plate or the comb drive (Figure 2.6). The two designs can be used for both out-of-plane and in-plane actuation. The simplest geometry with parallel plate is, in fact, a classic capacitor C, which stored energy is:

$$E_c = \frac{1}{2}CV^2 \tag{2.6}$$

where V is the applied voltage between the two plates.

From this, we can derive the electrostatic force F:

$$\overrightarrow{F} = \frac{dE_c}{dx} = \frac{1}{2}\frac{dC}{dx}V^2 \tag{2.7}$$

In the case of the parallel plate capacitance, neglecting the fringing fields, it gives:

$$C = \frac{\epsilon A}{d} \tag{2.8}$$

where A is the area of the plate ($A = LW$), ϵ is the electrical permittivity of the material between the plates, and d the distance between the plates,

and

$$\frac{dC}{dx} = -\frac{\epsilon A}{x^2} = -\frac{C}{x} \tag{2.9}$$

where x is the distance between the plates.

Finally, one obtains:

$$\overrightarrow{F} = \frac{1}{2} \times -\frac{\epsilon A}{x^2}V^2 = -\frac{1}{2}\frac{CV^2}{x} \tag{2.10}$$

(a) Configuration 1:
Parrallel plate

(b) Configuration 2:
Comb fingers
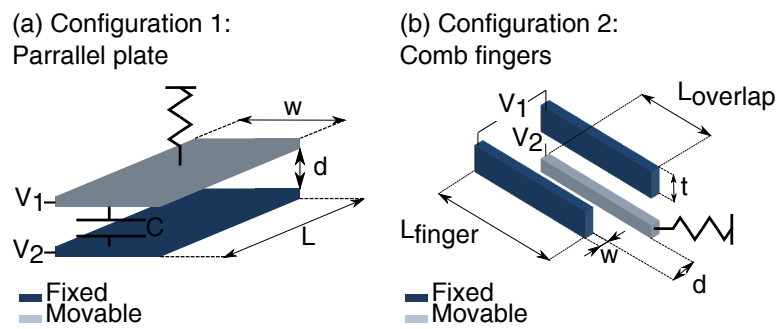
Figure 2.6: Electrostatic actuator design: (a) Parallel plate, (b) Comb fingers

The only constraint is that the material used for the capacitance surface must be conductive. Then, highly doped silicon is usually used but comb drive based on other materials like GaN [100], CMOS based (SiO_2 and metal layer)[101] or even metallized polymer [102] have also been demonstrated. This unique constraint, in terms of material, makes this principle easy to implement, which is why it is widely used in MEMS systems.

2.1.4.2/ EXAMPLES

As the purpose of this thesis is the development of vertical microscanner, the focus is made on vertical actuation.

Parallel plate actuators are often implemented according to a technology, called Poly-MUMPS, based on the creation of a free standing polysilicon membrane, creating a first electrode, which is facing the silicon substrate on which the second electrode has been deposited. The gap between the two electrodes is created by etching a sacrificial layer, which thickness determines the gap distance. Therefore, this thickness limits the range of actuation which is further limited by the pull-in effect (defined in Sec. 2.2.1.2). Consequently, researchers have worked on different strategies to increase this critical gap, either with a thicker sacrificial layer or a double polyMUMPS process [103] or by levering beams [104, 105, 106]. The polyMUMPS process is presented below according to [104] in Fig. 2.7.
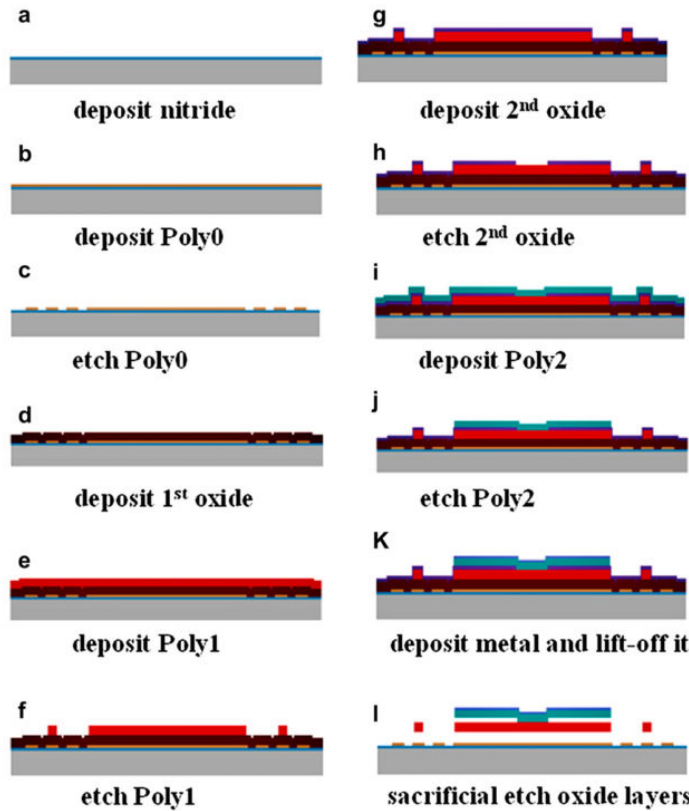
Figure 2.7: Fabrication flow chart based on polyMUMPS process [104].

In [104], the gap between the two parallel plates is increased using an unbalanced electrostatic force experienced by the supported beams that moves upward the structure (Fig. 2.8).
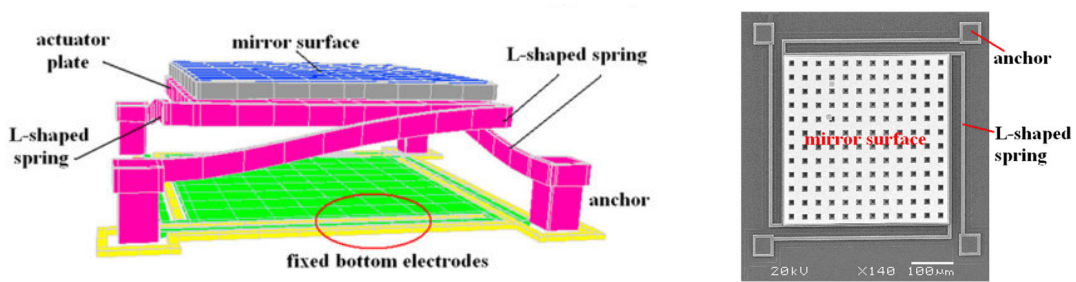
Figure 2.8: Parallel plate vertical actuator based on polyMUMPS process [104].

Finally, a well-know problem with surface micromachined poly-Si-based technology is a residual stress leading to initial deformation of released structures. This is an important issue for larger array of micromirrors like in our case. Moreover, the actuated micromirrors that are designed based on parallel plate actuation are usually working in reflection. For devices, working in "transmission", i.e. the micromirror plane must also be optically transparent around the micromirror, transparent electrodes must be used, like ITO, or

specific complicated design must implemented, for example with the assembly of two structured wafers [107].

Comb drive structures have been widely developed, first, for lateral optical scanning purposes, and then, for out-of-plane actuation. This geometry is easy to be implemented because it is based on an in-plane fabrication whereas parallel plate requires vertical fabrication of movable and fixed parts leading to "3D" MEMS. Though, when it deals with out-of-plane actuation, comb drives also require vertical elements in order to create an out-of-plane electrostatic field.

Table 2.1 summarizes the typical characteristics of each actuation principle. Each principle has its own advantages and drawbacks. For our targeted application, we do not need large actuation displacement. Moreover, our vertical microscanner is meant to be integrated within a Mirau micro-interferometer which implies a high level of integration combining different technologies. Then, the vertical microscanner must be compatible with bonding technologies such as anodic bonding and be resistant to high temperature. Here, we give a priority to the degree of difficulty of the fabrication and the simplicity of the material used. According to these two parameters, electrostatic actuation is the most suited. Moreover, electrostatic comb drive technology has a lot of advantages with respect to the three other main technologies: standard microfabrication materials as silicon can be used, the out-of-plane actuation can be easily coupled with "transmissive" micromirrors when comb fingers are placed around the structure, and the energy is provided by an electrical potential that is, for small displacement such as the one targeted for phase shifting applications, relatively small and compatible with medical imaging. For these reasons, electrostatic comb drive technology is chosen for the design of our vertical microscanner and is described in details in the next section.

Table 2.1: Comparison of the actuation principles

Actuation principle	Voltage range	Disp. range	Speed	Techno. difficulty	Comments
Electrostatic	10 V - few 100 V	$\sim 30\ \mu m$	Fast	+	Small displacement
Electrothermal	1 V - 10 V	$\sim 500\ \mu m$	Medium	++	Slow response time
Electromagnetic	<1 V	~ 1 mm	Fast	+++	Hysteresis effect Need of a coil
Piezoelectric	10 V - few 100 V	$\sim 100\ \mu m$	Fast	+++	Hysteresis effect

2.2/ ELECTROSTATIC VERTICAL COMB DRIVE SCANNERS

2.2.1/ PRINCIPLES

Figure 2.9 shows three types of vertical comb fingers configurations. All the design are based on a vertical asymmetry of the structure, which creates a vertical asymmetry of the electric field that leads to a vertical electrostatic force.
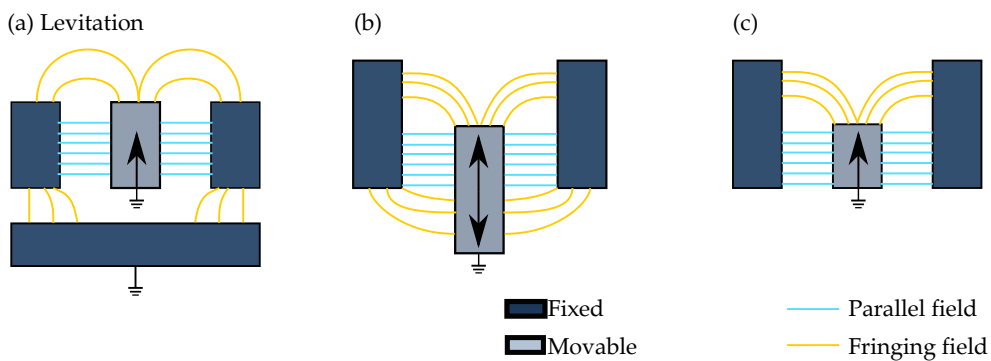
Figure 2.9: Types of vertical comb finger configurations.

For vertical comb drive, the electrostatic force can be derived from 2.7:

$$\overrightarrow{F} = \frac{dE_c}{dz} = \frac{1}{2}N\frac{dC}{dz}V^2 \qquad (2.11)$$

where N is the number of comb fingers that creates N capacitances in parallel, and $\frac{dC}{dz}$ is the variation of the capacitance of one movable finger facing two fixed fingers (Fig. 2.9).
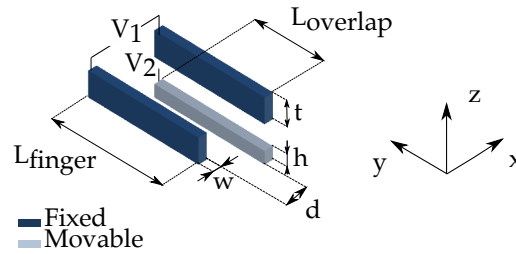
Figure 2.10: Annotations used in the following detailed calculations.

2.2.1.1 / CALCULATION OF THE CAPACITANCE

Depending on the design, the variation of the capacitance is based either on the variation of the parallel plate capacitance and the fringing field capacitance (Fig. 2.9, (b)) or only on the variation of the fringing field (Fig. 2.9, (c)). The configuration presented in Fig. 2.9 (a) is a specific case where a bottom substrate is necessary. In this case, the electrostatic force is called the levitation force [108] and is given by:

$$F = \gamma_z V^2 \frac{(z_0 - z)}{z_0} \tag{2.12}$$

where γ_z is the vertical drive capacity, V is the potential applied between the comb fingers, and z_0 is the equilibrium vertical position.

For the configuration corresponding to Fig. 2.9 (b) and (c), the parallel plate capacitance is classically defined as in 2.8. The fringing capacitance is much more complicated to derive because the electrostatic field is not linear in this region. Conformal mapping based on the Schwartz-Christoffel transformation can be used to calculate the total electric field around a zero-thickness parallel plate capacitance taking into account the fringing field [109]. The aim of this transformation is to transform the plane where the electric field cannot be calculated into a plane where the electric field lines are uniformly spaced and straight and where the electric field is then easier to calculate. In 2000, this technique was used to derive an electrostatic model for vertical asymmetric comb drive [110]. Recently in 2014, E. Gallagher and W. Moussa compared this analytical model for zero-thickness plates with FEM analysis of non-zero thickness plate [111]. They have shown that the maximum error equals 2.8%.

Figure 2.11 represents the comb drive configuration considered in [111] and used to derive the electrostatic force:
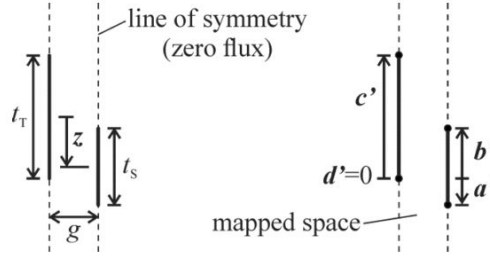
Figure 2.11: Configuration of comb finger and description of parameter used in the following equations [111].

$$F = f_1(g, t_s, t_t, z) \times \frac{\epsilon NL}{d} \times V^2$$

$$= \frac{\pi^2 \left(a \frac{b-d}{a-d} - b \frac{a-c}{b-c} \right)}{4(a-b) \left\{ F\left(\delta(u=0), q \right) + F\left(\kappa(u=0), q \right) \right\}^2} \times \frac{\epsilon NL}{d} \times V^2 \quad (2.13)$$

where

$$q = \sqrt{\frac{(b-c)(a-d)}{(a-c)(b-d)}}, \quad \delta = sin^{-1} \sqrt{\frac{(b-d)(u-c)}{(b-c)(u-d)}}, \quad \kappa = sin^{-1} \sqrt{\frac{(a-c)(b-u)}{(b-c)(a-u)}} \quad (2.14)$$

and F is the incomplete elliptic function of the first kind.

Finally a, b, c and d are defined as follows:

$$a = e^{\pi a'/g} = e^{\pi(b'+h)/g}$$
$$b = e^{\pi b'/g}$$
$$c = e^{\pi c'/g} = e^{\pi t/g}$$
$$d = e^{\pi d'/g} = 1$$
$$b' = -z - \frac{t+h}{2} \quad (2.15)$$

2.2.1.2/ CALCULATION OF THE MAXIMUM VOLTAGE

Lateral instability   The potential V, applied between the facing comb finger is limited due to lateral pull-in. Over a critical voltage, referred to as V_{crit}, the first derivative of the electrostatic force with respect to the lateral direction becomes higher than the restoring spring constant of the springs, referred to as k_x. Therefore over this critical voltage, the facing comb fingers are attracted between each other and the restoring force of the spring is not sufficient to prevent the comb finger to enter in contact. This principle is detailed

in [112]. Neglecting the fringing capacitance, the electrostatic force in the lateral direction x is:

$$F_{el} = N\frac{\epsilon h L_{overlap}}{2}V^2\left(\frac{1}{(d-x)^2} - \frac{1}{(d+x)^2}\right) \tag{2.16}$$

The actuator is stable when:

$$k_x > \left[\frac{\partial F_{el}}{\partial x}\right]_{x\to 0} \tag{2.17}$$

This leads to:

$$V_{crit-x} = \sqrt{\frac{k_x d^3}{2N\epsilon h L_{overlap}}} \tag{2.18}$$

In 2004, W. Huang *et al.* developed another formalism which is equivalent to the one presented before. However, they also took into account the rotational stiffness of the spring, referred to as k_θ, which leads to rotational pull-in if $k_x > k_\theta$.
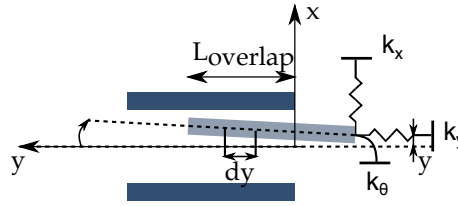
Figure 2.12: Schematic of the comb finger design taking into account rotational and lateral stiffness.

In this case, by solving the equation (Fig. 2.12):

$$\int_0^{L_{overlap}} y\, dF_{elx} = k_\theta\theta \tag{2.19}$$

where

$$dF_{elx} = \frac{\epsilon h\, dy}{2}V^2\left(\frac{1}{(d-x-y\theta)^2} - \frac{1}{(d+x+y\theta)^2}\right) \tag{2.20}$$

One can obtain:

$$V_{crit-\theta} = \sqrt{\frac{3k_\theta d^3}{2N\epsilon h L_{overlap}^3}} \tag{2.21}$$

In the case where the rotational stiffness and the lateral stiffness are of the same order, one obtains, after applying the Taylor expansion for a small number of θ and calculating

$lim_{\theta\to 0}(x/\theta) = x^{'}(\theta)\mid_{\theta=0}$:

$$V_{crit-\theta-x} = \sqrt{\frac{k_x d^3}{2N\epsilon h}\frac{r}{L_{overlap} + rL_{overlap}}} \qquad (2.22)$$

where

$$r = 2\left(-\frac{1 - 3\left(k_\theta/(k_x L_{overlap}^2)\right)}{3} + \sqrt{\left(\frac{1 - 3\left(k_\theta/(k_x L_{overlap}^2)\right)}{3}\right)^2 + \left(k_\theta/(k_x L_{overlap}^2)\right)}\right)$$
$$(2.23)$$

The critical pull-in voltage is usually around 150-200 V, for typical values of vertical electrostatic comb drive parameters, which is well above the specification of voltage for our medical application (maximum 50 V).

Electrical breakdown of the medium   The electrical breakdown voltage is defined as the voltage applied between two electrodes that enables a current to flow between the two electrodes. The electrical breakdown of a gas occurs when a free electron in a gas is accelerated by an electric field with enough energy so that it ionizes a neutral atom after collisions of the two particles. Moreover, this phenomena is associated with an "avalanche" phenomena which results in Townsend breakdown. The ionization of the atom will create another free electron that is also able to create another ionization and so on. The result of this "avalanche" phenomena is the occurrence of a spark in the ionized gas. In 1889, F. Paschen shows empirically that the voltage breakdown is a function of the gas pressure and the gap between the two facing electrodes. The Paschen curves describe the phenomena for different gases. The breakdown voltage has been studied experimentally for different gas and gap spacing. It has been shown that for metallic planar electrodes with micro-scale gap the Paschen law is no more applicable [113]. This can be explained by the fact that for these values of gap spacing, the Townsend breakdown is no more dominant but field emission occurs from the cathode surface so that the cathode is locally vaporized which results in electrical breakdown [114, 115]. However, for silicon electrodes such as comb drive structures, the Paschen law is still valid. For typical comb drive actuators, the voltage breakdown is between 300 and 350 V, which is higher than the maximum voltage that can be used for medical applications.

2.2.2/   FABRICATION TECHNIQUES

In 2012, E. Gallagher *et al.* have published a detailed review of the methods of fabrication of vertical comb drives [116]. Here, the different strategies of fabrication of silicon comb drive will be separated depending on the mechanism used to create the vertical offset between the comb fingers. Indeed, in term of microfabrication, this point is critical. Three main strategies are detailed here: creation of the two sets of comb fingers in two different layers (2.13,(a-b-c)), etching of both the top of one set of fingers and the bottom of the other set of fingers (2.13,(d)) and etching of the top of one set of fingers (2.13,(e)).
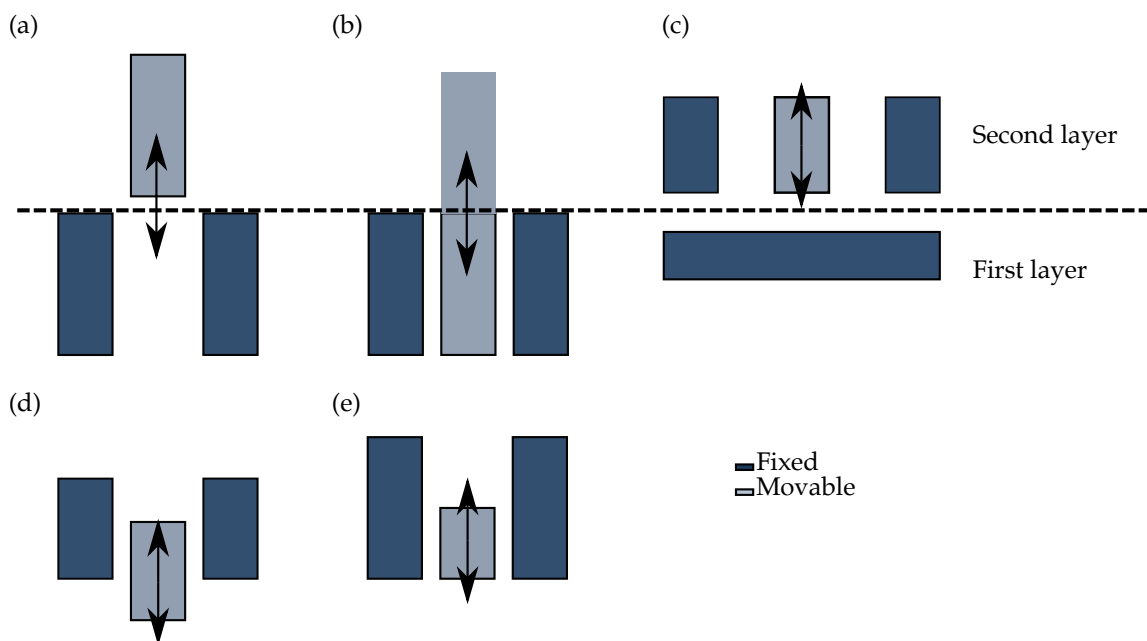
Figure 2.13: Three main strategies of vertical comb finger fabrication: (a-c)) Strategy 1 based on the structuration of two different layers, (d) Strategy 2 based on the structuration of one layer from the top and the bottom, (e) Strategy 3 based on the structuration of one layer from the top.

Strategy 1 consists in the selective etching of two different layers.

Figure 2.13 (a-b): One solution is to assemble two wafers in which one set of comb drive is etched. A first possibility is to create the comb fingers in two different silicon wafers and then bond them [117, 118]. The assembly of comb drive, fabricated separately in the device layer of two SOI wafers or with two PDMS structures has also been demonstrated [119, 120]. This technique presents the disadvantage to be very sensitive to the alignment precision between the two sets of combs. Asymmetric vertical comb drives have been also developed based on the assembly of two silicon wafers in which vertical comb drives are etched, respectively before and after the bonding of the two silicon wafers [121, 122] (Fig. 2.14).
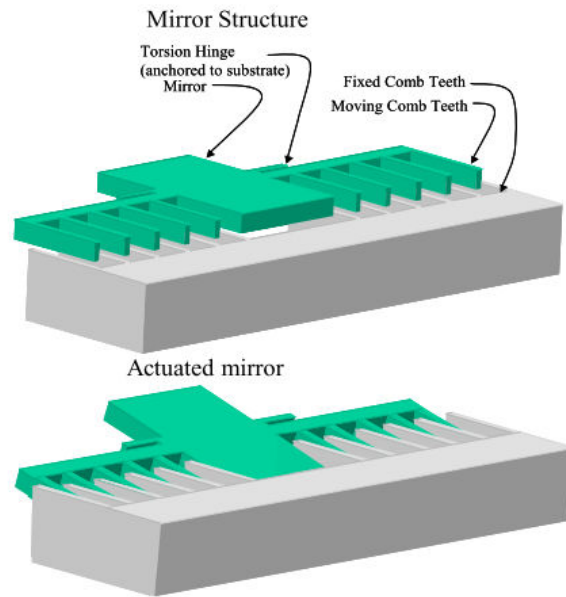
Figure 2.14: Fabrication of asymmetric comb drive by assembly of two wafers creating top and bottom electrodes [121].

In [123], Kumar *et al.* use the bonding of a silicon wafer onto a SOI wafer. One set of comb fingers is etched in the device layer of the SOI, whereas the other set of comb fingers is etched in the silicon wafer which has been previously thinned and polished. The fabrication flow chart is presented in Fig. 2.15 and shows that there is a self alignment between the two sets of comb fingers. This fabrication process has been also used in [124]. The 2D scanning micromirror fabricated is integrated in a fiber based SS-OCT for 3D imaging. Another technique, presented by Yeh *et al.*, consists in the deposition of a polysilicon layer on top of a silicon wafer. One set of comb fingers is created in the bulk silicon whereas the other set of fingers is created in the deposited polysilicon [125, 126]. More advanced technologies including the use of specific SOI wafers with embedded mask in the buried oxide were also proposed by Kwon *et al.* [127]. With this method, comb fingers are created in both the handle and the device layer created by back-side DRIE through the embedded mask. Their technology also includes the creation of backside island isolation to provide electrical isolation as well as mechanical coupling of SOI structures.

Figure 2.14 (c): Finally, another possibility is to use a SOI wafer to create classic comb fingers in the device layer over the handle layer to use the levitation force [128].

Strategy 2 consists in etching both the top of one set of comb fingers and the bottom of the other set of comb fingers (Fig. 2.14 (d)). This has been demonstrated in silicon wafer by Kim *et al.* in 2002 and by Zhang *et al.* in 2005 [129, 130]. In the two presented processes
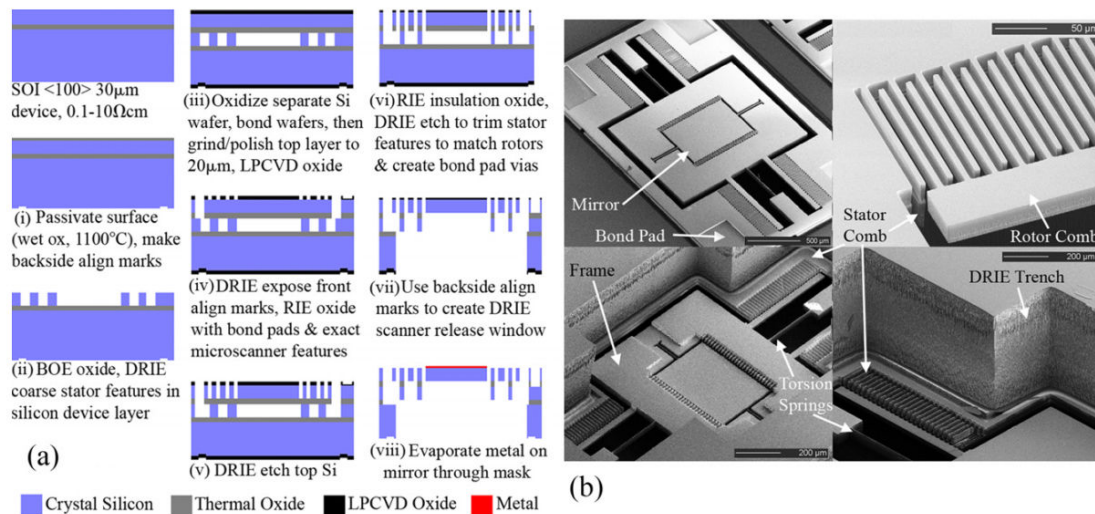
Figure 2.15: Strategy 1 of fabrication of vertical comb drives based on the assembly of two wafers [123].

(Fig. 2.16), the vertical offset created on the top of the finger is realized classically by protecting one set of comb fingers while the other one is etched. Quite the reverse, the selective etching of the bottom of the fingers is more difficult. By protecting preferentially specific comb fingers side walls, an isotropic etching, using XeF_2 in [129] or an alkaline solution in [130], is realized to create asymmetric comb fingers.

Strategy 3 consists in the creation of standard comb fingers with no vertical offset followed by a selective etching of one set of comb fingers (Fig. 2.14 (d)). Tsuchiya *et al.* have been the first to propose this method in 2004 [131] (Fig. 2.17). A first mask is used to create comb fingers in the device layer. A second mask is used to protect one set of comb fingers while the other is etched down to half the thickness of the device layer. In [131], this configuration is used for the implementation of an accelerometer, i.e. a sensor (described in the next section), but the potential of this design for electrostatic actuation is also highlighted. This strategy of fabrication have been implemented for different applications such as positioning application, and phase shifting device [132, 133, 134]. The success of this method is due to a great advantage of simplification compared to the other methods presented above. The alignment is simplified, there is no need of deposition of another material layer nor the need of assembly of two wafers.

A last strategy of fabrication of vertical comb drive for CMOS-MEMS has been demonstrated in 2002 by H. Xie *et al.* [101]. This design is very interesting because it is completely compatible with CMOS structure as the comb fingers are created in a CMOS post-processed wafer (Fig. 2.18, A.). The CMOS post-processed wafer is composed of successive metallic layers separated vertically and horizontally by dielectric layers. This metallic layers are used as masking layer to create the comb fingers. Driving voltage to

(a)

(b)

Figure 2.16: Strategy 2 of fabrication of vertical comb drives based on the etching of top and bottom of the set of facing comb fingers [129, 130].

specific metallic layers enables the creation of vertical capacitances that lead to vertical actuation (Fig. 2.18, B.).
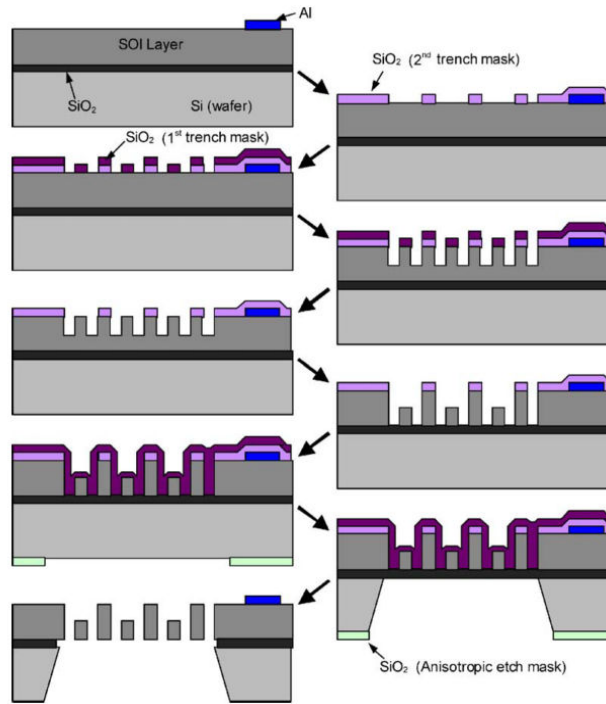
Figure 2.17: Strategy 3 of fabrication of vertical comb drives based on the etching of top one set of facing comb fingers [131].
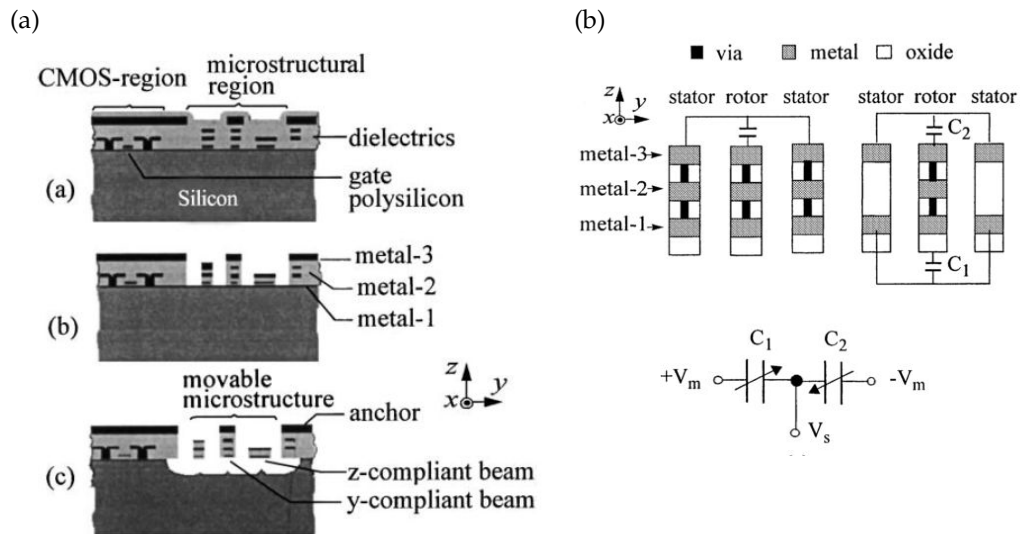
Figure 2.18: CMOS based technology: (a) main steps of fabrication of vertical comb drive micro-actuator based on a CMOS wafer, (b) schematic of the vertical comb fingers and the associated capacitances [101].

2.2.3/ EXAMPLE OF APPLICATIONS

There are few examples of MEMS optical phase-shifter in the literature. In 2006, H. Choo and al. deposited a patent which demonstrates MEMS-based, phase shifting interferometer at 23 Hz [135] (Fig. 2.19). The fabrication process is based on Strategy 3.
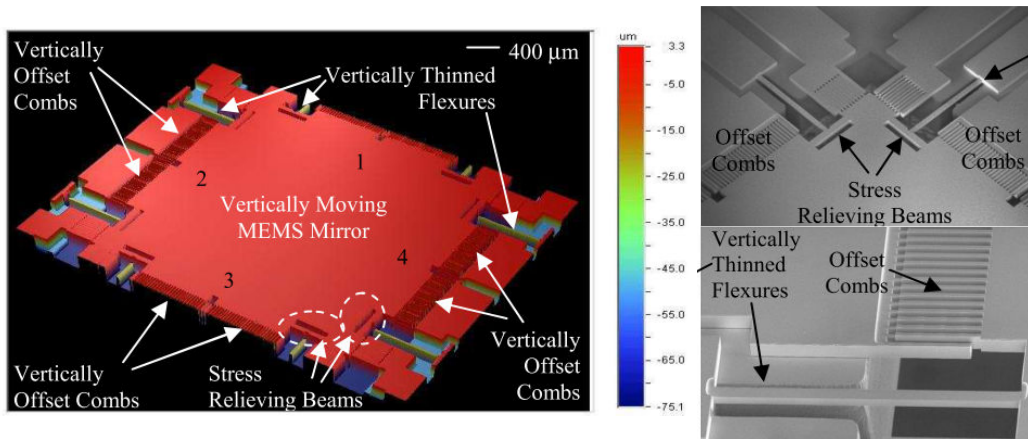
Figure 2.19: Vertical comb drive actuator developed based on SOI for phase shifting interferometry.

In 2012, K. Oda *et al.* demonstrated vertical comb drive on SOI wafer for phase shifting device and they also integrated a sensing function that is described in the next section (Fig. 2.20). Sensing is based on Strategy 3 whereas actuation is based on Strategy 1 [134]. However, only static behaviour was characterized.
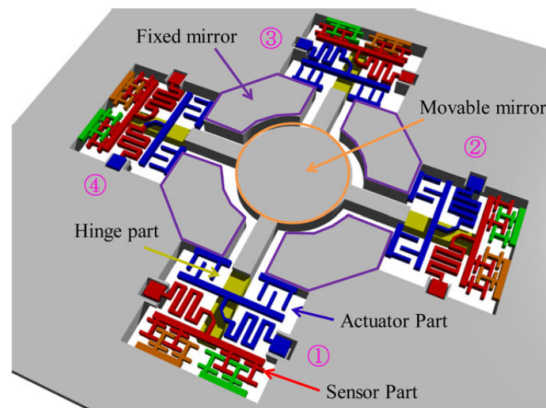
Figure 2.20: Vertical comb drive actuator based on SOI developed for phase shifting interferometry with embedded sensing function.

Finally, vertical comb drive implemented for a phase shifting device was also presented in 2010 by Chiou *et al.* based on the CMOS-MEMS fabrication process described above [136] (Fig. 2.21). An array of 3x3 micromirrors is fabricated with individual driving and sensing. The device is designed to have a resonant frequency at 3.71 kHz and a static displacement of 128 nm is achieved with a driving voltage of 38 V which corresponds to an optical phase shift of $\frac{\lambda}{4}$ in the designed system.
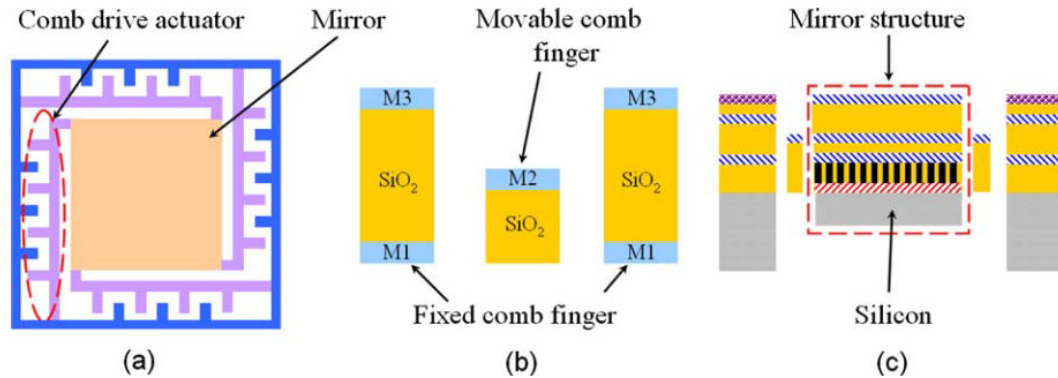
Figure 2.21: Vertical comb drive actuator based on CMOS technology developed for phase shifting interferometry [136].

2.3/ EMBEDDED SENSING FUNCTION IN ELECTROSTATIC VERTICAL COMB DRIVE SCANNERS

Accurate positioning is of great importance for many applications of MEMS and MOEMS. Microscanners for example have a high potential as phase-shifters for interferometry where the nanometer-scale position accuracy is requested over a displacement range of few micrometers. In order to make such systems both economically viable as well as compact, on chip position sensing appears to be a requirement. Among the possible strategies of position sensing, the piezoelectric and the electrostatic effects are the most used. When it deals with electrostatic actuation, electrostatic sensing is preferred. Indeed, it is more convenient to implement the same technology for both sensing and actuation on a same chip. All the configurations presented before for actuation can be used in a reverse way for sensing purposes. In the case of the electrostatic principle, the displacement of one electrode towards the other creates a change of capacitance that can be detected. When vertical electrostatic comb drive actuators are used, comb sensing is easily integrated. If the capacitance between a moving comb finger and two fixed neighbouring comb fingers is not a linear function of the vertical displacement, H. Xie et al proposed a differential design based on CMOS type comb finger which leads to a linear variation of the sensing differential capacitance regarding the vertical displacement [101]. Tsuchiya *et al.* adapted this differential sensing using two designs of silicon comb fingers, one small moving finger and one high moving finger [131]. The differential capacitance of these two complementary asymmetric designs is a linear function of the vertical displacement of the moving fingers and is not sensitive to in-plane displacements. In 2012, two papers presented such a design for phase shifting devices [133, 134]. The two configurations of comb fingers are presented in Fig. 2.22, (a).

(a)   (b)
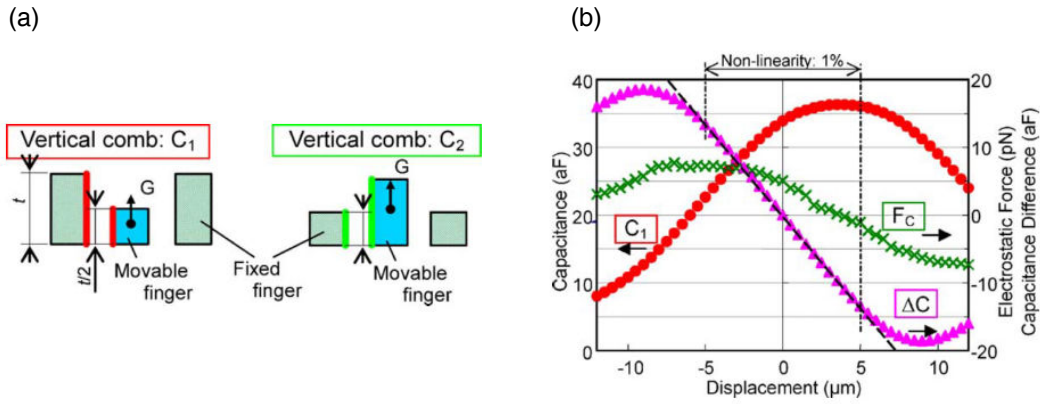
Figure 2.22: Differential capacitance sensing: (a) Design of the two differential comb fingers configuration, (b) Simulation of the capacitance, the differential capacitance and the electrostatic force associated with C_1 variation.

The typical variations obtained are presented in 2.22 (b).

If the fringe effect is neglected, the variation of the capacitance C_1 of Fig. 2.22, (a) can be written as:

$$\Delta C_1 = -2\epsilon \frac{h}{d}\Delta l \tag{2.24}$$

and the variation of the capacitance C_2 of Fig. 2.22 (a),

$$\Delta C_2 = 2\epsilon \frac{h}{d}\Delta l - 2\epsilon \frac{l}{d}\Delta h \tag{2.25}$$

Finally, one obtains:

$$\Delta C = \Delta C_1 - \Delta C_2 = 2\epsilon \frac{l}{d}\Delta h \tag{2.26}$$

Another solution is also to create parallel plate sensing using the back-side of the actuated micromirror as a first electrode and the substrate as a second electrode. This solution is suited when reflective micromirrors are designed or a transparent ITO electrode must be integrated which complicates the technology. This reflective micromirror approach has been proposed in 2003 by A. Lee *et al.* in [128] (2.23).
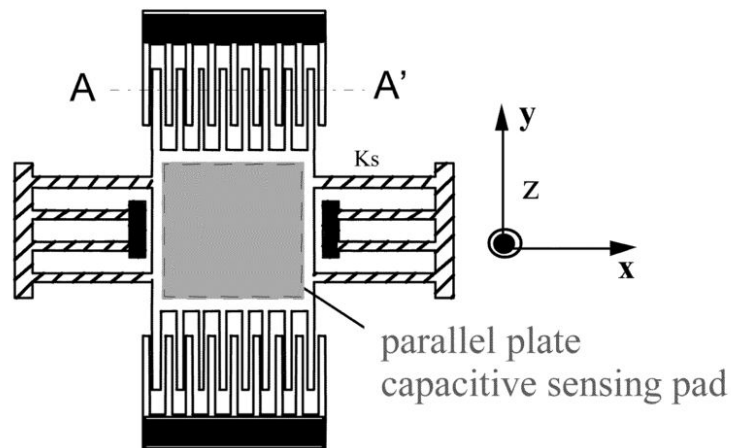
Figure 2.23: Vertical actuation with comb fingers and sensing with parallel plates.

2.4/ CONCLUSIONS

The main actuation principles have been presented and illustrated with typical examples of fabrication. Among the possible solution of implementation, electrostatic actuation is chosen for its relatively simple fabrication process due to its compatibility with silicon standard technologies. In particular, the electrostatic design based on comb fingers has several advantages for the integration of a phase-shifter producing the out-of-plane displacement of the reference mirror of a Mirau micro-interferometer. As the displacements required are relatively small (hundreds of nanometers), the required voltage is typically below 50 V, depending on the overall design. Moreover, the other possible design, i.e. parallel plate capacitance, is not well suited in the case of a Mirau interferometer as it requires a bottom electrode, that is usually not transparent and that prevents the light from going through the micromirror plane. To implement a electrostatic vertical comb drive actuator, several solutions have been highlighted. Though, Strategy 3 is chosen for its simple design and is compatibility with the integration of an embedded capacitive position sensing function based on the same technology. Few examples in the literature have shown that the vertical electrostatic comb drive is well suited for the phase-shifting technique and only one proposes an embedded sensing function. The aim of this thesis is to realize such a movable structure, carrying an array of 4x4 micromirrors that is designed to be implemented in a Mirau micro-interferometer. This last requirement is essential and is the guideline for the optimal design of the actuated array of micromirrors. The next chapter presents the design and the simulation of the electrostatic comb drive actuator in terms of optical, electrical and mechanical aspects.

3

DESIGN AND SIMULATION OF VERTICAL MICROSCANNER

The vertical microscanner developed in this thesis is a building block of a monolithically integrated array-type Mirau micro-interferometer. For the targeted application, i.e. skin visualisation for early diagnosis of skin pathologies, the Mirau micro-interferometer is integrated in a swept-source OCT system. The design of the vertical microscanner must be adapted to this purpose, i.e. meet the OCT specifications. Thus, the concept of the Mirau micro-interferometer, as part of the OCT system, is firstly presented in terms of optical design and technological implementation. Secondly, two designs of the vertical microscanner, based on two different strategies of fabrication, are proposed. Electromechanical simulations have been also conducted to optimise the vertical microscanner design in order to find the suitable parameter values.

3.1/ OPTICAL DESIGN OF THE SS-OCT SYSTEM

3.1.1/ GENERAL INTRODUCTION

According to the requirements linked to the visualisation of skin cancers at an early stage, three parameters are first considered: the image area, the axial and lateral resolutions. As mentioned earlier, in order to visualize the borders of the common lesions, an area of 8x8 mm^2 is targeted together with a resolution of 5-7 μm in both directions. The field of view of an interferometer is directly linked to the size of the reference mirror. Imaging of such a large field of view (8x8 mm^2) would require the use of a large mirror and thus a large diameter lens. Indeed, the diameter of the Mirau lens must be much larger than the reference mirror, as the latter creates a central obscuration of the light beam. Moreover, the lateral resolution of an optical system is proportional to its lens diameter and its focal length. If a high resolution is targeted and a large diameter lens is used,

it means that a long focal length is necessary. Obviously, a large diameter lens with a long focal length leading to a large device is not compatible with the objective of a miniaturised system. Moreover, large diameter lenses cannot be fabricated with micro-fabrication process that usually limits the lens diameter to few millimetres. Finally, from an optical point of view, it is difficult to maintain a high resolution over a large field of view. Indeed, the spatial sampling of the field of view must be high enough to keep the resolution. However, a high spatial sampling is possible with a high magnification between the sample and the detector and with a very large detector [137]. Here, the array of micro-interferometers offers a good compromise using low magnification to benefit from relatively long working distance and wide field of view while high resolution is obtained. Each micro-interferometer is composed of microcomponents and can image a small part of the targeted field of view. Then, a full image can be reconstructed through lateral and axial scanning along with a stitching of the different zones of interest. This solution has been chosen and a 4x4 array-type Mirau micro-interferometer has been designed.

3.1.2/   DESCRIPTION OF THE SYSTEM

The optical design of the SS-OCT is presented in Fig. 3.1. The different functional blocks of the system are described below.

3.1.2.1/   ILLUMINATION

The light is generated by a swept-source and is brought to the microsystem through an optical fiber creating a spatially incoherent source. The swept-source consists of a superluminescent diode (SLD), commercially available [138], which is filtered by a MEMS Fabry-Perot interferometer (FPI) developed by VTT Technical research center of Finland in the frame of the project [139]. For the optical design, the SLD chip (size 4 µm x 4 µm) can be assumed as a point source. This point source is collimated by an aspheric lens. The collimated light is then filtered by the FPI and finally coupled to a multi-mode (MM) fiber thanks to the same collimation lens. An appropriate collimation lens is a Thorlabs lens (C150TME-B). The MM fiber has a core diameter of 1.2 mm. The light coming out from the fiber is recovered by a condenser lens triplet whose goal is to collimate the light over the matrix aperture.

3.1.2.2/   MICRO-INTERFEROMETER

The collimated light is then split by a beam splitter cube so that half of the light is directed onto the micro-interferometer. The light travels through the Mirau micro-interferometer.
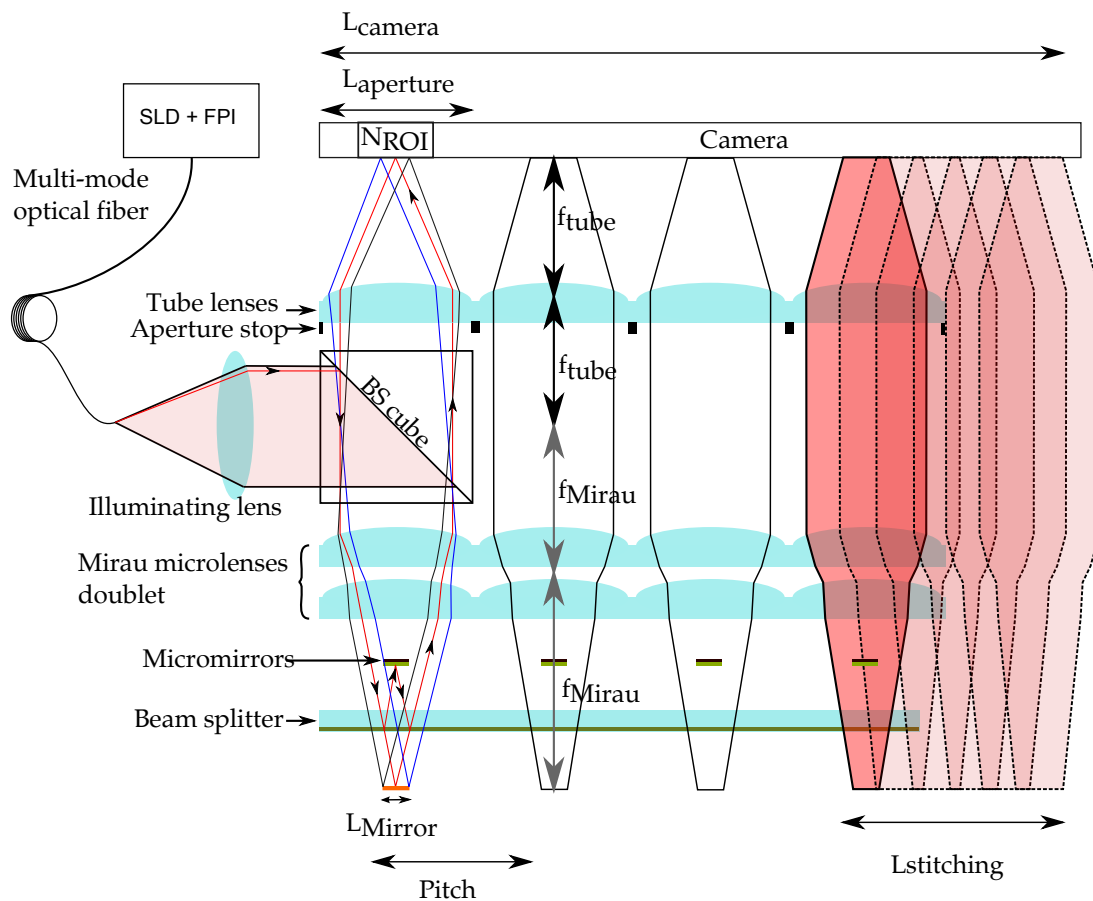
Figure 3.1: SS-OCT design: The light path and the stitching principle are illustrated in only one channel for clarity. In reality, the beam splitter cube (BS cube) is as large as the lens matrix to redirect the light coming from the source in all the channel and all the channels are moved at the same time. The full-field is illustrated by showing three light rays (black, blue and red) whose direction is shown for the red ray. SLD: Super-Luminescent Diode, FPI: Fabry-Perot Interferometer

The Mirau microlens focusses the light in the skin. The focused light propagates simultaneously thanks to the Mirau beam splitter to the skin and until the Mirau reference micromirror. Light going back from the skin and from the micromirror interfere and goes out from the interferometer through the Mirau microlens. The condenser lens and the Mirau lens creates a 4-f optical system.

3.1.2.3/ IMAGING

The light coming back from the micro-interferometer, and carrying the interference signal, goes through to the beam splitter cube where one part of the light goes to the camera. The light is focused on the camera by a tube lens. The Mirau lens and the tube lens creates a 4-f optical system, which focus the light on the camera. The camera is a high speed camera (framerate=4 kpfs), developed by the CSEM. It is based on a 1024x1024 matrix of

12 μm pixels.

3.1.3/ OPTICAL DESIGN

The targeted parameters are an axial and lateral resolution around 5-7 μm and a final field of view of 8x8 mm^2. In FD-OCT, the lateral and axial resolution are not directly coupled allowing to equalize them.

On the first hand, the axial resolution is limited by the light source bandwidth and central wavelength as shown in Eq. 1.13. We choose a bandwidth $\Delta\lambda$ of 50 nm and a central wavelength λ_0 of 850 nm. These two parameters are a good compromise because the bandwidth should not be too large to limit the effect of dispersion and the central wavelength set to 850 nm gives a good contrast when imaging skin. The calculated axial resolution δz is equal to 6.38 μm which is within the specifications:

$$\delta z = \frac{2ln(2)}{\pi} \frac{\lambda_0^2}{\Delta\lambda} = 6.38 \, \mu m \tag{3.1}$$

On the other hand, the lateral resolution is calculated based on the Rayleigh criteria according to Eq. 1.15 which results in 5.2 μm if a numerical aperture of 0.1 is considered:

$$\delta x, y = 0.61 \frac{\lambda_0}{NA} = 5.2 \, \mu m \tag{3.2}$$

The axial resolution and the lateral resolution are close providing a isotropic imaging system. In the following, the axial and the lateral resolution are supposed to be the same and equal to 6 μm. The Nyquist criteria states that the imaging sample rate, i.e. the pixel size, should be one half of the size of the smallest imaged object, i.e. the lateral resolution. Then the imaging magnification should be equal to:

$$M_{imaging} = \frac{2\Delta x}{\delta x, y} = \frac{2 \times 12}{6.38} = 3.7 \tag{3.3}$$

where Δx is the pixel size equal to 12 μm.

Finally, to image a field of view of 8x8 mm^2, different arrays of micro-interferomters are possible: 2x2 lenses (diameter 4 mm), 3x3 lenses (diameter 2.7 mm), 4x4 lenses (diameter 2 mm), and so on. A good compromise corresponds to lenses providing a good trade-off between field of view, focal length and lateral resolution. Technological considerations must also be taken into account because it limits the lens parameters, and in particular

the diameter [140]. Based on these considerations, a diameter lens of 1.9 mm has been chosen to form a 4x4 matrix. A larger diameter would be difficult to fabricate by microfabrication techniques and a smaller diameter would induce a small field of view. An array of microlenses is superposed to an array of micromirrors to create the Mirau micro-interferometers. A volume stop is placed in front of the camera to avoid the cross talk between the channels. This volume stop limits the aperture on the camera to 1.5x1.5 mm^2 per channel. According to the imaging magnification, the reference micromirror size, L_{Mirror}, is calculated equal to 400 μm which results in a field of view of 1480x1480 μm^2 in the image plane. The micromirror creates a central obscuration which leads in a transmission of the mirror plane of 94% which is higher than typical values studied in the literature (70%-80%) [141, 142]. The distance between the microlenses and the micromirrors is not critical in itself, as long as its impact on the obscuration ratio is not significant. In order to avoid the use of an additional spacer, the distance between the microlens and the micromirror is set to the thickness of the micromirror wafer, which is typically around 500 μm. Finally, the effective diameter of the lens is limited by an aperture stop of diameter equal to 1.5 mm to minimize the effect of spherical aberrations present at the lenses borders. Then, assuming a paraxial approximation, the Mirau lenses effective diameter is 1.5 mm and it corresponds to a focal length of 7.5 mm (NA=0.1).

$$f_{Mirau} = \frac{D_{Mirau}}{2 \times NA} = \frac{L_{aperture}}{2 \times NA} = \frac{1.5mm}{2 \times 0.1} = 7.5\,mm \tag{3.4}$$

In the Mirau micro-interferometer, the distance between the micromirror and the beam splitter is optically critical as it ensures that the micromirror is in the "focal plane" of the microlens. Indeed, it has been shown previously that the optical path difference between the sample arm and the reference arm should be small to benefit from a higher sensitivity [21]. Taking into account that the distance between the lenses and the micromirrors is equal to 0.5 mm, it results that the distance between the Mirau micromirrors and the beam splitter is set to 3.5 in order to have the micromirrors in the focal plane of the Mirau lenses (7.5 mm = 2 x 3.5 mm + 0.5 mm).

The total optical path length defines the vertical size of the final optical system. It is the sum of the focal length of the Mirau lens and the tube lens, which are calculated as follows:

$$f_{tube} = M_{imaging} \times f_{Mirau} = 3.7 \times 8 = 27.75\,mm \tag{3.5}$$

$$f_{Mirau} + f_{tube} = 35.25\,mm \tag{3.6}$$

Note that the Mirau lens has been modified into a doublet of lenses in order to improve the quality of the focussing beam. Indeed, the optical system is less sensitive to spherical aberrations when using two successive lenses. This can be explained by the diminution of the required refractive power when using two lenses compared to one lens.

Finally, the condenser focal length is chosen equal to 16 mm to obtain a magnification of 0.47. This results in a lateral field of view in the skin of 560 μm (MM fiber core diameter is equal to 1.2 mm), which is larger than the field of view that we want to image on the camera (400 μm).

$$M_{illumination} = \frac{f_{Mirau}}{f_{Condenser}} = 0.47 \tag{3.7}$$

The aim is to image a 3D volume with an imaging depth of 600 μm according to the targeted application of detection of early skin cancers. The imaging depth depends on the axial field of view of the system as explained in 1.2.1.5. It is calculated as follows:

$$FOV_{axial-coherent} = \frac{4ln(2)}{\pi} \frac{\lambda_0^2}{\delta\lambda}$$
$$= 638 \,\mu m \tag{3.8}$$

where $\delta\lambda$ is the linewidth of the light source.

However, the axial field of view is also limited by the geometrical optics as:

$$FOV_{axial-geometric} = 1.77 \frac{\lambda}{NA^2}$$
$$= 150 \,\mu m \tag{3.9}$$

Here, the axial field of view is then limited by the optics and is equal to 150 μm.

The parameters of the optical design are summarized in Table 3.1.

Table 3.1: Parameters of the optical design of the SS-OCT system and their value.

System parts	Parameters	Values
Illumination	SLD Central wavelength/Bandwidth	850 nm / 50 nm
	MM Fiber core diameter	1.2 mm
	Condenser focal length ($f_{Condenser}$)	16 mm
	Magnification	0.47
Beam splitter cube	Ratio / size	50-50 / 10 mm
Micro-interferometer	Matrix	
	Array	4x4
	Pitch	2 mm
	Lens fill factor	1.9/2
	Mirau lens	
	Focal length (f_{Mirau})	7.5 mm
	Diameter (D_{Mirau})	1.9 mm
	Mirau mirror	
	Mirror size	400 μm x 400 μm
	$d_{lens-mirror}$	500 μm
	$d_{mirror-BS}$	3.5 mm
	Mirau beam splitter ratio	70/30 (T/R in %)
Imaging	Tube lens	
	Focal length (f_{tube})	27.75 mm
	Diameter (D_{tube})	1.9 mm
	Camera	
	Number of pixels (N_{pixel})	1 Mpixels (1024x1024)
	Pixel size (L_{pixel})	12 μm x 12 μm
	Diameter of the aperture stop ($L_{aperture}$)	1.5 mm
	Magnification	3.7
Aperture stops	Diameter size	1.5 mm

3.1.4 / STITCHING

To be able to record B-Scans, or potentially a 3D image, the array is laterally moved so that each micro-interferometer can image a total area covering the gap between two neighbouring micro-interferometers. This gap corresponds to the pitch of the array which is 2 mm. Then, each micro-interferometer must image a total 2D area of 2x2 mm^2 thanks to scanning and stitching. Hence, due to the matrix arrangement, lateral movements of 2 mm range lead to image continuously 8x8 mm^2. Moreover, the total targeted depth of field is 600 μm to be able to reach and recover the dermo-epidermal junction. Z-stitching is necessary to image such a depth. Figure 3.2 shows a 3D view of the array of micro-interferometers. Each micro-interferometer has a field of view represented by a small pink square. After x and y stitching, the black square represents the total lateral field of view. The axial field of view of the SS-OCT image is also shown for 4 stitched images.
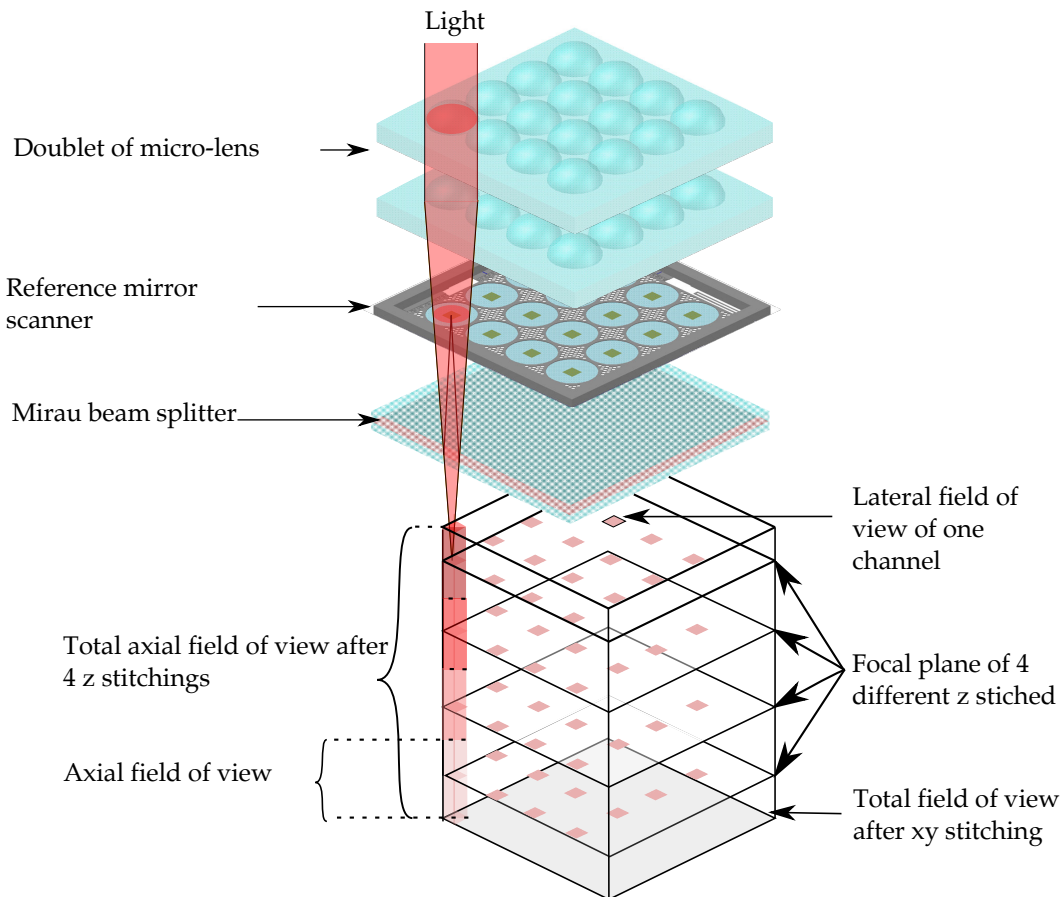
Figure 3.2: 3D visualisation of the array of micro-interferometer and its corresponding field of view. The field of view of each micro-interferometer is shown as well as the total volume imaged after x, y, z stitching.

An overlap between each image, acquired after the lateral and the vertical movements of the whole interferometer, is necessary to stitch correctly the image. The overlap region is

set to 20% of the field of view according to the results presented in [137]. In this case, the number of stitched images is calculated as follows:

$$2mm = N_{stitching}L_{Mirror} - (N_{stitching} - 1) \times 0.2 \times L_{Mirror}$$
$$N_{stitching} = \frac{2mm - 0.2 \times L_{Mirror}}{L_{Mirror} - 0.2 \times L_{Mirror}}$$
$$= 6 \tag{3.10}$$

Finally, the camera is fixed and a dynamic region of interest is used to record the interferogram. Then, the total number of pixel, taking into account the lateral stitching process and the 20 % overlap regions, must be smaller than 1024:

$$N_{pixel}\Delta x = (N_{channel} - 1)xPitch + L_{stitching}$$
$$= 3 \times 2mm + N_{ROI}\Delta x + (N_{stitching} - 1) \times (1 - Overlap) \times L_{Mirror}$$
$$= 3 \times 2mm + M \times L_{Mirror} + (N_{stitching} - 1) \times 0.8 \times L_{Mirror}$$
$$N_{pixel}\Delta x = 9.08 \, mm$$
$$N_{pixel} = 757 \, pixels \tag{3.11}$$

where $L_{stitching}$ is shown in Fig. 3.1.

Note that the number of pixels necessary to image the field of view of one micro-interferometer, i.e. corresponding to an image of 400x400 μm and referred to as N_{ROI}, is equal to 123x123 pixels.

To image a depth of 600 μm, vertical stitching is also required since the axial field of view is equal to 150 μm. Therefore, the Mirau interferometer is vertically moved 5 times by an external mechanical actuation, with overlapping regions to obtain the targeted depth of image. The external mechanical macro-actuator will not be described in this thesis. The sequence of image acquisitions is the following: one acquisition is done in all channels, and then the micro-interferometer is moved in the x direction and a second acquisition is performed. This is repeated six times and then the interferometer is moved once in the y direction and again the micro-interferometer is laterally moved 6 times in the x direction. There is a total of 6 stitching in the y direction. Then, the interferometer is moved in the z direction and the sequence is repeated. All the acquisitions are used to reconstruct the 3D volume (Fig. 3.3). The image processing is coded in the visual programming language, also called graphical language, LabVIEW (National Instruments) [143].
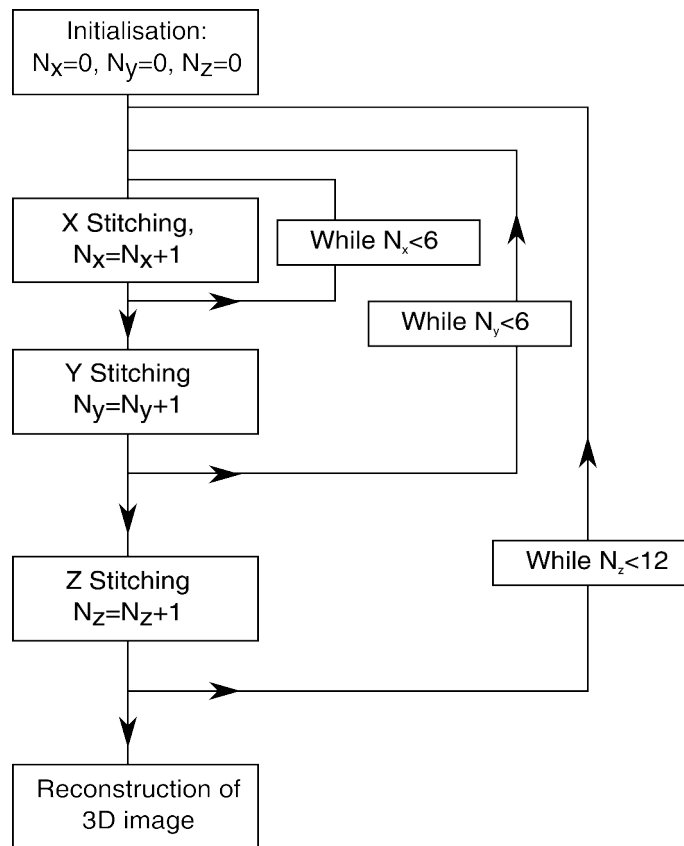
Figure 3.3: Flow chart of the sequence of image acquisition for all the channels. The image processing is coded in LabVIEW.

The system can provide different types of images. Firstly, 4 B-scans can be visualized, based on x and z scanning and stitching, in order to give a first rapid information on the lesion. Then, a 3D image can be reconstructed, based on x,y and z scanning and stitching, to give a complete view. Note that dermatologists are used to interpret histopathological images that correspond to B scans. Moreover, in practice, a 3D image is much more difficult to visualize.

3.1.5/ PHASE MODULATION

Sinusoidal phase modulation, based on the theory presented in Sec. 1.2.1.5, is used to get rid of the parasitic terms obtained in FD-OCT techniques and increase the signal dynamic of the system [22, 23]. The algorithm depends on the frequency, the initial phase and the amplitude of the sinusoidal phase modulation. To reconstruct properly the modulation, 8 acquisitions per period of the modulation must be recorded. Our high speed camera has a maximum frame rate of 4 kfps, which is why the modulation frequency is set to 500 Hz (4,000 Hz/8). Moreover, the modulation amplitude is set to $2x\frac{2.63\lambda_0}{4\pi}$, which is the optimum value for the implementation of this algorithm as defined in [22]. Ac-

cording to our parameters, the modulation displacement should then be equal to 352 nm. The initial phase depends on the electric signal phase which drives the actuator. Here, a swept-source OCT system is designed and the phase modulation algorithm must be implemented for each wavelength. Fig.3.4 shows the time line of an acquisition.
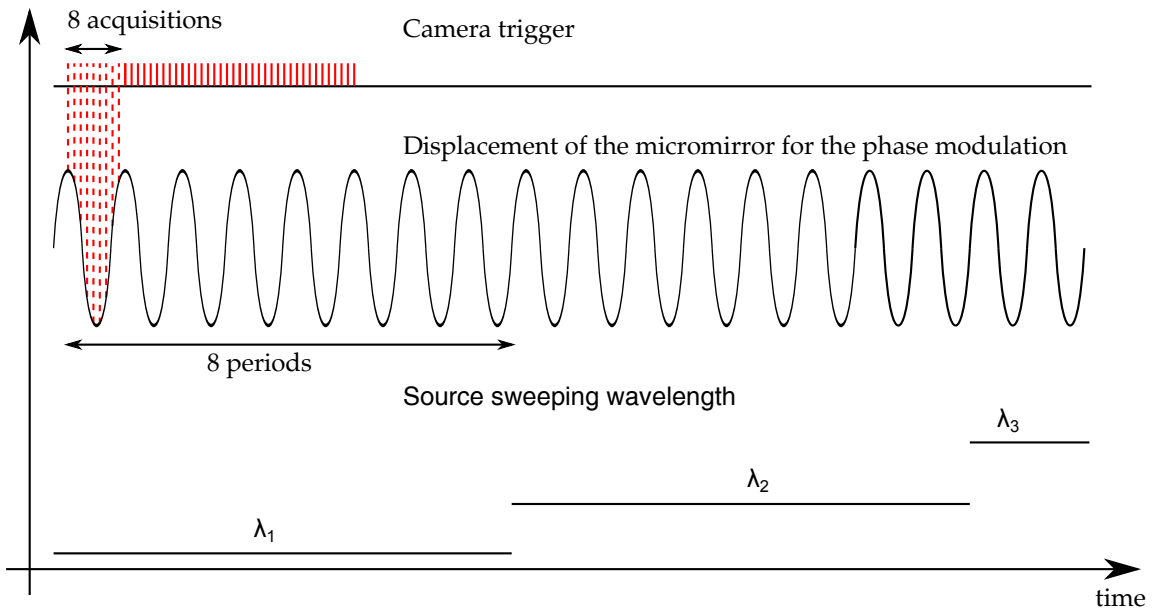
Figure 3.4: Time line acquisition for the camera, the actuated micromirror and the light source.

In order to compare our system with commercial ones (Tab. 1.2) and with the literature (Tab. 1.1), it is interesting to calculate the A-scan rate of our system. Without z scanning, the A-scan rate is calculated as:

$$
\begin{aligned}
Rate_{A-scan} &= \frac{Rate_{Source}}{N_{period-modulation}} N_{ROI}^2 N_{channel}^2 \\
&= \frac{10}{8} x123x123x4x4 \\
&= 302.6 kHz
\end{aligned}
\tag{3.12}
$$

If phase modulation is not performed, then the speed is multiply by 8. Despite a slow source, the acquisition speed is at the state of the art and our system is adapted for tissue imaging.

3.2/ DESIGN OF THE VERTICAL MICROSCANNER

As explained previously, the success of the realization of MOEMS systems relies on the capacity to combine a well designed optical system with an adequate technology of mi-

crofabrication. Based on the considerations presented in Chapters 1 and 2, a Mirau micro-interferometer has been designed for SS-OCT with an array of actuated micromirrors that enables the use of phase shifting techniques. The actuation parameters defined by the optical designs are a sinusoidal actuation which frequency equals to 500 Hz and a minimal displacement amplitude of 352 nm to be reached with a maximum voltage of 50 V required by the medical application.

3.2.1/   Vertical assembly of the Mirau micro-interferometer - MEMS concept

The 4x4 array of Mirau micro-interferometer consists of a doublet of an array of microlenses, a SOI wafer with MOEMS vertical microscanners, carrying an array of reference micromirrors, a spacer used for focus adjustment, and a planar beam splitter wafer, as shown in Fig. 3.5. Each microlens wafer consists of a Si wafer bonded with a glass wafer. Therefore, a complete Mirau micro-interferometer is a stack of 7 wafers. The assembly of this stack requires the development of an "N-bonding process", in which N substrates made from different materials will be sequentially stacked and bonded. These steps will be detailed in Sec 5.5.
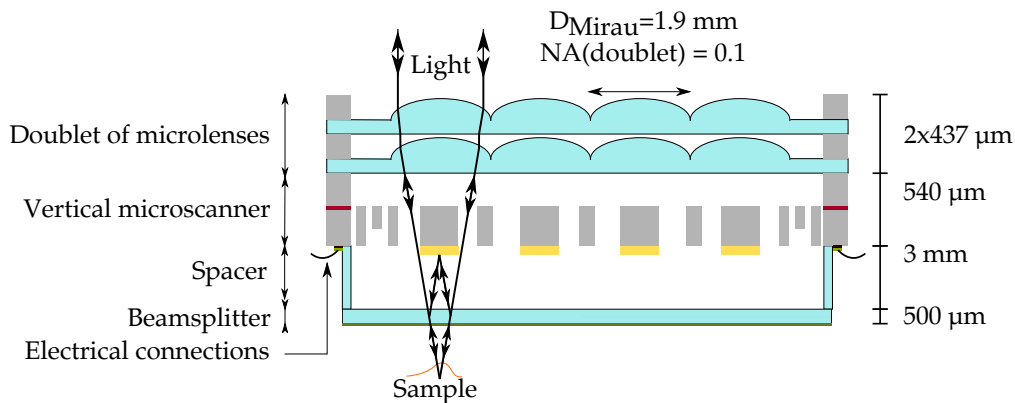
Figure 3.5: Cross-section view of the vertically integrated Mirau interferometer composed of 4x4 Mirau micro-interferometer and its main dimensions (not to scale). Light path is shown for one channel with the two border rays.

The construction of the microscanner has to fulfil several requirements related to the vertical integration within the Mirau micro-interferometer. Firstly, the microscanner wafer must be positioned up-side down in the wafer stack to ensure that the reference mirror faces the beam splitter (Fig. 3.5). Then, the distance between the Mirau lens wafer and the microscanner wafer is equal to the microscanner wafer (540 μm) and these two wafers are directly bonded together. Moreover, the microscanner wafer must be compatible with the overall integration strategy based on anodic bonding (materials, process temperature,

surface quality). Finally, electrical interconnections have to be provided to drive the actuators and sensors by external electronics. For this purpose, holes in the spacer are placed in such a way to enable side access to the contact pads, located on the border of each chip, during wire bonding [144]. The specificity of this microscanner design is that it works in transmission, i.e. the area around the micromirror must be transparent, whereas microscanners presented in the literature usually work in reflection. Moreover, the implementation of PSI method implies that the micromirrors cannot be simply deposited on the backside of the lenses [64], which are static, but must be integrated onto an actuated platform. In this thesis, two solutions are proposed, either the micromirrors are deposited on a transparent support [145] or they are held by suspensions. The two designs are presented below.

3.2.2/ MICROMIRROR PLATFORM

3.2.3/ DESIGN OF THE SILICON PLATFORM

Here, we focus on the design of the vertical microscanner. The scanner design is based on a structured silicon platform, which contains a 4x4 array of micro-mirrors. The platform is attached to the frame by use of four silicon multi-folded springs, is actuated by electrostatic comb drive and its position is sensed by additional electrostatic comb drive. A schematic of the global design is shown in Fig. 3.6.
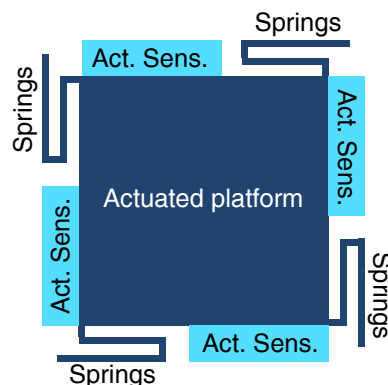
Figure 3.6: Global design of the vertical microscanner. Act.: actuation, Sens.: sensing.

The array of micromirrors is embedded in a single actuated platform because all the micromirrors must be actuated synchronously. Therefore, there is no need to individually control the displacement of the micromirrors which would require an array of individually actuated platforms. Such an array of platform with individual actuators would also be restrictive with respect to the density of the array. The platform must be as light and stiff as possible. Hence, the platform is structured with holes in order to decrease its mass. Indeed, the resonant frequency of the actuated platform with micromirrors is

related to the mass and the suspensions stiffness according to the following equation: $f_{resonant} = \frac{1}{2\pi} \times \sqrt{\frac{k}{m}}$. If m, the mass, is reduced, then k is reduced and the vertical actuation force equal to $F_z = k_z \times z$ is minimized and so the actuation energy. Moreover, the platform must be stiff enough to avoid deformations in static but also in dynamic. Indeed, if the distance between the mirrors and the beam splitter varies from one mirror to another, i.e. the optical path length in the reference arm of the interferometer changes, then the area imaged by the system varies in depth from one mirror to another. This is not a problem if the vertical offset between adjacent channels is below the axial resolution of the system (6.4 μm). If it is higher than this value, then the image treatment to recover the 3D image becomes more complicated. The actuated platform is designed as a square which dimensions respect the optical design of the array of micromirror. In particular, the side length of the platform, noted $L_{platform}$, is 8.1 mm (Eq. 3.13). The platform is structured with disk holes corresponding to the light beam diameter in the mirror plane, i.e $D_{hole} = 1840\,\mu m$. This value is smaller than the lens diameter because the light beam is focussed and then its diameter decreases along its propagation.

$$L_{platform} = 3Pitch + D_{hole} + 2L_{Border}$$
$$= 3 \times 2.0 + 1.84 + 2 \times 0.130 = 6 + 1.84 + 0.26 = 8.1\,mm \qquad (3.13)$$

where L_{Border} is the distance between the holes and the border of the platform.

To limit its mass, the square silicon platform is structured, in between the disk holes, with a honeycomb matrix. This pattern is chosen for its good trade-off between mass and stiffness. The parameters of this structure are to be defined by the simulations.

3.2.3.1/ FIRST DESIGN : GLASS SUPPORT FOR THE MICROMIRROR INTEGRATED ON SILICON ACTUATED PLATFORM

The first design deals with the integration of a transparent support for the micromirror on the silicon platform. This support must be optically transparent, mechanically supporting the micromirror, resistant to high temperature due to the use of anodic bonding during the vertical assembly and compatible with silicon that will be used for the micro-actuator. These criteria are well satisfied by the Borofloat glass. Borofloat glass is a borosilicate glass (presence of sodium ions necessary for anodic bonding) and has the advantage of having a good thermal compatibility with silicon which is critical to limit the residual stress after key technological steps such as anodic bonding for which high temperature is used (350°C). Indeed, borofloat glass and silicon have close thermal ex-

pansion coefficient around this temperature. Moreover, glass benefits from a long-term stability of its mechanical and optical properties which is necessary for MOEMS devices. Fir these reasons, a glass support is aimed at being embedded in the actuated platform to support the glass micromirrors.

The glass supports are structured as disks, covering each channel, to limit the mass of the actuated platform (15% decrease). The diameter of the glass disk bonded to the silicon is set to 2.1 mm. This ensures a bonding ring whose width is equal to 130 μm. This thickness takes into account the potential underetching due to the structuration of the glass. The glass support thickness is set to 25 μm. This thickness is thin enough to avoid a perturbation of the optical signal and to be light enough while being feasible from a technological point of view. Finally, the underetching can be as large as 25 μm if an isotropic etching technique is used.

The micromirrors (400 μm x 400 μm) are centered on the glass disks.
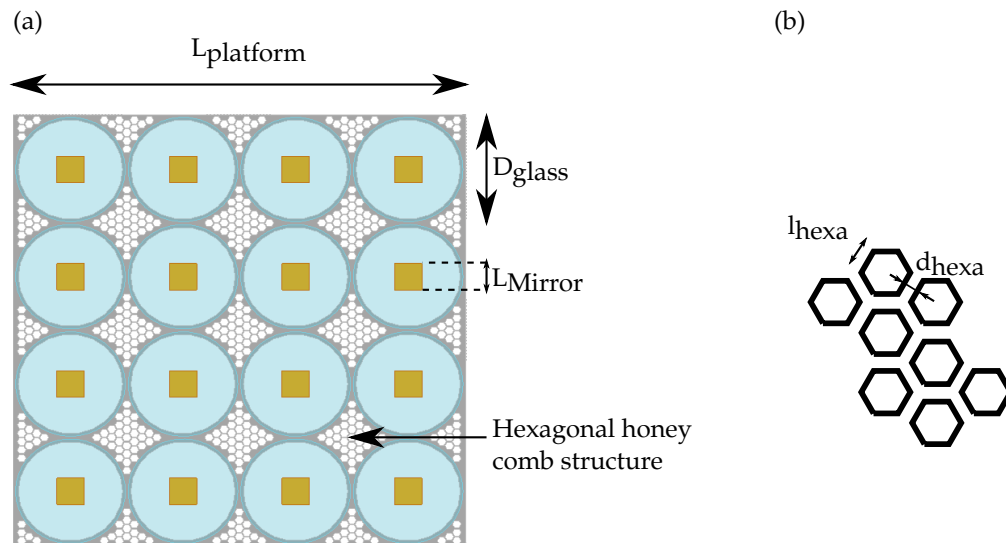
Figure 3.7: Design 1: Integration of a glass membrane, (a) Top view of the silicon platform and (b) Hexagonal honeycomb matrix parameters

The monolithic integration of a glass micro-component on an actuated silicon platform is a technological challenge in term of microfabrication. Indeed, this design results in a high topography surface MEMS because of the glass thickness. Then the basic steps used in microfabrication, such as the photolithography process becomes complicated. This point will be developed in Ch. 4. Moreover, whereas the glass is well compatible with silicon, its release is a problem since active structures are usually released by HF vapor that also etches the glass. To conclude, this design being highly challenging, a second design, more compliant with the MEMS processes, is studied in parallel.

3.2.3.2/ SECOND DESIGN : SILICON SPIDERS INTEGRATED TO SILICON ACTUATED PLATFORM

The second design aims to realize a suitable vertical microscanner only based in silicon. Macro Mirau objectives are usually based on reference mirrors suspended in the air by thin arms. This solution can be easily implemented by creating silicon suspensions and a silicon support for the micromirror. The proposed design is shown in Fig. 3.8. The overall platform design is the same than the glass integrated design except for the micromirror support.
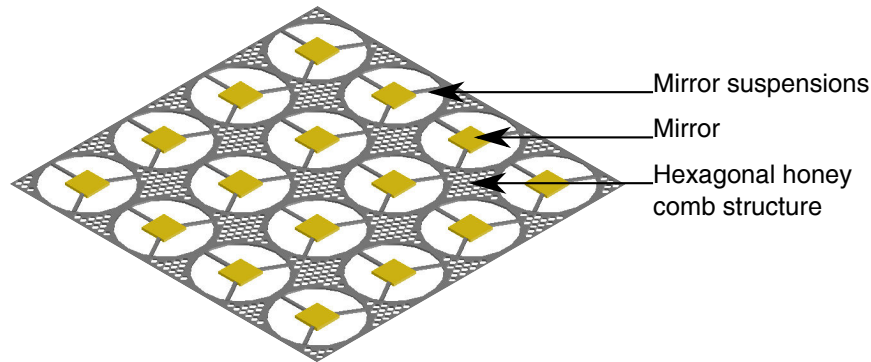
Figure 3.8: 3D view of the platform with suspended micromirrors.

3.2.4/ THE SPRINGS

The springs are positioned around the silicon platform so that the stiffness in the x and y directions are the same. The springs are designed to be stiff in the in-plane directions in order to avoid in-plane parasitic movements but soft in the out-of-plane direction. For a simple fixed-guided end beam [1], the stiffness are given by:

$$k_z = E\frac{wh^3}{L^3} \tag{3.14}$$

$$k_y = E\frac{hw^3}{L^3} \tag{3.15}$$

$$k_x = E\frac{hw}{L} \tag{3.16}$$

where E is the Young modulus of the material and w, h, l are the dimensions of the beam as described in Fig. 3.9.

---

[1]A fixed-guided end beam is a beam whose one end is fixed and the other end can only move in the plane orthogonal to its length.
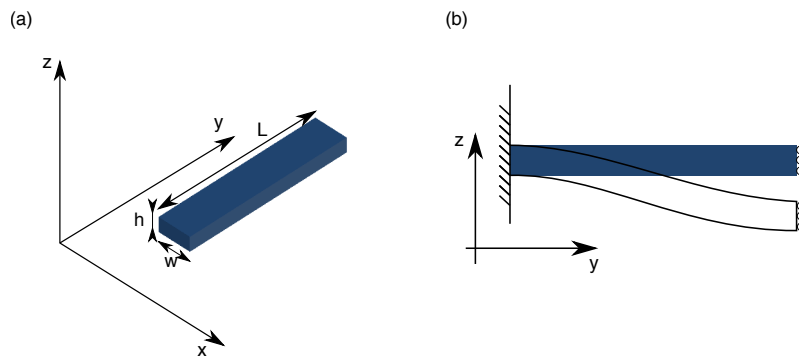
Figure 3.9: Simple beam: (a) 3D view, (b) fixed-guided end beam condition.

From Eq. 3.14, it can be concluded that when the length increases, the stiffness in the z direction decreases to the power of three. In our case, the actuation frequency is relatively small (500 Hz), then low stiffness beams, i.e. long beams, are necessary according to the formula $f = \frac{1}{2\pi} \sqrt{\frac{k}{m}}$. Moreover, for miniaturization purposes, serpentine springs are typically used to limit the area used by the springs, called the footprint. Hence, two designs, shown in Fig. 3.10, will be considered in the simulations presented later.

(a) Spring 1
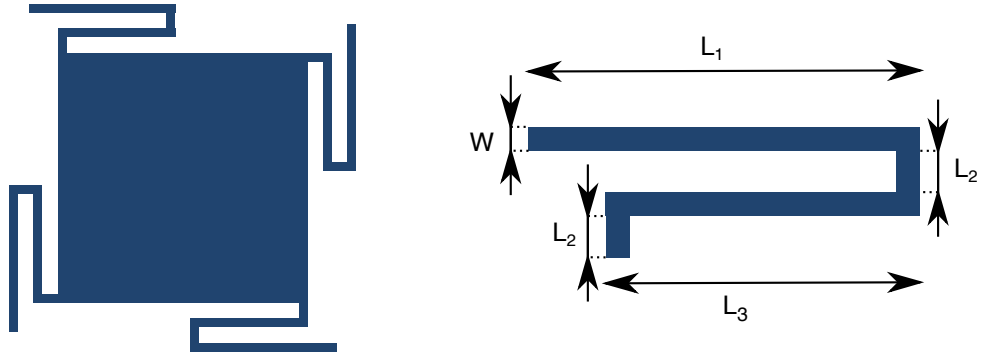
(b) Spring 2
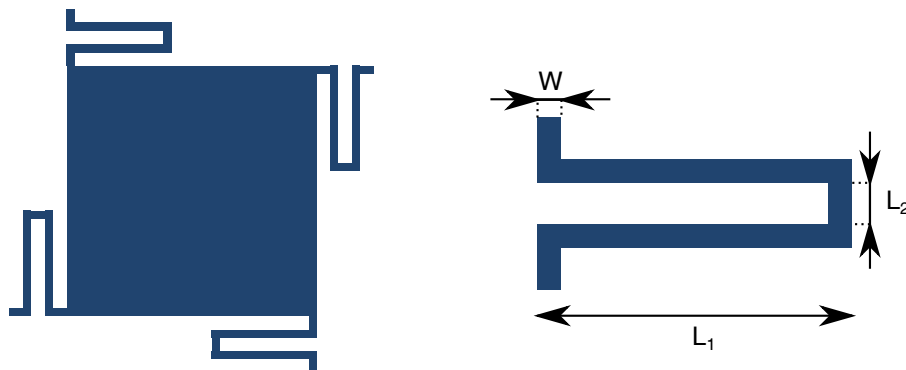
Figure 3.10: Two studied designs: (a) spring 1, (b) spring 2.

3.2.5/   THE MICRO-ACTUATORS AND THE MICROSENSORS

According to the conclusions made in Ch. 2, vertical electrostatic comb drive technology is chosen as the micro-actuation and the microsensing technique. The chosen design is the one presented in [131] and described in Ch. 2. This design has many advantages such as the relative easiness of fabrication and the compatibility of the technology with differential position sensing function. Both the vertical actuators and sensors are based on the electrostatic field created by vertical comb fingers. The design parameters to be tuned in the electro-mechanical simulations are shown in Fig. 3.11.
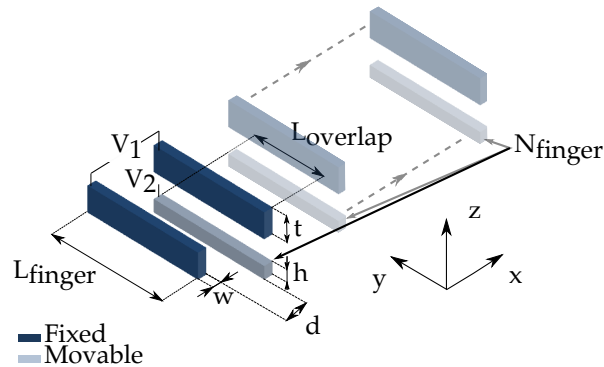
Figure 3.11: Design parameters of the comb fingers shown in 3D.

In order to use the phase shifting algorithm, it is necessary to move the platform but also to know the displacement amplitude of the micromirrors. Therefore, a capacitive sensor is also integrated to the structure. It has two interests. Firstly, it enables to control the position of the platform in case the platform is not parallel to the lens matrix and its planarity must be adjusted by vertically moving the platform. Secondly, for the phase-shifting control, it is important to know the amplitude of vibration of the platform. The design of the sensing part is shown in more details in Fig. 3.12. All the movable fingers are surrounded by fixed comb fingers. There are two configurations: one for which the movable comb finger is smaller than the fixed ones (Configuration 1) and one for which the movable comb fingers are higher than the fixed ones (Configuration 2). The sensing is realized by measuring the differential capacitance ($\Delta C = C_1 - C_2$) as the platform is vertically moving. With this differential configuration of sensing, the sensing part is more sensitive than with only one configuration. Indeed, in Fig. 3.12 (b), it is shown that when the platform moves upward, the parallel plate capacitance of C2 changes whereas only fringing capacitance impacts on C1. When the platform moves downward, it is the opposite. Then, with the two configurations, the parallel plate capacitance depends on the platform movements in the two directions and the sensor is sensitive over a wider range of movements.
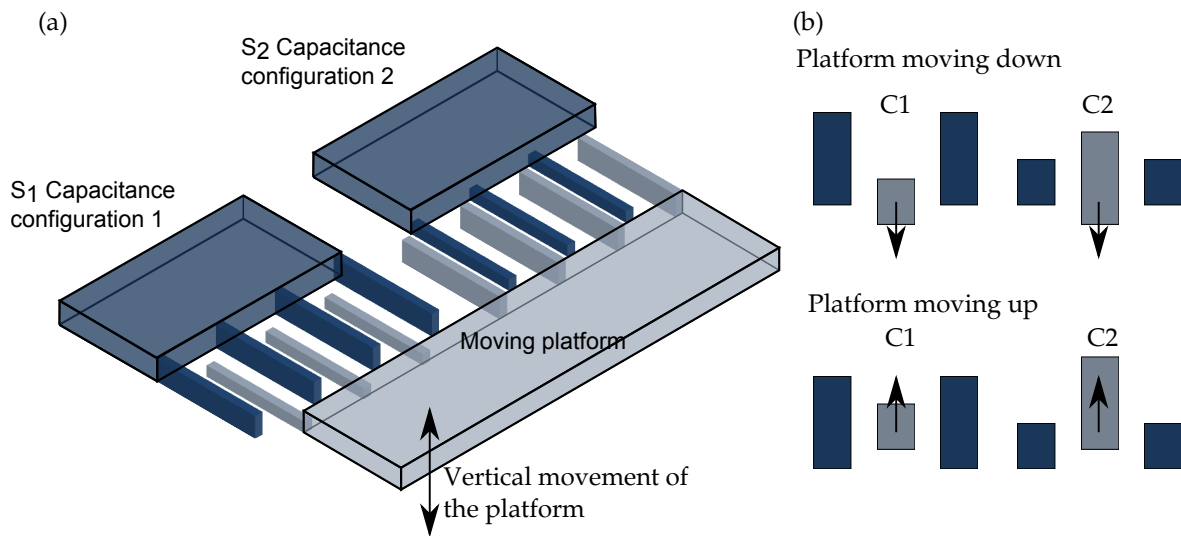
Figure 3.12: Comb finger configuration for the sensing parts: (a) fixed and moving parts facing each other taking into account the two configuration of sensors (configuration C1 and configuration C2, (b) illustration of the movement of the platform and its consequences on the movable fingers for C1 and C2.

Finally, the micro-actuators and the microsensors must be electrically isolated to use them individually. The electric isolation is realized by creating trenches in the device layer of the SOI wafer. The structure of SOI wafers, with a buried isolating layer, is adapted to realize this kind of isolation.

One goal in miniaturized device design is to limit the footprint area of the systems. Here, we take advantage of the already large silicon platform to position the electrostatic vertical comb fingers on the border of the silicon platform for the actuation and the sensing function. Moreover, the comb fingers are placed symmetrically around the platform in order to symmetrically actuate and sense the platform displacements (Fig. 3.13).
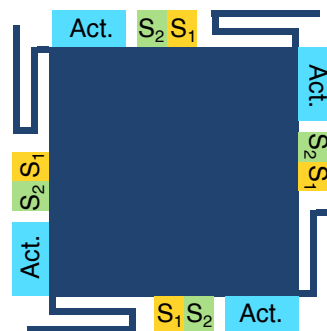
Figure 3.13: Position of the differential microsensors (S_1 and S_2) and the micro-actuators (Act.) around the platform.

According to the design of the platform, the springs, the micro-actuators and the microsensors described before, the obtained final configurations corresponding to the two

platform designs are presented in Fig. 3.14 and Fig. 3.15.
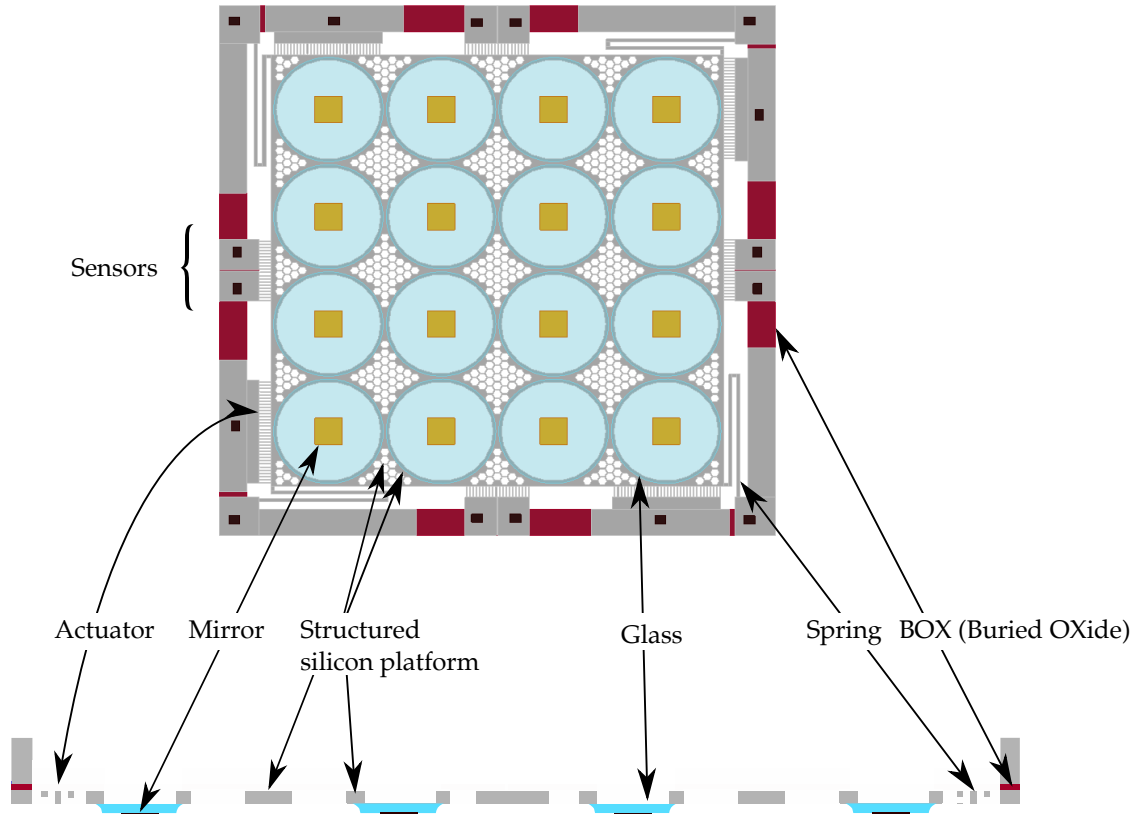
Figure 3.14: Design 1: Integration of a glass membrane, top view (top) and cross-section view (bottom) of the microscanner with integrated glass support for the micromirrors.
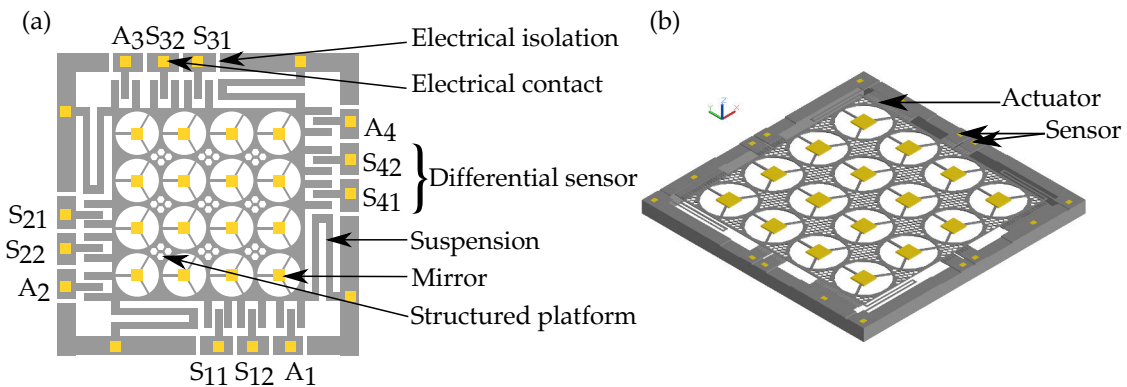
Figure 3.15: Design 2: Integration of suspension for the micromirror, (a) schematic and (b) 3D view.

The next section reports the simulation of the different parts necessary to optimize the design parameters.

3.3/ SIMULATIONS OF THE VERTICAL MICROSCANNER

In this section, the simulations relative to the design presented before are detailed. For each simulation, the model, including the materials and the boundary conditions used, is detailed.

3.3.1/ MECHANICAL STUDY OF THE VERTICAL MICROSCANNER

3.3.1.1/ SILICON: MEMS BASIC MATERIAL

The vertical microscanner presented in this thesis is based on silicon electrostatic comb drive actuation and sensing. This technology has been chosen for its good compatibility with MEMS as silicon is also a basic material for mechanical systems. More details about silicon wafer fabrication and properties are given in Annexe B.

When designing a vertical microscanner, the vertical dimensions are critical. In particular, the spring vertical stiffness has an impact on the resonant frequency corresponding to the piston mode. Moreover, for a simple beam Eq. 3.14 shows that k_z highly depends on the length and on the thickness of the beam. On the one hand, the length is an in-plane dimension that is mainly controlled by photolithography process during the fabrication. This process is very precise and resolution down to ± 1 μm can be obtained. On the other hand, the vertical dimensions, such as the spring and the platform thicknesses, are difficult to control with microfabrication techniques. One solution, widely employed, is to use a silicon on insulator wafer (SOI). This type of wafer is a stack composed of one thick silicon handle layer (300-500 μm), an insulating layer usually a silicon dioxide layer, called buried oxide layer (BOX) (1-5 μm), and on top a thinner silicon device layer (10-50 μm). The advantage of SOI wafers is that layers thicknesses are really well controlled during the fabrication process which enables the fabrication of devices close to the designed ones. In our case, SOI is also very useful to isolate the micro-actuators and the microsensors between each other. Indeed, if trenches are created in the device layer then the different parts are only connected mechanically by the handle layer and the BOX but are isolated electrically.

For the microfabrication, (100) SOI wafer were purchased to fabricate the vertical microscanner since they are the more common and are compatible with our design. Then, when considered as an isotropic material, the silicon Young's modulus is chosen equal to $E_{x,y} = 170$ GPa [146]. Moreover, the value of the Poisson's ratio, which reflects the capacity of the material to experience shear deformation, is chosen to be equal to 0.64.

According to simulations results, these values give results close to the anisotropic model results. Moreover, the SOI wafer parameters chosen are 500 μm for the handle layer, 1.5 μm for the BOX and 40 μm for the device layer. These parameters are standard so that the wafers can be easily purchased. The SOI wafer have been ordered to the company Ultrasil with the specifications given in Tab. 3.2. The cost of 25 wafers is in the order of $200.

Table 3.2: Parameters of the SOI wafer used, in this thesis, for the fabrication of the vertical microscanner. TTV stands for total thickness variation.

Parameter	Value
Diameter	100 ± 2 mm
Orientation	$(100) \pm 0.5$ deg
Type of Dopant	P (Boron)
Device layer thickness	40 ± 0.5 μm
Handle layer thickness	500 ± 5 μm
Resistivity	< 0.02 Ohm/cm
TTV	< 2 μm
Edge exclusion	< 3 mm
Finish	Double side polished

3.3.1.2/ THE PLATFORM

The function of the platform is to provide a rigid actuated support for the micromirrors. A honeycomb structure is chosen for its good trade-off between mass and stiffness, preventing the possible vertical deformation of the platform. Parameter d_{hexa} and l_{hexa} play a role on the mass and the stiffness (Fig. 3.7). The larger the width d_{hexa} and the shorter the length l_{hexa}, the stiffer and the heavier the platform. The worst case in term of stiffness, i.e. when d_{hexa} is small and l_{hexa} is large, is studied. Then in the following simulations, d= 20 μm and l = 80 μm. First, the integrated glass membrane design is modelled. A finite element model (FEM) analysis software, called Intellisuite, is used. The model, used to simulate the deformation of the structured silicon platform, is as close as possible to the real structure. The end of each spring is defined as fixed and the rest of the model is free. The material is isotropic silicon except for the glass that is defined as borofloat glass. Since the actuated platform is formed in the device layer of a SOI wafer, the thickness of the platform corresponds to the device layer thickness, i.e. 40 μm. In term of fabrication, different solutions are possible: either the BOX is removed completely or the BOX is

let under the actuated platform. In the latter case, a deformation of the platform can be expected due to the different mechanical properties of the BOX layer and of the silicon layer. The BOX is commonly fabricated by high quality thermal oxidation which requires high temperature. However, silicon and silicon dioxide have different thermal expansion coefficients, which generates a stress gradient and then a deformation. The vertical deformation linked to the stress gradient is investigated thanks to a static analysis. In this simulation the gravity is not taken into account. Two simulations have been done. The first one takes into account the glass disks while the second one does not. The results show that the static vertical deformation due to the BOX generates too much deformation for the suspended system (Fig. 3.16). Indeed, 27 μm of vertical displacement is much larger than the axial resolution of the optical system (equal to few μms). Then the BOX needs to be removed during the fabrication processes.

(a)   (b)

z_1-z_2=27 µm z_1-z_2=68 µm
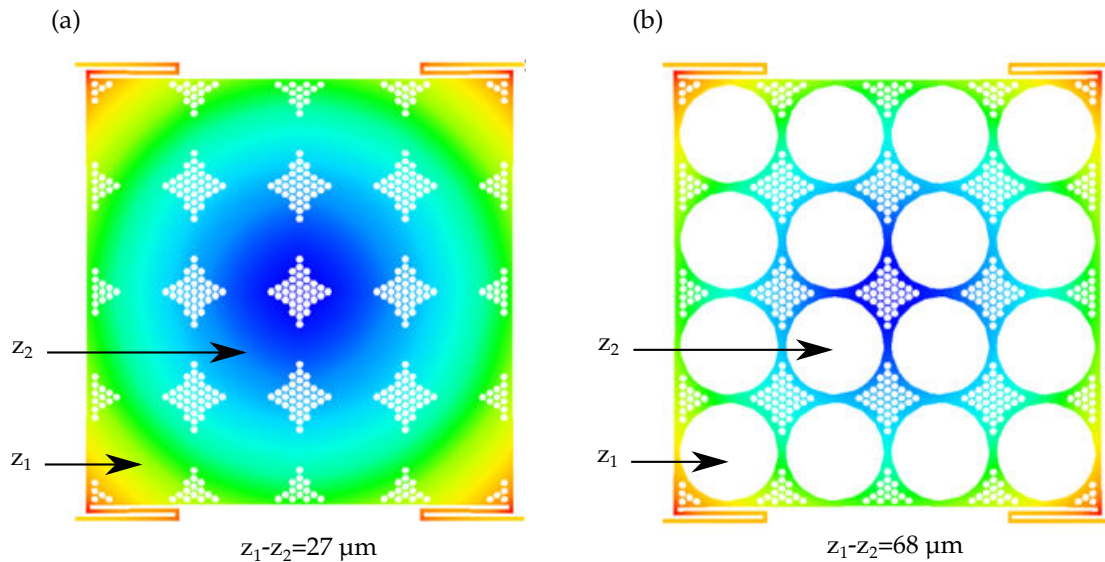
Figure 3.16: Vertical deformation of the actuated platform due to the BOX: (a) with glass disk, (b) without glass disks.

A second static simulation is used to investigate the deformation of the structured silicon platform linked to its own weight. Fig. 3.17 shows the obtained vertical deformation of the platform accross the platform. The vertical offset between a micromirror near the border and a micromirror in the center of the platform is equal to 54 nm. This value is much smaller than the axial resolution of the system, then this vertical deformation can be neglected.
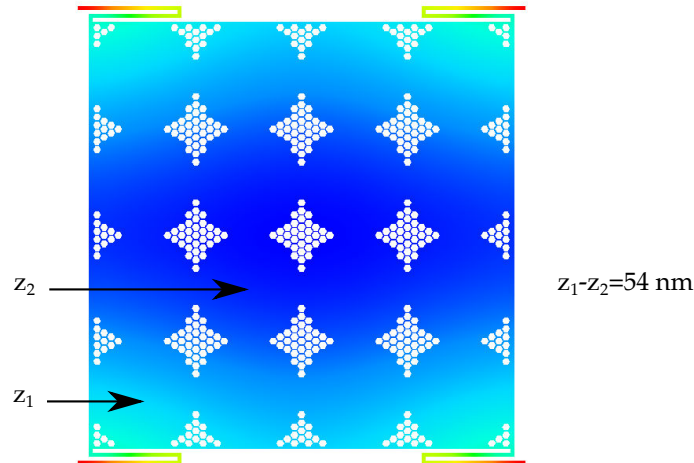
Figure 3.17: Integrated glass platform design: vertical deformation of the membrane under its own weight. The maximal deformation between two micromirrors is 54 nm.

A similar analysis is used to simulate the static deformation of the second platform design with suspended micromirrors. However, direct modelling of such complicated structure, containing the honeycomb structuration with small dimensions with respect to the platform, is problematic due to a very heavy mesh. Therefore, a simpler model, with nine 700 μm x 700 μm square holes replacing the hexagonal array, is used. The square dimensions result in the same surface than the hexagonal array so that the mass remains unchanged. This model is implemented with the suspended micromirror design. An analysis of the static vertical deformation of the platform under its own weight is performed with Comsol. Another model without any structuration of the platform is also used to compare the two limit cases in term of structuration. For the suspended micromirror design, the maximum vertical deformation equals 140 nm which is much smaller than the axial resolution of the system that is 6 μm (Fig. 3.18). Then, this static deformation has no impact on the imaging system. Moreover, optical simulations, made with Zemax, were done taking into account a tilt tolerance between the optical surface of 0.05 degree [147]. The angle, created by the vertical displacement simulated here, corresponds to a maximum micromirror angle of 0.002 degree, which is below the optical tolerance specification. Finally, the results show that the difference of vertical deformation between the two models is negligible. Then the model with square holes replacing the hexagonal array will be used in the following simulations.
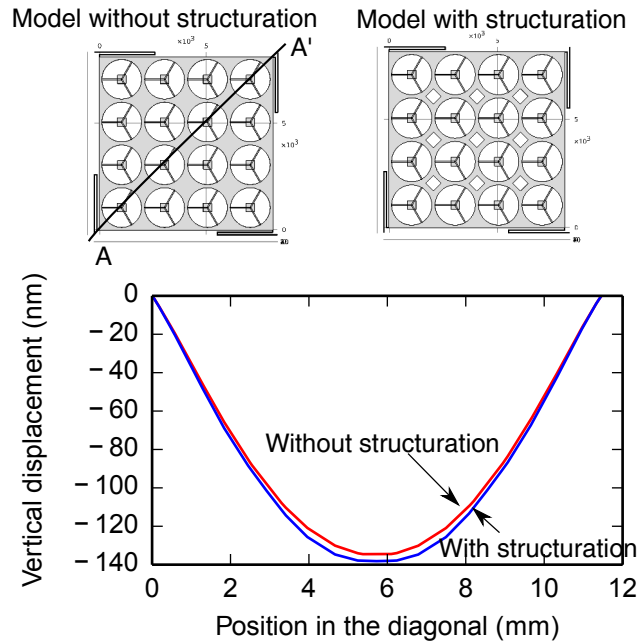
Figure 3.18: Impact of structuration of the suspended platform on its vertical static deformation (diagonal direction). Two simulations are performed to analyse two limit cases in terms of structuration: one without any structuration of the platform and one with nine 700 μm x 700 μm square holes centered between the optical apertures. These two simulations represent two limit cases in term of structuration.

The parameters of the hexagonal array are chosen arbitrarily knowing that the worst case scenario studied before gives an acceptable static deformation. The parameters are chosen to be $d_{hexa} = 30~\mu m$ and $l_{hexa} = 30~\mu m$. The mass of the platform for the integrated glass design is $4.96.10^{-6}$ kg (i.e. 5 mg) and the one of the suspended micromirror design is $2.46.10^{-6}$ kg (i.e. 2.5 mg).

Note that the vertical displacement of the platform due to gravity is a function of its weight and the spring stiffness. In fact as $z = \frac{F}{k_z} = \frac{mg}{k_z}$, the vertical displacement is a function of the ratio $\frac{k_z}{m}$ which is defined by the targeted resonance frequency according to the relation $f = \frac{1}{2\pi}\sqrt{\frac{k_z}{m}}$. Thus, the vertical displacement corresponding to a resonant frequency of 500 Hz is 1 μm. This vertical displacement must be taken into account in the simulation of the micro-actuator as an initial vertical offset between the comb fingers.

3.3.1.3 / THE SPRINGS

Von Mises stress In order to avoid in-plane parasitic movement of the actuated platform, spring suspensions have been designed to be stiff along the in-plane directions. Folded springs are suited for this kind of requirements. Moreover, they benefit from a

small footprint (Fig. 3.10). However, folded springs have the disadvantage to undergo more internal stress than straight beams. In order to check if a design can survive a specific load, the Von Mises yield criterion is usually used. Under a specific load, a ductile material experiences some deformation leading to normal and shear stresses. Von Mises stress, also called equivalent tensile stress, is a figure that takes into account both types of stresses and that can be compared to the yield strength of the material. The yield strength defines the maximal stress that a material can experience before starting to deform plastically. If the Von Mises stress is higher than the yield strength, then the material will start yielding. Von Mises stress is defined as follows:

$$\sigma_v^2 = \frac{1}{2} \left[(\sigma_{11} - \sigma_{22})^2 + (\sigma_{22} - \sigma_{33})^2 + (\sigma_{33} - \sigma_{11})^2 + 6 \left(\sigma_{23}^2 + \sigma_{31}^2 + \sigma_{12}^2 \right)^2 \right] \qquad (3.17)$$

with σ_v the Von Mises stress, and σ_{ij} the stress in the ij direction where i and j stand for x,y and z.

The Von Mises stress can be simulated with FEM simulations using Comsol software. A simulation has been performed to evaluate the stress for the two spring designs. Four springs are attached around a 3x3 mm^2 square platform. The material is defined as isotropic silicon. The free-end of each spring has a fixed boundary condition. A vertical force is applied on the platform leading to a vertical displacement of the platform and a vertical deformation of the springs. The mesh is refined in the area of interest, i.e. where the maximal stress occurs. This corresponds to the edge of the folded spring and to both ends of the springs. Fig. 3.19 shows the Von Mises stress in the structure, corresponding to a vertical displacement of 40 μm, which is much higher than the targeted displacement for our device (around 500 nm). It results that the maximal Von Mises stress obtained for the two spring designs is equal and much smaller than the yield strength of silicon. However, for the spring design 2, there is an additional area where stress is high, due to one more fold in the spring.
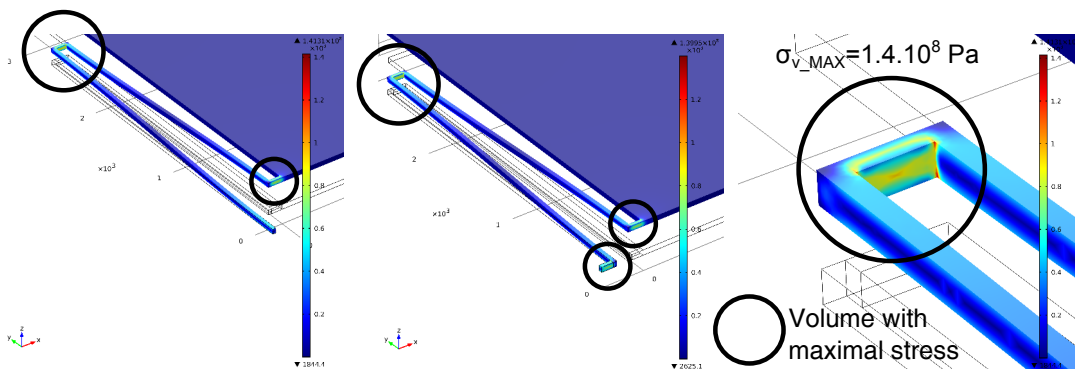
Figure 3.19: Von Mises stress in the folded springs simulated with Comsol.

Stiffness-Theory The vertical stiffness is set by the targeted resonant frequency (500 Hz $\pm$ 50 Hz, given by the specification of the system) and the mass of the platform according to the formula $f = \frac{1}{2\pi}\sqrt{\frac{k}{m}}$. Note that, taking into account the error on the device layer thickness (40 $\mu m \pm$ 0.5 μm), the resonant frequency error is $\pm$ 10 Hz. Then, with the masses estimated before, the targeted vertical stiffness for the design 1 is 12.3 N/m and for the design 2 is 6.1 N/m. The springs are placed around the platform so that the in-plane total stiffness is the same in x and y directions. Both analytical theory and Finite Element analysis are presented. Stiffness values can be derived using the energy method. This method is well detailed in [148] and is based on Castigliano's second theorem. To use this method, the serpentine spring is decomposed in 4 straight beams that are analysed in term of moment and torsion (Fig. 3.20). The spring design 1 is used to illustrate the methodology.
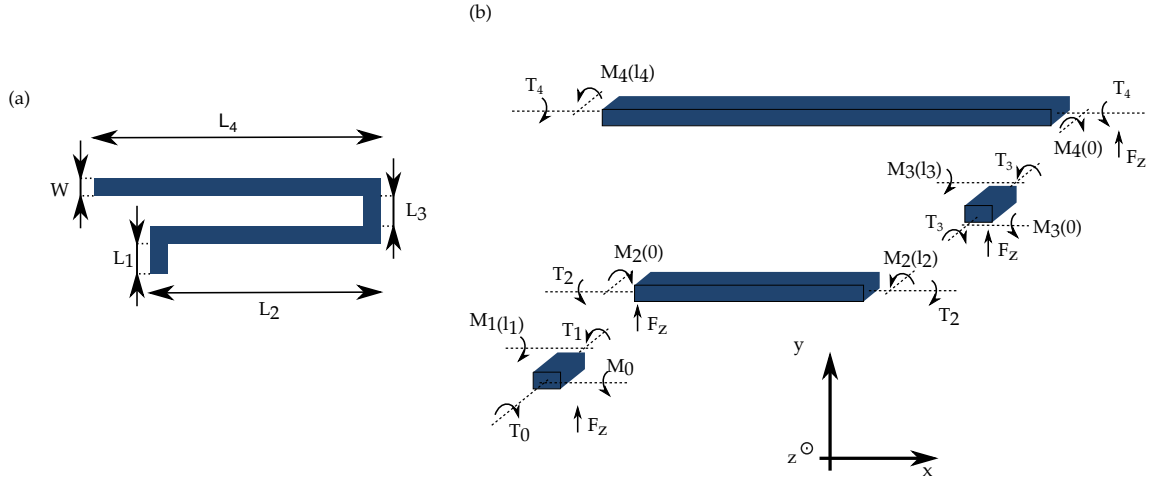
Figure 3.20: Spring: (a) spring design 1, (b) dividing into 4 straight beam for the energy method stiffness calculations.

The total strain energy of the linearly elastic structure is calculated as follows:

$$U = \frac{1}{2}\left(\sum_{i=1}^{n}\int_{0}^{l_i}\frac{M_i^2}{EI_i}d\epsilon + \sum_{i=1}^{n}\int_{0}^{l_i}\frac{T_i^2}{GJ_i}d\epsilon\right) \tag{3.18}$$

where l_i is the length of *beam$_i$*, M_i is the Moment of *beam$_i$*, T_i is the Torsion of *beam$_i$*, I_i is the Moment of Inertia of *beam$_i$*, J_i is the Torsion constant of *beam$_i$* and G and E are respectively the shear modulus and the Young modulus of the material.

For a rectangle cross-section, $I = \frac{wt^3}{12}$ and $J = \frac{1}{3}w^3t(1 - \frac{192w}{\pi^5 t}\sum_{i=1,i\,odd}^{\infty}\frac{1}{i^5}tanh(\frac{i\pi t}{2w}))$ [148].

The moment and the torsion of each beam, created by M_0, T_0 and F_z are defined as follows:

$$M_1 = M_0 - F_z \epsilon \qquad\qquad T_1 = T_0$$
$$M_2 = T_1 + F_z \epsilon = T_0 + Fz\epsilon \qquad T_2 = M_1(l_1) = M_0 - F_z l_1$$
$$M_3 = T_2 - F_z \epsilon = M_0 - F_z(l_1 + \epsilon) \quad T_3 = M_2(l_2) = T_0 + F_z l_2$$
$$M_4 = T_3 - F_z \epsilon = F_z * (l_2 - \epsilon) + T_0 \quad T_4 = M_3(l_3) = M_0 + F_z(l_1 + l_3)$$

$$\text{(3.19)} \qquad\qquad\qquad\qquad \text{(3.20)}$$

With the conditions:

$$\frac{\partial U}{\partial M_0} = 0, \frac{\partial U}{\partial T_0} = 0 \text{ and } \frac{\partial U}{\partial F_z} = \delta z$$

$$\text{(3.21)}$$

and $l_1 = l_3 = a$, $l_2 = b$ and $l_4 = c$, one obtains:

$$k_z = \frac{F_z}{\delta z} = \frac{12EGIJ(2EIa + GJ(b+c))(EI(b+c) + 2GJa)}{SUM} \qquad \text{(3.22)}$$

$$
\begin{aligned}
SUM = {} & 12E^3I^3a^2b(2ac + b^2 + bc) \\
& + 4E^2GI^2Ja\ (4a^3b + 16a^3c + 6a^2b^2 + 3ab^2c + 3abc^2 + 2b^4 + 5b^3c - bc^3 + 2c^4) \\
& + EG^2IJ^2 \quad (32a^5 + 8a^3b^2 + 40a^3bc + 32a^3c^2 + 16a^2b^3 + 24a^2b^2c - 24a^2bc^2 \\
& \qquad\qquad + 16a^2c^3 + b^5 + 5b^4c - 2b^3c^2 - 2b^2c^3 + 5bc^4 + c^5) \\
& + 2G^3J^3a \quad (8a^3b + 8a^3c + b^4 + 4b^3c - 6b^2c^2 + 4bc^3 + c^4)) \qquad\qquad \text{(3.23)}
\end{aligned}
$$

A code in Python has been written to facilitate the calculation. Note that the choice of a, b and c, i.e. the way how the folded spring is cut into 4 beams matters. There is no specific indications in the literature on how to choose these dimensions. One way is to consider the neutral fiber of the folded spring. However, it does not correspond well to the fact that the energy of each small beams is calculated. There are two other ways to cut the folded spring, while having $l_1 = l_3 = a$, as shown in the Fig. 3.21.

However, it can be found that solution 2 presented in Fig. 3.21 (b) gives results close to the simulation for lateral stiffness calculations whereas Fig. 3.21 (a) gives results close to the simulation for vertical stiffness calculation. Then, a solution taking into account the two different dividing ways is chosen.

This method is also used to calculate the lateral stiffness of spring design 1 and for all
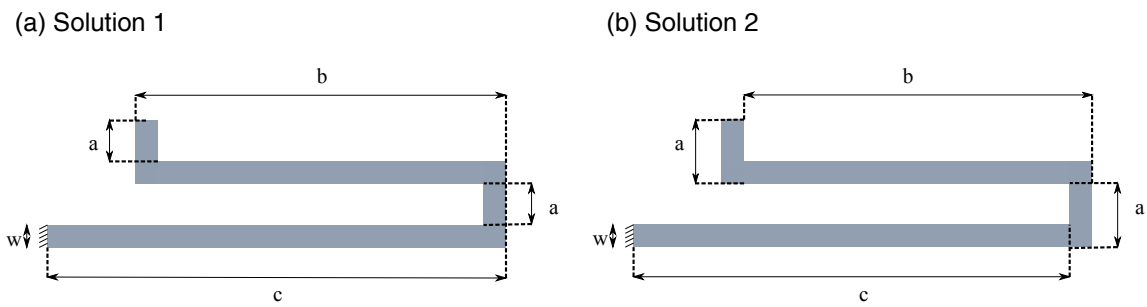
Figure 3.21: Dividing the folded spring into straight beams: (a) solution 1, (b) solution 2.

stiffness of spring design 2 (see Annexe C).

According to this formalism, length, width and thickness parameters have been determined and summarized in the Tab.3.3 and 3.4. The parameters, given in the Tab. 3.3 and 3.4, are dimensions corresponding to Solution 1 for dividing the springs into fours beams as shown in Fig. 3.21 (a).

Stiffness-Simulation Finite Element Model (FEM) simulation is also used to calculate the spring stiffness. A simple model of a 3 mm x 3 mm square platform is used for the mass (Fig. 3.10). A stationary study is performed and the boundary conditions are the following one: fixed for the spring ends, free for the rest. A force is applied sequentially in the x, y and z directions, and the displacement of the platform is simulated. According to the formula $F_i = k_i i$, where i is the displacement, k_i are the stiffnesses and F_i are the applied forces in the directions x, y or z, the stiffness in each direction is retrieved. Simulations were done successively with an isotropic and an anisotropic model as defined previously in Sec. 3.3.1.1. As explained previously, the orientation of the mechanical design with respect to the crystallographic orientation is of great importance. When using Comsol software, the x and y directions correspond to the x and y directions of a (100) wafer rotated by 45°. Thus, in order to match the crystallographic orientation of the design and the one of the model, the model has to be rotated by 45 ° in the Comsol interface. The obtained stiffnesses are summarized in Tab. 3.3 and 3.4.

A second simulation was done in order to investigate the mode shapes of the platform, using the Eigenfrequency study. The model is a simplified model of the design with suspended mirrors and square holes concerning the structuration of the actuated platform. The mode shapes of the actuated platform are simulated to confirm stiffness calculations (Fig. 3.22). The modes are of the same type for the two designs of platform and for the two designs of springs. For the suspended spring platform design with the spring design 1, the first mode is confirmed to be the piston mode at 487 Hz, whereas the second mode and third mode are torsion modes at 731 Hz. Finally, for the spring design 2, the first

mode is confirmed to be the piston mode at 494 Hz, whereas the second mode and third mode are torsion modes at 738 Hz.
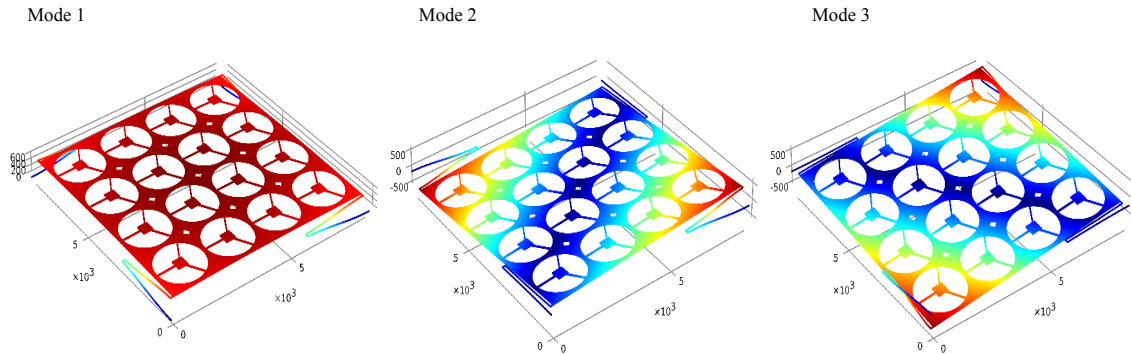
Figure 3.22: Simulation of the three first natural modes of the vertical microscanner with suspended micromirrors.

The spring parameters have been optimized to obtain a resonant frequency around 500 Hz for the two designs. The three different ways to calculate the stiffness constants are in good agreement and all the results are summarized in Tab. 3.3 and 3.4.

An important precision is that, for the suspended micromirrors design, the spring-mass systems created by the 16 micromirrors-suspensions systems have a very high resonant frequency. Indeed, the stiffness of the three suspensions is high and the mass of the micromirrors is relatively small. Then, when the platform is actuated at 500 Hz, these 16 spring-mass systems are not excited.

Table 3.3: Platform with suspended micromirrors: Parameters of the spring design 1 and 2. The simulated values correspond to the isotropic (anisotropic) values.

Symbol	Description	Spring design 1	Spring design 2
w	Beam width	27 μm	27.5 μm
t	Beam thickness	40 μm	40 μm
$l_1 = a$	Beam 1 length	90 μm	115 μm
$l_2 = b$	Beam 2 length	2590 μm	2550 μm
$l_3 = a$	Beam 3 length	90 μm	90 μm
$l_4 = c$	Beam 4 length	2800 μm	2550 μm
$l_5 = b$	Beam 5 length	-	90 μm
I_z	Bending moment of inertia	$1.44.10^{-19} m^4$	$1.47.10^{-19} m^4$
$I_x y$	Bending moment of inertia	$6.561.10^{-20} m^4$	$6.56.10^{-20} m^4$
J	Torsion constant	$1.53.10^{-19} m^4$	$1.60.10^{-19} m^4$
k_x	Lateral stiffness in x		
	Calculated	3.1 N/m	3.6 N/m
	Simulated	3.2 N/m (3.2 N/m)	3.7 N/m (3.7 N/m)
k_y	Lateral stiffness in y		
	Calculated	525.5 N/m	388.6 N/m
	Simulated	550.1 N/m (545.2 N/m)	376.8 N/m (371.8 N/m)
k_z	Out-of-plane stiffness		
	Calculated	6.1 N/m	6.1 N/m
	Simulated	6.2 N/m (6.2 N/m)	6.5 N/m (6.4 N/m)

Table 3.4: Platform with integrated glass : Parameters of the spring design 1 and 2. The simulated values correspond to the isotropic (anisotropic) values.

Symbol	Description	Spring design 1	Spring design 2
w	Beam width	50 μm	50 μm
t	Beam thickness	40 μm	40 μm
$l_1 = a$	Beam 1 length	90 μm	100 μm
$l_2 = b$	Beam 2 length	2590 μm	2635 μm
$l_3 = a$	Beam 3 length	90 μm	100 μm
$l_4 = c$	Beam 4 length	2800 μm	2635 μm
$l_5 = b$	Beam 5 length	-	100 μm
I_z	Bending moment of inertia	$4.17.10^{-19}$ m^4	$2.7.10^{-19}$ m^4
$I_x y$	Bending moment of inertia	$6.561.10^{-20}$ m^4	$4.2.10^{-20}$ m^4
J	Torsion constant	$2.18.10^{-19}$ m^4	$5.6.10^{-19}$ m^4
k_x	Lateral stiffness in x		
	Calculated	20.2 N/m	21.1 N/m
	Simulated	20.1 N/m (19.8 N/m)	21.1 N/m (20.8 N/m)
k_y	Lateral stiffness in y		
	Calculated	$2.4.10^3$ N/m	$2.2.10^3$ N/m
	Simulated	$2.3.10^3$ N/m ($2.5.10^3$ N/m)	$2.0.10^3$ N/m ($1.9.10^3$ N/m)
k_z	Out-of-plane stiffness		
	Calculated	12.3 N/m	12.3 N/m
	Simulated	12.3 N/m (12.1 N/m)	12.9 N/m (12.7 N/m)

3.3.2 / ELECTROSTATIC STUDY OF VERTICAL COMB-DRIVE PRINCIPLE

Actuating and sensing are the core functions of the device. In order to use a phase shifting algorithm, it is necessary to know the displacement amplitude of the micromirrors. Therefore, a capacitive sensor is also integrated to the structure. Both vertical actuators and sensors are based on the electrostatic field created by vertical comb fingers (Fig. 3.23). This technology has been widely used due to its relative easiness of implementation in silicon-based MEMS [131, 133, 134]. Indeed, the combination of SOI substrates and Deep Reactive Ion Etching (DRIE) allows fabrication of both the micromechanical structures as well as the electrostatic actuators and sensors.
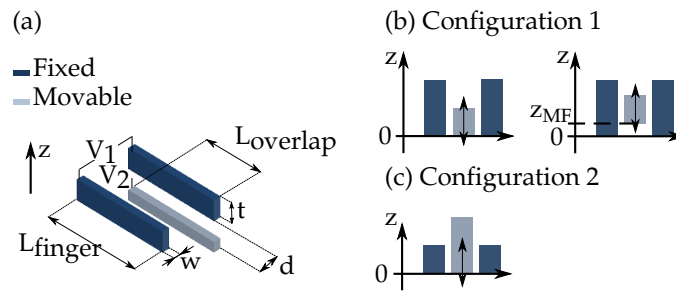
Figure 3.23: Asymmetrical comb finger design : (a) Dimensions of one pair of fingers, (b) Configuration 1, (c) Configuration 2. z_{MF} is the vertical position of the moving finger and is simply noted z in the following.

The comb fingers are also formed in the device layer. Then, the height of the higher fingers is set to 40 μm and to 20 μm for the smaller ones. The gap between the finger is set to 5 μm. These are typical values found in the literature that are in agreement with the feasibility of microfabrication processes.

3.3.2.1 / ACTUATION

The vertical electrostatic force is created by a change of capacitance in the vertical direction. This is possible when a vertical asymmetry exists in the design of the comb fingers (Fig. 3.23, (b)). If parallel plate capacitances are used to create lateral electrostatic actuator, the fringing capacitances are here responsible for the actuation. The electrostatic force, between two opposite fingers, is proportional to the derivative of the capacitance between these fingers according to the following relationship:

$$F_{el} = \frac{1}{2}\frac{\partial C}{\partial z}V^2 \tag{3.24}$$

where C is the capacitance and V is the potential between the two fingers.

3.3.2.2/   SENSING

The sensing function is created by differential capacitance sensing. It has been shown that the design of two specific types of comb fingers provide a linear detection (Fig. 3.23) [131]. When the movable finger moves up, the capacitance mainly changes for the Configuration 2 (Fig. 3.23, (c)) whereas if the movable finger moves down then the capacitance mainly changes for the Configuration 1 (Fig. 3.23, (b)). This method is used to design the four differential sensors, each composed of one set of fingers with the Configuration 1 and another with Configuration 2, that are placed around the movable platform as shown in Fig. 3.13.

3.3.2.3/   ANALYTICAL CALCULATIONS

From the state of the art presented in Sec. 2.2.1.1, it is possible to calculate the fringing capacitance with [111]:

$$\frac{1}{2}\frac{\partial C}{\partial z}V^2 = Fel = f_1(g, t_s, t_t, z) \times \frac{\epsilon NL}{d} \times V^2$$
$$\frac{\partial C}{\partial z} = 2\frac{Fel}{V^2} = f_1(g, t_s, t_t, z) \times \frac{\epsilon NL}{d} \qquad (3.25)$$

with all the parameters as defined in Sec. 2.2.1.1. A code in Python has been developed to make these calculations.

It results that the derivative of the capacitance at z=0 μm is equal to 0.34 fF/μm, with z as shown in Fig. 3.23. However, it must be pointed out that when the microscanner is turned upside down, there is a vertical shift of the actuated platform due to its own weight equal to approximately 1 μm. Around z=1 μm, the derivative of the capacitance is lower and equal to 0.23 fF/μm.

3.3.2.4/   SIMULATIONS

Simulations of the capacitance have been performed with 2D FEM simulation using Comsol and with 3D FEM simulation using Intellisuite to study both the actuation and the sensing functions since they are based on the same physical phenomena. Indeed, both functions are based on changes in capacitance, i.e. changes of the electrostatic field. A model composed of one central movable finger facing two fixed fingers is used for both 2D and 3D simulations and is called a pair of comb fingers. First, the electrostatic field

is studied thanks to FEM analysis with the software Comsol. The 2D model represents the cross section of the 3 fingers presented in Fig. 3.23 (b). The surrounding medium is defined by a box as air. The central finger potential is set to 0 V whereas the potential of the surrounding fingers is set to 15 V. The material of the finger is defined as isotropic silicon. A parametric study is realized where the vertical position of the central finger is the parameter to be tuned. The result of the simulation is shown in Fig. 3.24 for two vertical positions: (a) the bottom of central finger is at the same vertical position that the bottom of surrounding finger, i.e. z=0 μm and (b) the bottom of central finger is 5 μm higher than the bottom of surrounding finger, i.e. z=5 μm. The equipotential lines are plotted. It is clear that there is a change in the distribution of the electric potential lines and thus in the capacitances.
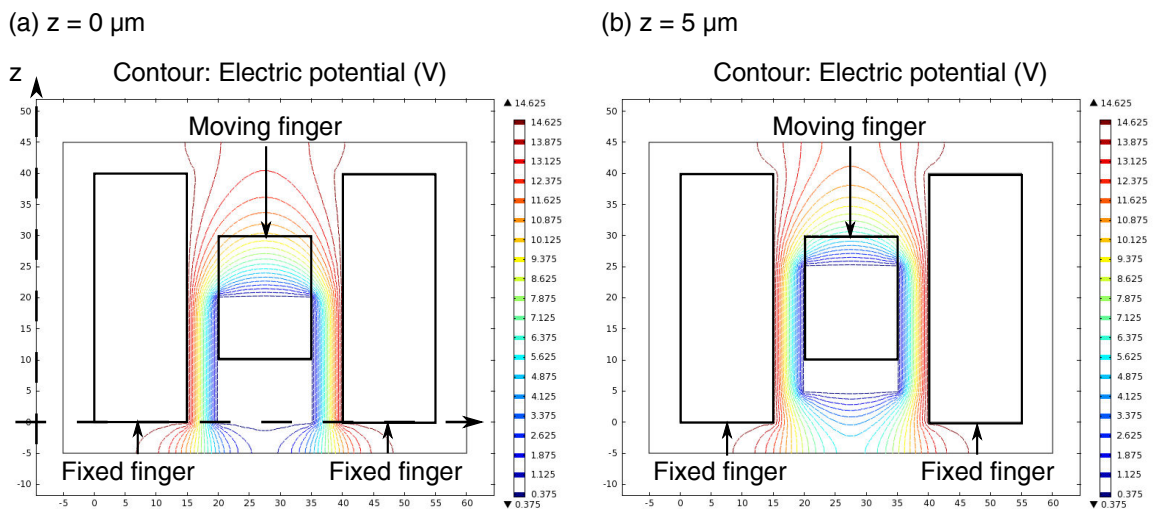
Figure 3.24: Electrostatic simulation results-equipotential lines: (a) z=0 μm and (b) z=5 μm. The comb fingers shown with a black contour correspond to the comb fingers at their last position in the parametric study, i.e. z=10 μm.

From this simulation, it is possible to derive the total electric energy by integrating the energy density over the surface considered in the model. Finally, the capacitance is calculated according to the formula:

$$E = \frac{1}{2}CV^2 \tag{3.26}$$

where E is the total energy, C is the capacitance and V is the potential between the two fingers. The 3D capacitance is then calculated by neglecting the effect at the end of the comb fingers which results in multiplying the 2D capacitance by the overlapping length of the comb fingers ($L_{overlap}$). The length of the finger is chosen to be 200 μm with an overlapping length of 190 μm. Fig. 3.25 shows the total electric energy and the capacitance as a function of the vertical position of the central comb finger. By linear fitting, it is found

that at $z = 0$ μm, the derivative of the capacitance is equal to 0.3 fF/μm. At 1 μm (vertical offset when the microscanner is turned upside down), the derivative of the capacitance is equal to 0.27 fF/μm. On the contrary, if the microscanner is turned upside up, the derivative of the capacitance is equal to 0.33 fF/μm. This initial derivative of the capacitance is especially important for the actuation as the initial actuation force is proportional to this value. However, since the microscanner is designed to be used at resonance, the final amplitude of the vibration is also linked to the quality factor of the system.
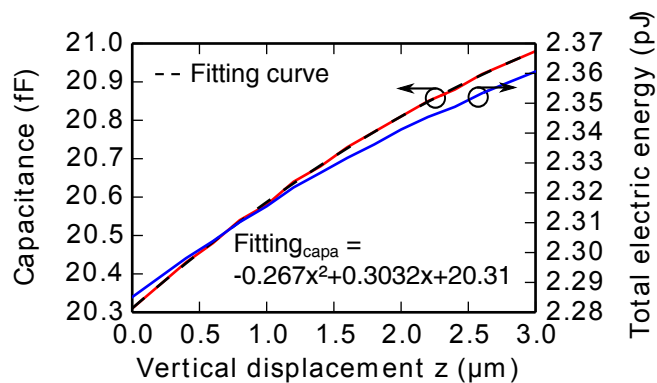
Figure 3.25: Calculated total electric energy for a couple of comb finger in 2D with Comsol and calculation of the capacitance as a function of the vertical position of the central comb finger. The fitting of the capacitance curve gives a fitting equation equal to $f(z) = -0.267z^2 + 0.3032z + 20.31$

For the sensing function, the second configuration of comb fingers that enables the use of differential sensing is also modelled and its capacitance change must be simulated. A 3D model with a fine mesh is used to obtain finer results for both configurations. For this purpose, the Thermo-Electro-Mechanical module of Comsol was used. A MacroModelExtraction/Capacitance vs. displacement analysis and a Static/Electro Thermo Relaxation analysis are chosen to process the capacitance change and the static displacement of the platform as a function of an applied voltage between fixed and moving parts. Figure 3.27 shows the capacitance change for each of comb finger configurations with one single movable finger versus the platform displacement as well as their differential capacitance. The fitting of the capacitance in the Configuration 1 (same than with the 2D model) gives a fitting curve equation equal to : $0.0241x^2 + 0.2809x + 21.71$. This results is really close to the one obtained in 2D and validates the first calculations. The small difference can be easily explained from the fact that the 2D model neglects the effect at the end of the comb fingers to calculate the 3D capacitance and that the mesh is not the same in the two simulations. Note that the mesh is really important in these kind of simulations where small changes are calculated. The mesh is presented in Fig. 3.26. The mesh size is especially fine on the bottom and the top of the comb fingers that are

the most important for the calculation of the fringing capacitance.
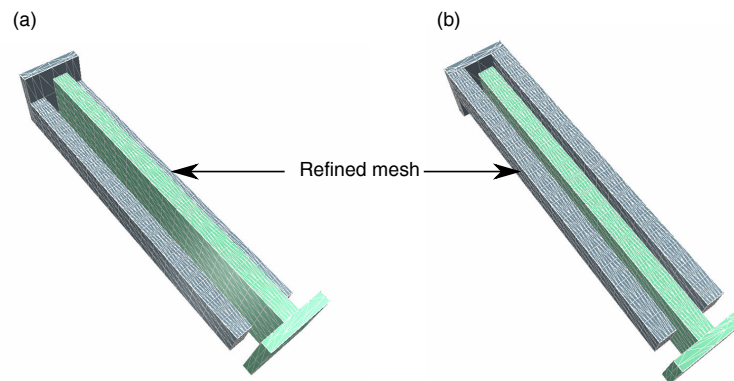
Figure 3.26: Refined mesh of the comb finger model with Intellisuite: (a) 3D view of the top, (b) 3D view of the bottom. The mesh is mainly refined at the bottom and top of the comb fingers.

On the one hand, linear fitting of the differential curve ($C_1 - C_2$) allows to determine the sensitivity of one couple of fingers 0.64 $fF/\mu m$. The number of couple of comb fingers is set to 34 for each sensors. Then, the sensitivity of a differential sensor is 22 $fF/\mu m$. The same simulation has been performed for a gap equal to 4 μm and a sensitivity of 0.81 $fF/\mu m$, corresponding to a total sensitivity of 27 $fF/\mu m$ for one differential sensor, has been obtained. It is worth to note that the differential capacitance in the range of some fF has to be measured to sense the displacement amplitude whose value is used for the implementation of the PSI.

On the other hand, the static displacement of the platform as a function of the applied voltage was simulated, based on a capacitance change simulation. Figure 3.28 shows the static vertical displacement obtained for a number of movable comb fingers, i.e. the number of couples of comb fingers, equal to 400. This number of comb fingers leads to a static displacement of the platform whose amplitude is high enough for our application. Indeed, the vertical microscanner is designed to work at resonance which implies that the quality factor will lead to higher displacements. However, if the quality factor of the microscanner were not high or it would be necessary to work in static, it is also possible.

The results of the capacitive simulation are coherent with the literature results (Sensitivity=0.66 $fF/\mu m$ and 0.68 $fF/\mu m$ respectively in [133] and in [134] for similar parameters and technology).
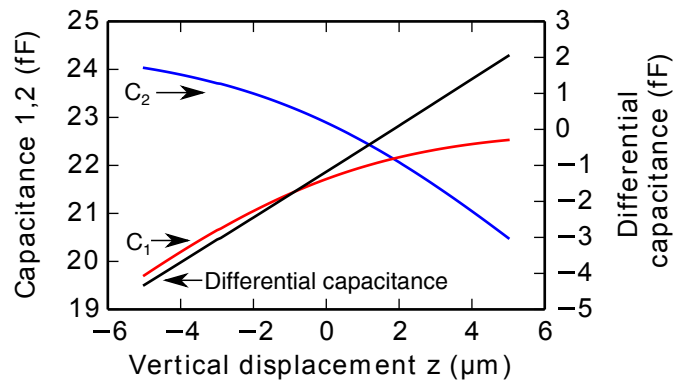
Figure 3.27: Capacitance versus displacement of Configuration 1 and Configuration 2 and differential capacitance for one movable finger facing two fixed fingers. Linear fitting of the differential capacitance gives a sensitivity of 0.64 $fF/\mu m$.
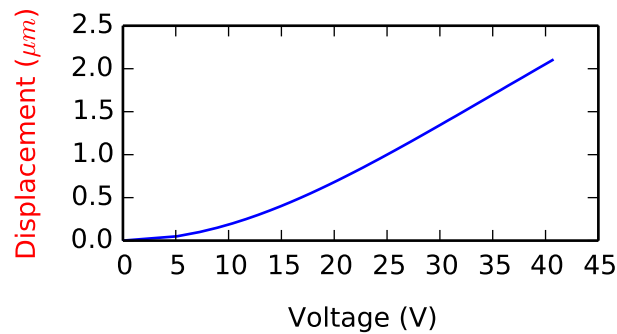
Figure 3.28: Static vertical displacement simulated with Intellisuite for $N_{finger} = 400$

The design parameters of the vertical microscanner are summarized in Tab. 3.5.

Table 3.5: Design parameter of the vertical microscanner.

Symbol	Description	Value
SOI wafer		
Orientation		(100)
$t_{device-layer}$	Device layer thickness	40 μm
$t_{handle-layer}$	Handle layer thickness	500 μm
t_{BOX}	BOX layer thickness	1.5 μm
Platform		
$L_{platform}$	Platform side length	8000 μm
D_{glass}	Glass disks diameter	2100 μm
t_{glass}	Glass disks thickness	25 μm
D_{holes}	Holes diameter (optical aperture)	1840 μm
L_{mirror}	Micromirror side length	2100 μm
d_{hexa}	Distance between two hexagons	30 μm
l_{hexa}	Hexagon side length	30 μm
Comb drive		
L_{finger}	Finger length	200 μm
$L_{overlap}$	Finger overlap	190 μm
d	Gap	5 μm
t	Finger thickness	40 μm
w	Finger width	10 μm
$N_{actuator}$	Total movable finger number	400
N_{sensor}	Total movable finger number per sensor type	136

3.3.3 / IMPACT OF SPIDER LEGS ON THE OPTICAL QUALITY

The difference between the two platform designs is not only mechanical but also optical. The suspensions used to held the micromirrors are a source of obscuration and diffraction (Fig. 3.29). The relation between the design of the suspensions, referred to as spider legs, and the optical quality of the system is investigated. These results are presented in [149].
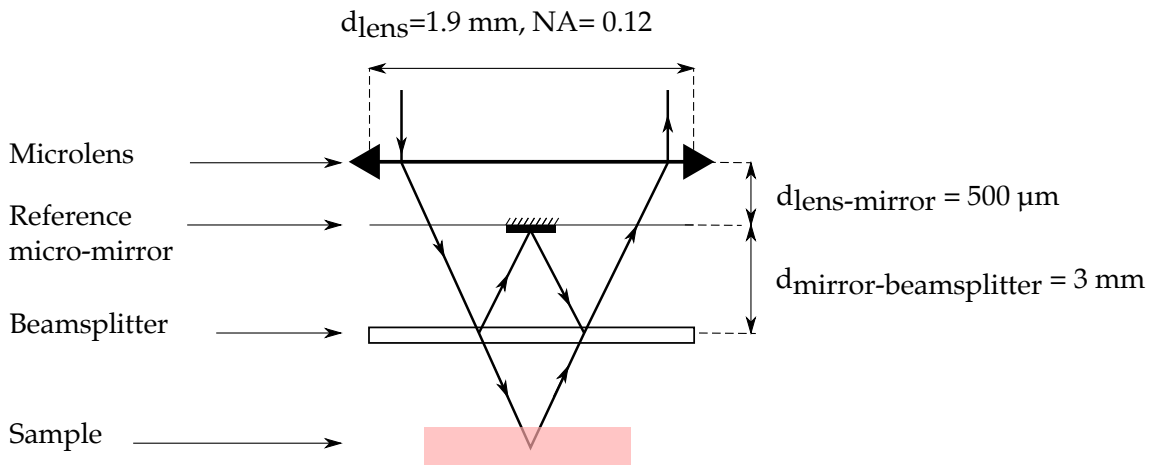
Figure 3.29: Mirau interferometer schematic (only one ray is represented).

In astronomical instruments, the diffraction due to the secondary mirror spider legs is well known. In the past, scientists have studied the impact of the central obscuration due to the mirror and the thickness of the spider legs [142, 141]. It has been shown that curved spiders enable the reduction of the diffraction spikes. The authors explained that the full width at half maximum (FWHM) of the point spread function (PSF), which is a commonly used image quality criteria, is only slightly increased by the presence of spider legs. Finally, the impact of the curvature of the spider legs has been only highlighted by strongly saturated experimental images (Fig. 3.30). Richter [142] showed that curved spiders do not generate diffraction spikes but increase the background brightness by about half a magnitude when compared to straight spiders.

Here, we study how the radius of curvature (RoC) of the suspensions, combined with their number and their thickness, affects the lateral resolution of the system, using the PSF and the Modulation Transfer Function (MTF). In particular, we show how the symmetry of the 2D MTF depends on the RoC over a large range of values. The symmetry of the MTF is important because it ensures an isotropic resolution in the image plane.
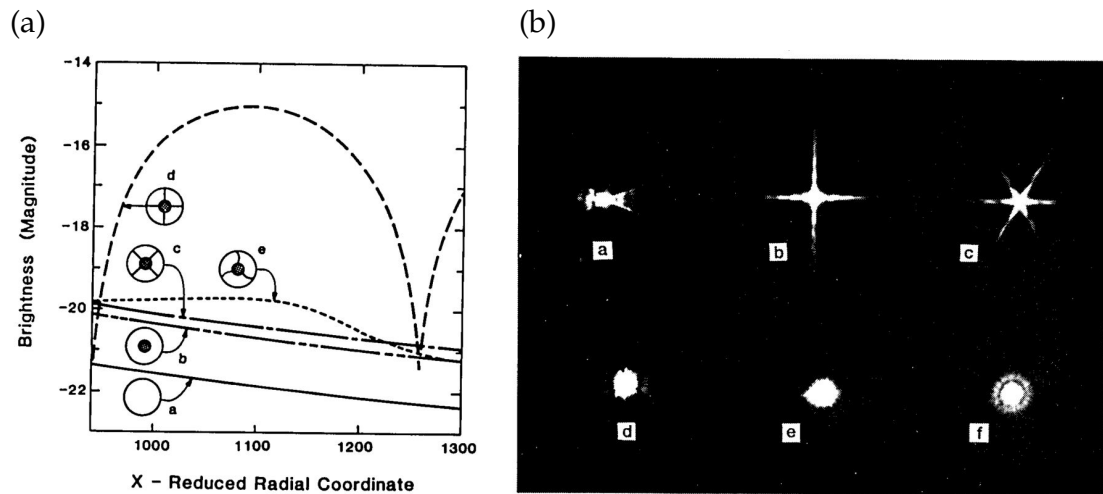
Figure 3.30: (a) Brightness analysis with far-field diffraction envelopes and (b) diffraction photographs for different spider configurations [142].

3.3.3.1/ IMAGE CRITERIA

The mirror, which is the main source of diffraction, creates an obscuration ratio of 0.2. It corresponds to typical ratio studied in the literature [142, 141]. It has been checked that the square shape of the mirror does not influence the study in terms of trend. The square shape of the mirror is linked to the use of in-plane stitching, for the reconstruction of a 2D image. The Fresnel diffraction is investigated using Fourier Optics, i.e. by calculating the PSF and the MTF of the pupil with Fourier transforms:

$$APSF = \mathcal{F}(P(x,y)) \tag{3.27}$$

where P is the Pupil function

and APSF is the Amplitude of the PSF

$$PSF = |APSF|^2 \tag{3.28}$$

$$MTF = |OTF(P)| \tag{3.29}$$

where $OTF = mathcalF^{-1}(PSF)$ (3.30)

and $\mathcal{F}^{-1}$ is the inverse Fourier Transform

The PSF describes the impulse response of the optical system to a point source. The MTF represents the contrast transfer of an optical system as a function of the imaged object frequencies.

Although the mirror is not in the lens plane, it has been demonstrated that in the paraxial approximation, when a mask is placed after the lens, the Fourier transform can be used

to calculate the intensity in the focal plane [150]. Here, the resolution of the system is defined by the Rayleigh criterion that states that the resolution corresponds to the distance for which the maximum of an Airy disk coincides with the first minimum of the other Airy. Following this definition, we can calculate that the resolution is equal to the critical size for which the contrast in an image is equal to 26.4 % [151]. Then, MTF is analyzed in terms of the Rayleigh frequency (f_R), which is particularly interesting in our case since we need to image small features.

The pupil function describes the mirror plane, including the mirror, the spider legs and the pupil aperture (Fig. 3.31). Here we study the impact of the thickness parameter ϵ, the RoC parameter β and its corresponding angle of curvature α and the number of spider N defined as follows: $T_{spider} = \epsilon \times D_{pupil}$, $RoC = \beta \times D_{pupil}/2$.

$$\sin\left(\frac{\alpha}{2}\right) = \frac{D_{pupil}}{4RoC}$$
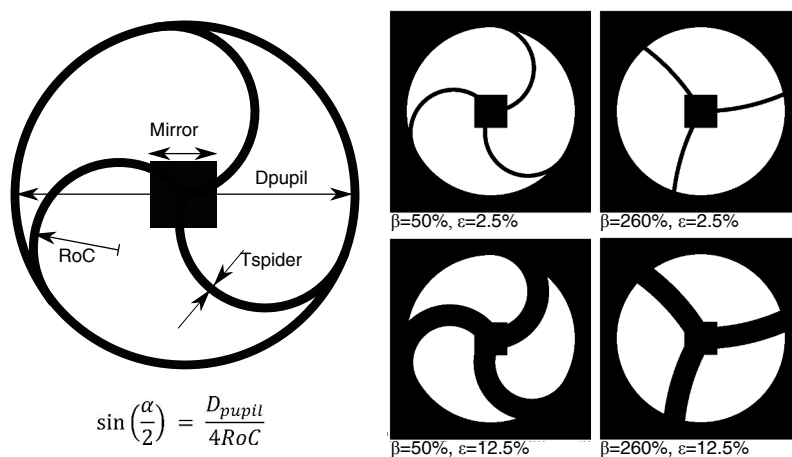
Figure 3.31: Schematic of the pupil including the reference mirror suspended by 3 spider legs and their parameter relationship.

In [142, 141], the benefit of curved spiders has been shown with long exposure photographs that enable to see diffraction spikes being invisible with short exposure times. Figure 3.32 shows the PSF of pupil functions plotted with different scales. We can see diffraction spikes, as in [142, 141], in the binary plot only if intensities below 0.01 % of the peak intensity value are put to 0 and the ones above are put to 1 (Fig. 3.32,(b)). However, diffraction spikes cannot be seen when the threshold is increased to 1 % or in the greyscale plot (Fig. 3.32, (c),(d)). In fact, the intensity of the diffracted light is small compared to the main intensity peak. Therefore, its dependence on the geometry of the spider cannot be seen, unless the main peak is strongly saturated. Then, criteria based on the PSF are difficult to analyze in order to show a dependence to the spiders geometry. Instead, the spider legs create an asymmetry in the MTF function which varies depending on the parameters. As shown in Fig. 3.33, where limit cases in terms of RoC and number of spider are plotted, f_R is not constant in the 2D plane. It implies that the resolution will not be the same in all the directions of the plane. The mean and the relative standard deviation

values of the f_R, f_R *mean* and f_R *rstd* respectively, are studied as a function of the three parameters. The aim is to maximize f_R *mean* and minimize f_R *rstd*. The lower f_R *rstd* is, the better the symmetry of the MTF is. The f_R *mean* decreases with the increase of the three parameters and is mainly affected by the thickness of the spider legs and the number of spiders, i.e. the covered area. In the case free of spider legs, $f_R = 0.63$ (normalized to the cut-off frequency). The cut-off frequency is chosen to be the frequency for which the contrast is equal to zero.
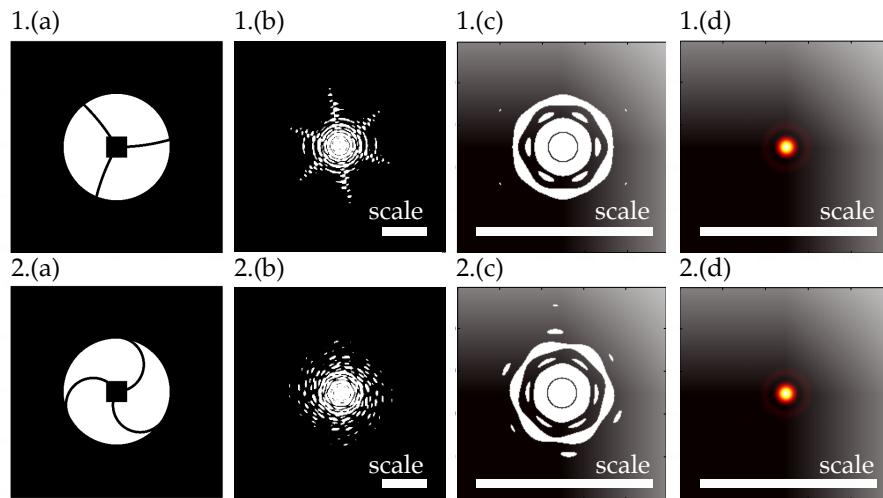
Figure 3.32: Comparison between almost straight spiders (1) and highly curved spider (2). (a) Pupil function, (b) PSF as a binary image (Threshold = 0.01 % of the normalized PSF), (c) x4 Zoom on the PSF as a binary image (Threshold = 0.1 % of Max(PSF)), (d) x4 Zoom on the PSF as a greyscale image.
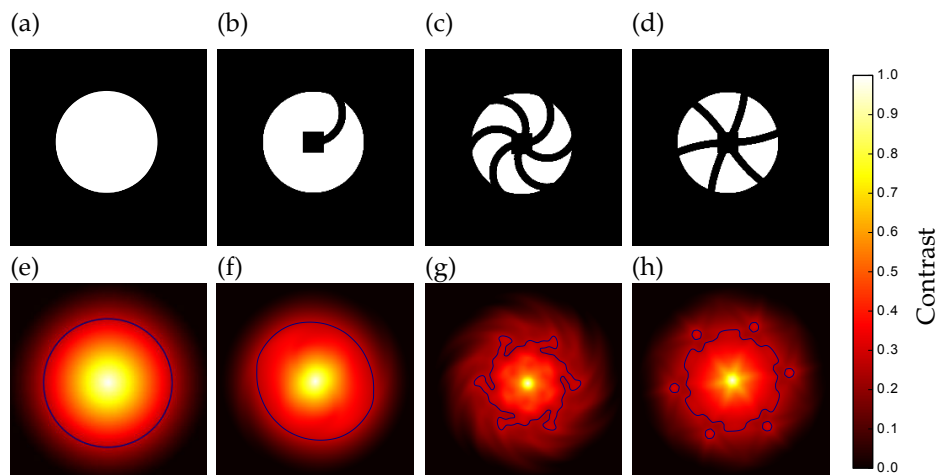
Figure 3.33: Pupil function and its corresponding MTF for ϵ = 7.5 %, (a) and (e) N = 0, (b) and (f) β = 0.5 and N = 1, (c) and (g) β = 0.5 and N = 6, (d) and (h) β = 2.6 and N = 6). MTF contour lines correspond to 0.264 contrast.

3.3.3.2/   STUDY OF THE IMPACT OF SPIDER LEGS ON THE MTF

In Fig. 3.34, the thickness is set to ϵ = 7.5 % and we can see that f_R *rstd* highly depends on the number of spiders. Note that for N = 0, f_R *rstd* $= 0$ (up to the numerical error), i.e. the MTF is axially symmetric. In the case of 4 spiders, f_R *rstd* is multiplied by 5 compared to the one in the 3 spiders case. Moreover, if f_R *mean* and f_R *rstd* do not vary significantly as a function of β, it is shown that N = 3 is the only case for which curved spiders provide a higher and more isotropic resolution than straight legs (down to f_R *rstd* $= 5.6 \times 10^{-3}$). Indeed, for N = 3 and ϵ = 7.5 %, an optimum RoC exists around β = 75 %. Furthermore, N = 3 is the best configuration in terms of the resolution symmetry and value, for any RoC.
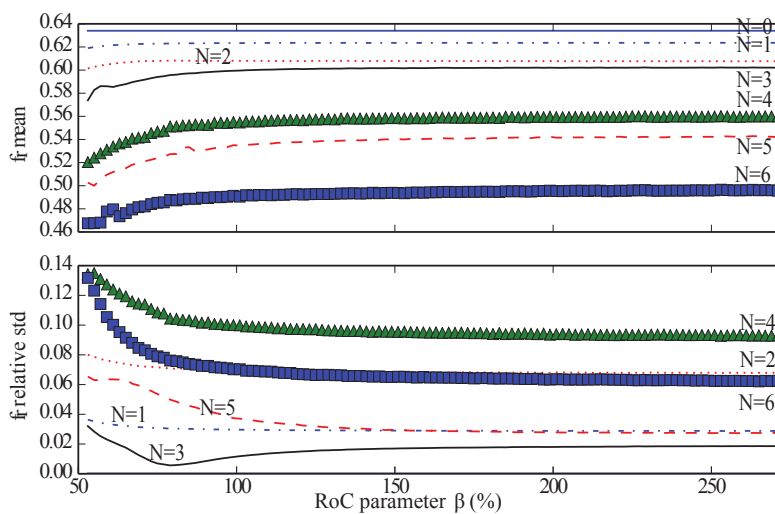
Figure 3.34: Study of the variation of the Rayleigh frequency as a function of N and β (ϵ = 7.5 %). The frequencies are normalized to the cut-off frequency.

Figure 3.35, where β is set to 75 %, shows that for thickness parameters below 3 % the number of spider has a small impact. N = 3 is again a specific case, for which f_R *rstd* is the lowest and constant for thickness up to ϵ = 7.5 %. Moreover, for 5 spiders and large widths, the symmetry of the MTF is good but f_R *mean* is in this case highly decreased. In general, small thickness should be preferred. Finally, Fig. 3.36 shows that the optimum RoC depends on the thickness parameter. When ϵ tends to zero, the optimal RoC tends to a β parameter corresponding to an angle of curvature of 120°. In [142], the concept of searchlight is introduced to understand the diffraction created by the curved spiders. Following this concept, it is found that three evenly spaced curved spiders with an angle of 60° cover one circle, and cover two circles when the angle is equal to 120°. Here, the simulation shows that in terms of resolution, defined with the f_R, an angle of 120° is preferred. For $N = 3$, leg thickness should not exceed 7.5 % of the aperture diameter.
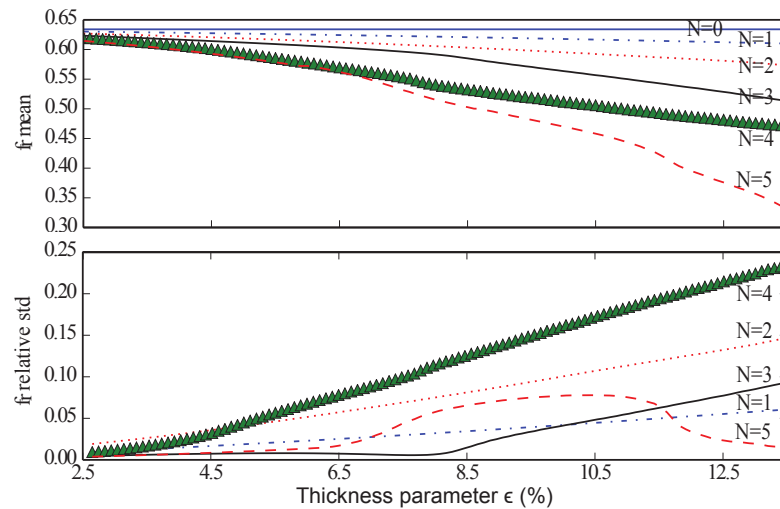
Figure 3.35: Study of the variation of the Rayleigh frequency as a function of N and ϵ (β = 75 %). The frequencies are normalized to the cut-off frequency.
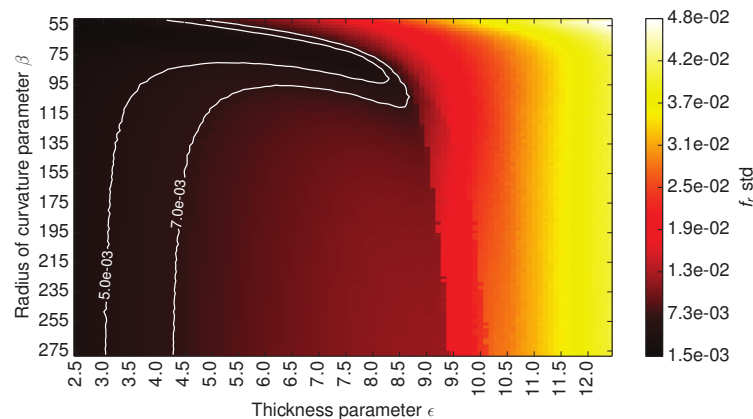
Figure 3.36: Relative standard deviation values of the Rayleigh Frequency when varying the parameters β and ϵ for N = 3. The frequencies are normalized to the cut-off frequency.

3.3.3.3/ EXPERIMENTAL PART

In order to confirm the numerical results, an experimental setup has been developed [152]. The characterization optical setup allows measuring the PSF, generated by the Mirau lens, from which the MTF is then derived. A probing beam ($\lambda = 633nm$) is focused by the Mirau lens. Then, the focal plane, i.e. the PSF, is collected by the magnifying system, which consists of a microscope objective (x50, NA = 0.45) and a tube lens to project the image onto a camera. The Mirau lens is matching with the object focal plane of the microscope objective. Three optical configurations of the Mirau lens have been investigated. In the first configuration, the lens is free of mirror and arms, i.e. the lens itself is characterized. The second and the third configurations involve a mirror held by

three straight and three curved spider legs, respectively. The thickness of the spiders is $100\mu m$ (ϵ = 5 %). Both the symmetry of the frequencies and the resolution losses, i.e. f_R *rstd* and f_R *mean*, are derived. Figure 3.37 shows the contour plots at four contrast values of the measured (Fig. 3.37 (a), (c), (e)) and simulated (Fig. 3.37 (b), (d), (f)) MTFs for the three configurations. The two dimensional MTFs are displayed as function of the spatial frequencies f_x and f_y.

As expected, without mirror and spiders, both experimental (Fig. 3.37 (a)) and theoretical (Fig. 3.37 (b)) MTFs present a rotational symmetry for each contrast value, i.e. the resolving power of the lens is similar in all radial directions. In the second configuration (Fig. 3.37 (c) and (d)), the mirror held by three straight arms is placed against the lens. Compared to the first configuration, the rotational symmetry of both MTFs is degraded. This is due to the diffraction effects of the spider legs and the mirror. At a contrast value of 26.4 %, six lobes appear corresponding to the arms. Furthermore, the amplitude of two lobes is accentuated because of the combination of diffraction patterns from the mirror and from the spider legs. These frequency variations lead to an increased f_R *rstd* (Table 3.6). In other words, the lateral resolution of the Mirau lens is slightly deteriorated and depends on the lateral direction. Then, for the third configuration, the three straight spiders have been replaced by three curved spiders corresponding to $\beta = 100\%$ (Fig. 3.37 (e) and (f)). The two lobes are still perceptible due to the mirror diffraction pattern. However, comparing to the second configuration, f_R *rstd* is 20 % lower (Table 3.6). This experimental factor well matches the simulation one. Due to the thickness of the spiders (100μm, ϵ = 5 %), the impact of the diffraction effect is not negligible. Keeping the curved shape and reducing the spider thickness to 50μm (ϵ = 2.5 %) would allow a f_R *rstd* similar to the configuration without mirror and spiders, i.e. 1.2×10^{-3} cycles/μm.
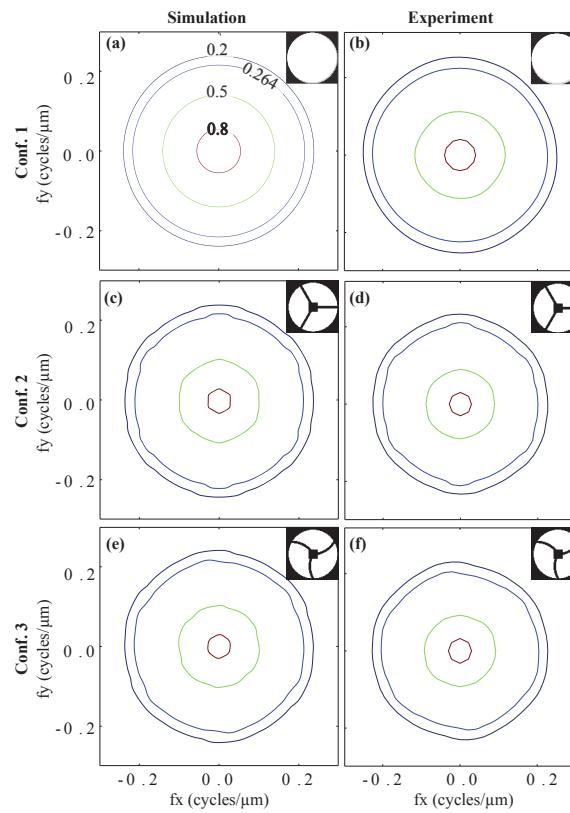
Figure 3.37: Contour profiles of the MTF at four contrast value: 0.2, 0.264 (Rayleigh criterion), 0.5 and 0.8. The experimental results (on the right column) and the simulation results (on the left column) are plotted corresponding to pupils on insets.

Table 3.6: Values of the Rayleigh frequencies mean (in cycles/μm) and standard deviation (in cycles/μm) in the three configurations of Fig. 3.37.

	Conf. 1	Conf. 2	Conf. 3
f_r *mean*	0.225	0.205	0.203
f_r *rstd*	$5.3\text{x}10^{-3}$	$1.8\text{x}10^{-2}$	$1.6\text{x}10^{-2}$

3.3.3.4/ CONCLUSIONS

Diffraction effects, in a Mirau micro-interferometer, due to the mirror and the spider legs are studied. Results of both simulations and experimental measurements demonstrate that the diffraction effects have a low influence onto the quality of the point spread function. However, they are not negligible in terms of spatial frequency variations. In particular, it has been shown that curved spiders are beneficial only in the case of three spider legs and that the optimum RoC is around to 80 %. For this value of RoC, the

resolution is constant for any spider legs thickness up to ϵ = 7.5 %. As a conclusion, the Design 2 is a competitive alternative to the Design 1 in term of optical quality. In the following, the parameters of the spider legs are set to 100 % and ϵ = 2.7 % which corresponds to a thickness for which the effect of the spider legs on the optical quality is negligible.

3.4/   Conclusions

To conclude, two different designs have been discussed for the mechanical silicon platform that carries the array of micromirrors. One design is based on the integration of glass disks on the silicon platform to carry the micromirrors while keeping a clear aperture around the micromirrors. This design represents a technological challenge and therefore a second simplified design is proposed. The second design includes silicon suspensions to support the micromirrors. This design is not optimal in term of optical quality as the aperture around the micromirrors is not completely clear. However, the impact of the silicon suspensions on the optical quality has been studied and results show that the impact is negligible, especially for specific curved silicon suspensions. The silicon platform is suspended with folded-spring silicon suspensions. Two different spring designs have been studied and no major differences appear between the two. Finally, the comb drive actuator and position sensor have been studied. Simulations show that the design chosen in Ch. 2 is suitable and meet the specifications of displacement for the phase-shifting application. The next chapter focuses on the microfabrication of the vertical microscanners introducing the specificities of microfabrication and discussing the results of the microfabrication.

4

FABRICATION OF VERTICAL MICROSCANNER

The microfabrication of a designed device, i.e. practical processing of the wafers, is preceded by several important preparation steps. The first step is the writing of the flow chart, which requires choosing the best technological process for each step of the flow chart. The best technological process is the most suited process taking into account previous and following steps, the available equipments and technologies. These choices are critical for the success of the fabrication. The main microfabrication technologies and equipment used in this thesis are described in Annexe D. The second step is the design and drawing of the hard masks used for the photolithography steps. Finally, the implementation of the process can start in a third step. Then, simple technological tests, to experimentally confirm the feasibility of particular "non-standard" processes, are realized and finally the full flow chart is tested. This chapter proposes a methodology to analyse risks linked to the choice of a technological flow chart. Finally, three technological fabrication flow charts, for the two platform designs described in Ch. 3, are presented.

4.1/ METHODOLOGY FOR THE RISK ANALYSIS OF A PROCESS FLOW

A microfabrication flow chart aims to describe each step of the technological process of a device. Each step consists in an action on/with a specific material, with a specific equipment and with specific parameters. To design a microfabrication flow chart, different points must be taken into account. First, the knowledge of the capability of the microfabrication techniques is the basis to choose adapted technologies and has been presented before. However, another important point is the compatibility of the technological steps between each other. The compatibility between two steps usually depends on a compati-

bility process/material or equipment/material. For example, a wafer with a metal mask can be forbidden in some etching equipment to avoid contamination of the equipment. Secondly, the knowledge of the microfabrication techniques available in the cleanroom limits the possible choices. Indeed, cleanroom equipments are usually expensive and all the cleanrooms are not equipped identically. It is possible to realize different steps of the microfabrication in different cleanrooms; however, it is usually time-consuming, sometimes expensive and overall the transport is risky for the device. These aspects of microfabrication are practical but must be taken into account when elaborating a flow chart for a successful microfabrication. It is proposed to include these major points by evaluating the risks linked to each step and to help the identification of critical steps in a flow chart.

Each step of the flow chart is analysed in terms of risk linked to the process and to the equipment. Each risk is represented by a risk factor that is equal to the probability factor multiplied by the impact factor. The probability and the impact factors are defined as given in the Tab. 4.1. The scale is the same for the probability and the impact factor. The risk factor is classically defined as shown in Fig. 4.1. This method supposes a good knowledge of both fabrication process and cleanroom equipments. Note that a microfabrication step has a minimum risk factor of 1 due to the manipulation of the wafer.

Table 4.1: Definition of the probability and the impact factor.

Factor	Impact	Probability	Description of the risk
1	Very low	Unlikely to occur	Negligible impact
2	Low	May occur occasionally	Minor impact on time, cost or quality
3	Medium	Is as likely as not to occur	Notable impact on time, cost or quality
4	High	Is likely to occur	Substantial impact on time, cost or quality
5	Very high	Is almost certain to occur	Threatens the success of the project

Impact factor					
	1	2	3	4	5
1	1	2	3	4	5
2	2	4	6	8	10
3	3	6	9	12	15
4	4	8	12	16	20
5	5	10	15	20	25

Figure 4.1: Table showing the risk factor depending on the probability and the impact factor. The red blocks show high risks that can lead to the failure of the process and for which appropriate actions must be adopted to reduce the risk. The orange blocks represent a lower risk though it must be taken into account for a better success of the process. Finally, the green blocks represent a low risk.

4.2 / FIRST FABRICATION DESIGN: GLASS BASED TECHNOLOGY

4.2.1 / FLOW CHART CONSTRUCTION AND ANALYSIS OF RISK

In the literature, there are very few example of monolithic integration of a glass optical component on an actuated structure. To my knowledge, only Yoo *et al.* have proposed a solution for this type of integration [153]. The fabrication, shown in Fig. 4.2, involves the monolithic fabrication of a glass microlens on a silicon lateral comb drive scanner. The glass is first fabricated using thermal reflow in a silicon cavity. Then, a structured glass wafer is bonded to the silicon and serves as a mechanical support to polish the other surface of the silicon wafer in order to obtain a thin layer of silicon in which the comb drive is finally realized and also to liberate the back side of the microlens that was in contact with the silicon.

(a) Thermally reflowed glass microlens.

(b) 2nd Thermal reflow and thermal pad deposition for DRIE release.

(c) Anodic bonfing with wet-etched BSG.

(d) Backside CMP and Al mask patterning.

(e) Half-dicing.

(f) Structure release through DRIE

(g) Thermal pad removal with O$_2$ plasma

(h) Manual separation of each device

Si   BSG   Al   Cr
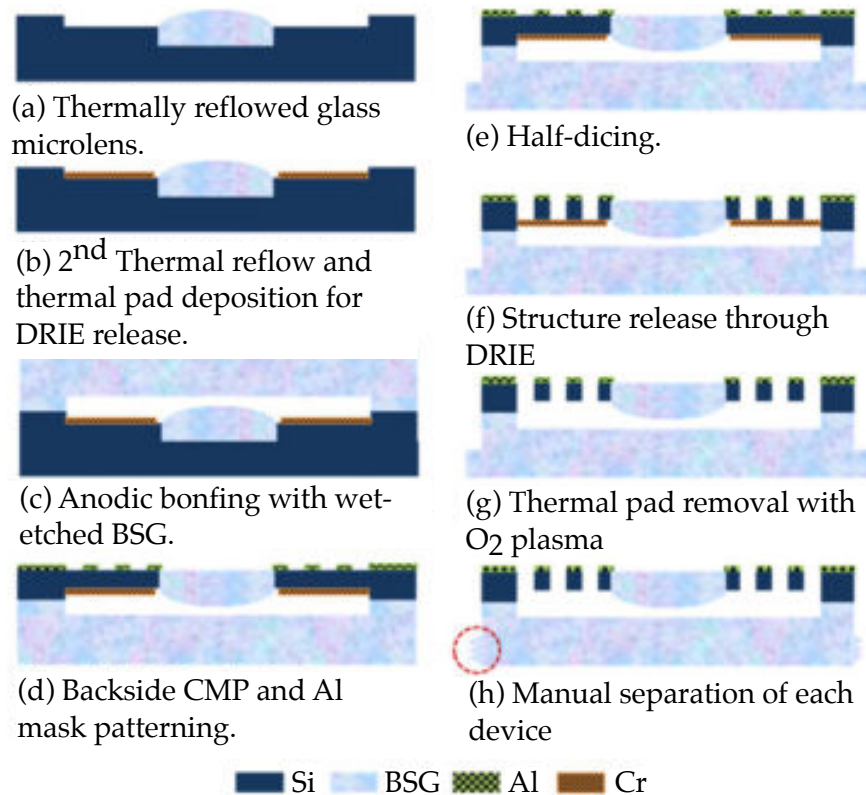
Figure 4.2: Monolithic integration of a glass microlens on a silicon lateral scanner proposed by Yoo *et al.* in [153].

In our case, this solution is difficult to implement as it involves two wafers, one in glass and one in silicon. Here, we need to take into account that the vertical microscanner is meant to be integrated with a glass lens wafer and a beam splitter (in total 7 wafers to be stacked). The integration of wafers is more and more complicated when the number of wafer is increasing. Then, another integration strategy must be chosen. The integration of glass is challenging for two main reasons that are identified here. First, the glass integrated design is schematically represented in Fig. 4.3. In this schematic, the glass support is represented on top of the structured device layer. The structured device layer illustrates both the silicon platform on which the glass support is integrated and the comb fingers that constitute the micro-actuators and the microsensors. The aim of the process flow chart is to show the different steps to realize this structure starting from a SOI wafer.
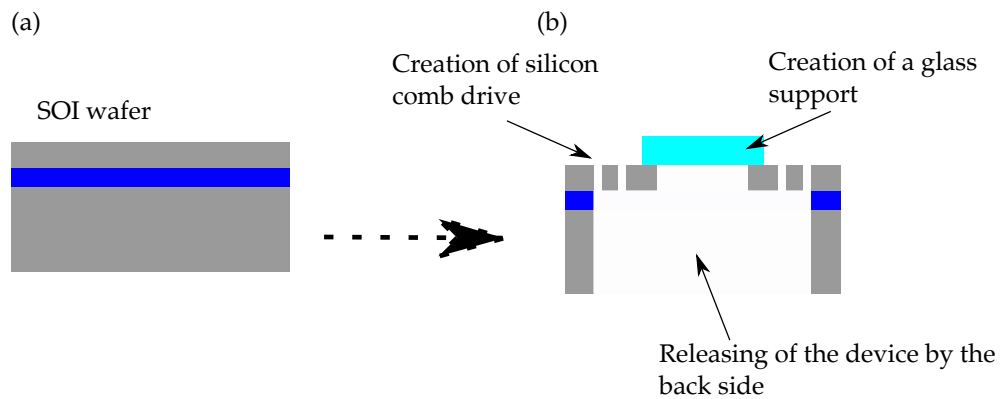
Figure 4.3: Schematic representation of the structure to realize: (a) bare SOI wafer, (b) integration of the glass support.

Figure 4.4 suggests two solutions to integrate the glass support showing the main steps of the flow chart. Basically, the glass can be integrated before the structuration of the device layer (Fig. 4.4 (a)) or after the structuration of the device layer (Fig. 4.4 (c)). In the two cases, a problem is identified and illustrated in Fig. 4.4 (b) and (d).

In the first case (Fig. 4.4 (a)), the SOI device layer is structured to remove silicon from below the glass support and then the glass support is bonded to the silicon (step 2) and etched to form the glass disks (step 3). After this step, the comb fingers are created in the device layer (step 4). This realization requires two steps: a photolithography step to create a masking layer and an etching step to etch silicon where it is not protected by the mask. The problem is that the photolithography step cannot be realized with a standard process because the wafer surface is not flat. The non-flatness has two consequences, spin coating of photoresist cannot be performed and the hard mask cannot be in contact with the surface to be exposed by UV light. A solution is to use a non-standard photolithography process associating spray coating of photoresist and projection photolithography. The two associated processes are non-standard and require non standard equipments. A spray coater is available in MIMENTO cleanroom but this process is based on spraying small droplets of photoresist on the wafer which has the disadvantage to create a non-homogeneous thickness that can have variation of $\pm 0.5 \ \mu m$. In our case, the gap between the comb drive is equal to 5 μm, therefore, the quality of the photolithography must ensures an alignment error inferior to 1 μm. The variation of the photoresist thickness can provoke a bad transfer of the pattern into the photoresist and lead to a bad quality of photolithography. Moreover, a specific alignment machine equipped for projection photolithography is needed. This type of machine is based on an optical system that is placed between the hard mask and the wafer that enables to focus light on the wafer surface. This machine is very specific and few cleanrooms are in possession of such an equipment. In MIMENTO cleanroom, a start-up called Freque|n|sys has an industrial projection aligner.

(a) Strategy 1
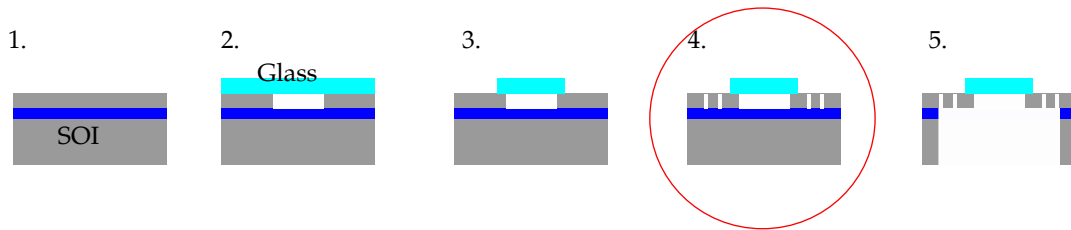
Classic photolithography not adapted because of
high topology surface

(b) Problem of strategy 1

Incident Light

Gap between mask and resist

Mask
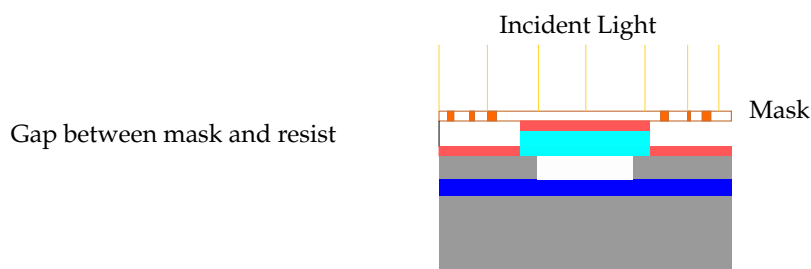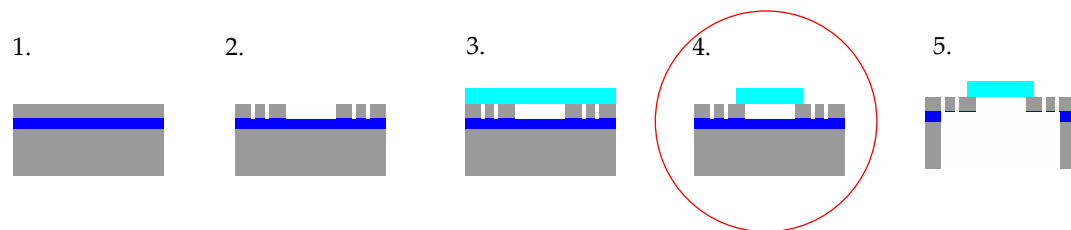
(c) Strategy 2

Structuration of glass component not
adapted without damaging the BOX

(d) Problem of strategy 2

Damaged fingers
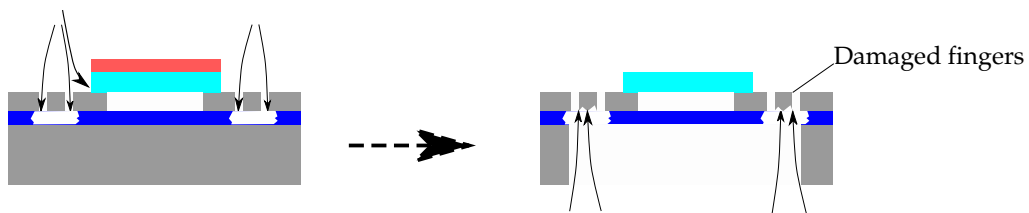
Figure 4.4: Problem linked to the integration of a glass membrane on a SOI wafer: (a)
strategy of integration 1, (b) problem linked to strategy 1, (c) strategy of integration 2, (d)
problem linked to the strategy of integration 2

However, the machine is adapted for industrial production and not research which makes
the process very delicate. To conclude, the association of these two non-standard process
requires some research and development that will be shown further.

In the second strategy (Fig. 4.4 (c)), the comb drive (step 2) is realized on the bare SOI wafer which makes the photolithography and the etching steps of the comb drive easier than in the first strategy. Then, the glass is bonded to the silicon (step 3) and etched to form the glass disks support (step 4). The etching of the glass, which thickness is around 25 μm, can be realized by wet etching. Indeed, dry etching of such a thickness would be too long and is not practically realisable. Wet etching of glass is based on concentrated hydrofluoric acid (HF, 49%). This solution attacks SiO_2 that is the main compound of glass. The drawback is that it will also attack the BOX that is by definition SiO_2 and that is unprotected because of the structuration of the device layer. If the BOX is removed, then the bottom of the device layer is no more protected for the last step of the process that consists in etching the silicon handle layer to release the microscanner. The result is that the comb fingers will be destroyed (Fig 4.4 (d)). A solution is to protect the BOX from the etching solution by deposition a protecting masking layer. This layer must resist to the bonding, be resistant to HF and deposited at the bottom of the thin trenches that constitutes the gap between two comb fingers (width=5 μm, depth= 40 μm). The proposed solution is to deposit a layer of chromium and gold. Chromium is an adhesion layer and gold is a resistant masking layer for HF etching. The idea is also to use these metal layers to do the bonding of glass and silicon by thermocompression. This second solution is also non standard and is tested in the following.

The basic principle of the two integration strategies has been exposed previously. Now, a detailed flow chart for both strategies is presented and a risk analysis is done. The strategy 1 is called the "projection photolithography" strategy and the strategy 2 is mentioned as the "thermocompression" strategy.

Figure 4.5 shows the main steps of the projection photolithography strategy. Step (a) consists in first cleaning the wafer in piranha and then creating alignment marks on the back side of the wafer. These alignment marks will serve at the end of the process to align the mask used for the back side release. Thus chromium is sputtered (100 nm) on the back side, a photolithography is realized followed by a wet etching of the chromium. Finally, silicon is etched where the chromium has been removed to create alignment marks. The silicon etching is realized by RIE. Step (b) aims to create silicon cavities in the device layer that will correspond to the optical aperture below the glass disks. A double side photolithography is used to align the marks from the back side with the photoresist mask created on the front side. The silicon cavities are etched down to the BOX by DRIE (SPTS). During step (c), the wafer is cleaned to remove the photoresist and to prepare the SOI wafer for anodic bonding. Both SOI wafer and glass wafer are cleaned in piranha and prepared in CL200 cleaner. The glass wafer is borofloat from Schott (Borofloat 33). Anodic bonding is realized in the EVG bonder. Lapping and polishing of the wafer is

realized by an expert engineer to obtain 25 μm thick glass layer. Cleaning in piranha must be performed after the polishing. Next step (d) aims to create a mask for the glass etching. To etch selectively the glass, a metal masking layer made of chromium and gold is deposited on the glass and a photolithography is realized to remove the chromium and the gold from the areas where the glass has to be etched. Different masks including double layer of chromium and gold and photoresist will be tested. Note that this photolithography is a double side photolithography, where the mask of the glass must be aligned with the back side alignment marks. Indeed, the marks at the front side surface of the silicon wafer cannot be used due to the presence of the glass. Then, the glass disks are etched by wet etching in HF (step e). At this stage, the chromium/gold/photoresist mask is removed and the micromirrors and the contact pads are realized by sputtering of chromium and gold, followed by a photolithography done with a spray coated photoresist and wet etching of gold and chromium (step f). Next, the comb drive are created by a two steps DRIE process realized with two different masks. The two different mask must be realized with material that can be removed selectively (step g). A mask is created in aluminium or in chromium (aluminium is etched by the developer which complicates the tests) by sputtering, spray coated photoresist and projection photolithography and finally wet etching. The alignment of this first comb drive mask is not critical as it must only be aligned with the glass disks. The second mask is realized in spray coated photoresist and projection photolithography. The alignment of the second mask of the comb drive with the first mask is very sensitive. The first DRIE step is realized with the two masks to etch silicon down to the BOX and create the comb drive (step g). Then, the photoresist mask is removed in acetone and the second DRIE is performed to etch one in every two combs down to half the device layer thickness (step h). Note that the DRIE cannot be performed in the SPTS equipment because of the presence of the metal mask, thus the Alcatel machine is used. The wafer is cleaned from the aluminium mask by wet etching (step i). The final steps consists in releasing the scanner by etching the back side. Spray coating photolithography is realized on the back side to created the releasing aperture (step j). The front side of the wafer is protected by gluing a support wafer with oil. Then, DRIE is performed to etch silicon down to the BOX (step k). The wafer support is removed in acetone and oil residues are removed by oxygen plasma. Finally, RIE of the BOX is achieved.
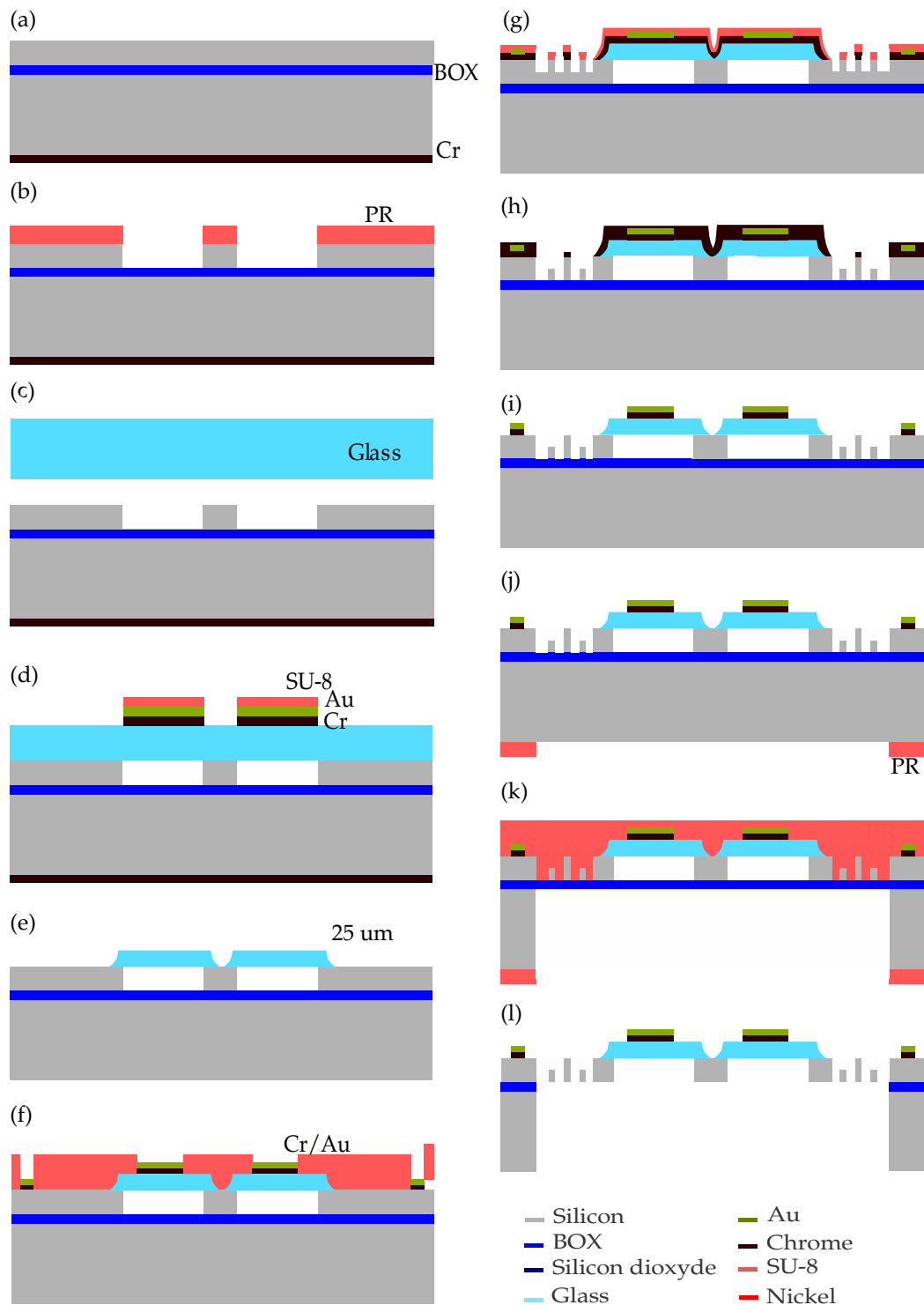
Figure 4.5: Flow chart 1: projection photolithography based technology, (a) sputtering of Cr, photolithography, etching of Cr and Si on back side for the creation of alignment marks, (b) photolithography and DRIE of silicon cavities, (c) cleaning and anodic bonding of SOI and glass wafer, (d) deposition of Cr/Au/Cr/Au/SPR 220 mask on glass, (e) HF etching of glass, (f) deposition of Cr/Au micromirrors and contact pads, (g) two step photolithography in Cr and photoresist and first steps DRIE, (h) stripping of photoresist mask and second step DRIE, (i) etching of Cr and cleaning of the SOI wafer, (j) Photolithography on the back side, (k) DRIE of handle layer, (l) RIE of the BOX.

A risk analysis of this flow chart is conducted for each steps of the process. Table 4.2 shows a description of the risks associated with each step of the flow chart. Risks linked to the process, to the compatibility of the process within the flow chart and to the equipment used are discussed. The probability and the impact factor corresponding to each risk is established and the risk factor is calculated. The sum of each risk factor illustrates the global risk factor of the flow chart. For this first flow chart, the total risk factor equals 173 and the risk analysis shows some critical steps that require testing and development to lower the risk. In particular, steps 19 and 22, which are linked to the projection photolithography process and steps 30 and 31, which are linked to the back side release of the microscanner, are highly risky and the success of the fabrication depends on the management of these processes. The risk linked to the projection photolithography steps is mainly linked to the capacity of the machine that cannot be adapted to non classical procedure. The release step is always critical in MEMS/MOEMS system as it consists in making free a very fragile platform. Moreover, after this step, wet processes are forbidden as it can provoke stiction between fixed and moving parts. The lapping and polishing steps are also critical as it must ensure a good planarity of the glass support as well as a good optical quality without breaking the glass that is suspended over the silicon cavities created in step (b). Finally as the micromirrors are deposited in the middle of the flow chart, it is critical to keep their optical quality until the end of the fabrication.

Table 4.2: Risk analysis of the "projection photolithography" flow chart. The risk factor is illustrated by a blue bar which length is proportional to the risk factor. The total risk factor is equal to 175. BS and FS stands respectively for back and front side.

Step	Description of step	Description of the risk	Probability	Impact	Risk factor
1	Cr deposition (BS)		1	1	1
2	Photolitho 1/Mask 1 (BS)	Bad alignment between backside and front side	2	1	2
3	Cr etching (BS)		1	1	1
4	RIE of silicon (BS)		1	1	1
5	Photolitho 2/Mask 2		1	1	1
6	DRIE 1		1	1	1
7	Cleaning of glass wafer		1	1	1
8	Bonding of glass and SOI wafer	Bonding SOI and glass: bad quality of bonding	1	2	2
9	Lapping-Polishing	Lapping and polishing: breaking of membrane + bad optical quality	5	5	25
10	Deposition of Cr/AU/Cr/Au (FS)		1	1	1
11	Photolitho 3/Mask3		1	1	1
12	Wet etching of Cr/Au/Cr/Au		1	1	1
13	Wet etching of glass: Liquid HF (FS)	Degradation of the glass quality	3	3	9

14	Etching of Cr/Au/Cr/Au		1	1	1
15	Cleaning of glass wafer		1	1	1
16	Photolitho 4/Mask4	No flat surface, hard mask not in contact with silicon surface: bad definition of the contact pads	3	2	6
17	Deposition of Ti/Au		1	1	1
18	Deposition of Aluminium		1	1	1
19	Spray coating		1	1	1
20	Projection photolithography 5/Mask 5	Instability of the equipment (Perkin Elmer)	5	3	15
21	Automatic development		1	1	1
22	Spray coating		1	1	1
23	Projection photolithography 6/Mask 6	Bad alignment of the two masks with projection photolithography	4	5	20
		Instability of Perkin Elmer	5	3	15
24	Manual development		1	1	1

#	Process	Description			
25	DRIE 2	DRIE in Alcatel machine: breaking due to clamping + instability of equipment	3	3	9
26	Stripping of mask 2		1	1	1
27	DRIE 3	Second DRIE: Under etching or over etching	1	1	2
		DRIE in Alcatel machine: breaking due to clamping + instability of equipment	3	3	9
28	Wet etching of Cr	Degradation of the mirror quality	2	1	2
29	Cleaning of the wafer	Degradation of the mirror quality	2	1	2
30	Photolitho /Mask 7 (BS)		1	1	1
31	DRIE 4 (BS)	BS DRIE: cracking of BOX and etching of FS	4	4	16
32	RIE of the BOX	Degradation of back side of the glass membrane and mirror quality	5	4	20

Total risk factor 173

The second strategy of glass integration is based on thermocompression which metal layers serve also for the protection of the BOX against the HF solution used for the wet etching of glass (Fig. 4.6). Step (a) is the same than in the first flow chart and consists in creating alignment marks on the back side. Then, the comb drive are created in the device layer in the same two steps photolithography/DRIE process than presented before (step b-c). In step (d), a chromium and a gold layer are deposited by sputtering on both glass and structured silicon wafer after cleaning of the wafers. A photolithography (S1813) followed by a wet etching of chromium and gold is processed on the glass wafer to remove the metals from the optical aperture created by the glass disks. Step (e) illustrates the bonding by thermocompression of the two wafers, the lapping and polishing of the glass wafer down to 25 *μm* and the selective deposition of the masking layer for HF etching (Cr/Au/Cr/Au/SPR 3.0). Then, step (f) shows the wet etching in HF by the same means than in the first flow chart. In step (g), the metal layers used for the bonding are removed by wet etching and the wafer is cleaned. Note that the micromirrors and the contact pads cannot be deposited at this step by deposition of metal layers and photolithography because the spray coated photoresist would penetrate between the comb finger gap and would be too difficult to remove. Back side release is performed following the same step than in the first flow chart: first DRIE of the handle layer is conducted while the front side is protected by a support wafer (step h) and then RIE of the BOX is done (step i). Finally, the micromirrors and the contact pads are deposited on the released device by use of a shadow mask wafer and sputtering. This solution is very interesting because it enables the deposition of the micromirrors as a last step, avoiding any possible contamination and keeping a good optical quality. The contact pads will be formed on the silicon surface, which is not in contact with the shadow mask; however, the definition of the border of the contact pads is not important compared to the one of the micromirrors which have an impact on the optical quality of the final system.

The risk analysis is also realized for this flow chart and presented in Tab. 4.3. The table shows that there is less step of fabrication, which is an advantage because it decreases the risk. Moreover, there is less critical steps since the projection photolithography steps have been removed and the deposition of the micromirrors in the last steps decreases the risk of the degradation of their optical quality. Note that this strategy of deposition of the micromirrors can be adapted to the first flow chart. Though, in the second flow chart, there is a risk of attack of the BOX during the wet etching of the glass if the metal layers do not protect correctly the BOX. It can happen if the deposition is not conformal or has been deteriorated during the thermocompression. The total risk factor is equal to 125 which is much lower than the total risk factor of the first flow chart.
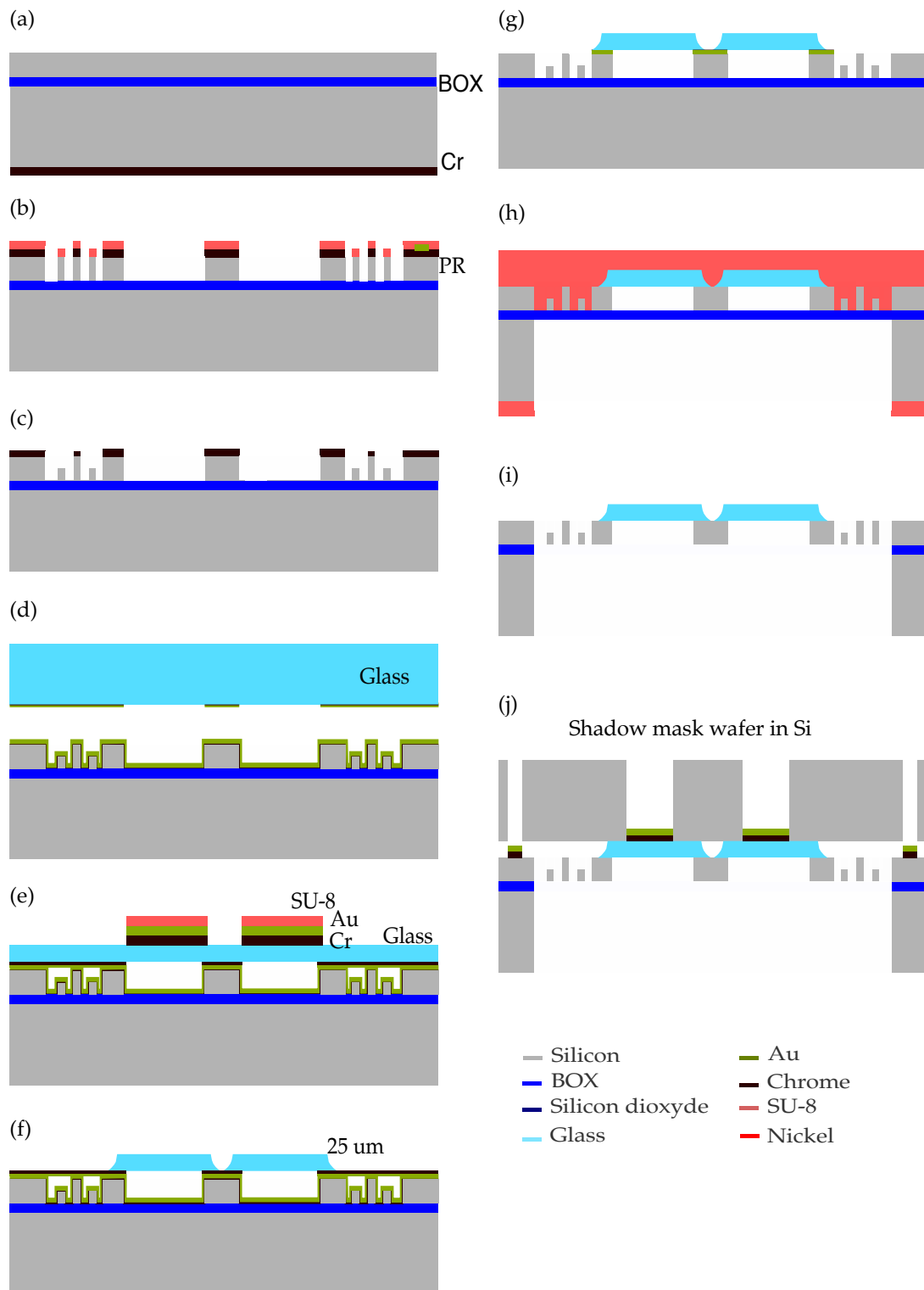
Figure 4.6: Flow chart 2: thermocompression based technology, (a) sputtering of Cr, photolithography, etching of Cr and Si on back side for the creation of alignment marks, (b) two step photolithography in Cr and photoresist and first steps DRIE, (c) stripping of photoresist mask and second step DRIE, (d) etching of Cr on SOI wafer and sputtering of Cr/Au on SOI and glass, (e) thermocompression and deposition of Cr/Au/Cr/Au/SPR 220 mask on glass, (f) HF etching of glass,(g) etching of Cr/Au and cleaning of the wafer, (h) photolithography on the back side and DRIE of handle layer, (i) RIE of the BOX, (j) sputtering of Cr/Au micromirrors and contact pads through shadow mask.

Table 4.3: Risk analysis of the "thermocompression" flow chart. The risk factor is illustrated by a blue bar which length is proportional to the risk factor. The total risk factor is equal to 119. BS and FS stands respectively for back and front side.

Step	Description of step	Description of the risk	Probability	Impact	Risk factor
1	Cr deposition (BS)		1	1	1
2	Photolitho 1/Mask 1 (BS)		1	1	1
3	Cr etching (BS)		1	1	1
4	DRIE 1		1	1	1
5	Photolitho 2/Mask 2	Bad double side alignement	1	2	2
6	Photolitho 3/Mask 3	Bad alignment of the two masks	2	3	6
7	DRIE 2	DRIE in Alcatel machine: notching effect +pb machine	3	3	9
8	Stripping of mask 3		1	1	1
9	DRIE 3	Second DRIE: Under etching or over etching	2	1	2
		DRIE in Alcatel machine: notching effect +pb machine	3	3	9
10	Deposition of Cr/Au	No conformal depostion	2	3	6
11	Photolitho 4/Mask 4		1	1	1
12	Cr etching on glass wafer		1	1	1
13	Thermocompression	Bad alignment between glass and SOI wafer	2	1	2

#	Process	Risk			
14	Lapping-Polishing	Lapping and polishing: breaking of membrane + bad optical quality	5	5	25
15	Deposition of Cr/AU/Cr/Au (FS)		1	1	1
16	Photolitho 5/Mask 5		1	1	1
17	Wet etching of Cr/Au/Cr/Au		1	1	1
18	Wet etching of glass: Liquid HF (FS)	Degradation of the glass quality through mask pinholes and attack of the BOX if not correctly protected	3	5	15
19	Etching of Cr/Au		1	1	1
20	Cleaning of wafers		1	1	1
21	Wet etching of Cr		1	1	1
22	Cleaning of the wafer		1	1	1
23	Photolitho 6/Mask 6 (BS)		1	1	1
24	DRIE 4 (BS)	BS DRIE: cracking of BOX and etching of FS	4	4	16
25	RIE of the BOX	Degradation of backside of glass membrane	3	4	12
26	Cleaning of wafer by plasmas O2		1	1	1

27	Alignment with shadow mask	Bad allignment with shadow mask	3	1	3
28	Deposition of Cr/Au	Bad quality of deposition at the edge through the physical mask	2	2	4
		Total risk factor			**127**

Two solutions to integrate the glass support on the silicon microscanner have been given and studied. Each flow chart has been described in details and each step has been analysed in terms of risk. The critical points of each technology have been discussed in terms of equipment and process. In the next section, the fabrication of the microscanner following the two presented strategies is exposed after introducing some considerations on the fabrication of the hard masks.

4.2.2/ FABRICATION RESULTS

Microfabrication is based on photolithography steps that enables the selective deposition and the etching of material layers according to a specific pattern. The pattern is transferred to the wafer through a hard mask that hides specific region of the wafer during the exposure of the photoresist to UV light. The mask pattern is defined by the design of the structure to be fabricated. The hard mask is realized with a high resolution aligner that exposes point by point the photoresist according to a path that depends on the mask file. The mask file is a drawing of the design that can be realized with different softwares. In this thesis, the masks have been drawn with KLayout, which is a free software. With this software, the masks can be easily coded using Ruby language which is an advantage when complicated mask are designed and which parameters can change over the progress of the research. Here, the masks have been coded putting the design parameters as variables of implemented functions. In practice, if the number of comb fingers, the gap between two comb fingers d or the diameter of the optical aperture D_{holes} are changed, the mask can be automatically regenerated. Finally, the drawing of a mask must take into account the type of process that is realized to first draw alignment marks according to the targeted alignment precision and secondly to adjust the pattern size with the potential underetching of the processes. The alignment marks used in this thesis are shown in Fig. 4.7. The alignment marks, placed both on the wafer and on the hard mask, must be able to align the two entities in the two directions and be large enough to be found easily with the optics of the alignment equipment. The alignment marks are placed symmetrically with respect to the y axis of the wafer, near the right and the left border. The bigger the distance between the alignment marks, the better the alignment. Indeed, when the alignment marks are far away from each others, the angle error, usually referred to as "theta error", is minimized.
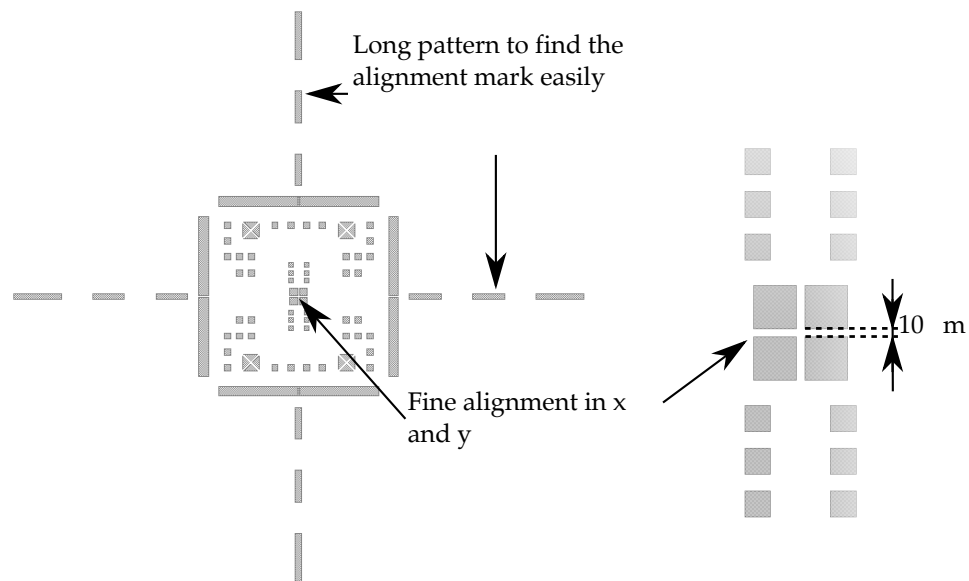
Figure 4.7: Alignment marks with a zoom on the central marks. The alignment marks are placed at the left and right border of the wafer in the zones shown in Fig. 4.8.

However, the alignment marks cannot be placed everywhere on the wafer because of some exclusion zones. Figure 4.8 gives an overlook of different forbidden zones. First the border of the wafer is usually not patterned because processes are less qualitative on the edge of the wafer (red ring). Moreover, the objectives of the alignment equipment cannot image the whole wafer area but are usually constraint to a certain area (blue zones) in which the alignment marks must be placed. Finally, another type of alignment marks is used to make a first alignment between a bare wafer and a hard mask. Transparent rectangles are placed at the bottom of the wafer to align the wafer flat, adjust the angle and the y position of the wafer with respect to the mask and others rectangles are placed on the left and right of the wafer to adjust the x position of the wafer (grey rectangles). For the fabrication of the hard mask, it is convenient to add four little marks around the wafer pattern to help finding the center of the wafer and center the pattern on the hard mask. A small non symmetrical marks is also added to see easily if the pattern is mirrored or not. Indeed, in practice, the wafer pattern is drawn as the researcher wants to see it on the wafer which is the mirrored pattern with respect to the one on the hard mask in contact with the wafer. Then, the mask pattern must always be mirrored compared to what is expected on the wafer surface.
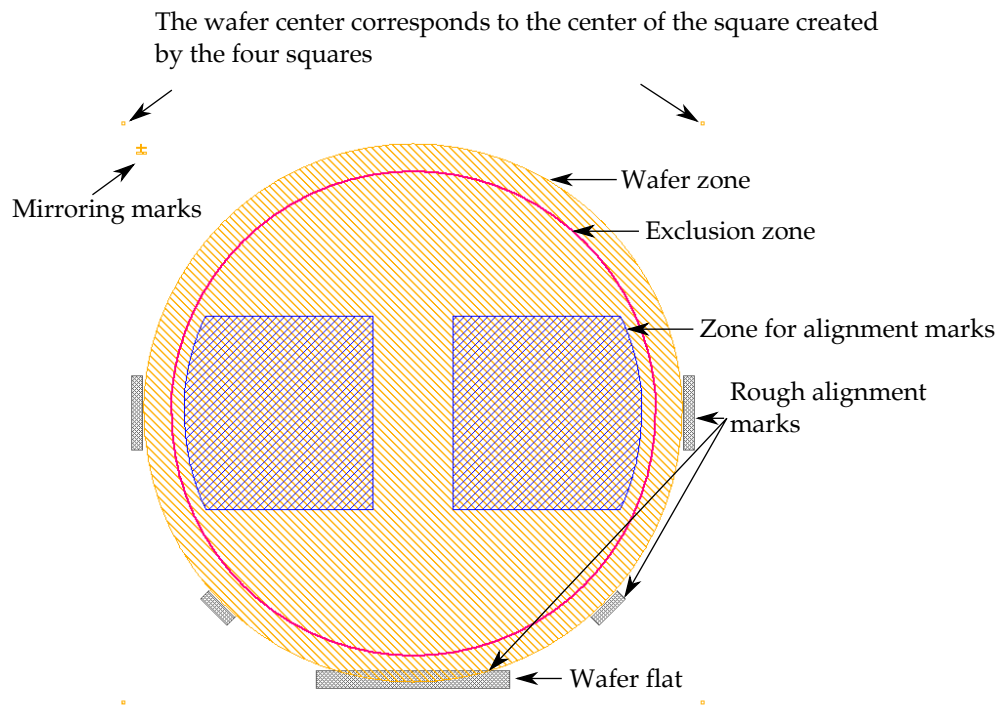
Figure 4.8: Typical zones on a wafer and alignment marks.

The masks for the two flow chart have been generated and are shown in Annexe E. The hard masks are fabricated by an engineer specially trained to use the mask aligner, which is a very sensitive machine [1].

The fabrication based on the first flow chart is now described. In the first integration strategy, the glass disks supporting the micromirrors are first fabricated on SOI with etched cavities, whereas actuator structures are performed later by use of spray coating and projection photolithography. An advantage of this strategy is that the glass layer can be processed in concentrated HF without damaging the BOX for any thickness and shape of the glass. However, 3 main steps have been revealed by the risk analysis as very dangerous: the creation of the 25 μm thick glass, the projection lithography and the release of the structure. Therefore, a particular attention is paid to these steps.

First the 1.8 mm diameter cavities are etched into the device layer of SOI wafer by use of SPR 220 photoresist and DRIE. The glass and the SOI wafer are anodically bonded at 350°C and the maximum applied voltage is 900 V. Then, the glass is lapped and polished to obtain a thickness of 25 μm. Figure 4.9 shows the results of this three frist steps at wafer level.

---

[1]Unless mentioned otherwise, I have realized all the steps of the microfabrication presented in this thesis.

(a)						(b)

(c)
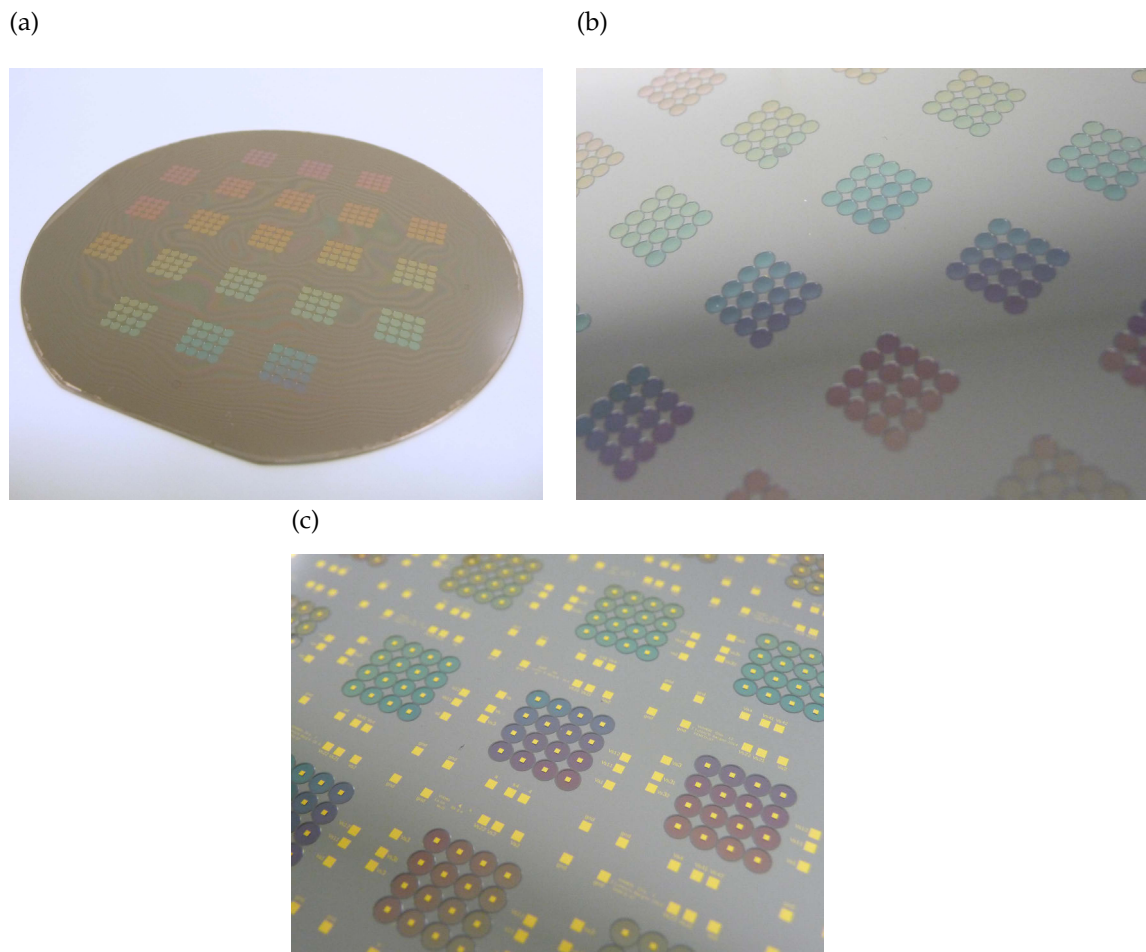
Figure 4.9: Results of the three first steps of fabrication: (a) glass bonded to SOI with etched cavities and lapped and polished down to 25 μm (optical fringes are visible), (b) HF etching of the glass to create glass supports, (c) deposition of Cr/Au micromirrors and contact pads on the glass and the SOI surface respectively.

First tests have shown that the glass, which is suspended over the silicon cavities and lapped and polished, breaks easily when the thickness is below 25 μm (Fig. 4.10). Consequently, for the future run, the thickness of the glass support will be adapted to 30 μm. This change has no significant influence on the optical design. Before the glass is wet etched in HF 49% during 6 minutes, it is protected with a sputtered Cr/Au/Cr/Au/photoresist (10nm/2x200nm/ 10nm/2x200nm/5 μm) mask. This mask has been optimized in terms of chemical resistance and to minimize risk of pinholes generation. The double layer of Cr/Au combined with thick photoresist (20 μm) is proposed in [154]. Here the thickness of the resist is reduced compared to [154] because the etching depth is smaller than in the article. Figure 4.11 shows clearly that the presence of the photoresist SPR 220 3.0 on the same Cr/Au/Cr/Au mask prevents the HF from penetrating through the pinholes in the gold mask. The thickness of structured glass layer was measured in the range of 25-27 μm, leading to a wafer-level thickness uniformity of 3.8%. The mirrors are then

deposited by sputerring Cr/Au (10-180 nm).

(a)
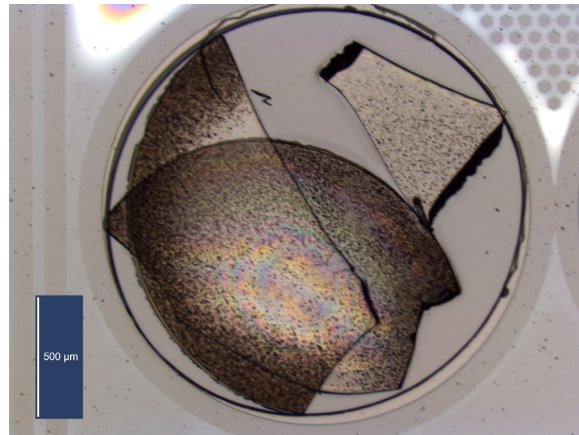
Figure 4.10: Broken glass support after lapping and polishing.

(a)   (b)
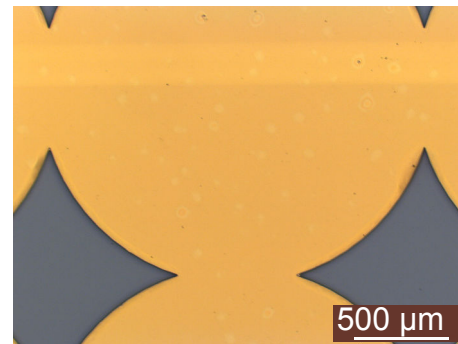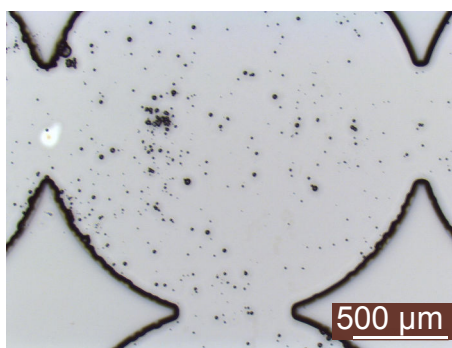
(c)   (d)
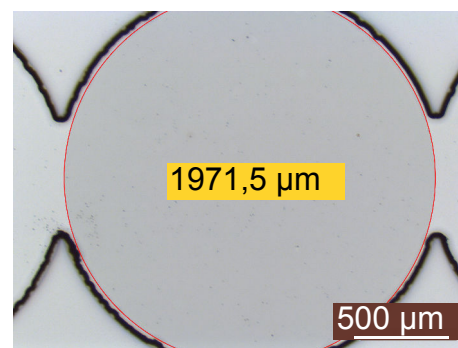
Figure 4.11: Test of masking layer for HF etching of glass: (a-c) Cr/Au/Cr/Au , (b-d) Cr/Au/Cr/Au/SPR 220, (a-b) mask layer surface after 6 min etching, (c-d) glass surface after removal of the mask.

The micromechanical structures are then formed in the SOI device layer by the two steps DRIE down to the BOX. The construction of vertical comb-drive actuators requires two types of finger electrodes, having the same width of 10 μm but whose height differs (40 μm for stationary and 20 μm for movable fingers). This etching technique requires sub-

micrometer alignment precision between the two masks in chromium and in photoresist. For that purpose, the photoresist (S1813, 3.0-μm thick) is spray-coated on the silicon surface (SUSS MicroTec AltaSpray 8) and projection photolithography (SVG Micralign 740) is used to transfer the actuator pattern into the photoresist. This thickness of photoresist is optimal to limit the fluctuation of the thickness of the resist and to transfer correctly the pattern with the projection photolithography. Because the alignment marks are not well visible through spray-coated photoresist, special alignment procedure has been developed to align the second mask with the first mask in chromium. Instead of using the alignment marks, the comb fingers present on the wafer are aligned with the comb fingers on the hard masks directly. As comb fingers are around the platform, two perpendicular sets of comb fingers are successively used to align the x and y directions. The developing procedure has also been adjusted compared to the standard procedure used by the start-up Freque|n|sys. For the first photolithography, the post exposure bake is removed because tests have shown that it generates small photoresist residues after the development. For the second photolithography, the development is realized manually because automatic development is not able to remove the exposed photoresist efficiently. Indeed, the pattern used for this second step is transparent for the most part which means that most of the resist mus be removed. Therefore, an energetic agitation is required during the development. The DRIE step is performed with the Alcatel machine because of the presence of the metal mask that is forbidden in the SPTS machine. Figure 4.12 shows the microscope images of the mask patterns. The measured alignment error of ± 700 nm was obtained. Figure 4.13 shows an image of the actuator at the level of the chip.

(a)

Micromirror

Springs

Sensor part 1

Sensor part 2

Actuator

(c)

(b)

4.51 μm   3.12 μm
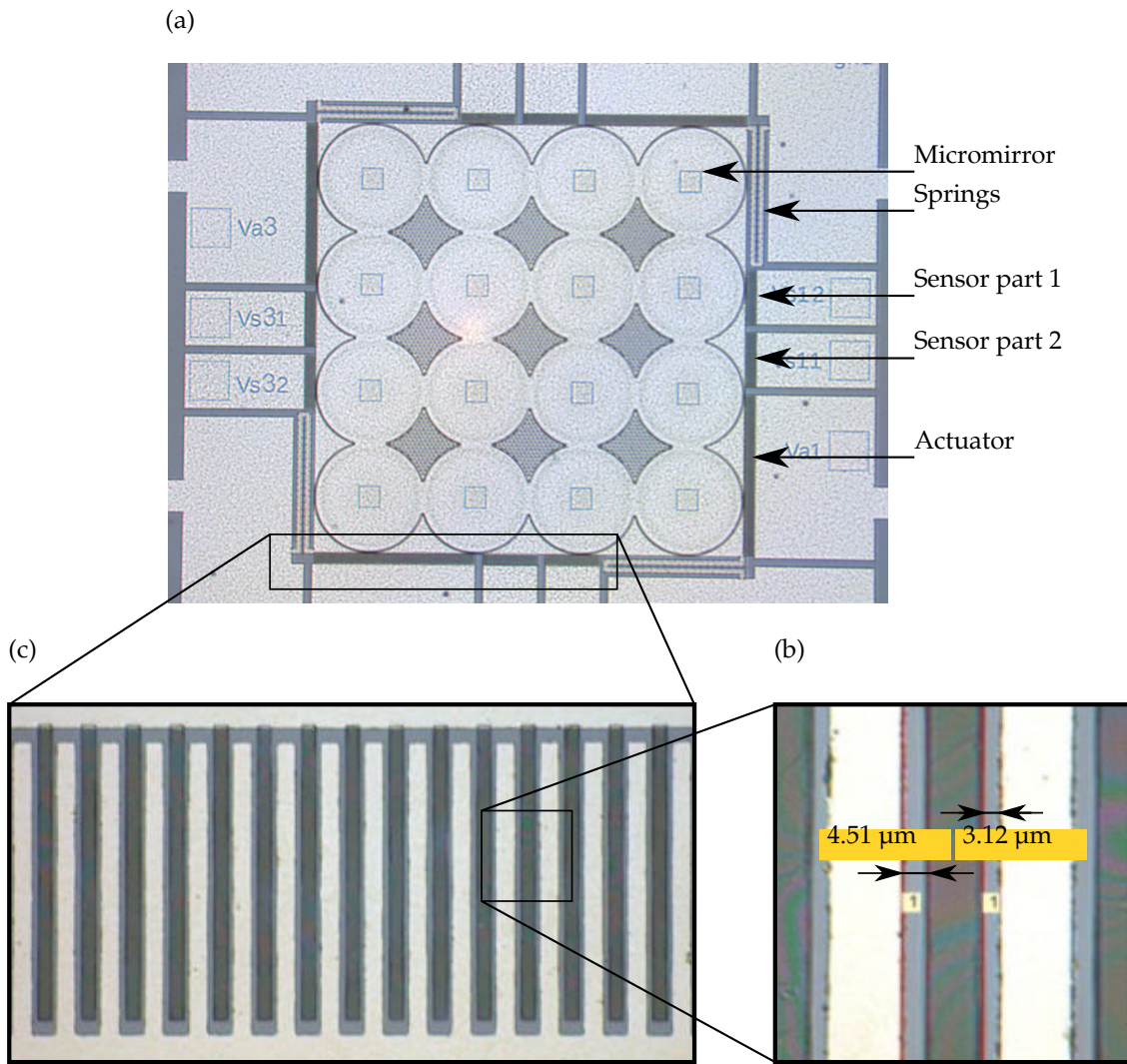
Figure 4.12: Two successive projection photolithographies results: (a) image of one chip, (b) zoom on the comb fingers, (c) zoom on the comb fingers to see alignment precision. The alignment error is around ± 700 nm.
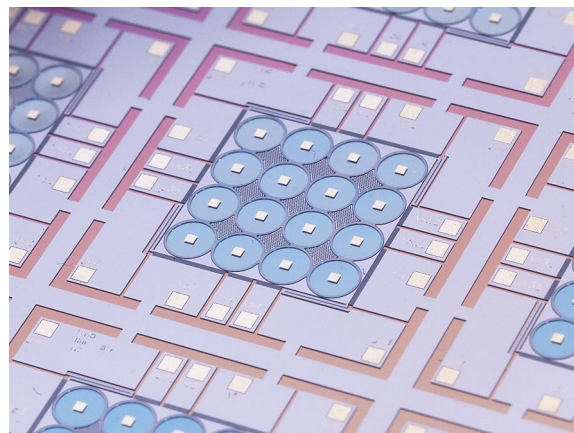
Figure 4.13: Image of the microscanner chip before the back side release.

After that, the whole structure is first pre-released by DRIE of the backside (Fig. 4.14). This step revealed the problem of broken BOX, which allows plasma penetration into already formed structures in the device layer. This effect may be caused by the stress and the weight of the suspended platform. Unfortunately, one of the consequences of this effect is a creation of deep trenches at the basis of fingers or even complete breaking of fingers (Fig. 4.15).

(a)   (b)   (c)

Broken BOX
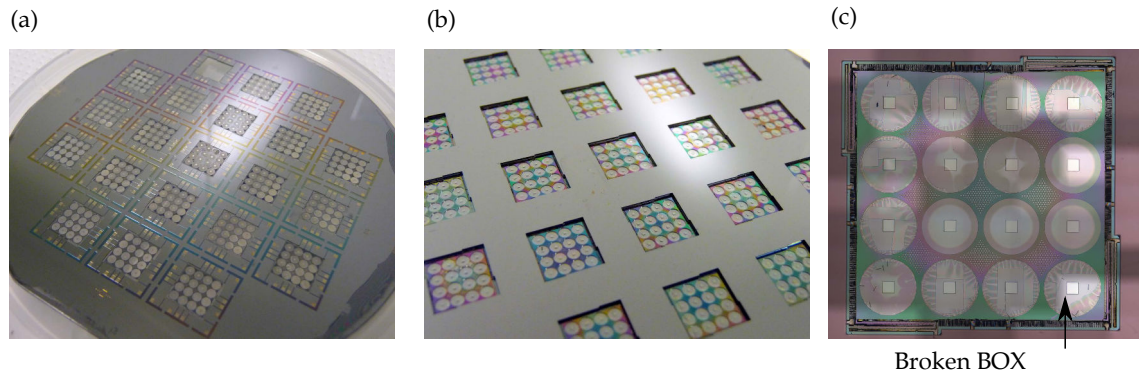
Figure 4.14: Result of the DRIE of the handle layer: (a) image of the wafer front side, (b) image of the wafer back side, (c) zoom on on chip.

(a)   (b)   (c)

(d)

Trenches in the comb finger created from the back side
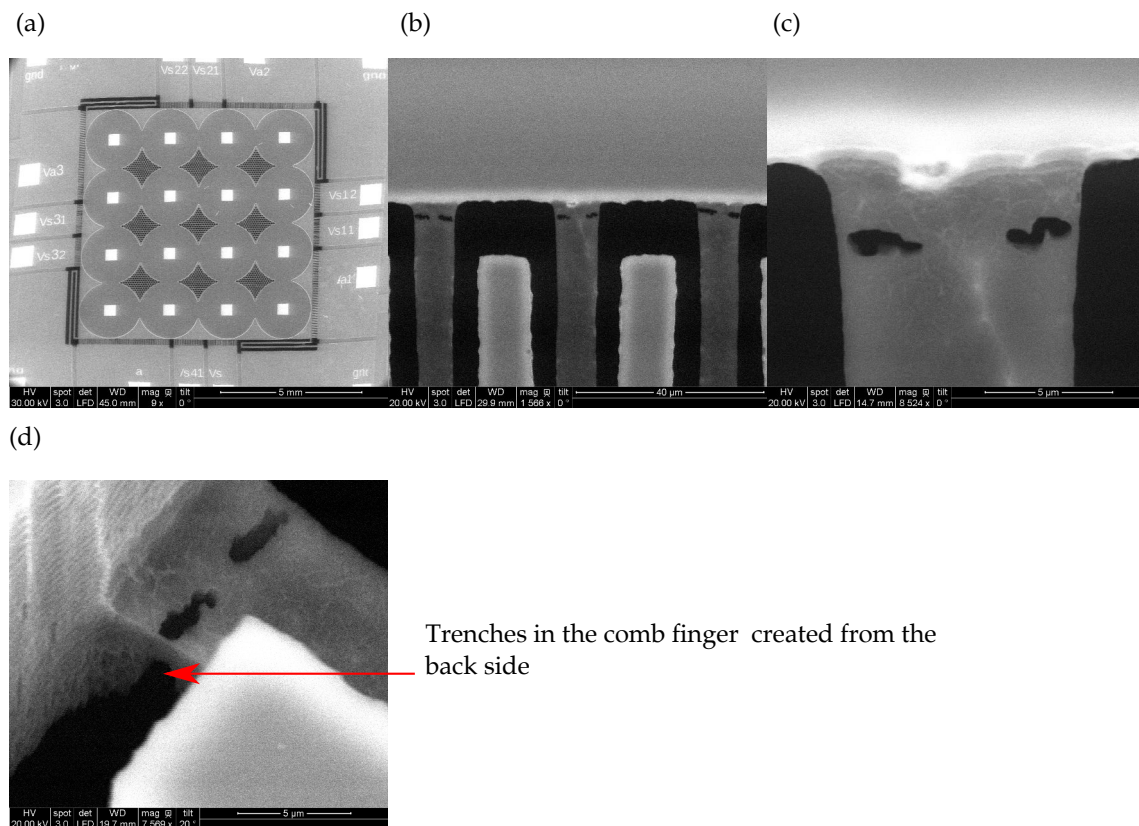
Figure 4.15: SEM images of the structure after DRIE of the handle layer: (a) front side view of one chip, (b) result of the etching of the comb drive from the back side, (c-d) zoom on one finger etched from the back side with top view and 3D view.

Broken BOX complicates also its etching in order to completely release the suspended platform. For example, application of RIE method (BOX surface on top) leads to BOX falling down into the cavity and non-uniform exposing of glass membrane to the etching plasma. Figure 4.16 shows SEM images of the structure at the end of the process. It appears that some parts of the BOX are stuck to the glass membrane after etching of the BOX. However, the alignment precision is well conserved even after the release of the structure. Note that the facing set of comb fingers have not the same width (7.9 and 11.9 μm) and that the width corresponding to this pattern must be adjusted during the hard mask design.

(a)   (b)   (c)
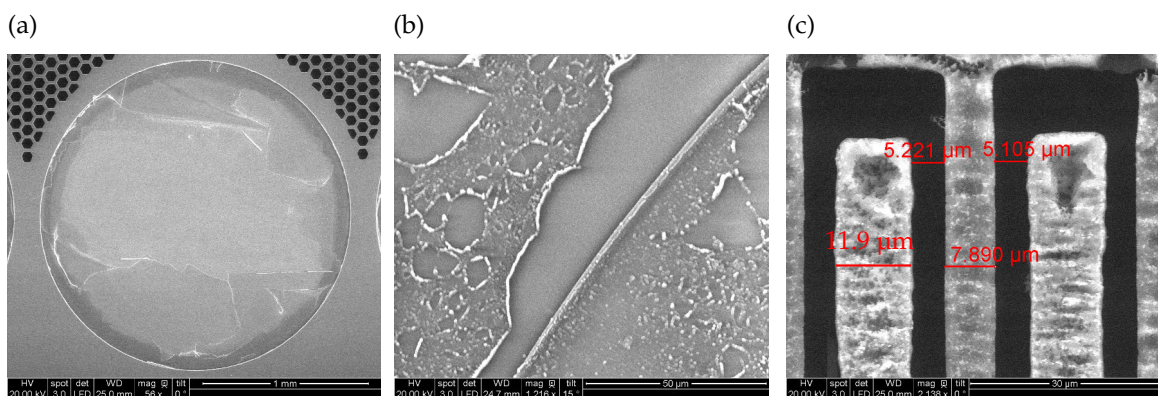
Figure 4.16: SEM images of the back side of the structure at the end of the fabrication: (a) broken parts of BOX stuck onto the glass membrane, (b) zoom on the broken BOX stuck on the glass membrane, (c) alignment data after release.

To conclude, two out of the three risky steps have been overcome. For the last step, i.e. the release step, a new solution must be implemented. A first solution consists in etching the BOX at the bottom of the cavities right after etching the silicon cavities to avoid that it falls down at the end of the process. This step can be realized easily after the etching of the cavities in the same DRIE machine used to etch the silicon by changing the gas composition of the plasma to etch silicon dioxide. However, the glass support is then completely exposed to the RIE plasma used for etching the BOX which will also etch the glass. Then, the back side of the glass must be protected before the glass wafer is bonded to the silicon. The protection layer must resist to the temperature used for the anodic bonding, to the etching plasma but must be removed by dry etching afterwards to let the glass membrane transparent. Wet etching is not possible because, at this step, the structure is already released and it would provoke stiction. A solution is to use parylene to protect the glass. Parylene tolerates wide range of temperature and can be removed by oxygen plasma. Moreover, Higo *et al.* showed the potential of a parylene/Al/parylene sandwich protection mask for HF vapour release for MEMS [155]. This solution is still to be tested. Another issue that was not taken into account in the risk analysis is that the BOX breaks and let the silicon etching plasma reach the front side during the back side

release. A solution is to deposit a thin layer of silicon dioxide by PECVD on the front side of the wafer to protect the comb fingers during the back side etching. Adding this layer requires that the micromirrors are deposited at the end of the flow chart as proposed in the flow chart 2. This solution still needs further tests of development.

The second flow chart is based on the combination of thermocompression and glass etching. The aim is to protect the BOX from the HF solution during glass structuration with the Cr/Au layer deposited for the thermocompression of silicon to glass. This technology enables the photolithography to be performed as a first step on the flat surface of SOI device layer, resulting in high quality mask for subsequent DRIE. Consequently, the structures of comb drive actuator can be etched with high precision and high quality of wall surface. The chromium mask is first realized based on a lift-off process that is more precise and qualitative than an etching step. The lift-off relies on realizing a photolithography with a negative photoresist, which means that the photoresist is removed where the chromium must stay. Then, the chromium is deposited and finally the wafer is cleaned in acetone which removes the photoresist and the chromium that has been deposited on. In order to have a clean lift-off the side walls of the resist should have a negative angle as shown in Fig. 4.17 and that is why negative photoresist is used (a-b). However, here another solution is used. A first resist is deposited, called LOR 7B, and then the photoresist is deposited on top of it. When this double layer is developed, the LOR 7B is underetched which creates perfect sidewall profiles for a lift-off (c).
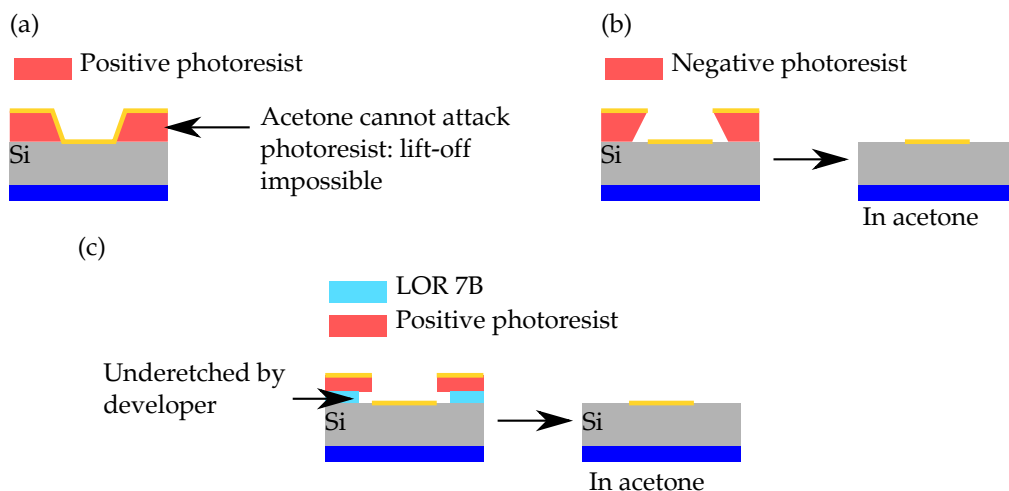
Figure 4.17: Lift-off process: (a) use of positive photoresist, (b) use of negative photoresist, (c) use of LOR 7B and positive photoresist.

Figure 4.18 shows images of the comb finger structure. The alignment precision of the two masks is presented in Fig.4.18 (a). The alignment precision is much higher than with projection photolithography ($\pm$ 60 nm). In (c) the focus is made on the surface of the wafer, but it can be seen that one in every two fingers is etched. It is possible to measure

the etch depth by focusing successively on the wafer surface and on the etched comb and comparing the two vertical positions of the microscope.
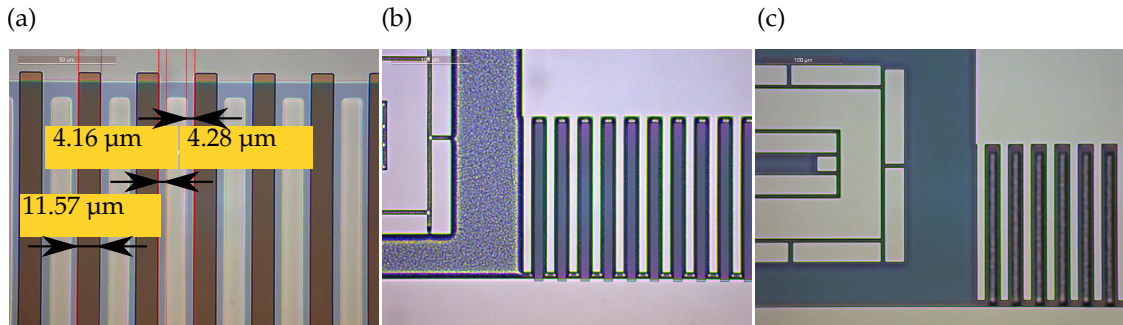
Figure 4.18: Fabrication of the comb fingers: (a) alignment of the two masks, (b) first DRIE step, (c) second DRIE step.

The design of the two DRIE masks is not well adapted in case of a higher misalignment. Figure 4.19 illustrates the result of the two steps DRIE process in the case of a misalignment between the two masks (a). It is relatively easy to avoid this issue by simply removing the first mask where it is not needed thanks to the presence of the second mask (b). Moreover, as expected and mentioned above, it can be observed that the quality of etching of the comb fingers is much better than with the first flow chart.
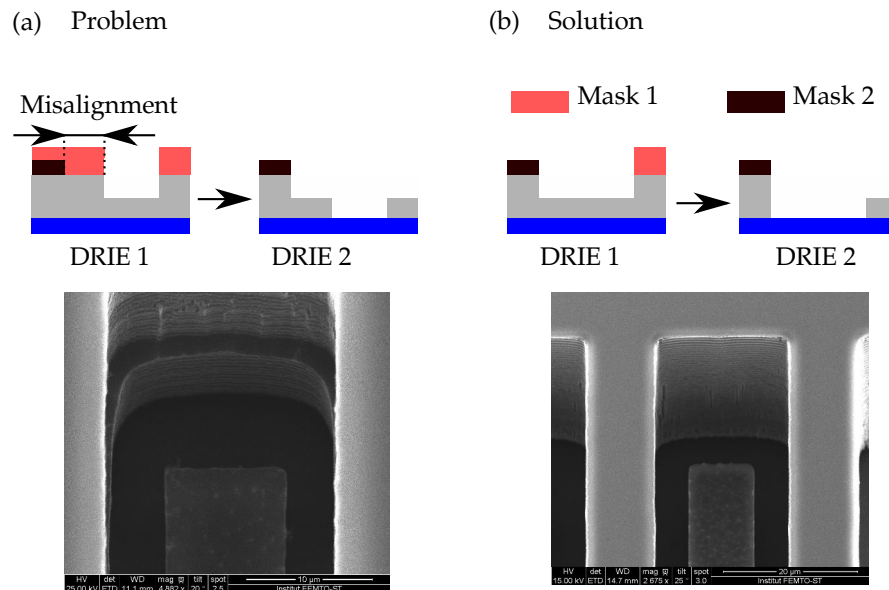
Figure 4.19: Design of the mask and misalignment: (a) impact of misalignment of the two masks on the two steps DRIE, (b) impact of misalignment of the two masks on the two steps process with modified masks designs.

The bonding of glass is realized by thermocompression with Cr/Au (10/300 nm) layers deposited on silicon and glass surfaces during 13 hours and with a compression force of 4 kN at 100°C. Cr/Au layer is previously removed from the silicon cavities by spray

coating, photolithography and wet etching (Fig. 4.20 (a)). An image of the thermocom-pressed wafers is shown with the glass wafer on the top in Fig. 4.20 (b). A misalignment is visible between the optical aperture realized on the glass wafer and the silicon cavities in the SOI wafer (17 μm). This error is acceptable because this alignment is not critical.

(a)   (b)

Cr/Au layer deposited on SOI wafer and removed from cavities

Misalignement between SOI and glass wafer

Cr layer deposited on Glass
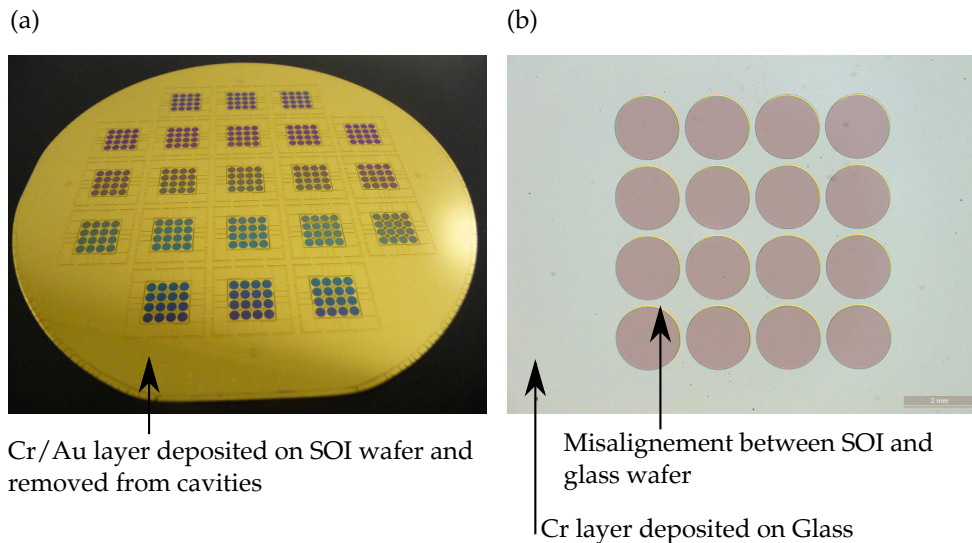
Figure 4.20: Thermocompression: (a) structured Cr/Au layer on SOI wafer, (b) image of the thermocompressed wafers seen from the glass wafer side.

The glass disks have survived the lapping/polishing and structuration steps. Thus, ob-tained results indicate that the bonding by thermocompression is strong enough for this application. Moreover, the quality of the bonding created has been investigated in terms of homogeneity. A scanning acoustic imaging technique was used to investigate the bonded interface. Fig. 4.21 shows that the bonding is well homogeneous.

(a)   (b)

Trenches through the SOI to manually detach the chips at

Contact pads
Silicon cavities (no bonding)

SOI surface
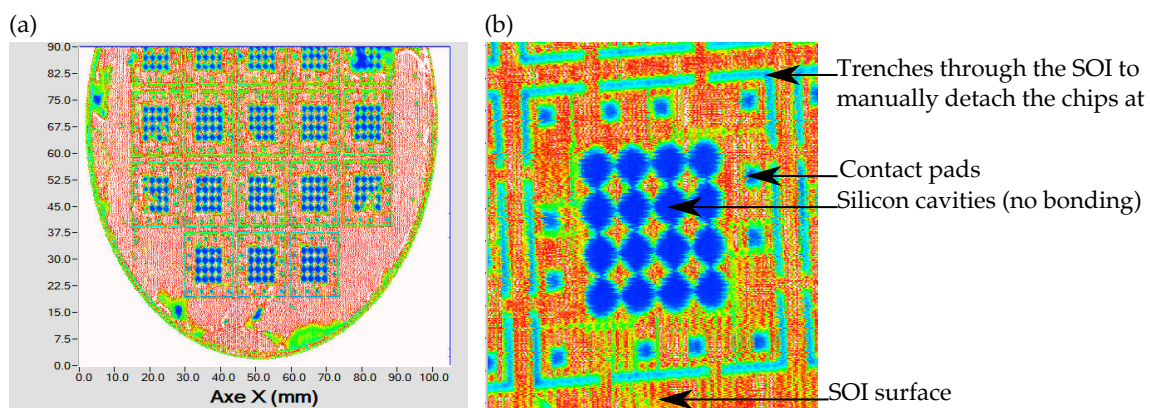
Figure 4.21: Acoustic measure of the bonding quality. Red areas correspond to bonded areas whereas blue zones correspond to unbonded zones.

The main problem of this technology is that the conformality of the Cr/Au layer de-posited for the thermocompression on SOI wafer is not good enough and do not protect efficiently the BOX. Hence, when the glass is structured in HF, it has been observed that

the BOX is also etched releasing partially the structure (Fig. 4.22). It is expected that, during the backside release, the etching plasma will easily penetrate the front side of the wafer and damage the front side structure (as presented before for the first flow chart). The idea of protecting the front side with a thin oxide can be also applied but then this technology has only the advantage of a low temperature process when anodic bonding cannot be used (high temperature can be a problem for other devices).
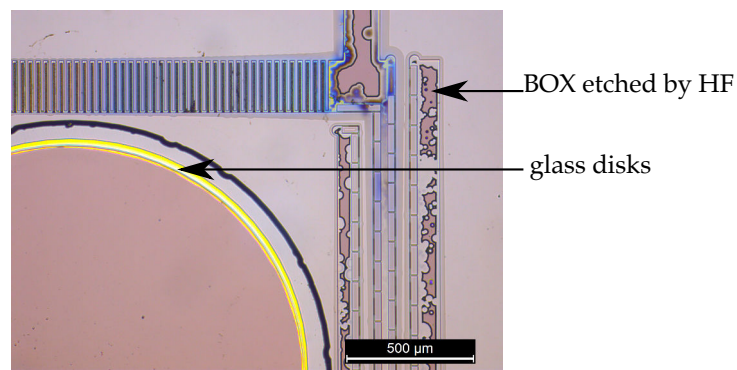
Figure 4.22: Images of the structure after Cr/Au layer etching. The BOX has been attacked by HF and underetched below the silicon.

To conclude, the two strategies proposed in this thesis have been tested and proven to be efficient to integrate glass disks. The optical quality of the glass disks will be characterized in the next chapter. The main critical steps revealed by the risk analysis have been optimized and overcome. Overall, a new combination of spray coating and projection photolithography have been completely developed. With the two strategies, the limiting steps are the releasing steps due to deterioration of the BOX. A solution based on the deposition of silicon dioxide on the front side is proposed. However, for the second flow chart, if the thermocompression is a good alternative to anodic bonding, the Cr/Au layer tested here is not efficient to protect the BOX. A more conformal deposition, with higher thickness could be tested using the atomic layer deposition technique. Above all, for both strategies, the main issue is the protection of the back side of the glass support during the etching of the BOX. A solution is the deposition of a protective layer before the bonding but this solution has not been tested yet.

4.3 / SECOND FABRICATION DESIGN: SILICON BASED TECHNOL-OGY

4.3.1 / FLOW CHART CONSTRUCTION AND ANALYSIS OF RISK

The integration of the glass support on the silicon actuated platform is difficult. To ensure the success of fabrication of the vertical microscanner, a second microscanner design has been proposed. Here, the flow chart of this simplified design, which is only based on silicon, is presented in Fig 4.23. The fabrication starts with the creation of the comb fingers based on the two steps DRIE explained before. Silicon dioxide is used as a first mask and photoresist as the second (step a-c). Silicon dioxide was not a possibility when glass was used because it is grown thermally at a temperature above the melting temperature of glass. In the absence of metal mask, the SPTS DRIE can be used to reduce the risks due to the Alcatel machine. In the same DRIE steps, the suspensions of the micromirrors are formed in the device layer (step d-e). The wafer is then oxidized (step f) to protect the front side during the back side etching. The structure is released by the back side by DRIE of the handle layer and HF vapour etching of the BOX (step g). Finally the micromirrors and the contact pads are deposited through a shadow mask by sputtering (step h).
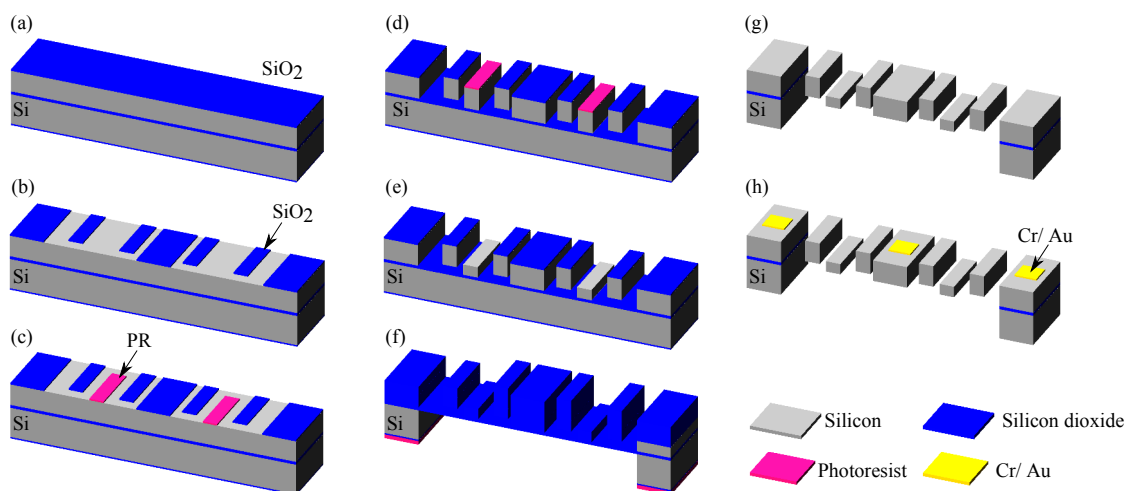
Figure 4.23: Flow chart of the fabrication process: (a) oxydation of SOI wafer (800 nm), (b) photolithography and ICP DRIE for structuration of SiO_2 layer (Mask 1), c) photolithography of S1828 photoresist layer (Mask 2), d) first DRIE, e) removal of Mask 2 and Second DRIE, f) oxidation of the wafer (200 nm) to protect front side during back side release followed by back side DRIE with thick photoresist mask, g) vapour HF etching of SiO_2 layers and BOX, h) deposition of Cr/Au (10 nm/150 nm) by sputtering though physical mask.

This flow chart is much shorter which reduces the total risk factor (37). Moreover, the risk analysis shows that there are less critical steps and that they have a low risk factor

(Tab. 4.4). Indeed, the maximum risk factor is 8 which is much lower compared to the integration strategies flow charts which maximum risk factor is 25. Then, with this flow chart, there is no step that might jeopardize the success of the fabrication.

Table 4.4: Risk analysis of the "spider" flow chart. The risk factor is illustrated by a blue bar which length is proportional to the risk factor. The total risk factor is equal to 37. BS and FS stands respectively for back and front side.

Step	Description of step	Description of the risk	Probability	Impact	Risk factor
1	Oxidation of the wafer 500 nm		1	1	1
2	Photolitho 1/Mask 1		1	1	1
3	SiO2 Etch DRIE	Silicon dioxide residues	2	4	8
4	Photolitho 2/Mask 2	Bad alignment with Mask 1	2	4	8
5	DRIE 1		1	1	1
6	Stripping of Mask 2		1	1	1
7	DRIE 2	Over etching of the comb finger	2	1	2
8	Oxidation of the wafer 210 nm		1	1	1
9	Photolitho 4/Mask 4 (BS)		1	1	1
10	DRIE 3 SiO2 (BS)		1	1	1
11	DRIE 4 Si (BS)		1	1	1
12	Vapor HF of BOX		1	1	1
13	Cleaning of wafer by plasmas O2		1	1	1
14	Alignment with shadow mask	Bad alignment between wafer due to movements	2	4	8
15	Deposition of Ti/Au		1	1	1
	Total risk factor				37

4.3.2/ FABRICATION RESULTS

The technology of vertical scanner is based on double-side processing of SOI wafer using DRIE method. The first stage of the scanner fabrication, i.e. structuration of device layer, depends directly on the fabrication method of asymmetric comb fingers. It is realized by a two steps DRIE process (Fig. 4.23). First, two mask layers, one in a silicon dioxide (t = 0.8 μm) and the other in a photoresist (t = 2.5 μm), are formed on the device layer in two subsequent photolithography procedures (Fig. 4.23, steps (a)). The alignment precision achieved was $\pm$ 0.75 μm. These mask patterns, corresponding to the two different sets of the facing fingers through the device layer (t_{dl} = 40 μm), are used in the first DRIE process to etch all comb fingers down to the BOX layer. Simultaneously, other micromechanical structures, i.e. the springs, the platform and the mirrors, are also realized. After stripping the resist mask, one set of comb fingers is still protected by SiO_2 mask, whereas the other is exposed to the etching plasma during the second DRIE process. In consequence, the thickness of unprotected fingers is reduced by half ($\frac{1}{2}t_{dl}$ = 20 μm), which creates a vertical asymmetry between the facing comb fingers. This second DRIE process has been optimized to prevent the notching effect due to the BOX. The actual gap between finger was measured to be 4 μm, instead of the targeted 5 μm, because of an overestimated under-etching (250 nm instead of the estimated 500 nm) during masks creation and silicon etching. Finally, an important drawback of this step is linked to its "maskless" character. Realization of classic Bosch process leads in this case to the creation of thin silicon "walls" at the edges of the processed fingers (Fig. 4.24). This phenomena has already been observed in [131] where a passivation layer was deposited before RIE etching step. One of the possible explanation is that during this second DRIE step, the teflon-like polymer that is deposited on the finger side-walls, has finally no more silicon support and become a mask during the following etching cycle by falling down on the structure. Another explanation would be a micromasking effect, related to high selectivity of silicon etching in SPTS system towards polymer ($S = 150$) and oxide ($S = 250$) masks as well as the deformation of local electric field due to sharp edges of fingers. In [131], solutions were suggested but not tested. Here, the proposed solution relies on increased time of SF$_6$ etching cycle of Bosch procedure in order to systematically under-etch the remaining thin silicon wall.

The second stage of the scanner fabrication deals with the release of the structure. This part is always very sensitive when it comes to active structure. Here, the back side of the device, i.e. the handle layer (t_{hl} = 500 μm), must be completely etched to allow light transmission through the platform, around the micromirrors. This etching step is realized through a 15 μm thick AZ9260 resist mask deposited on the SiO_2 layer. Note that
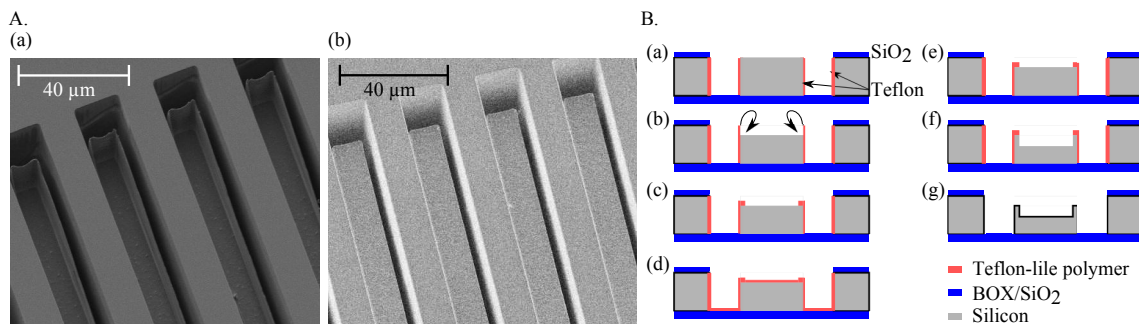
Figure 4.24: SEM image of fabricated comb fingers. A) SEM images : (a) Creation of silicon "wall" during second DRIE where there is no masking layer (Fig. 4.23 step e)) (b) Improved DRIE process to limit silicon "wall" creation. B) Schematic of the formation of silicon walls during DRIE process : (a) Deposition of teflon everywhere and isotropic etching of the teflon on horizontal surfaces, (b) Silicon etching , with formation of free teflon walls, (c) Falling of teflon walls on the silicon, d) Deposition of teflon, (e) Isotropic etching of teflon on horizontal surfaces, some teflon is left, (f) Silicon etching with teflon residue on horizontal surfaces creating silicon walls, (g) Cleaning of the wafer.

SiO_2 etching step should be preferably done with successive short etching times to limit an elevation of the temperature that leads to difficulties in removing the resist. Moreover, it has been found that some cracks appear in the BOX when it is reached by the etching plasma. The consequence is the penetration of the etching plasma through the BOX layer and then the partial etching of the device layer, destroying the structure like with the testing of the first flow chart (Figure 4.25). Therefore, a thin thermal silicon dioxide layer ($t = 150\ nm$) is thermally grown to protect the front side during the back-side etching. Finally, the release of the platform is done by etching of the silicon dioxide layers in vapour HF (Fig. 4.23, step (f)). In order to ensure the best possible quality of micromirror surface as well as contact pads, the deposition of the metal layer is performed as a last step. For the fabrication of micromirrors, the sputtering of Cr/Au layer (10 nm/150 nm) is realized through a physical mask, aligned thanks to bonding tools (Fig. 4.26). For this purpose, both the microscanner and physical wafers are aligned directly in a EVG bonding tool using EVG620 mask alignment system, and then brought into contact in EVG501 wafer bonder. The alignment is maintained in the sputtering machine thanks to an adhesive teflon tape. The physical mask has been designed in order to minimize the tolerance sensitivity. Note that in the final fabricated wafers, the adhesion layer in chromium has been replaced by titanium which has two advantages; it diffuses less in gold when high temperatures are reached which is important to resist to anodic bonding, and chromium based material will soon be forbidden in industry.
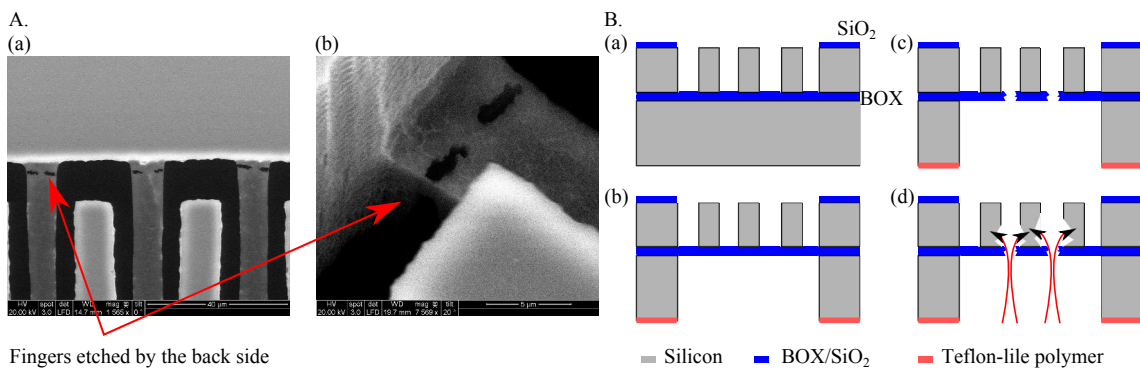
Figure 4.25: SEM image after back side DRIE. A : SEM images (a) Comb fingers that are partially etched from the back side, (b) Zoom on one finger. B : Schematic of the etching of comb fingers by the back side through BOX cracks : (a) Comb fingers SOI wafer, (b) Back side DRIE etching down to the BOX, (c) Creation of cracks in the BOX, (d) Penetration of etching plasma through the BOX from the back side to the front side of the wafer resulting in comb fingers destruction.
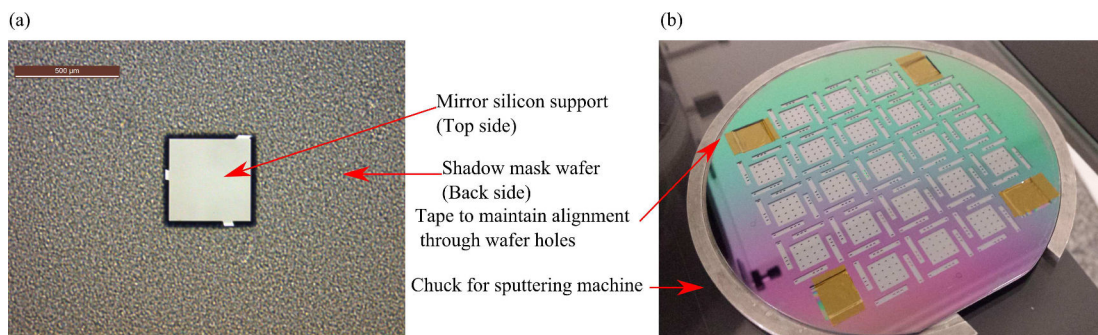
Figure 4.26: Deposition of Cr/Au layer on micromirrors and pads using shadow mask wafer: (a) image of the shadow wafer aligned with the SOI wafer showing the mirror silicon support, (b) a global view of the aligned wafers (top : shadow mask, bottom : SOI wafer) ready for the mirror sputtering.

Two strategies of fabrication were implemented: the first to enable the separation of individual chips from the wafer and thus facilitate the characterization (Fig. 4.27) and the second for the future wafer-level integration within the Mirau micro-interferometer (Fig. 4.28). With the first design, individual chips were separated using UV tape to maintain them while manually cutting small silicon bridges and sucking up the dust using vacuum system (Fig. 4.27). Finally, short exposure of tape to UV light allows gentle releasing the chips. One wafer with this "chip" design was fabricated without optimization and a yield of 71% was obtained. For the second design, three wafers were fabricated to test the vertical integration of the microscanner with the glass microlenses wafer and the beam splitter. The yield of fabrication of these wafers was 100% (Fig. 4.28 (a)).
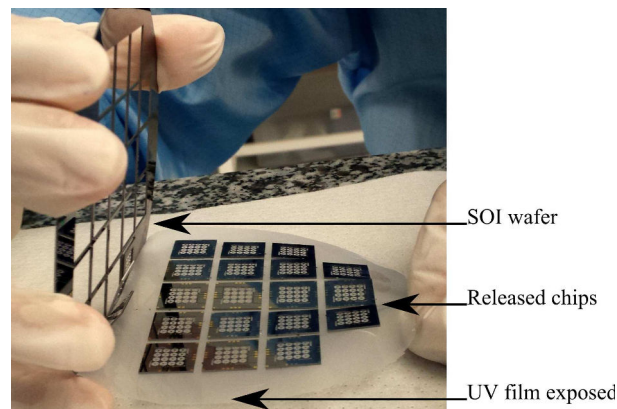
Figure 4.27: Design 1: Individual chips separated from the wafer for characterization.
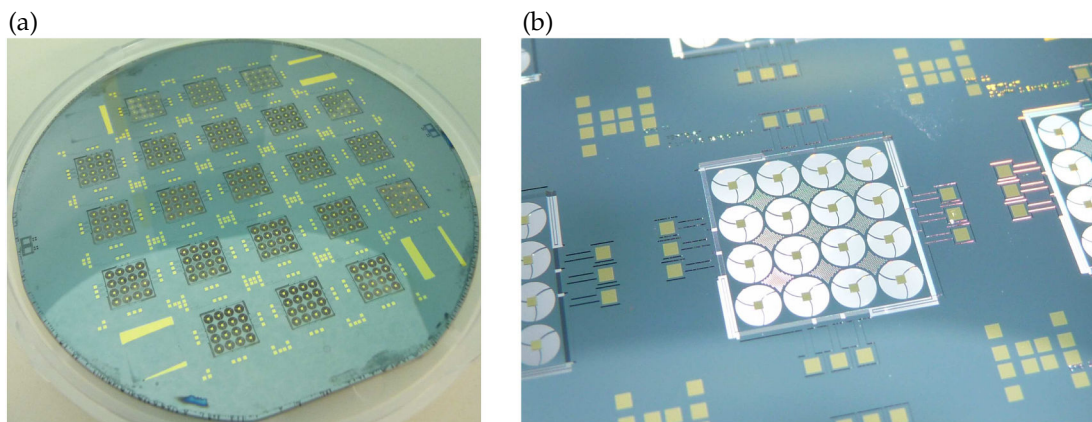
Figure 4.28: Design 2: Released microscanner that are kept at wafer level for future vertical wafer-level integration: (a) Photograph of the wafer, (b) Zoom on one structure.

4.4/ PERSPECTIVES

The success of the silicon based strategy gives an insight on adapting the flow chart for the glass integration strategy. Indeed, the use of thermal oxidation of the wafer to protect the front side is an effective solution to protect the front side before the back side etching. The thermal oxidation cannot be realized if the glass support is already on the wafer because the temperature used for oxidation would lead to the destruction of the glass. Then, the glass must be integrated after the oxidation. In this case, the complete etching of glass would also etch the thermal oxide. A new solution is proposed and the corresponding flow chart is shown in Fig. 4.29. The idea is to etch the glass after the back side etching which is possible without releasing the structure as the glass can be used as a mechanical support layer. The first steps are identical to the "spider strategy' and consists in the fabrication of the comb structures and the mechanical parts in the device layer followed by the oxidation of the wafer(step (a-e)). Then, the glass is protected

by deposition of parylene combined with photolithography and dry etching in the areas facing the silicon cavities (step (f)). This layer will serve as a mask during the last HF vapour releasing step (step (n)). In step (g), the glass wafer is anodically bonded to the SOI wafer. In a next step, lapping and polishing are performed to obtain the 25 μm thick layer of glass. At this stage, it is easy to realize the back side DRIE, with a resist mask realized by photolithography, because the front side of the wafer is flat (step (j)). Then, the use of a support wafer and oil, that can potentially contaminates the wafer, is not needed. Finally, the glass surface is protected with the mask developed for HF etching of glass (Cr/Au/Cr/Au/SPR) and etched in 49% HF in order that a thin layer is remaining to prevent the release of the structure (step (l)). As a last step, the double metal layer mask is removed and replaced by a layer of parylene to protect the glass from the HF vapour etching that follows and which removes both the remaining thin layer of glass, the BOX and the thermal oxide (step (n)). The protective layers in parylene, on the front side and the back side of the glass disks, are removed by oxygen and argon plasma. The very last step consists in depositing the micromirrors and the contact pads through the shadow mask (step (o)). This flow chart has been analysed in terms of risks and a total risk factor of 80 has been obtained. This total risk factor is much lower than the two other flow chart concerning the integration of the glass support. Therefore, this new solution is very promising.
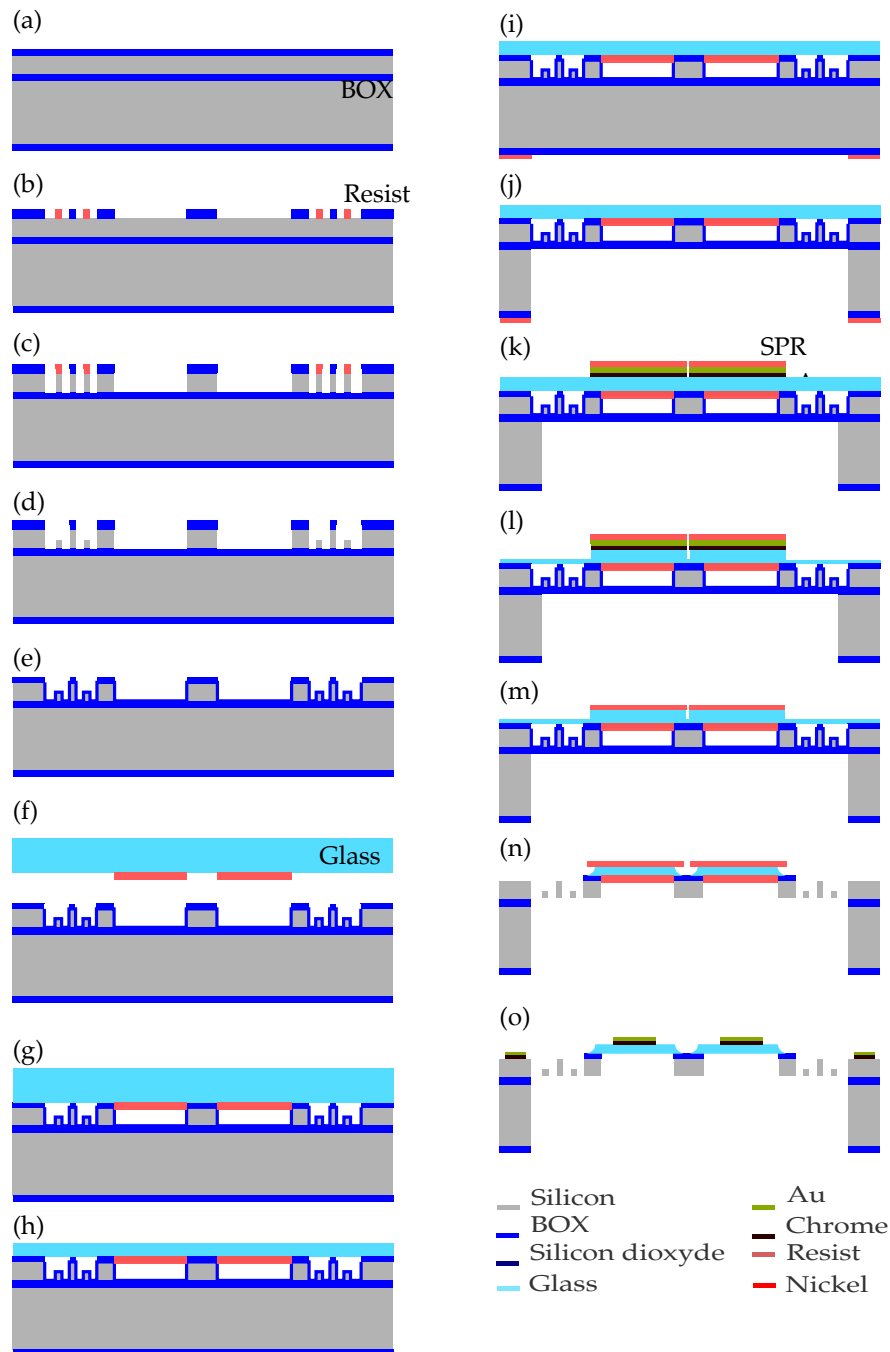
Figure 4.29: Flow chart of a new technology in perspectives: (a) oxidation of SOI wafer (800 nm), (b) photolithography and ICP DRIE for structuration of SiO$_2$ layer (Mask 1), c) photolithography of S1828 photoresist layer (Mask 2), d) first DRIE, e) removal of Mask 2 and Second DRIE, f) oxidation of the wafer (200 nm) to protect front side during back side release followed by back side DRIE with thick photoresist mask, (g) sputtering of aluminium on the glass wafer, (g) anodic bonding, (h) lapping an polishing, (i) back side photolithography, (j) DRIE of the handle layer, (k) sputtering of Cr/Au/Cr/Au/SPR 220 mask on glass, (l) 49% HF wet etching of glass, (m) removal of Cr/Au/Cr/Au/SPR 220 mask and deposition of photoresist on the glass, (n) vapour HF etching of the silicon oxides, (o) removal of the protecting layers and sputtering of Cr/Au (10 nm/150 nm) by sputtering though physical mask.

4.5/ CONCLUSION

In this chapter, standard microfabrication processes as well as the cleanroom environment have been introduced to better understand the possibilities of microfabrication. A method to analyse the risk linked to the succession of different technological steps is proposed and applied to our proposed technologies. Consequently, three different technological flow charts have been presented. Associated with each technological flow chart, a risk analysis has been performed to identify the critical steps of the flow chart. Two out of the three flow chart aims to integrate a glass disk to support micromirrors onto the silicon actuated platform. The first strategy, based on the combination of spray coating and projection photolithography, has been successfully implemented up to the releasing step and gives a new suitable solution for high topology surface glass integration. The alignment precision obtained is submicrometric. The second strategy based on a Cr/Au layer used for both thermocompression and protection of the BOX during HF etching of the glass has not been successful and would need further optimisation to be used. However, for these two technologies, the releasing step is critical and must be optimized to limit the deterioration of the optical quality of the glass support. Finally a third flow chart, targeting the fabrication of a silicon based design microscanner for which the micromirrors are suspended, has been successively tested and is a good compromise for optically transmissive structure. The critical steps, such as the protection of the device layer during the back side release etching and the deposition of the micromirror, have been overcome and solutions are given to reduce the risks. For example, to protect the front side during the back side release etching, the device layer is firstly thermally oxidized and the quality of micromirrors is insured by depositing the metal layers through a shadow mask as a last step of the process. It is also important to highlight the fact that the process developed is highly stable and reproducible. Finally, a new strategy of fabrication for the integration of the glass disks, using the advantages of the silicon based strategy flow chart, is proposed as a perspective. The risk analysis of this last flow chart is much lower (80) than the two first flow chart proposed (176 and 125). In the next chapter, the fabricated devices are characterized.

5

CHARACTERISATION OF VERTICAL MICROSCANNER AND ITS INTEGRATION IN THE MIRAU MICRO-INTERFEROMETER

To characterize a microcomponent with characterisation instruments which are adapted for the macroworld, it is necessary to create an interface to connect them. First, an interface between the microdevice and the macro-instruments used for the characterisation must be implemented to either power the device or simply be able to handle it in an "unclean" environment without damaging it. Hence, the interface starts with the realisation of an adequate packaging (printed circuit board (PCB) design, protective packaging,...). In this chapter, the packaging of the microsystem, at the chip level, is discussed and then the characterisation of the device in terms of optical quality, actuation and sensing is described. The principle of each measurement and of the instruments of characterisation are explained prior to the results presentation. The characterisation results are analysed and compared to the design, the simulation and the fabrication expectations. Then, the integration of the vertical microscanner into the Mirau interferometer is discussed and, finally, the vertical microscanner is characterized again to evaluate the performances deterioration consecutive to the assembly.

5.1 / Packaging of the vertical microscanner

5.1.1 / Design of Printed Circuit Boards

Our microscanner includes an electro-mechanical actuation system. Then, electrical power must be applied to drive the actuators whereas the sensing must be connected to a capacitive read-out circuit. Each fabricated chip is wired to a first PCB, referred to as the MOEMS PCB. The latter is connected through board-to-board vertical pin through-hole technology (THT) connectors to another PCB, referred to as Mother PCB, which integrates the bulky SMA (SubMiniature Version A) connectors. A coaxial cable (SMA to BNC, Bayonet Neill-Concelman) is used to connect the Mother PCB to an external controller. The advantage of using two PCBs is to keep the Mother PCB fixed in the setup while the MOEMS PCBs are exchangeable so that different chips can be easily characterized (Fig. 5.1).
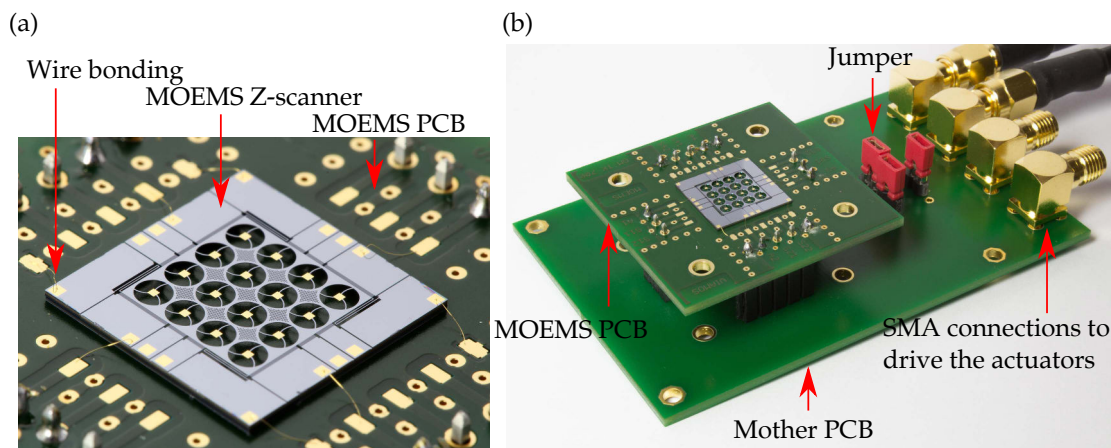
Figure 5.1: Images of the connected microscanner chips: (a) MOEMS PCB, (b) MOEMS PCB connected onto the Mother PCB.

The chips are first fixed with glue on the MOEMS PCB to enable the wire bonding between the chip and the PCB. The contact pads, present on the chips, are designed as squares whose dimensions are 750 μm x 750 μm (Fig. 5.1 (a)). Wire bonding is realized with thin gold wires (25 μm in diameter) that are wedge bonded on the contact pads of the device and ball bonded on the contact pads of the PCB. Wedge bonding is mainly based on ultrasonic power and force, whereas ball bonding is based on the creation of a small gold ball by heating the end of the wire with a high voltage. The end of the wire is lowered to the surface and the combination of heat, pressure and ultrasonic energy enables the bonding. The parameters used for the ball bonding are given in Tab. 5.1.

Table 5.1: Parameter used for the wire bonding of the chip to the PCB.

	Ball bonding	Wedge bonding
Ultrasonic power (mW)	200	250
Time (ms)	250	250
Force (mN)	400	400
Temperature (°C)	120	120

Then, standard macro soldering is realized to connect the vertical pin connector on the MOEMS PCB. In parallel, the Mother PCB is fabricated to allow the driving of the actuator. The four actuation signals are separated but jumpers can be positioned to apply the same signal to all the actuators (Fig. 5.1 (b)).

5.1.2/ DESIGN OF A PROTECTING CAP WITH TRANSPARENT WINDOW

The electrostatic actuator is based on comb fingers that are separated by a small gap (5 μm). Moreover, the vertical microscanner includes an array of micromirrors. Then, the microsystem is very sensitive to any contamination, including dusts that can deteriorate the surface quality of the micromirror but also block the actuator. Therefore, an aluminium protecting cap has been designed and fabricated. The cap is simply screwed onto the PCB and a transparent windows is glued on top of the cap to allow optical measurements (Fig. 5.2).

Figure 5.2: Protecting cap in aluminium with a transparent window on the top to allow optical characterisation.

5.2 / CHARACTERISATION OF THE OPTICAL QUALITY OF THE SURFACES

5.2.1 / MEASUREMENT PRINCIPLE

An optical surface can be characterized in terms of roughness and deformation, i.e deviation from the planar shape. Both parameters are a variation in height of the surface but roughness represents the high spatial frequency variations whereas the deformation, or the waviness, corresponds to the lower spatial frequency variations. The surface roughness, referred to as R_a, is defined by:

$$R_a = \frac{1}{n} \sum_{i=1}^{n} \mid y_i \mid \tag{5.1}$$

where y_i are the vertical deviations of the surface profile from the mean height.

The vertical deviations taken into account are the ones whose period is smaller than the defined cut-off wavelength.

White light interferometry is used to measure the surface profile and retrieve the vertical deviations. White light interferometry is a type of low coherence interferometry using a white light source. As explained in Sec. 1.2.1.1, the reference mirror moves in time domain and constructive interferences are detected when the optical path difference between the two arms of the interferometer is smaller than the coherence length. Thus, it is possible to reconstruct the topography of the surface.

In this thesis, the MEMS Analyzer (MSA-500), from Polytec, is used. This commercial equipment includes several modules, one of which is a white light profilometer. This system uses a Mirau objective to create the interference pattern. The reference mirror is fixed and the objective is moved thanks to a piezoelectric stage to change the optical path length of the measurement arm. The movement of the piezoelectric stage has a minimum step height of 85 nm.

5.2.2 / MEASUREMENT RESULTS

The "projection photolithography" strategy has enabled the integration of a glass support for the micromirrors onto the silicon platform. Both the glass support and the micromirrors fulfil optical functions, i.e. light transmission and beam reflection, respectively. Therefore, the surface quality of the glass disks is studied to evaluate its planarity and its roughness. The topography measurements of glass disks, using the white light

interferometry module of the MEMS Analyzer (MSA-500, Polytec), are done before and after the release of the actuated platform (Fig. 5.3 (d)). The results show that, before the release, the backside surface of the membrane is slightly convex with an amplitude of 13.4 μm. After the membrane release, front and back sides of the glass disks are asymmetrically convex with amplitude of 7.5 μm and 4.1 μm, respectively (Fig. 5.3). These results might indicate a small underpressure inside the cavity below the glass disk after anodic bonding. This leads to the membrane deformation, which increases during mechanical thinning of glass. Although this deviation is small compared to the membrane diameter (0.4%), it must be taken into account in the optical design. Indeed, the glass disks plays the role of an additional lens and are responsible for a defocus. The defocus in the object arm can be easily adjusted by stitching vertically the Mirau interferometer. However, it must be compensated in the reference arm by adjusting the thickness of the spacer placed between the micromirrors and the beamsplitter. Future tests must be performed to try to understand and minimize the effect of the pressure in the cavity on the deformation of the glass support. In particular, the parameters of pressure during the anodic bonding must be tuned. Measurement of glass surface with mechanical profilometer shows that the glass roughness does not increase during the process (Ra<10 nm before and after processing of the glass).
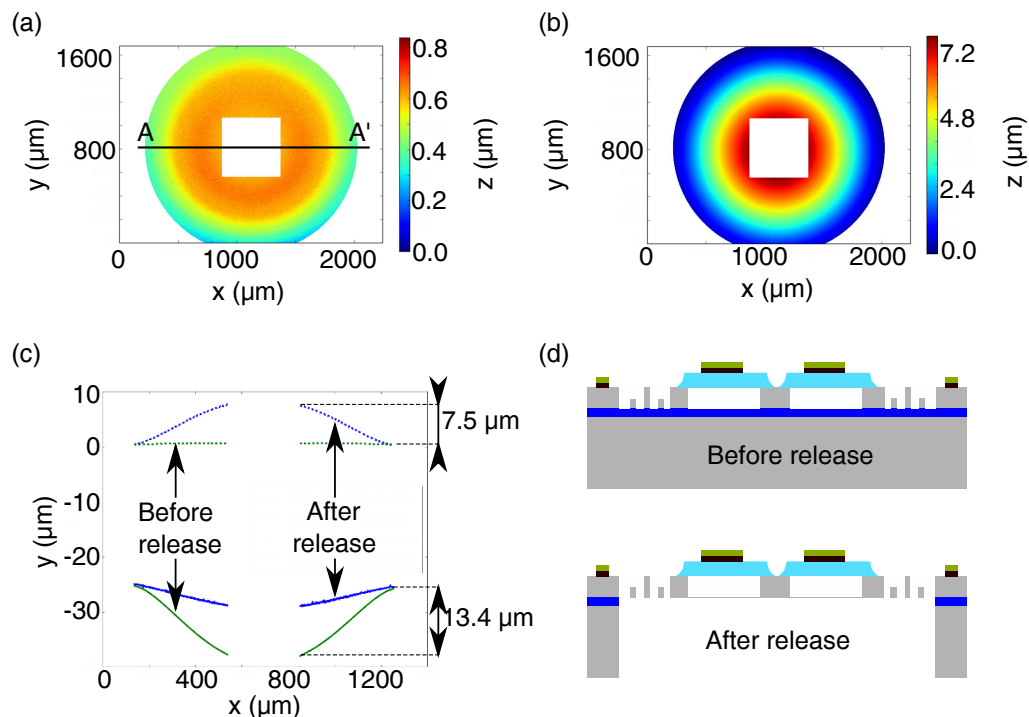
Figure 5.3: Characterisation of the glass disks surface: 2D graph of the surface topography of the glass disk front side (a) before and (b) after release, (c) topography profile along the A-A' line of the front and back side of the glass disks before and after the release and (d) shematic of the chip before and after release.

The quality of the micromirrors is characterized in terms of roughness and reflectivity of the Cr/Au layers deposited on test sample. Optical profilometer using white light interferometry is used and a surface average roughness (S_a) of 3 nm and a 1D average roughness (R_a) of 1.7 nm are measured when using a cut-off wavelength of 0.25 mm. The flatness of the micromirror is also important for the OCT application. The profile of the mirror is shown in Fig. 5.4 and a radius of curvature of 700 mm is measured by polynomial fitting of the curve. This static deformation of a single reference micromirror does not affect the optical system since its maximal deformation (52 nm) is much smaller than the axial resolution of 6 μm. Finally, a high reflectivity of 97 % is measured for different incidence angles at λ=850 nm.
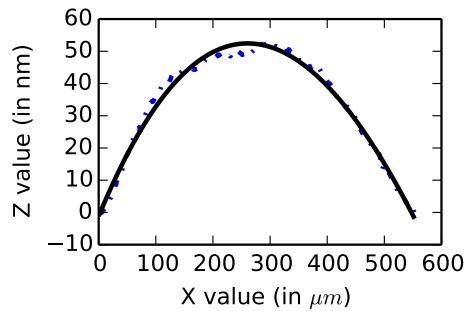
Figure 5.4: Vertical deformation of a single micromirror along its diagonal.

5.3/   CHARACTERISATION OF THE ACTUATION

5.3.1/   MEASUREMENT PRINCIPLE

The actuation function of the microsystem is first characterized based on laser Doppler vibrometry (LDV). This principle is based on the Doppler effect that is a frequency shift of the light backscattered by a surface moving in the direction of the travelling light. The frequency shift is related to the moving surface velocity according to:

$$f_D = 2 \times \frac{v}{\lambda} \tag{5.2}$$

where f_D is the Doppler frequency shift, v is the moving surface velocity and λ is the wavelength of the light.

As a result, if the frequency shift can be measured, the velocity of the moving surface can be retrieved. This type of measurement is typically useful for out-of-plane displacement. To sense the Doppler shift, a laser interferometer is used. The typical setup used for

LDV includes an acousto-optic modulator, usually a Bragg cell, in one of the arms of the interferometer (Fig. 5.5). The acousto-optic modulator shifts the light frequency (30-40 MHz). Then, the signal detected, which is the interference between the light coming from the reference and the object arm, is modulated by the Bragg cell frequency and the Doppler frequency. The light frequency, typically superior to 10^{14}, is higher than the response of the photodetector. Then, the carrier frequency of the detected signal is the Brag cell frequency and the modulation frequency of the Doppler frequency. Finally, the signal is demodulated and the velocity of the moving surface is derived.
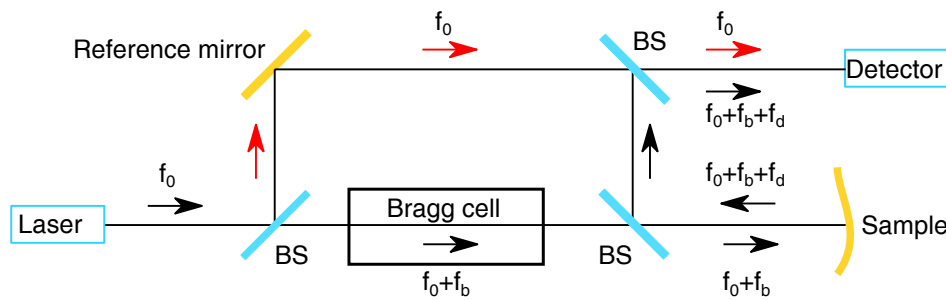
Figure 5.5: Laser interferometer for laser Doppler vibrometry. BS: Beam splitter, f_0, f_b, f_d are the the frequency of the laser, the shift of the Bragg cell and the Doppler shift, respectively.
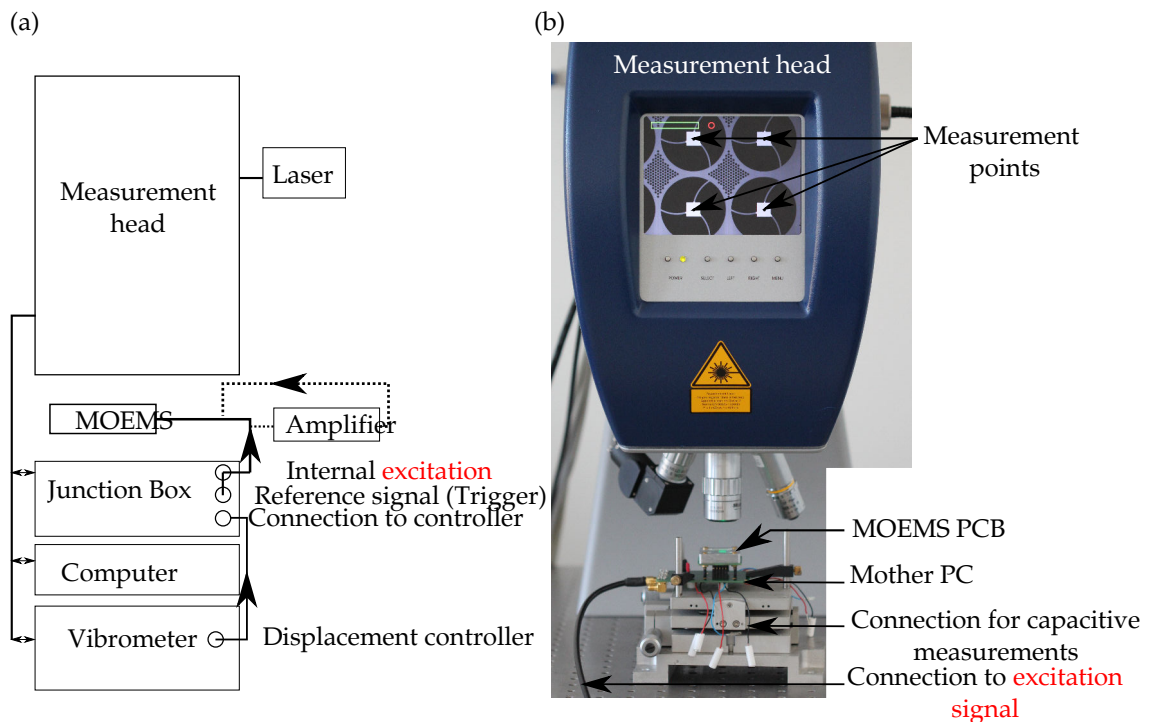
Figure 5.6: MEMS analyzer setup for the displacement characterisation: (a) Schematic of the connections, (b) Photograph of the setup.

The MEMS Anlayzer MSA-500 has a scanning laser Doppler vibrometry module that is

used for the characterisation of individual chips. The setup is shown in Fig. 5.6. Two different controllers can be used to either retrieve the velocity or the displacement information. Here, the displacement controller is used to directly obtain the displacement of the actuated platform. The function generator is provided by the Junction Box whereas an amplifier is used to amplify the signal if needed. Finally, for time domain measurements, the excitation signal is used as a Trigger (Fig. 5.6 (a)). Quasi-static and dynamic measurements are realized. Note that adequate filters are used to stabilize the signal during the measurements.

Finally, the vertical microscanner chip characterized here has the spring parameters given in Tab. 5.2.

Symbol	Description	Value
w	Beam width	30 μm
t	Beam thickness	40 μm
$l_1 = a$	Beam 1 length	90 μm
$l_2 = b$	Beam 2 length	2610 μm
$l_3 = a$	Beam 3 length	90 μm
$l_4 = c$	Beam 4 length	2820 μm
k_z	Vertical stiffness (Calculated)	6.8 N/m
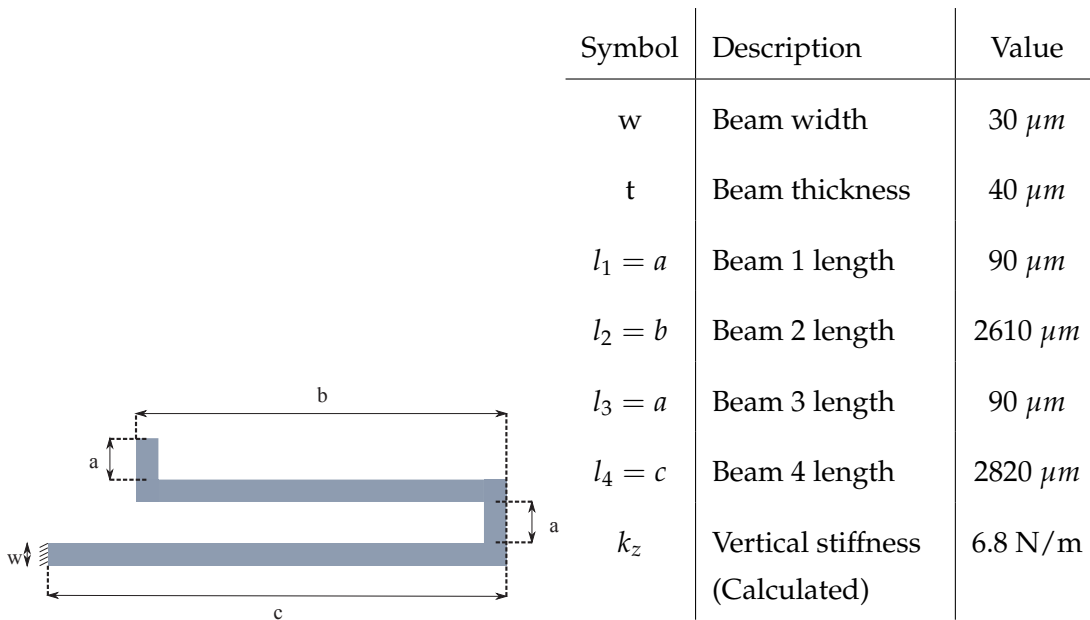
Figure 5.7: Asymmetric springs dimensions.

Table 5.2: Design parameter of the asymmetric springs.

5.3.2/   DYNAMIC MEASUREMENT

Dynamic measurements consist in analysing the spectral response of the system. The excitation signal used is a sinusoidal chirp, with equivalent energy for each swept frequency, applied to all actuators. The resonant frequency and the quality factor can also be calculated based on the free oscillation response of the system. In this case, the system is simply excited by a voltage step. The first resonant frequency, which corresponds to a piston mode, is measured at 543 Hz based on the spectral response. Using the free oscillation method, a resonant frequency of 554 Hz is measured. However, this measure is less precise because the time between two measurements is set to 1.10^{-4} s. The quality factor of the system is 50 based on calculations with the spectral response (-3 dB) and the

free-oscillations characterisation (exponential decrease, damping=0.01) (Fig. 5.8 and 5.9, respectively). For such a large platform, this quality factor is relatively high compared with the 3x3 array of individually driven micromirrors presented in [136], for which the quality factor of each micromirror is 41. The measured resonant frequency corresponds to a vertical spring stiffness of 7.2 N/m, which is coherent with the simulations, if we take into account $mass = 2.46.10^{-6} \ kg$. Finally in Fig. 5.8, the peak corresponding to the second and third modes cannot be seen because it is too small when symmetric actuation is provided by driving of the four actuators. Then, the torsional modes will not interfere when piston mode vertical actuation at the resonant frequency is performed.
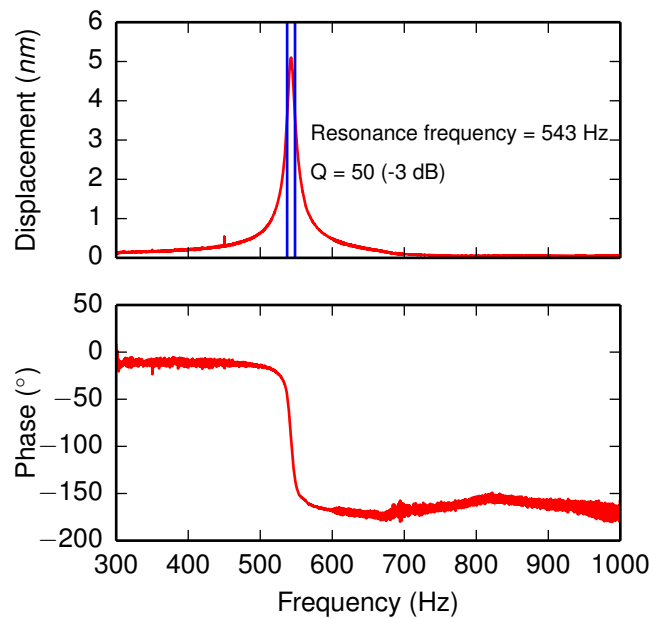
Figure 5.8: Spectral response analysis of the device: (a) displacement, (b) phase.
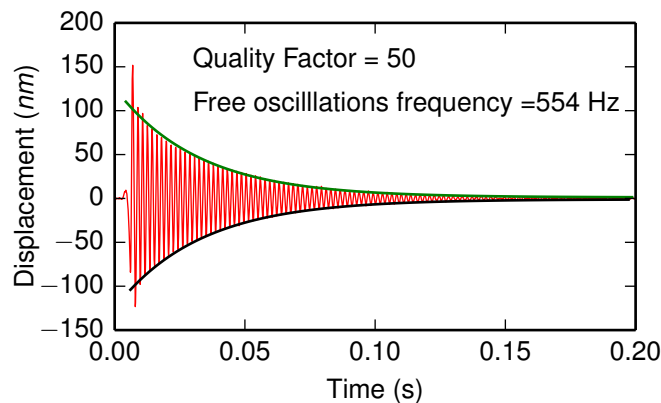
Figure 5.9: Free oscillation in response to a square signal (0-5 V).

For the phase shifting, it is important to know the displacement amplitude of all the

micromirrors. The dynamic displacement of the platform at resonant frequency was investigated at different points of the platform, i.e. at the center position of the four micromirrors (see Fig. 5.6,(b)) forming a quarter of the platform (Fig. 5.10). The actuation voltage is set to $V_d = 1 + 1 \times sin(w_0 t)$ V for all the actuators. Note that the electrostatic force is proportional to the square of the voltage. Then, with the applied voltage V_d, the obtained force is a sum of a DC force, a force proportional to $sin(w_0 t)$ and a force proportional to $sin(2w_0 t + \frac{\pi}{2})$. Here, the quality factor Q of the first mode (w_0) is much higher than the one of the harmonic ($2w_0$) so that the signal in $sin(2w_0 t + \frac{\pi}{2})$ is negligible and the electrostatic force is synchronous with the driving voltage. However, by definition, the displacement of the platform and the actuation force have a phase difference of $\frac{\pi}{2}$ at the resonance. The measured displacement, much larger than the targeted one, shows the great potential of this microscanner for medical imaging applications. Indeed, actuation performed with small voltages is particularly important since the device is in contact with the patient. The displacement of the micromirror in the middle of the platform is 70 nm higher than the one next to the spring because of the vertical mechanical deformation of the suspended platform. Sasaki *et al.* studied the impact of the error of the displacement amplitude on the sinusoidal modulation in interferometric applications [22]. This displacement of 70 nm is within the tolerances presented in the article.
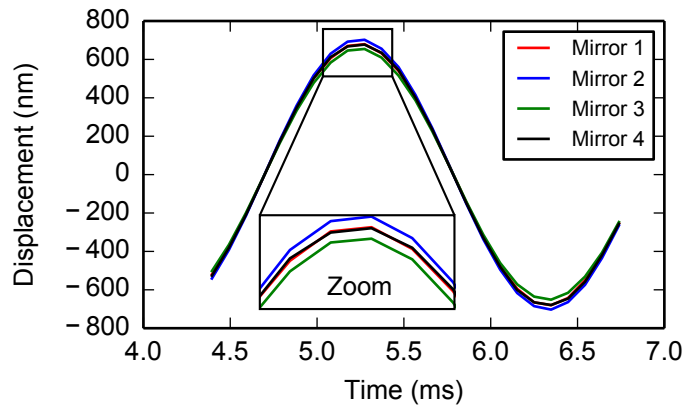
Figure 5.10: Vertical displacement of the micromirror under dynamic driving voltage: (a) Mirror 1, (b) Mirror 2, (c) Mirror 3, (d) Mirror 4.

5.3.3/ STATIC MEASUREMENT

Quasi-static measurements were done by applying simultaneously a square signal to the 4 actuators at very low frequency (10 Hz) so that Doppler vibrometry could be used. The static displacement is retrieved as a function of the peak-to-peak amplitude

of the excitation square signal, between 0 V and the actuation voltage (0 - 40 V). Due to a limitation of the internal excitation signal of the MSA-500, an external amplifier is connected between the signal excitation output and the MOEMS (Fig. 5.6 (a)). The static displacement is plotted as a function of the applied voltage for voltages between 0 and 40 V in Fig. 5.11. The amplitude of vertical displacement is measured between 0 and approximately 2.8 μm, slightly depending on the gap fingers. Though, the measured static displacement curve is closer to the simulated curve obtained for 4 μm gap between moving fingers. This result is consistent with the SEM measurements of the fabricated structures that show a finger gap close to 4 μm.
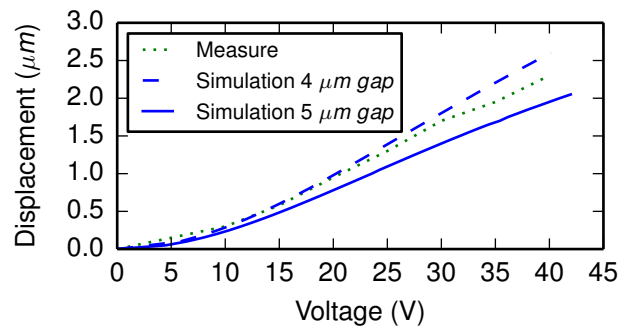
Figure 5.11: Static displacement as a function of applied voltage, measured by Laser Doppler vibrometry.

5.4/ CHARACTERISATION OF THE SENSING

5.4.1/ MEASUREMENT PRINCIPLE

The sensing function is based on a change in capacitance between the comb fingers when the platform is moving. Moreover, a differential capacitance design is implemented in our vertical microscanner. The change in capacitance to measure is very small (few fF) so that the design of an adequate read-out circuit is not trivial. Different solutions are possible. In [133, 134], two different commercially available capacitive read-out circuits are used. In this thesis, we have chosen to work with an impedance analyzer. The impedance analyzer used is the Agilent HP 4194A, whose measurement method is the auto balancing bridge. The capacitance range of this equipment is from 10 fF to 0.1F with a maximum resolution of 0.1 fF. However, capacitance measurement is always very sensitive to parasitic capacitance due to the testing circuit and the environment, then special care is taken in the elaboration of the measurement setup. Figure 5.12 shows the setup realized for the measurement of the capacitance. The device under test is directly connected to the

"low" and "high" inputs of the impedance analyzer. The equipment enables to choose different parameters such as the integration time of the measure, the number of measurement for averaging, the frequency range (100 Hz - 40 MHz) and the oscillation level of the impedance analyzer. Moreover, the continuous polarization of the micro-actuators is obtained by an association of batteries in series ($5 \times 9V$) to limit noise effects during the measurements. The polarization is increased manually step by step between 9 and 45 V.
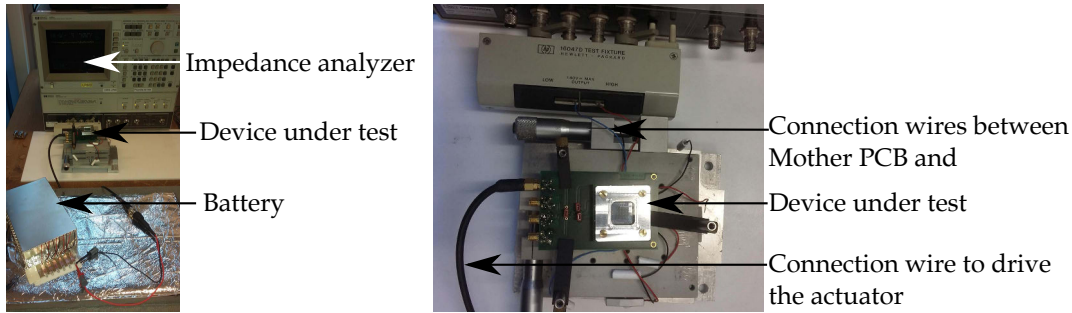
Figure 5.12: Setup for the characterisation of the capacitance sensing.

5.4.2/ MEASUREMENT RESULTS

The impedance analyser is used to measure successively the capacitance of the different sensors as a function of the applied voltage. A high nominal capacitance was measured around 50 pF with a precision of ± 5 fF. This can be explained by parasitic capacitances. However, here, the variations of the capacitances are interesting to retrieve the vertical displacement. Therefore this nominal capacitance, i.e. the capacitance measured at $V_{actuation} = 0\ V$, which is stable during the measurement time, has been subtracted from the measured values. The measures were taken at $f = 1.1$ MHz, and eight measures were used to obtain each average value. The oscillation level of the impedance analyser was set to 0.5 V. The capacitances were measured as a function of the applied voltage and then retrieved as a function of the vertical displacement using the results presented in Fig. 5.11. The differential capacitance of each sensor, i.e. the capacitance of Configuration 1 minus the capacitance of Configuration 2, is plotted as a function of the vertical displacement in Fig. 5.13. The sensitivities for each sensors correspond to the simulated sensitivity for a gap of 4 μm, i.e. 27 $fF/\mu m$. One of the four sensors has a higher sensitivity of 36 $fF/\mu m$. One explanation is that the platform is slightly tilted toward the side corresponding to this sensor creating an offset. Also a local structural defect can explain such a small increase of the sensitivity.

The results of the characterisation of the vertical microscanner are summarized in Tab. 5.3 and have been published in [156].
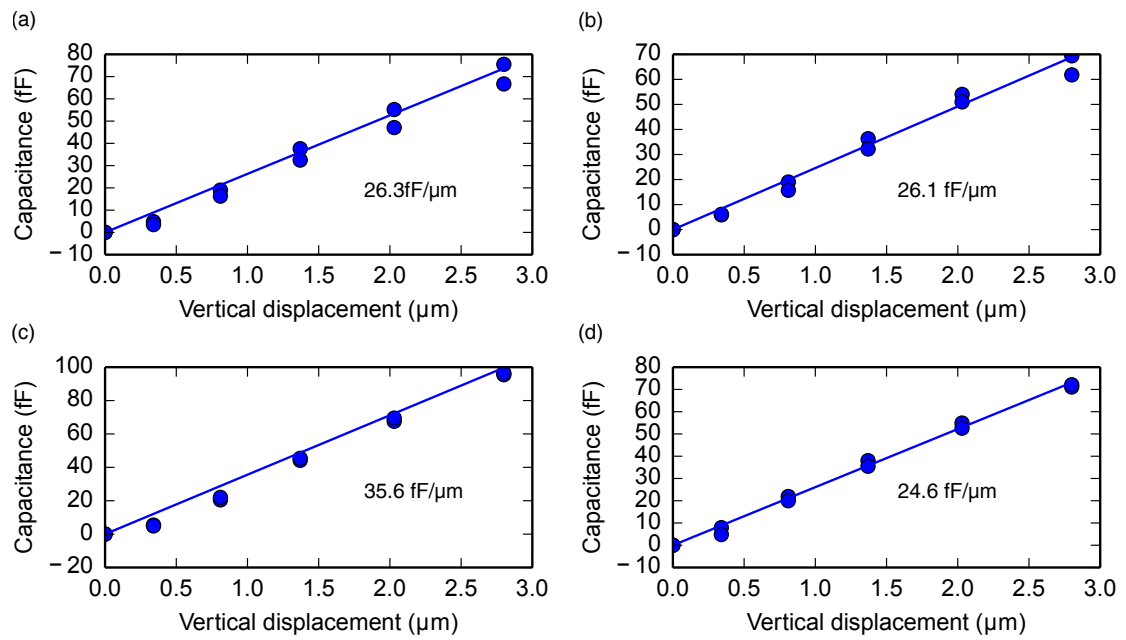
Figure 5.13: Measured differential capacitance for each sensor of a chip and their corresponding sensitivity: (a) Sensor 1, (b) Sensor 2, (c) Sensor 3, (d) Sensor 4.

Table 5.3: Parameter of the vertical microscanner after characterisation.

Components	Parameters	Values
Micromirror	Roughness	3 nm
	Reflectivity	97 %
	Radius of curvature	700 mm
Glass support	Roughness	< 10 nm
	Vertical deformation (Top/Bottom)	7.5 μm/4.1 μm
Microscanner	Resonant frequency	543 Hz
	Quality factor	50
	Sensing sensitivity	~ 27 fF/μm

5.5/   Integration of the microscanner in Mirau interferometer

5.5.1/   Discussion on technological processes adapted for vertical integration

The array-type Mirau micro-interferometer is composed of a matrix of lenses doublets, the vertical microscanner, a planar beam splitter and spacers, as shown in Fig. 5.14. The fabrication of these components at wafer level enables their collective vertical integration. Moreover, the choice of the technological techniques involved in the fabrication of the microcomponents as well as in the integration processes must be discussed in parallel to take into account the limitations of all the steps. This section aims to introduce the technology used to fabricate these components, using microfabrication techniques, as well as the integration steps.
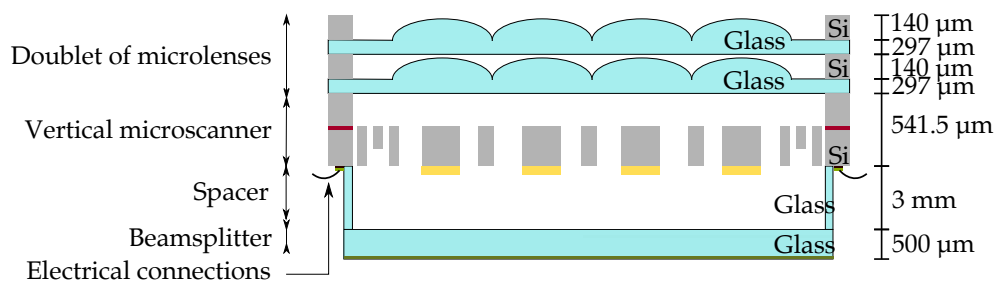
Figure 5.14: Simplified cross-section view of the Mirau micro-interferomter stack.

First, the choice of the bonding technology must guarantee optimal optical properties after the bonding. More specifically, the surface quality of the optical microcomponents (beam splitter, micromirrors and microlenses) and the alignment precision are key parameters for the optical system. Here, most of the interfaces are composed of silicon and glass which makes possible the fabrication of optical components but which is also compatible with anodic bonding. The latter technology has another advantage which is that it does not require an intermediate layer. Typically, anodic bonding is realized by heating the substrates between 300°C and 500°C and applying a voltage between 400 V and 1500 V for a time up to 90 min. Note that, to make the glass compatible with silicon, its thermal expansion coefficient must be close to the one of the silicon, so that they can be bonded together by anodic bonding. In this optic, glasses highly concentrated in alkali ions (borosilicate glasses) are used. For example, Borofloat glass has a thermal expansion coefficient close to silicon which leads to a reduction of the stress after bonding. The microfabrication technologies, used to fabricate the microcomponents to be integrated,

must be compatible with these conditions.

The miniaturization of **lenses** has been developed since decades leading to well mastered techniques for wafer-level integration. Lenses techniques can be separated in two categories: contactless fabrication or fabrication thanks to a mold that is pre-fabricated. Contactless fabrication techniques are usually based on the reflow of a pillar, whereas the second technique is based on the prefabrication of a mold that is used to create a microlens. Based on these methods, polymer microlenses have been widely developed. Polymer reflow and its numerous evolutions are now widely used due to its relative easiness to be fabricated[157, 158, 159]. The drawback of polymer lenses is that they cannot tolerate harsh environment such as high temperature and are more eager to be degraded with time, whereas glass microlenses are more stable. In our case, these considerations are really important since the microlenses are meant to be integrated by anodic bonding. Therefore, a focus is done on microlenses, made of borosilicate glass, that have a great potential for MOEMS, i.e. the monolithic integration of both optical and mechanical part on a same substrate. A "molding" technique based on the reflow of glass in silicon molds have been developed by Albero *et al.* [160]. This technique is of great interest because it can achieve higher numerical aperture with large diameter than contactless reflow techniques; however, the surface quality highly depends on the surface quality of the molds. The advantage of the contactless method is the good surface quality of the obtained microlenses but this method limits the achievable numerical aperture and diameter. In Fig. 5.15, three different techniques for the fabrication of microlenses are presented. Firstly, in 2003, Merz. *et al.* published a technique based on the reflow of glass in silicon cavities. This technology is interesting because the lenses obtained are monolithically integrated onto the silicon wafer. This technique has been also used for the realisation of a Mirau interferometer for MEMS metrology [161]. In 2008, two groups, Yang Chen *et al.* and Sung-Kil Lee *et al.*, published another solution to fabricate glass reflowed microlens [162, 163]. Both strategies of fabrication are based on the construction of glass pillars, followed by a reflow at high temperature. In those articles, the structuration of glass is done by compression molding or wet etching. Moreover, Sung-Kil Lee *et al.* proposed a solution already compatible with the monolithic integration on silicon. The reflow based technique also enables the fabrication of ball micro-lenses as it has been shown by Dong-Whan Lee *et al.*. These works have recently conducted to a publication demonstrating the monolithic integration of glass microlenses on a silicon scanner using two successive thermal reflows, first to structure the glass as pillars and then to form the microlens [153]. Here, the fabrication technology of the dense array of mm-size lenses is based on the reflow of glass in a cavity in which the pressure is lower than the atmospheric pressure [140]. The pressure difference creates a vertical force which, combined with the reflow of the glass, leads to the creation of a lens once the concave side is polished. When used for

a dense matrix of lenses, a specific design is used to enable an homogeneous deformation of the glass across the dense matrix. Moreover, the silicon wafer, used during the fabrication of the microlenses, is kept partially to serve as a spacer and an aperture stop in the final device.
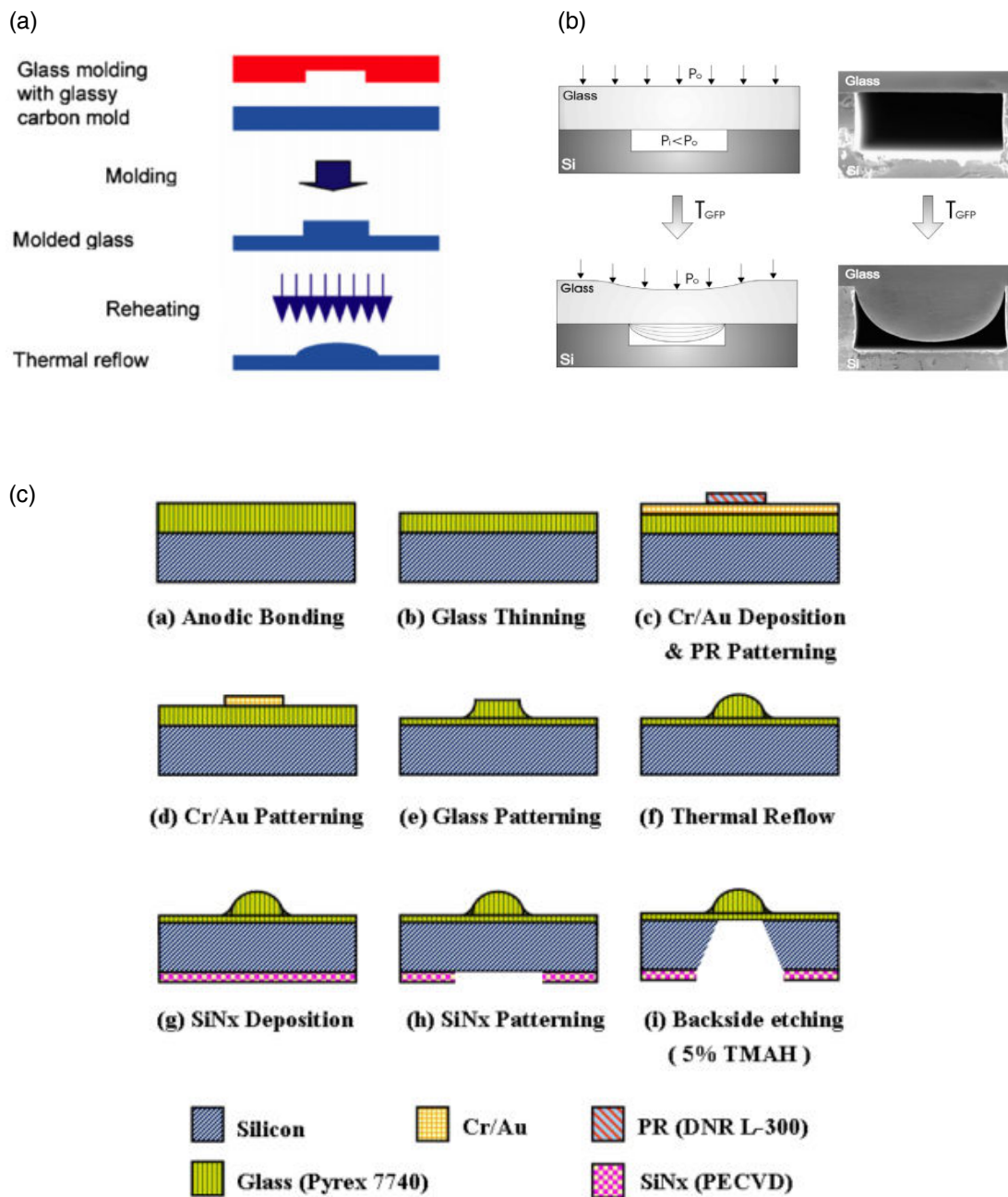
Figure 5.15: Three different process of fabrication of glass micro-lens: (a)[162], (b)[164], (c)[163]

The **beam splitter** can be realized with successive depositions of thin dielectric layers on a glass substrate. Thus, different types of beam splitters can be microfabricated such as polarizing beam splitter [165, 166] but also more advanced beam splitters based on the

deposition of dielectric layer on already micromachined 45 ° beam splitters [167]. For example, the Mirau beam splitter can be made of mono- or multi-layers of silicon oxynitride (SiOxNy) deposited by PECVD a glass substrate [64]. The multi-layer structure is a stack of alternate high and low-index thin films, all one-quarter-wavelength thick (often referred as Bragg reflectors). By doing so, reflected beams encounter a phase shift at the different boundaries (only from high to low-index layers) as well as during propagation so that they can interfere constructively or destructively. Since the absorption in such layers is negligible, we consider that no energy is lost. Depending on the beam-splitting ratio required, the number of layers, as well as their refractive indices, have to be adjusted. Here, the beam splitter has been realized by sputtering a TiO_2 layer, which is sufficient to reach 70/30 splitting ratio under normal incidence. Moreover, using only one layer ensures a higher tolerance with respect to wavelengths and angle of incidence.

Finally, the spacers, which are 3 mm thick, are made of glass because it can be structured by ultrasonic drilling and it is also compatible with anodic bonding.
In conclusion, all the components of the micro-interferometer can be microfabricated and hence they can be adapted in the wafer-level integration strategy.

5.5.2/ COMPATIBILITY BETWEEN THE MICROSCANNER AND THE BONDING TECHNIQUES

The vertical integration of the doublet of lenses, the vertical microscanner, a spacer and the beam splitter has been performed at the Fraunhofer Institute ENAS in Chemnitz. The different components to integrate are shown in Fig. 5.16.
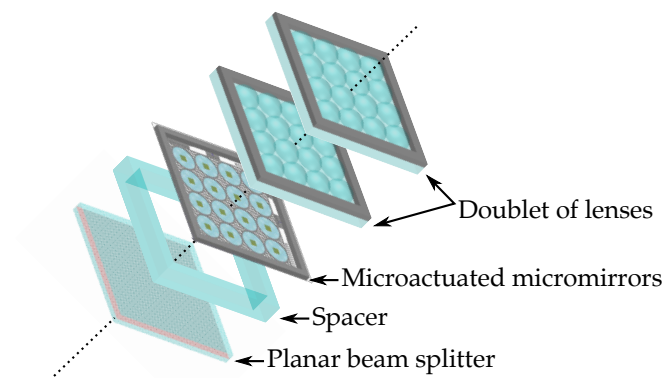
Figure 5.16: 3D schematic representation of the micro-optical components involved in the vertical integration of the Mirau interferometer.

The bonding temperature is kept lower than 400°C to be compatible with the metallic

and dielectric layers of the micromirrors and beam splitter. Note that the spacer must integrate openings to access the contact pads of the vertical microscanner from the bottom of the stack. Finally, the last interface, between the beam splitter and the spacer, is a glass-glass interface that is anodically bonded by depositing an aluminium layer on the spacer surface. For the Mirau micro-interferometer, the most fragile and sensitive component is the vertical microscanner. To further decrease influences of temperature and bonding process on the microscanner, the beam splitter and the spacer are first bonded at 500 V. The stack obtained is bonded to the microscanner in a second step at 600 V and 320°C. Finally, the doublet of microlenses is integrated to the stack. This sequence of bonding has been tested several times. The first tests with blank wafers have shown good results. However, for one of the final demonstrator with functional wafers, the last step of bonding has required a voltage up to 1000 V to realize the anodic bonding. The result is shown in Fig. 5.17.
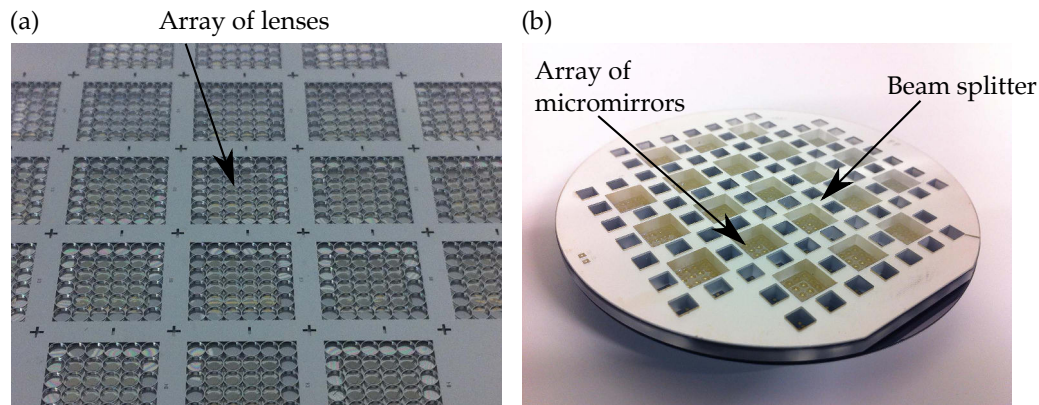
Figure 5.17: Fabricated Mirau stack at wafer level: (a) top side with the array of lenses, (b) bottom side with the array of micromirrors visible through the beam splitter and the openings of the spacer.

A first conclusion is that the electric field, generated by the potential difference applied between the bonding interface, does not lead to a displacement of the microscanner high enough to break the silicon springs. A second conclusion is that the quality of the micromirror is sometimes deteriorated. This phenomena has been observed inconsistently so that it is hard to explain what is the source of the degradation. Our hypothesis is that both the temperature but also the "age" of the layer have an impact. The temperature can cause a migration of titanium or chromium ion in the gold leading to a degradation of the mirror quality. Moreover, it seems that some gold layers deteriorates with time. Further tests must be conducted to understand this phenomena and stabilize the gold layer.

5.5.3/ COMPATIBILITY BETWEEN THE MICROSCANNER AND THE DICING TECH-
NIQUES

Once the optically functionalized wafers are integrated, the vertical stack must be diced
into chips. There are several dicing techniques that are used for wafer dicing. The most
common technique is saw dicing. Conventionally, MEMS are first diced and then released
to protect them from the sawing process. This is called die level packaging. Alterna-
tively, wafer level packaging consists in, first, releasing the MEMS, then, realizing wafer
bonding to protect the released MEMS, and finally, performing dicing. In this sense, our
MOEMS microscanner has been packaged at wafer level and is encapsulated inside the
stack. However, saw dicing is not possible in our case because the encapsulation is not
fully hermetic while this method uses cooling water. Indeed, the isolation trenches, re-
alized to isolate the micro-actuators and the microsensors between each others, creates
a path for the dicing cooling solution to penetrate inside the Mirau stack. Figure 5.18
shows a 3D view of the vertical microscanner around the dicing line. The schematic illus-
trates the possible access for the dicing solution to the Mirau cavity through the isolation
trenches (shown in green). These isolation trenches are outside the Mirau cavity because
the contact pads must be outside the cavity to connect the vertical microscanner with the
outside world. The trenches are 40 μm deep and 100 μm large. The tests have shown that
the dicing solution does penetrate inside the cavity. In this condition, the electrostatic
vertical microscanner cannot be used.
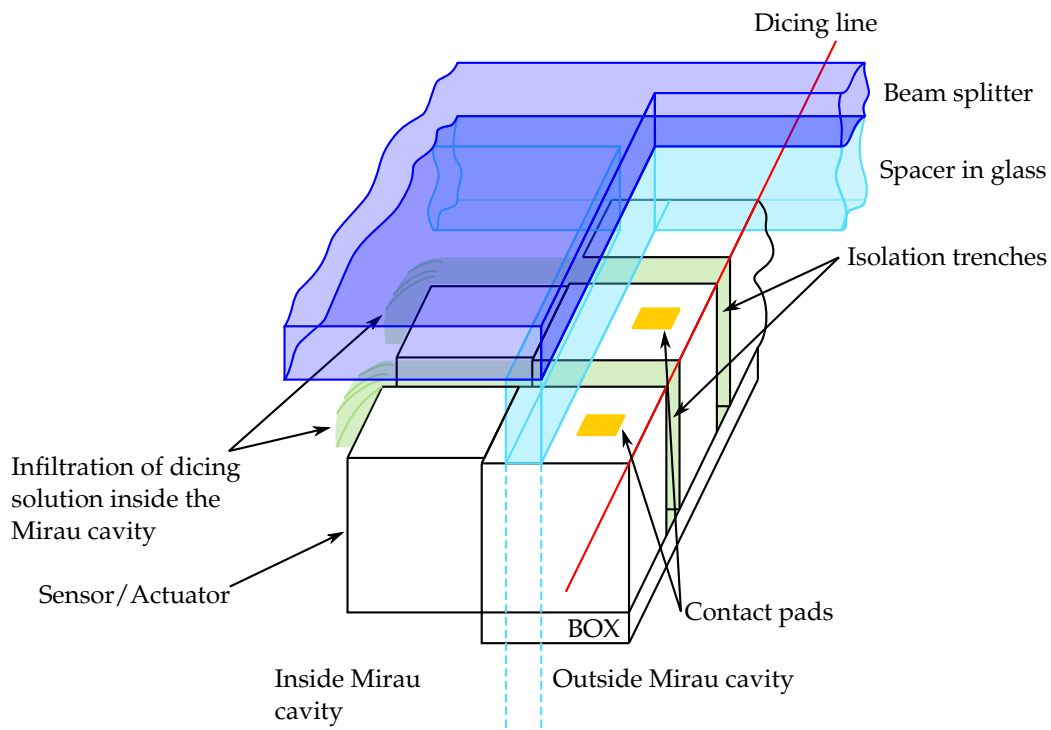
Figure 5.18: 3D view of the vertical microscanner isolation trench with the glass spacer bonded to it and the opening windows to access the contact pads.

To overcome this issue, fabrication can be changed to ensure embedded insulation trenches, keeping the top surface flat. For example, the trenches can be filled partly or completely with silicon dioxide or polymer. Though, these solutions are not trivial and further discussion is necessary to integrate such a process in the flow charts. However, two other solutions are possible to deal with these trenches. The first possibility is to seal the isolation trenches and the second one is to use a dry dicing technique. To fill in the trenches, a polymer such as a photoresist can be dispensed at the interface glass-silicon. However, the dispensing is critical because the polymer must not cover the contact pads that are close to the dispensing site (Fig. 5.18). Figure 5.19 shows several tests of glue dispensing using different wires. The images show that the result is satisfactory, but it is manual and thus time consuming and not compatible with industrial production.

(a)

(b)

(c)

Fiber 2

Fiber 3

Wire

Fiber 3

Syringe

Penetration of water during dicing

Stiction of comb finger due to water in the Mirau chamber
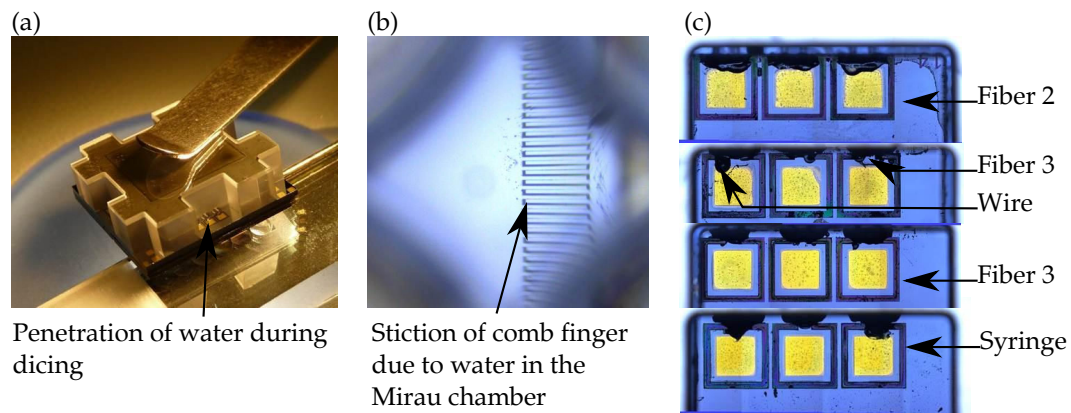
Figure 5.19: Test for glue dispensing to fill the trenches: (a) Image of the Mirau stack to show the entrance of water in the Mirau chamber, (b) Stiction of the comb fingers due to water in the Mirau chamber and (c) results of the glue dispensing using a wire (200 μm), three different optical fibers and a syringe (400 μm).

Consequently, the second solution, based on laser cutting, has been tested. Laser cutting is widely used for wafer dicing and has the advantage that it does not require a cooling liquid. In our case, this method is still a challenge because of the high thickness of the Mirau micro-interferometer stack (4.9 mm) and its multi-material property. Taking into account these two parameters, the laser dicing has been performed in two steps at the Fraunhofer Institute (Chemnitz); a first step to partially dice the stack from the top (2 mm deep) and a second step from the top to complete the dicing (3 mm deep). The laser cut has a maximum vertical shift of 600 μm between the top and the bottom of the cut which is acceptable as there is a space of 1.8 mm between two chips. The chip is protected from generated dust with thermal tapes at the top and the bottom of the stack. Still, a lot of dust sticks onto the gold pads. To clean the gold pads, wet cleaning is required (Fig. 5.20).

(a)

(b)
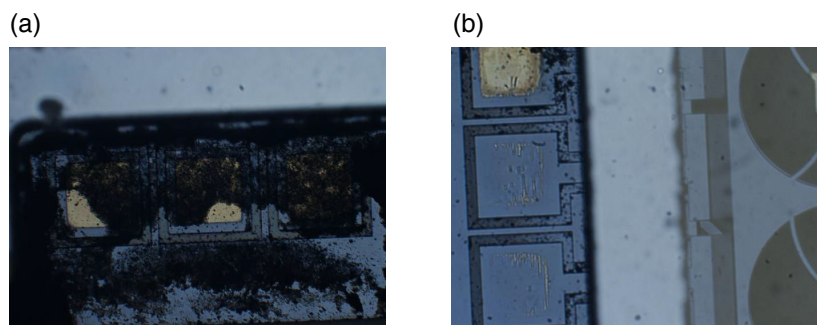
Figure 5.20: Gold contact pad (a) after laser cutting and (b) after cotton swab (some are scratched away).

Finally, the first solution consisting in filling the trenches with polymer is adopted to enable wet cleaning of the gold pads. The polymer is hardened by thermal treatment at 150 °C during 30 minutes. In the future, the dispensing of polymer could be used before saw dicing to facilitate the dicing that is time consuming (70 min/chip) and expensive when

laser cutting is used. Finally, the chips are cleaned and prepared for flip-chip bonding. Flip chip bonding is realized between the Mirau contact pads and a PCB with gold stud bumps. A specialized tool is used to handle the Mirau micro-interferometer and maintain the PCB. However, the gold stud bumps on the PCB have not all the same height (variation up to 30 μm) which does not allow a good connection. Therefore, silver-filled epoxy (EPO-TEK H20E), which is specifically designed for chip bonding, is used. Moreover, to insure a good mounting of the Mirau micro-interferometer on the PCB , low-stress die attach adhesive (DELOMONOPOX) is applied at the corners of the chip and cured at 100 °C during 30 minutes. Figure 5.21 shows photographies of the Mirau micro-interferometer mounted on the PCB.
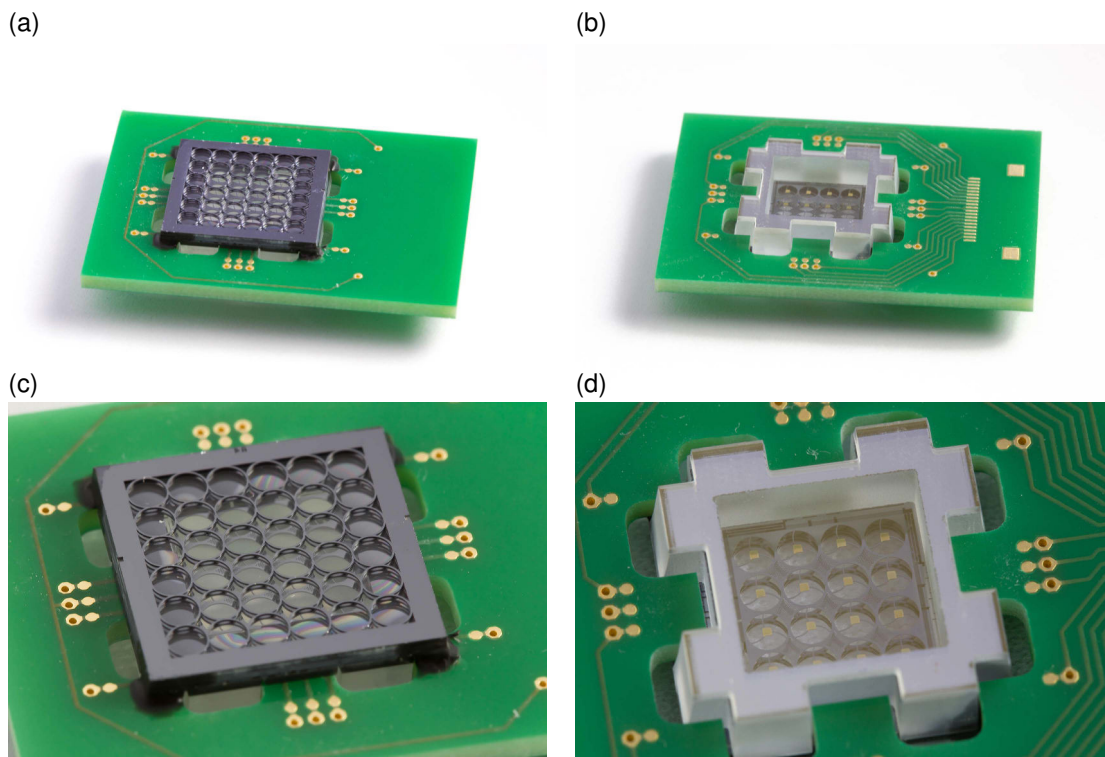
Figure 5.21: Photography of the Mirau micro-interferometer vertical integrated and mounted on PCB: top view (a) general view and (c) zoom, and bottom view (b) general , (c), (d) .

The influence of the packaging steps on the micromirror quality have been monitored along the different processes. Figure 5.22 shows a microscope image of four micromirrors after anodic bonding, after laser cutting and after flip-chip bonding. A significant degradation of the micromirror quality with the apparition of black dots is observed. As explained before, this degradation is not consistent for all the micromirrors and further tests must be conducted to clearly understand the phenomena. Though, the degradation appears clearly on Fig. 5.23 which shows topography of the surface before and after the assembly processes. Moreover, in terms of vertical deformation, the micromirrors

have not changed compared to the measurements realized before the vertical assembly. The measurements are realized with the white light profilometry of the MEMS Analyzer. Note that, to visualize the mirror surface, white light interferometry is realized through the Mirau beam splitter. In order to compensate the beam splitter thickness, present in the sample arm of the interferometer, a glass plate of the same thickness is introduced in the reference arm of the Mirau objective of the MEMS Analyzer (Polytec).
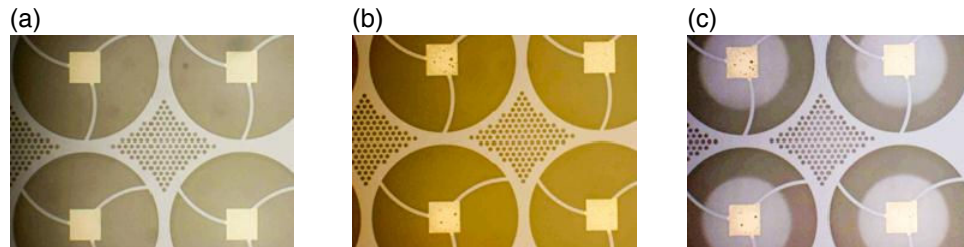
Figure 5.22: Microscope image of four micromirrors: (a) after anodic bonding, (b) after laser cutting and (c) after flip-chip bonding.
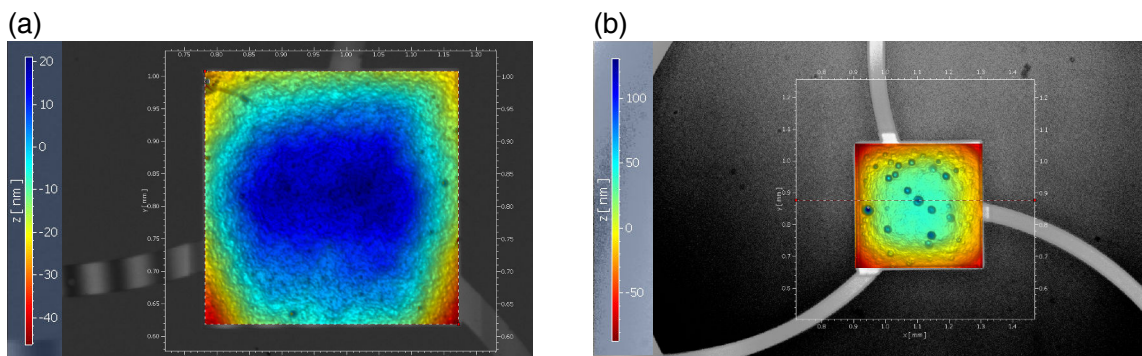
Figure 5.23: Mirror topography measurements based on white light interferometry: (a) before and (b) after assembly procedure.

5.5.4/ MICRO-SCANNER AS PHASE-SHIFTER IN THE OCT SYSTEM

Once vertically integrated at wafer level, diced and mounted on a PCB, the vertical microscanner is characterized a second time. Note that the microscanners, designed for the integration at wafer level, are not the same than the one designed for the characterisation at the chip level. Then, it is difficult to directly compare the results of the characterisation. First, the spectral response of the vertical microsacnner is analysed (Fig. 5.24). The first resonance frequency is measured at 485 Hz. Theoretically, the microscanner characterized here has a first resonant frequency of 513 Hz. The difference between the characterisation value and the simulation one is not negligible, though it is in the tolerances of our system. The difference is not trivial to explain but some hypothesis can be made. First, the frequency depends on the mass and the spring stiffness that are highly

sensitive to the device layer thickness. The tolerance on the device layer can be responsible for a variation of $\pm$ 10 Hz. Moreover, the packaging process might have an impact on the stress induced in the microstructure, resulting in a change of the resonant frequency. The second peak is much higher than the one measured before integration on other chips. However, the dynamic analysis of the microsystem is not perturbed by this second peak at 724 Hz. Indeed, using the same method presented above, the dynamic displacement under sinusoidal excitation is characterized. An amplitude of 350 nm is reached for a electric signal equal to $V = 2.5 + 1.5sin(w_0t)$. Fig. 5.25 shows the recorded displacement of the structure. This voltage will be used for the actuation of the microscanner used as a phase-shifter in the OCT system developed.
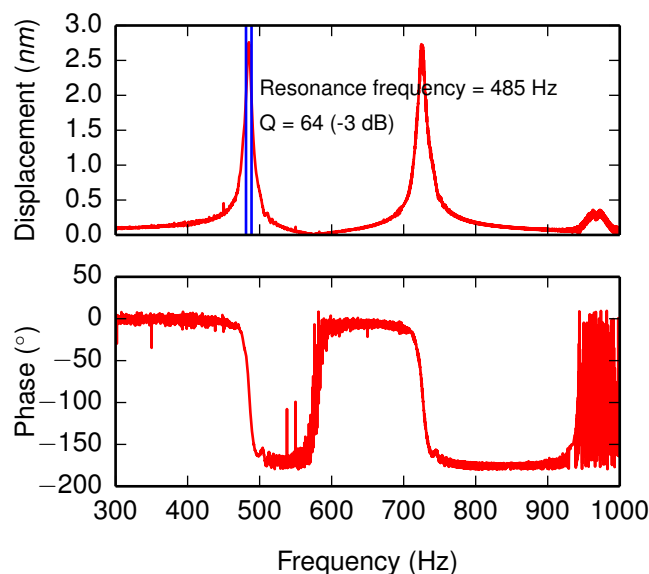
Figure 5.24: Spectral response analysis of the device after its integration into the Mirau micro-interferometer: (a) displacement, (b) phase.
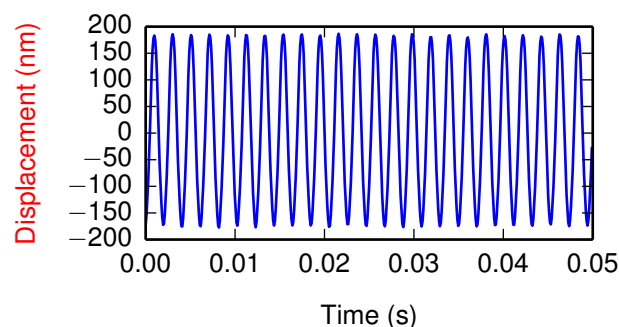
Figure 5.25: Vertical displacement of the micromirror under an excitation signal equal to $V = 2.5 + 1.5sin(w_0t)$.

5.6/ CONCLUSION

The vertical microscanner has been first characterized in term of optical quality of the micromirrors and the glass support, the actuation and the sensing. A adaptive and protective packaging has been fabricated to enable the characterisation measurements at the chip level. White light interferometry measurement have shown that the glass support is deformed after releasing of the microscanner. The glass surface deformation changes the focus length of the Mirau micro-interferometer and must be integrated in the optical design. The roughness of the optical quality (glass support and micromirrors) has also been investigated and is lower than 10 nm which is suited for imaging purposes. Then, the actuation function has been studied in dynamic and in static thanks to laser Doppler vibrometry. The resonant frequency measured is coherent with the expected one as well as the displacement range as a function of the actuation voltage. Finally, the sensing function has been characterized by measuring the change of differential capacitance of the sensor with an impedance analyzer. The results are coherent with the simulated ones. In a second part, the vertical microscanner has been successively integrated into the Mirau micro-interferometer. The vertical integration has been developed based on a sequence of anodic bonding processes. The sequence order and parameters have been adapted to optimize the integration and prevent damages of the optical microcomponents. Moreover, a method to dice the Mirau interferometer, integrated at wafer level, has been developed. In order to avoid that the dicing solution penetrates inside the Mirau cavities, a dry dicing technique has been privileged. Laser cutting has been used to dice the thick vertical stack in two steps. However, the dust created during the process contaminates the contact pads and wet cleaning has been necessary. Then, a system of polymer dispensing to fill-in the trenches, which are responsible for the entry of liquids into the cavities, has been developed. In the future, the dispensing of polymer could be used before saw dicing to facilitate the wafer dicing that is time consuming and expensive when laser cutting is used. Moreover, the micromirrors quality seems to degrade along the processes without being able to understand the phenomena that is not consistent. Then, further tests must be conducted to overcome this situation. Finally, the vertical microscanner has been characterized in terms of actuation to check if the assembly processes have an impact on its behaviour. The results show that the vertical microscanner works correctly.

CONCLUSION AND PERSPECTIVES

New biomedical imaging tools are necessary for skin imaging application. This field is lacking of non invasive imaging tools, providing in vivo images, for the diagnosis and the follow-up of skin pathologies and, in particular, skin cancers. Among the existing technologies, optical coherence tomography (OCT) provides high resolution as well as appropriate skin depth penetration. Moreover, the frame rate and the sensitivity of OCT systems have been increased with the development of new techniques called Fourier domain OCT (FD-OCT) combined with phase-shifting interferometry techniques. However, the existing commercial systems have two main drawbacks: they are bulky and expensive. As a result, these systems are only affordable for the hospitals and thus, not sufficiently used by physicians or dermatologists as an early diagnosis tool. We believe that these reasons are responsible for the limited development of such systems in dermatology, for which biopsies and histopathological studies continues to be the gold standard despite a very high number of useless acts. Consequently, our first motivation was to develop a miniaturized system in order to reduce both the cost and the size of the existing systems.

In this thesis, the development of a vertical microscanner, adapted for the implementation of phase modulation in a miniaturized full-field array-type swept-source OCT, has been presented. The swept-source OCT is a low coherence interferometry technique, in which the light wavelength is swept and the spectral interferogram is recorded. A Fourier transform of the recorded signal allows the reconstruction of the different tissue layers in depth. Then, each acquisition provides a vertical scan line. Combined to full-field OCT, each acquisition is extended to a vertical scan frame. Moreover, the array-type configuration, proposed here, further increases the field-of-view imaged at each acquisition. The vertical scanner is designed to be integrated in a Mirau microinterferometer. Its functionality is to move an array of reference micromirrors so that series of interferograms with several phase differences can be recorded. Sinusoidal phase modulation is then used to isolate the cross-correlation term from its mirrored terms, the auto-correlation terms and from the DC term, improving the sensitivity. A position sensing function is also embedded in the vertical microscanner to detect the position of the micromirrors and in particular the amplitude of displacement.

Based on the state of the art of the actuation technologies, illustrated with examples from

185

the literature reported in Chapter 2, the comb finger electrostatic principle has been chosen for the implementation of both the actuation and the sensing. The advantage is that this technology is relatively easy to fabricate (silicon based) and compatible with the specifications of displacement amplitude (~ 350 nm) and frequency (500 Hz) targeted by our system. In parallel, the Mirau interferometer configuration is chosen for its good compatibility with the multi-wafer integration technique. In particular, its vertical architecture enables the superposition of the microcomponents with wafer level bonding techniques, which insures accurate alignment. Though, this configuration also imposes an optical transparent aperture around the micromirrors to let the light travels from the objective lenses to the tissue. Therefore, the vertical microscanner, proposed in this thesis, is very specific compared to most of the micromirrors presented in the literature, which works only in reflection. According to these considerations, two designs are presented in Chapter 3; one based on a glass support for the micromirrors and one based on silicon suspensions to held the micromirrors. Simulations are conducted to evaluate the mechanical behaviour of the vertical microscanner as well as the characteristics of the electrostatic actuation and sensing. The simulations results are used to optimize the design parameters (number of comb fingers, spring parameters, mass of the actuated platform,...). The two investigated designs are shown in Fig. 5.26.
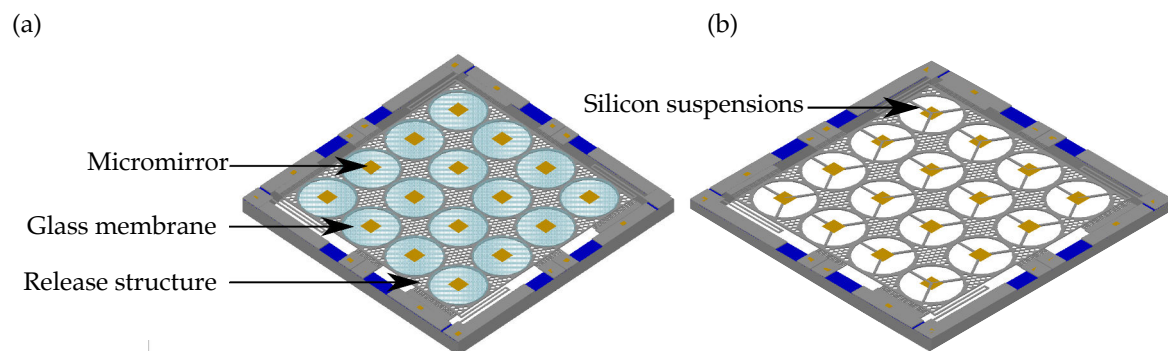
Figure 5.26: Vertical microscanner designs: (a) glass support design, (b) silicon suspensions design.

According to the design and the simulation, adapted fabrication flow charts have been proposed. The construction of the flow charts, along with the technological choices that they involved, have been detailed. In particular, an analysis of the flow charts, based on the risk analysis of each step, have been conducted to understand the main challenges of each flow chart and identify the more critical steps. Three different technologies have been investigated based on SOI wafers. The two first flow charts target the integration of the glass support on the silicon microscanner.

The first explored strategy is based on the integration of the glass support followed by a combination of spray coating and projection photolithography to pattern the high topol-

ogy surface created by the glass support. The second strategy is to first pattern and structure the silicon to create the mechanical parts and then integrate the glass support by Au/Au thermocompression. The gold layer is then used to both connect the silicon and the glass but also to protect the buried oxide (BOX) layer during the structuration of the glass realized with liquid HF. The viability of the first strategy have been successively demonstrated until the releasing step which causes a problem. Indeed, the HF vapor release attacks the glass support whose quality is then degraded. Therefore, a solution to protect the glass has been proposed but not yet tested. The second strategy has not been conclusive because the gold layer deposited did not protect efficiently the BOX as expected.

Finally, the third strategy aims at the fabrication of the vertical microscanner with suspended micromirrors. This technology is entirely based on silicon, except for the metallic micromirrors. Therefore, the silicon is first structured to create the designed structure and, once released, the micromirrors are deposited by sputtering through a shadow mask. The shadow mask is a structured silicon wafer, to create the openings corresponding to the micromirrors shape, and aligned to the SOI wafer. Two strategies of fabrication were implemented: the first to enable the separation of individual chips from the wafer and thus facilitate the characterization and the second for the future wafer-level integration within the Mirau micro-interferometer. This technology has been successively implemented and is stabilized since several runs have been processed with 100% yield. The fabricated vertical microscanners are shown in Fig. 5.27.

(a) (b)
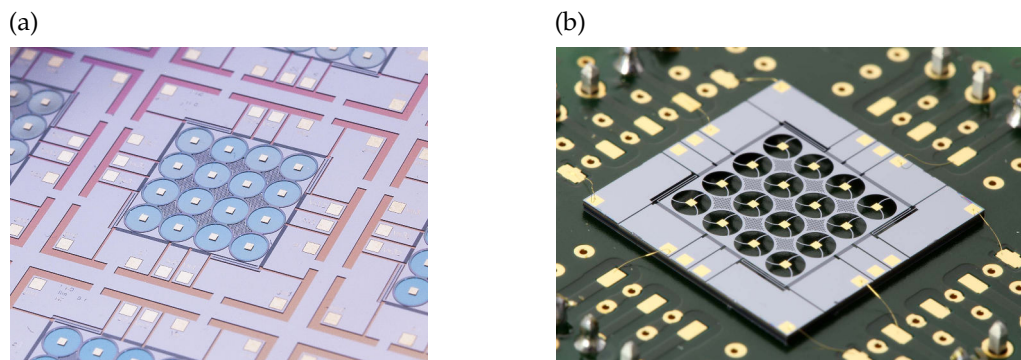
Figure 5.27: Fabricated vertical microscanner: (a) glass support design, (b) silicon suspensions design.

The fabricated device has been characterized at the chip level thanks to the development of a specific packaging. Different characterization methods have been used such as white light interferometry for the evaluation of the optical quality of the surface and laser Doppler vibrometry for the study of the displacement amplitude of the microscanner. The measured parameters (frequency, displacement amplitude, sensing sensitivity) are in good agreement with the simulated ones. Therefore, the vertical microscanner

has been integrated within the Mirau microinterferometer. Several anodic bonding steps have been realized, at Fraunhofer Institute, to integrate at wafer level, a doublet of glass lenses bonded at FEMTO-ST, the vertical microscanner, a glass spacer and a planar beam splitter. Then, the wafer stack has been diced into individual chips (Fig. 5.28).
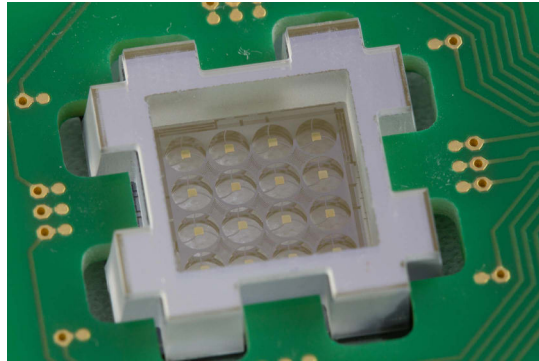
Figure 5.28: Mirau microinterferometer.

After the vertical integration, the vertical microscanner is characterized a second time to evaluate the impact of the bonding steps. The electro-mechanical behaviour of the microscanner is still similar but the optical quality of the micromirrors is degraded. The degradation phenomenon is not consistent and varies from one chip to another too much to make conclusions about the causes of this degradation.

This thesis has presented insteresting technologies for the development of a vertical microscanner, with an embedded sensing position, for phase modulation interferometry. Based on these results, some perspectives, such as an optimized flow chart whose total risk is decreased, still needs to be tested. Moreover, the protection of the glass microcomponents until the total release of the structure is an issue, for which new solutions have been proposed and should be tested. Further work also involves the development of an integrated read-out circuit to be able to use the sensing function synchronously with the actuation and to have the microscanner position in real-time. Finally, a systematic study of the surface quality of the micromirrors is necessary to understand its degradation during the bonding processes.

The technologies, developed in this thesis, have a great potential for the high level integrated optical microsystems and encourage new perspectives. First, the integration strategy of the glass disks onto the vertical microscanner can be easily applied for other types of glass microcomponents such as glass lenses or diffractive gratings. Indeed, the integration strategy demonstrated here, as well as the strategy presented in perspective, are well suited for this kind of applications. The integration of a glass microlens on a microscanner is particularly useful to laterally or axially scan a sample e.g. for a confocal

microscope. Moreover, the lateral scan can be easily adapted from the technology presented in this thesis, by creating lateral comb drives.

Finally, the European project VIAMOS has enabled the development of different technologies for OCT microsystems, which are now well mature. The Mirau micro-interferometer is being tested in terms of interferometric functionality and phase-modulation and the results will be presented in [143]. The complete OCT system is being assembled and will be tested at the university hospital of Besançon (CHRU) where clinical tests will be performed.

BIBLIOGRAPHY

[1] WANG, S. Q., RABINOVITZ, H., KOPF, A. W., AND OLIVIERO, M. **Current technologies for the in vivo diagnosis of cutaneous melanomas**. *Clin. Dermatol. 22*, 3 (May 2004), 217–222.

[2] FERLAY, J., SOERJOMATARAM, I., ERVIK, M., DIKSHIT, R., ESER, S., MATHERS, C., REBELO, M., PARKIN, D., FORMAN, D., AND BRAY, F. **F. GLOBOCAN 2012 v1.0, Cancer Incidence and Mortality Worldwide: IARC CancerBase No. 11 [Internet].Lyon, France: International Agency for Research on Cancer; 2013. Available from: http://globocan.iarc.fr, accessed on 07/04/2015.** Tech. rep., 2012.

[3] EISEMANN, N., WALDMANN, A., GELLER, A. C., WEINSTOCK, M. A., VOLKMER, B., GREINERT, R., BREITBART, E. W., AND KATALINIC, A. **Non-melanoma skin cancer incidence and impact of skin cancer screening on incidence.** *J. Invest. Dermatol. 134*, 1 (2014), 43–50.

[4] INCA. **La situation du cancer en France en 2012**. *Rapp. synthèses, INCa* (2012).

[5] NISCHAL, K. C., AND KHOPKAR, U. **Dermoscope**. *Indian J Dermatol Venereol Leprol 71*, 4 (2005), 300–303.

[6] WANG, T., QIU, J., AND MILNER, T. E. **Determination of Melanoma Lateral and Depth Margins: Potential for Treatment Planning and Five-Year Survival Rate**. *Ski. Cancer Overv.*, Table 1 (2010), 1–2.

[7] KAPSOKALYVAS, D., BRUSCINO, N., ALFIERI, D., DE GIORGI, V., CANNAROZZO, G., CICCHI, R., MASSI, D., PIMPINELLI, N., AND PAVONE, F. S. **Spectral morphological analysis of skin lesions with a polarization multispectral dermoscope.** *Opt. Express 21*, 4 (2013), 4826–40.

[8] SCHMITZ, L., REINHOLD, U., BIERHOFF, E., AND DIRSCHKA, T. **Optical coherence tomography: its role in daily dermatological practice.** *J. Dtsch. Dermatol. Ges. 11* (2013), 499–507.

[9] MACHET, L., SAMIM, M., GEORGESCO, G., AND MOURTADA, Y. **High Resolution Ultrasound Imaging of Melanocytic and Other Pigmented Lesions of the Skin**. *Ultrasound Imaging*, 1 (2011), 139–150.

[10] NWANESHIUDU, A., KUSCHAL, C., SAKAMOTO, F. H., ANDERSON, R. R., SCHWARZENBERGER, K., AND YOUNG, R. C. **Introduction to confocal microscopy.** *J. Invest. Dermatol. 132* (2012), e3.

[11] HUANG, D., SWANSON, E., LIN, C., SCHUMAN, J., STINSON, W., CHANG, W., HEE, M., FLOTTE, T., GREGORY, K., PULIAFITO, C., AND FUJIMOTO, J. G. **Optical coherence tomography**. Tech. rep., 1991.

[12] DREXLER, W., AND FUJIMOTO, J. G. **Optical Coherence Tomography: Technology and Applications**. Springer Science & Business Media, 2008.

[13] NGUYEN, V. D., AKCA, B. I., WÖRHOFF, K., DE RIDDER, R. M., POLLNAU, M., VAN LEEUWEN, T. G., AND KALKMAN, J. **Spectral domain optical coherence tomography imaging with an integrated optics spectrometer.** *Opt. Lett. 36*, 7 (2011), 1293–1295.

[14] LU, C. D., KRAUS, M. F., POTSAID, B., LIU, J. J., CHOI, W., JAYARAMAN, V., CABLE, A. E., HORNEGGER, J., DUKER, J. S., AND FUJIMOTO, J. G. **Handheld ultrahigh speed swept source optical coherence tomography instrument using a MEMS scanning mirror**. *Biomed. Opt. Express 5*, 1 (2014), 293–311.

[15] BONIN, T., FRANKE, G., HAGEN-EGGERT, M., KOCH, P., AND HÜTTMANN, G. **In vivo Fourier-domain full-field OCT of the human retina with 1.5 million A-lines/s.** *Opt. Lett. 35*, 20 (2010), 3432–3434.

[16] DUBOIS, A., VABRE, L., BOCCARA, A.-C., AND BEAUREPAIRE, E. **High-resolution full-field optical coherence tomography with a Linnik microscope.** *Appl. Opt. 41*, 4 (2002), 805–812.

[17] DUBOIS, A. **Full-Field Optical Coherence Microscopy**. In *Selected Topics in Optical Coherence Tomography*, G. Liu, Ed.

[18] SHEPPARD, C. J. R. **Depth of field in optical microscopy**. *J. Microsc. 149* (1988), 72–75.

[19] LEITGEB, R., HITZENBERGER, C., AND FERCHER, A. **Performance of fourier domain vs. time domain optical coherence tomography.** *Opt. Express 11*, 8 (2003), 889–894.

[20] CHOMA, M., SARUNIC, M., YANG, C., AND IZATT, J. **Sensitivity advantage of swept source and Fourier domain optical coherence tomography.** *Opt. Express 11*, 18 (2003), 2183–2189.

[21] KIM, D. Y., WERNER, J. S., AND ZAWADZKI, R. J. **Comparison of phase-shifting techniques for in vivo full-range, high-speed Fourier-domain optical coherence tomography.** *J. Biomed. Opt. 15*, October 2010 (2010), 056011.

[22] SASAKI, O., AND OKAZAKI, H. **Analysis of measurement accuracy in sinusoidal phase modulating interferometry.** *Appl. Opt. 25*, 18 (1986), 3152.

[23] BU, P., WANG, X., AND SASAKI, O. **Full-range parallel Fourier-domain optical coherence tomography using sinusoidal phase-modulating interferometry**. *J. Opt. A Pure Appl. Opt. 9*, 4 (Apr. 2007), 422–426.

[24] BEZERRA, H. G., COSTA, M. a., GUAGLIUMI, G., ROLLINS, A. M., AND SIMON, D. I. **Intracoronary Optical Coherence Tomography: A Comprehensive Review. Clinical and Research Applications**. *JACC Cardiovasc. Interv. 2*, 11 (2009), 1035–1046.

[25] **Some Historical Statistics on Companies in the Market of Optical Coherence Tomography Systems**. http://www.octnews.org/articles/4111178/some-historical-statistics-on-companies-in-the-mar/, 2012.

[26] BERARDESCA, E., MAIBACH, H. I., AND WILHELM, K.-P., Eds. **Non Invasive Diagnostic Techniques in Clinical Dermatology**. Springer Berlin Heidelberg, Berlin, Heidelberg, 2014.

[27] MAIER, T., SATTLER, E., BRAUN-FALCO, M., RUZICKA, T., AND BERKING, C. **High-Definition Optical Coherence Tomography for the in vivo Detection of Demodex Mites**. *Dermatology 225* (2013), 271–276.

[28] GAMBICHLER, T., MOUSSA, G., SAND, M., SAND, D., ALTMEYER, P., AND HOFF-MANN, K. **Applications of optical coherence tomography in dermatology**. *J. Dermatol. Sci. 40* (2005), 85–94.

[29] MOGENSEN, M., THRANE, L., JOERGENSEN, T. M., ANDERSEN, P. E., AND JEMEC, G. B. E. **Optical coherence tomography for imaging of skin and skin diseases.** In *Semin. Cutan. Med. Surg.* (Sept. 2009), vol. 28, pp. 196–202.

[30] GAMBICHLER, T., JAEDICKE, V., AND TERRAS, S. **Optical coherence tomography in dermatology: Technical and clinical aspects**. *Arch. Dermatol. Res. 303* (2011), 457–473.

[31] SALOMATINA, E., JIANG, B., NOVAK, J., AND YAROSLAVSKY, A. N. **Optical properties of normal and cancerous human skin in the visible and near-infrared spectral range**. *Journal of biomedical Optics 11* (2006), 1–9.

[32] WELZEL, J., AND LANKENAU, E. **OCT in Dermatology**. *Opt. Coherence Tomogr. - Technol. Appl.* (2008).

[33] XIE, T., MUKAI, D., GUO, S., BRENNER, M., AND CHEN, Z. **Fiber-optic-bundle-based optical coherence tomography.** *Opt. Lett. 30*, 14 (2005), 1803–1805.

[34] LEE, B. H., MIN, E. J., AND KIM, Y. H. **Fiber-based optical coherence tomography for biomedical imaging, sensing, and precision measurements**. *Opt. Fiber Technol. 19*, 6 (2013), 729–740.

[35] SUN, J., AND XIE, H. **MEMS-Based Endoscopic Optical Coherence Tomography**. *Int. J. Opt. 2011* (2011), 1–12.

[36] PAN, Y., XIE, H., AND FEDDER, G. K. **Endoscopic optical coherence tomography based on a microelectromechanical mirror.** *Opt. Lett. 26*, 24 (Dec. 2001), 1966–8.

[37] GORECKI, C., CHOLLET, F., BONNOTTE, E., AND KAWAKATSU, H. **Silicon-based integrated interferometer with phase modulation driven by surface acoustic waves.** *Opt. Lett. 22*, 23 (1997), 1784–1786.

[38] SASAKI, M., MI, X., AND HANE, K. **Standing wave detection and interferometer application using a photodiode thinner than optical wavelength**. *Appl. Phys. Lett. 75*, 14 (1999), 2008.

[39] CULEMANN, D., KNUETTEL, A., AND VOGES, E. **Integrated optical sensor in glass for optical coherence tomography (OCT)**. *IEEE J. Sel. Top. Quantum Electron. 6*, 5 (Sept. 2000), 730–734.

[40] YURTSEVER, G., AND BAETS, R. **Towards integrated optical coherence tomography system on silicon on insulator.** *Annu. Symp. IEEE/LEOS* (2008), 163–166.

[41] YURTSEVER, G., DUMON, P., BOGAERTS, W., AND BAETS, R. **Integrated photonic circuit in silicon on insulator for Fourier domain optical coherence tomography**. *Biomedicine 7554* (2010), 75541B.

[42] YURTSEVER, G., POVAŽAY, B., ALEX, A., ZABIHIAN, B., DREXLER, W., AND BAETS, R. **Photonic integrated Mach-Zehnder interferometer with an on-chip reference arm for optical coherence tomography**. *Biomed. Opt. Express 5*, 4 (2014), 1050–1061.

[43] WOLFFENBUTTEL, R. F. **MEMS-based optical mini- and microspectrometers for the visible and infrared spectral range**. *J. Micromech. Microeng. 15*, 7 (2005), S145–S152.

[44] AKCA, B. I., NGUYEN, V. D., KALKMAN, J., ISMAIL, N., SENGO, G., SUN, F., DRIESSEN, A., VAN LEEUWEN, T. G., POLLNAU, M., WÖRHOFF, K., AND DE RIDDER, R. M. **Toward Spectral-Domain Optical Coherence Tomography on a Chip**. *IEEE J. Sel. Top. Quantum Electron. 18*, 3 (2012), 1223–1233.

[45] ALJASEM, K., FROEHLY, L., SEIFERT, A., AND ZAPPE, H. **Scanning and tunable micro-optics for endoscopic optical coherence tomography**. *J. Microelectromechanical Syst. 20*, 6 (2011), 1462–1472.

[46] WEBER, N., SPETHER, D., SEIFERT, A., AND ZAPPE, H. **Highly compact imaging using Bessel beams generated by ultraminiaturized multi-micro-axicon systems**. *J. Opt. Soc. Am. A 29*, 5 (2012), 808.

[47] MULLER, R. S., AND LAU, K. Y. **Surface-micromachined microoptical elements and systems**. *Proc. IEEE 86*, 8 (1998), 1705–1720.

[48] WU, M., LIN, L., LEE, S., AND PISTER, K. **Micromachined free-space integrated micro-optics**. *Sensors Actuators A Phys. 50* (1995), 127–134.

[49] WU, M. **Micromachining for optical and optoelectronic systems**. *Proc. IEEE 85*, 11 (1997), 1833–1856.

[50] SYMS, R. R. A., GORMLEY, C., AND BLACKSTONE, S. **Improving yield, accuracy and complexity in surface tension self-assembled MOEMS**. *Sensors Actuators, A Phys. 88*, 3 (2001), 273–283.

[51] WEBER, N., ZAPPE, H., AND SEIFERT, A. **A tunable optofluidic silicon optical bench**. *J. Microelectromechanical Syst. 21*, 6 (2012), 1357–1364.

[52] BARGIEL, S., RABENOROSOA, K., CLÉVY, C., GORECKI, C., AND LUTZ, P. **Towards micro-assembly of hybrid MOEMS components on a reconfigurable silicon free-space micro-optical bench**. *J. Micromech. Microeng. 20*, 4 (2010), 045012.

[53] **3D Plus company website: www.3d-plus.com**.

[54] **Georgia Tech 3D Integration research team website: http://www.gtcad.gatech.edu/ and http://arch.ece.gatech.edu/**.

[55] DI CIOCCIO, L., RADU, I., GUEGUEN, P., AND SADAKA, M. **Direct bonding for wafer level 3D integration**. In *IC Des. Technol.* (2010), pp. 110–113.

[56] MEHRA, A., ZHANG, X., AYÓN, A. A., WAITZ, I. A., SCHMIDT, M. A., AND SPADACCINI, C. M. **Six-wafer combustion system for a silicon micro gas turbine engine**. *J. Microelectromechanical Syst. 9*, 4 (2000), 517–527.

[57] MIKI, N., ZHANG, X., KHANNA, R., AYO, A. A., WARD, D., AND SPEARING, S. M. **Multi-stack silicon-direct wafer bonding for 3D MEMS manufacturing**. *Sensors And Actuators 103* (2003), 194–201.

[58] DICKENSHEETS, D. L., AND KINO, G. S. **Micromachined scanning confocal optical microscope.** *Opt. Lett. 21*, 10 (1996), 764–766.

[59] KWON, S. K. S., AND LEE, L. **Stacked two dimensional micro-lens scanner for micro confocal imaging array**. *Tech. Dig. MEMS 2002 IEEE Int. Conf. Fifteenth IEEE Int. Conf. Micro Electro Mech. Syst. (Cat. No.02CH37266)* (2002), 483–486.

[60] KWON, S., MILANOVIC, V., AND LEE, L. P. **Vertical Microlens Scanner for 3D Imaging**. *Tech. Dig. 2002 Solid-State Sens. Actuator Work.* (2002), 3–6.

[61] KWON, S., AND LEE, L. P. **Micromachined transmissive scanning confocal microscope.** *Opt. Lett. 29*, 7 (Apr. 2004), 706–8.

[62] BARANSKI, M., BARGIEL, S., PASSILLY, N., GORECKI, C., JIA, C., FRÖMEL, J., AND WIEMER, M. **Micro-optical design of a three-dimensional microlens scanner for vertically integrated micro-opto-electro-mechanical systems**. *Appl. Opt. 54*, 22 (2015), 6924–6934.

[63] OSTEN, W. **Optical Inspection of Microsystems**. CRC Press, 2006.

[64] ALBERO, J., BARGIEL, S., PASSILLY, N., DANNBERG, P., STUMPF, M., ZEITNER, U. D., ROUSSELOT, C., GASTINGER, K., AND GORECKI, C. **Micromachined array-type Mirau interferometer for parallel inspection of MEMS**. *J. Micromech. Microeng. 21*, 6 (June 2011), 065005.

[65] STRUK, P., BARGIEL, S., FROEHLY, L., BARANSKI, M., PASSILLY, N., ALBERO, J., AND GORECKI, C. **Swept Source Optical Coherence Tomography Endomicroscope Based on Vertically Integrated Mirau Micro Interferometer: Concept and Technology**. *IEEE Sens. J. 15*, 12 (Dec. 2015), 7061–7070.

[66] XU, W. **Modeling and fabrication of tunable 3D integrated Mirau micro-interferometers**. PhD thesis, Université Paris Sud (IEF), 2014.

[67] XU, W., BOSSEBOEUF, A., PARRAIN, F., AND MARTINCIC, E. **Design of a long range bidirectional MEMS scanner for a tunable 3D integrated Mirau interferometer**. In *Symp. Des. Test, Integr. Packag. MEMS/MOEMS* (Apr. 2014), IEEE, pp. 1–6.

[68] DINEVA, P. **Dynamic Fracture of Piezoelectric Materials - Chapter 2: Piezoelectric Materials**. No. Solid Mechanics and its applications - 212. Springer International Publishing, 2014.

[69] DIEULESAINT, E., ROYER, D., AND GENNES, P.-G. **Ondes élastiques dans les solides, tome 1 : Propagation libre et guidée**, elsevier masson ed. 1997.

[70] GE, P., AND JOUANEH, M. **Modeling hysteresis in piezoceramic actuators**. *Precis. Eng. 17*, 95 (1995), 211–221.

[71] JANG, L.-S., AND KUO, K.-C. **Fabrication and Characterization of PZT Thick Films for Sensing and Actuation**. *Sensors 7* (2007), 493–507.

[72] DE CICCO, G., AND MORTEN, B. **Thick-film Piezoelectric Actuators for Micropositioning**. *J. Intell. Mater. Syst. Struct. 20*, 14 (July 2009), 1689–1697.

[73] FILHOL, F., DEFAŸ, E., DIVOUX, C., ZINCK, C., AND DELAYE, M.-T. **Resonant micro-mirror excited by a thin-film piezoelectric actuator for fast optical beam scanning**. *Sensors Actuators A Phys. 123-124* (Sept. 2005), 483–489.

[74] SCHROTH, A., LEE, C., MATSUMOTO, S., AND MAEDA, R. **Application of sol-gel deposited thin PZT film for actuation of 1D and 2D scanners**. *Sensors Actuators, A Phys. 73*, April 1998 (1999), 144–152.

[75] SMITS, J. G., FUJIMOTO, K., AND KLEPTSYN, V. F. **Microelectromechanical flexure PZT actuated optical scanner: static and resonance behavior**. *J. Micromech. Microeng. 15* (2005), 1285–1293.

[76] AKTAKKA, E. E., PETERSON, R. L., AND NAJAFI, K. **A 3-DOF piezoelectric micro vibratory stage based on bulk-PZT/silicon crab-leg suspensions**. *Proc. IEEE Int. Conf. Micro Electro Mech. Syst.*, Figure 6 (2013), 576–579.

[77] GILCHRIST, K. H., MCNABB, R. P., IZATT, J. A., AND GREGO, S. **Piezoelectric scanning mirrors for endoscopic optical coherence tomography**. *J. Micromech. Microeng. 19* (2009), 095012.

[78] NAONO, T., FUJII, T., ESASHI, M., AND TANAKA, S. **A large-scan-angle piezoelectric MEMS optical scanner actuated by a Nb-doped PZT thin film**. *J. Micromech. Microeng. 24* (2014), 015010.

[79] QIU, Z., PULSKAMP, J. S., LIN, X., RHEE, C.-H., WANG, T., POLCAWICH, R. G., AND OLDHAM, K. **Large displacement vertical translational actuator based on piezoelectric thin films**. *J. Micromech. Microeng. 20* (2010), 075016.

[80] QUENZER, H.-J., GU-STOPPEL, S., STOPPEL, F., JANES, J., HOFMANN, U., AND BENECKE, W. **Piezoelectrically driven translatory optical MEMS actuator with 7mm apertures and large displacements**. In *Proc. SPIE 9375* (2015).

[81] FEDDER, G. K., AND HOVE, R. T. **Thermal assembly of polysilicon microstructures**. *Proc. IEEE Micro electro Mech. Syst. Work.* (1991), 63–68.

[82] LIN, L., AND CHIAO, M. **Electrothermal responses of lineshape microstructures**. *Sensors Actuators, A Phys. 55* (1996), 35–41.

[83] HUANG, Q.-A., AND LEE, N. K. S. **Analysis and design of polysilicon thermal flexure actuator**. *J. Micromech. Microeng. 9* (1999), 64–70.

[84] ZOU, J., YE, X., ZHOU, Z., AND YANG, Y. **A novel thermally-actuated silicon micropump**. In *1997 Int. Symp. Micromechanics Hum. Sci. (Cat. No.97TH8311)* (1997), IEEE, pp. 231–234.

[85] RIETHMULLER, W., AND BENECKE, W. **Thermally excited silicon microactuators**. *IEEE Trans. Electron Devices 35*, 6 (June 1988), 758–763.

[86] JAIN, A., QU, H., TODD, S., AND XIE, H. **A thermal bimorph micromirror with large bi-directional and vertical actuation**. *Sensors Actuators, A Phys. 122* (2005), 9–15.

[87] COMTOIS, J., AND BRIGHT, V. M. **Surface micromachined polysilicon thermal actuator arrays and applications**. In *Proc. Solid-State Sens. Actuator* (1996).

[88] LIU, L., WU, L., SUN, J., LIN, E., AND XIE, H. **Miniature endoscopic optical coherence tomography probe employing a two-axis microelectromechanical scanning mirror with through-silicon vias.** *J. Biomed. Opt. 16*, 2 (Feb. 2011), 026006.

[89] WITTWER, J. W., BAKER, M. S., AND HOWELL, L. L. **Simulation, measurement, and asymmetric buckling of thermal microactuators**. *Sensors Actuators, A Phys. 128* (2006), 395–401.

[90] ATRE, A. **Analysis of out-of-plane thermal microactuators**. *J. Micromech. Microeng. 16* (2005), 205–213.

[91] PHINNEY, L. M., BAKER, M. S., AND SERRANO, J. R. **Thermal Microactuators**. In *Microelectromechanical Syst. devices*, N. Islam, Ed. Intech, 2012.

[92] NOWOROLSKI, J. M., KLAASSEN, E. H., LOGAN, J. R., PETERSEN, K. E., AND MALUF, N. I. **Process for in-plane and out-of-plane single-crystal-silicon thermal microactuators**. *Sensors Actuators, A Phys. 55* (1996), 65–69.

[93] COWAN, W. D., AND BRIGHT, V. M. **Vertical thermal actuators for micro-optoelectromechanical systems**. In *Proc. SPIE 3226* (Sept. 1997), pp. 137–146.

[94] LIU, L., WANG, E., ZHANG, X., LIANG, W., LI, X., AND XIE, H. **MEMS-based 3D confocal scanning microendoscope using MEMS scanners for both lateral and axial scan**. *Sensors Actuators A Phys. 215* (2014), 89–95.

[95] LIU, C., TSAO, T., LEE, G. B., LEU, J. T. S., YI, Y. W., TAI, Y. C., AND HO, C. M. **Out-of-plane magnetic actuators with electroplated permalloy for fluid dynamics control**. *Sensors Actuators, A Phys. 78* (1999), 190–197.

[96] TSENG, V. F. G., LI, J., ZHANG, X., DING, J., CHEN, Q., AND XIE, H. **An electromagnetically actuated micromirror with precise angle control for harsh environment optical switching applications**. *Sensors Actuators, A Phys. 206* (2014), 1–9.

[97] JUDY, J. W., AND MULLER, R. S. **Magnetically actuated, addressable microstructures**. *J. Microelectromechanical Syst. 6*, 3 (1997), 249–255.

[98] SU, G. D. J., CHIU, C. W., AND JIANG, F. **Vertical micromirrors integrated with electromagnetic microactuators for two-dimensional optical matrix switches**. *IEEE Photonics Technol. Lett. 17*, 9 (2005), 1860–1862.

[99] LV, X., WEI, W., MAO, X., YANG, J., AND YANG, F. **A novel MEMS actuator with large lateral stroke driven by Lorentz force**. *J. Micromech. Microeng. 025009* (2015), 0–16.

[100] WANG, Y., SASAKI, T., WU, T., HU, F., AND HANE, K. **Comb-drive GaN micromirror on a GaN-on-silicon platform**. *J. Micromech. Microeng. 21*, 3 (Mar. 2011), 035012.

[101] XIE, H., AND FEDDER, G. K. **Vertical comb-finger capacitive actuation and sensing for CMOS-MEMS**. *Sensors Actuators, A Phys. 95* (2002), 212–221.

[102] ZHAO, Y., AND CUI, T. **Fabrication of high-aspect-ratio polymer-based electrostatic comb drives using the hot embossing technique**. *J. Micromech. Microeng. 13* (2003), 430–435.

[103] CORNELISSEN, S. A., BIERDEN, P. A., BIFANO, T. G., AND LAM, C. V. **4096-element continuous face-sheet MEMS deformable mirror for high-contrast imaging**. *J. Micro/Nanolithography, MEMS MOEMS 8*, 222000000888 (2009), 031308.

[104] HU, F., YAO, J., QIU, C., AND REN, H. **A MEMS micromirror driven by electrostatic force**. *J. Electrostat. 68*, 3 (2010), 237–242.

[105] REN, H., TAO, F., WANG, W., AND YAO, J. **An out-of-plane electrostatic actuator based on the lever principle**. *J. Micromech. Microeng. 21* (2011), 045019.

[106] QIAO, D.-Y., YUAN, W.-Z., AND LI, X.-Y. **A two-beam method for extending the working range of electrostatic parallel-plate micro-actuators**. *J. Electrostat. 65*, 4 (Apr. 2007), 256–262.

[107] BARGIEL, S., GORECKI, C., VERDOT, T., LASZCZYK, K., ALBERO, J., AND EL FISSI, L. **Electrostatically driven optical Z-axis scanner with thermally bonded glass microlens**. *Procedia Eng. 5* (Jan. 2010), 762–765.

[108] TANG, W. C., LIM, M. G., AND HOWE, R. T. **Electrostatic comb drive levitation and control method**. *J. Microelectromechanical Syst.* (1992).

[109] PALMER, H. B. **The Capacitance of a parallel-plate capacitor by the Schwartz-Cristoffel transformation.** *Am. Institue Electr. Eng. Trans. 56*, 3 (1937), 363–367.

[110] YEH, J. L. a., HUI, C. Y., AND TIEN, N. C. **Electrostatic model for an asymmetric combdrive**. *J. Microelectromechanical Syst. 9*, 1 (2000), 126–135.

[111] GALLAGHER, E., AND MOUSSA, W. **A Study of the Effect of the Fringe Fields on the Electrostatic Force in Vertical Comb Drives**. *Sensors 14* (2014), 20149–20164.

[112] LEGTENBERG, R., GROENEVELD, a. W., AND ELWENSPOEK, M. **Comb-drive actuators for large displacements**. *J. Micromech. Microeng. 6*, 3 (Sept. 1996), 320–329.

[113] DHARIWAL, R., TORRES, J.-M., AND DESMULLIEZ, M. **Electric field breakdown at micrometre separations in air and nitrogen at atmospheric pressure**. *IEE Proc. - Sci. Meas. Technol. 147* (2000), 261.

[114] SLADE, P., AND TAYLOR, E. **Electrical breakdown in atmospheric air between closely spaced (0.2 μm-40 μm) electrical contacts**. *IEEE Trans. Components Packag. Technol. 25*, 3 (Sept. 2002), 390–396.

[115] CHEN, C.-H., YEH, J. A., AND WANG, P.-J. **Electrical breakdown phenomena for devices with micron separations**. *J. Micromech. Microeng. 16* (2006), 1366–1373.

[116] GALLAGHER, E., MOUSSA, W., AND MCDERMOTT, M. **A review of fabrication processes for vertical comb drives**. *Microsyst. Technol. 18*, 4 (Jan. 2012), 381–397.

[117] LEE, J.-H., KO, Y.-C., CHOI, B.-S., KIM, J.-M., AND JEON, D. Y. **Bonding of Silicon Scanning Mirror Having Vertical Comb Fingers**. *J. Micromech. Microeng. 12* (2002), 644–649.

[118] LEE, J.-H., KO, Y.-C., KONG, D.-H., KIM, J.-M., LEE, K. B., AND JEON, D.-Y. **Design and fabrication of scanning mirror for laser display**. *Sensors Actuators A Phys. 96*, 2-3 (Feb. 2002), 223–230.

[119] LEE, J.-H., KO, Y.-C., JEONG, H.-M., CHOI, B.-S., KIM, J.-M., AND JEON, D. Y. **SOI-based fabrication processes of the scanning mirror having vertical comb fingers**. *Sensors Actuators A Phys. 102*, 1-2 (Dec. 2002), 11–18.

[120] IWASE, E., ONOE, H., MATSUMOTO, K., AND SHIMOYAMA, I. **Hidden vertical comb-drive actuator on PDMS fabricated by parts-transfer**. *Proc. IEEE Int. Conf. Micro Electro Mech. Syst.* (2008), 116–119.

[121] CONANT, R. A., NEE, J. T., LAU, K. Y., MULLER, R. S., AND SENSOR, B. **A flat high-frequency scanning micromirror**. In *Solid-State Sens. Actuator Work.* (2000), pp. 6–9.

[122] KRISHNAMOORTHY, U., AND SOLGAARD, O. **Self-aligned vertical electrostatic combdrives for micromirror actuation**. *J. Microelectromechanical Syst. 12*, 4 (Aug. 2003), 458–464.

[123] KUMAR, K., CONDIT, J. C., MCELROY, A., KEMP, N. J., HOSHINO, K., MILNER, T. E., AND ZHANG, X. **Fast 3D in vivo swept-source optical coherence tomography using a two-axis MEMS scanning micromirror**. *J. Opt. A Pure Appl. Opt. 10*, 4 (Apr. 2008), 044013.

[124] LEE, D., KRISHNAMOORTHY, U., YU, K., AND SOLGARRD, O. **Single-crystalline silicon micromirrors actuated by self-aligned vertical electrostatic combdrives with piston-motion and rotation capability**. *Sensors Actuators, A Phys. 114* (2004), 423–428.

[125] YEH, J.-L. A., MEMBER, S., JIANG, H., AND TIEN, N. C. **Integrated Polysilicon and DRIE Bulk Silicon Micromachining for an Electrostatic Torsional Actuator**. *J. Microelectromechanical Syst. 8*, 4 (1999), 456–465.

[126] CARLEN, E., BAKSHI, S., PAREEK, A., AND MASTRANGELO, C. **High-aspect ratio vertical comb-drive actuator with small self-aligned finger gaps**. *J. Microelectromechanical Syst. 14*, 5 (Oct. 2005), 1144–1155.

[127] KWON, S., MILANOVIC, V., AND LEE, L. P. **Vertical Combdrive Based 2-D Gimbaled Micromirrors With Large Static Rotation by Backside Island Isolation**. *IEEE J. Sel. Top. Quantum Electron. 10*, 3 (2004), 498–504.

[128] LEE, A. P., MCCONAGHY, C. F., SOMMARGREN, G., KRULEVITCH, P., AND CAMPBELL, E. W. **Vertical-actuated electrostatic comb drive with in situ capacitive position correction for application in phase shifting diffraction interferometry**. *J. Microelectromechanical Syst. 12*, 6 (2003), 960–971.

[129] KIM, J., PARK, S., AND CHO, D.-I. **A novel electrostatic vertical actuator fabricated in one homogeneous silicon wafer using extended SBM technology**. *Sensors Actuators A Phys. 97-98* (Apr. 2002), 653–658.

[130] ZHANG, Q. X., LIU, A. Q., LI, J., AND YU, A. B. **Fabrication technique for microelectromechanical systems vertical comb-drive actuators on a monolithic silicon substrate**. *J. Vac. Sci. Technol. B Microelectron. Nanom. Struct. 23*, 1 (2005), 32.

[131] TSUCHIYA, T., AND FUNABASHI, H. **A z-axis differential capacitive SOI accelerometer with vertical comb electrodes**. *Sensors Actuators A Phys. 116*, 3 (Oct. 2004), 378–383.

[132] ZICKAR, M., MITA, M., ATAKA, M., AND FUJITA, H. **Low cross talk design and simple fabrication process of electrostatic vertical comb-drive actuators for positioning application**. *IEEJ Trans. Electr. Electron. Eng. 2* (2007), 289–294.

[133] WANG, J., YANG, Z., AND YAN, G. **Silicon-on-insulator out-of-plane electrostatic actuator with in situ capacitive position sensing**. *J. Micro/Nanolithography, MEMS, MOEMS 11*, 3 (July 2012), 033006.

[134] ODA, K., TAKAO, H., TERAO, K., SUZUKI, T., SHIMOKAWA, F., ISHIMARU, I., AND OOHIRA, F. **Vertical comb-drive MEMS mirror with sensing function for phase-shift device**. *Sensors Actuators, A Phys. 181* (2012), 61–69.

[135] CHOO, H., KANT, R., AND GARMIRE, D. **Fast, MEMS-based, phase-shifting interferometer**. In *Solid-State Sens. Actuator Work.* (2006), pp. 94–95.

[136] CHIOU, J.-C., HUNG, C.-C., SHIEH, L.-J., AND TSAI, Z.-L. **Novel electrostatic MOEMS phase shifter array using CMOS-MEMS process**. *J. Micro/Nanolithography, MEMS MOEMS 9* (2010), 013030.

[137] WYANT, J. C., SCHMIT, J., CORPORATION, W., AND ROAD, E. E. **Large Field of View , High Spatial Resolution , Surface Measurements**. *Int. J. Mach. Tools Manuf. 38*, 5-6 (1998), 691–698.

[138] **SLD-37-HP: very wide-spectrum, high-power SLD modules for 800-870 nm spectral band: https://www.superlumdiodes.com/pdf/37hp.pdf**.

[139] ANTILA, J., MIRANTO, A., MÄKYNEN, J., LAAMANEN, M., RISSANEN, A., BLOMBERG, M., SAARI, H., AND MALINEN, J. **MEMS and piezo actuator-based Fabry-Perot interferometer technologies and applications at VTT**. In *SPIE Defense, Secur. Sens.* (Apr. 2010), M. A. Druy, C. D. Brown, and R. A. Crocombe, Eds., International Society for Optics and Photonics, pp. 76800U–76800U–12.

[140] ALBERO, J., PERRIN, S., BARGIEL, S., PASSILLY, N., BARANSKI, M., GAUTHIER-MANUEL, L., BERNARD, F., LULLIN, J., FROEHLY, L., KRAUTER, J., OSTEN, W., AND GORECKI, C. **Dense arrays of millimeter-sized glass lenses fabricated at wafer-level**. *Opt. Express 23*, 9 (2015), 11702.

[141] HARVEY, J. E., AND FTACLAS, C. **Diffraction effects of telescope secondary mirror spiders on various image-quality criteria.** *Appl. Opt. 34*, 28 (Oct. 1995), 6337–6349.

[142] RICHTER, J. L. **Spider diffraction: a comparison of curved and straight legs.** *Appl. Opt. 23*, 12 (June 1984), 1907–1913.

[143] PERRIN, S. **Full field swept source optical coherence tomography micro-system - Application to dermatology**. PhD thesis, Université de Franche-Comté, 2016.

[144] WANG, W.-S., LULLIN, J., FROEMEL, J., WIEMER, M., BARGIEL, S., PASSILLY, N., GORECKI, C., AND GRESSNER, T. **Multi-wafer bonding technology for the integration of a micromachined Mirau interferometer**. In *Proc. SPIE* (2015), vol. 1, pp. 3–9.

[145] LULLIN, J., BARGIEL, S., COURJON, E., PERRIN, S., BARANSKI, M., PASSILLY, N., AND GORECKI, C. **Monolithic integration of a glass membrane on silicon micro-actuator for micro-interferometry**. In *2014 Int. Conf. Opt. MEMS Nanophotonics* (Aug. 2014), IEEE, pp. 87–88.

[146] HOPCROFT, M. A., NIX, W. D., AND KENNY, T. W. **What is the Young ' s Modulus of Silicon ?** *J. Microelectromechanical Syst. 19*, 2 (2010), 229–238.

[147] KRAUTER, J., BOETTCHER, T., LYDA, W., OSTEN, W., PASSILLY, N., FROEHLY, L., BARGIEL, S., ALBERO, J., PERRIN, S., LULLIN, J., AND GORECKI, C. **Optical design of a vertically integrated array-type Mirau-based OCT system**. In *Photonics Eur.* (2014), vol. 49.

[148] FEDDER, K. **Simulation of Microelectromechanical Systems**. PhD thesis, U.C. Berkeley, 1994.

[149] LULLIN, J., PERRIN, S., BARANSKI, M., BARGIEL, S., FROEHLY, L., ALBERO, J., AND GORECKI, C. **Impact of mirror spider legs on imaging quality in micro-interferometry**. *Opt. Lett. 40*, 10 (2015), 2209–2212.

[150] GOODMAN, J. W. **Introduction to Fourier Optics**. McGraw-Hill, 1996.

[151] STELZER, E. **Contrast , resolution , pixelation , dynamic range and signal- to-noise ratio : fundamental limits to resolution in fluorescence light microscopy**. *J. Microsc. 189*, January (1998), 15–24.

[152] BARANSKI, M., PERRIN, S., PASSILLY, N., FROEHLY, L., ALBERO, J., BARGIEL, S., AND GORECKI, C. **A simple method for quality evaluation of micro-optical components based on 3D IPSF measurement.** *Opt. Express 22*, 11 (June 2014), 13202–12.

[153] YOO, S., HA, J.-G., JIN, J.-Y., JI, C.-H., AND KIM, Y.-K. **Monolithically integrated glass microlens scanner using a thermal reflow process.** *J. Micromech. Microeng. 23*, 6 (June 2013), 065012.

[154] BU, M., MELVIN, T., ENSELL, G. J., WILKINSON, J. S., AND EVANS, A. G. **A new masking technology for deep glass etching and its microfluidic application.** *Sensors Actuators A Phys. 115*, 2-3 (Sept. 2004), 476–482.

[155] HIGO, A., TAKAHASHI, K., FUJITA, H., NAKANO, Y., AND TOSHIYOSHI, H. **A novel Parylene/Al/Parylene sandwich protection mask for HF Vapor release for micro electro mechanical systems.** In *TRANSDUCERS 2009 - 2009 Int. Solid-State Sensors, Actuators Microsystems Conf.* (June 2009), IEEE, pp. 196–199.

[156] LULLIN, J., BARGIEL, S., LEMOAL, P., PERRIN, S., ALBERO, J., PASSILLY, N., FROEHLY, L., LARDET-VIEUDRIN, F., AND GORECKI, C. **An electrostatic vertical microscanner for phase modulating array-type Mirau microinterferometry.** *J. Micromech. Microeng. 25*, 11 (Nov. 2015), 115013.

[157] DALY, D., STEVENS, R. F., HUTLEY, M. C., AND DAVIES, N. **The manufacture of microlenses by melting photoresist.** *Meas. Sci. Technol. 1* (1999), 759–766.

[158] POPOVIC, Z. D., SPRAGUE, R. A., AND CONNELL, G. A. **Technique for monolithic fabrication of microlens arrays.** *Appl. Opt. 27*, April (1988), 1281–1284.

[159] SCHILLING, A. **Surface profiles of reflow microlenses under the influence of surface tension and gravity.** *Opt. Eng. 39*, 8 (Aug. 2000), 2171.

[160] ALBERO, J. **Mise au point d'une filière de fabrication de microlentilles par moulage silicium : Application à l'instrumentation optique miniature.** PhD thesis, Université de Franche-Comté, 2010.

[161] GORECKI, C., BARGIEL, S., ALBERO, J., PASSILLY, N., ROUSSELOT, C., ZEITNER, U., AND GASTINGER, K. **Micromachined array-type Mirau interferometer for MEMS metrology.** In *2011 16th Int. Solid-State Sensors, Actuators Microsystems Conf.* (June 2011), IEEE, pp. 546–549.

[162] CHEN, Y., YI, A. Y., YAO, D., KLOCKE, F., AND PONGS, G. **A reflow process for glass microlens array fabrication by use of precision compression molding.** *J. Micromech. Microeng. 18*, 5 (May 2008), 055022.

[163] LEE, S.-K., KIM, M.-G., JO, K.-W., SHIN, S.-M., AND LEE, J.-H. **A glass reflowed microlens array on a Si substrate with rectangular through-holes**. *J. Opt. A Pure Appl. Opt. 10*, 4 (Apr. 2008), 044003.

[164] MERZ, P., QUENZER, H., BERNT, H., WANGER, B., AND ZOBERBIER, M. **A novel micromachining technology for structuring borosilicate glass substrates**. *TRANS-DUCERS '03. 12th Int. Conf. Solid-State Sensors, Actuators Microsystems. Dig. Tech. Pap. (Cat. No.03TH8664) 1* (2003), 258–261.

[165] GUPTA, K., CHOO, H., KIM, H., AND MULLER, R. **Micromachined polarization beam splitters for the visible spectrum**. In *2003 IEEE/LEOS Int. Conf. Opt. MEMS*, IEEE, pp. 171–172.

[166] TYAN, R.-C., SALVEKAR, A. a., CHOU, H.-P., CHENG, C.-C., SCHERER, A., SUN, P.-C., XU, F., AND FAINMAN, Y. **Design, fabrication, and characterization of form-birefringent multilayer polarizing beam splitter**. *J. Opt. Soc. Am. A 14*, 7 (1997), 1627.

[167] BARANSKI, M., BARGIEL, S., PASSILLY, N., GUICHARDAZ, B., HERTH, E., GORECKI, C., JIA, C., FROMEL, J., AND WIEMER, M. **Wafer-Level Fabrication of Microcube-Typed Beam-Splitters by Saw-Dicing of Glass Substrate**. *IEEE Photonics Technol. Lett. 26*, 1 (Jan. 2014), 100–103.

[168] **https://en.wikipedia.org/wiki/Silicon**.

[169] HULL, R. **Properties of crystalline silicon**. The Institution of Electrical Engineers, 1999.

[170] KIM, C.-J., PISANO, A. P., AND MULLER, R. S. **Silicon-processe overhanging microgripper**. *J. Microelectromechanical Syst. 1* (1992), 31–36.

[171] KIM, C.-J., PISANO, A. P., MULLER, R. S., AND LIM, M. G. **Polysilicon microgripper**. *Sensors Actuators A Phys. 33* (1992), 221–227.

[172] FAN, L.-S. F. L.-S., TAI, Y.-C. T. Y.-C., AND MULLER, R. M. R. **IC-processed electrostatic micro-motors**. *Tech. Dig. Int. Electron Devices Meet. 20* (1988), 41–47.

[173] ROBBINS, H., AND SCHWARTZ, B. **Chemical Etching of Silicon**. *J. Electrochem. Soc. 107*, 2 (Feb. 1960), 108.

[174] HASEGAWA, M., CHUTANI, R., GORECKI, C., BOUDOT, R., DZIUBAN, P., GIORDANO, V., CLATOT, S., AND MAURI, L. **Microfabrication of cesium vapor cells with buffer gas for MEMS atomic clocks**. *Sensors Actuators A Phys. 167*, 2 (2011), 594–601.

LIST OF FIGURES

LIST OF TABLES

I

Annexes

A

MATHEMATICAL CONSIDERATIONS

A.1/ FOURIER TRANSFORM OF A GAUSSIAN

The Fourier transform of a Gaussian defined as $f(t) = e^{-Ct^2}$ is calculated as follows:

$$
\begin{aligned}
F(w) &= \mathfrak{F}^{-1}f(t) \\
&= \int_{-\infty}^{\infty} f(t)e^{(-jwt)}dt \\
&= \int_{-\infty}^{\infty} e^{-Ct^2}e^{(-jwt)}dt \\
&= \int_{-\infty}^{\infty} e^{-C(t^2+jwt/C)}dt \\
&= \int_{-\infty}^{\infty} e^{-C(t^2+jwt/C+(jw/2C)^2-(jw/2C)^2)}dt \\
&= \int_{-\infty}^{\infty} e^{-C(t^2+jwt/C+(jw/2C)^2)+C(jw/2C)^2}dt \\
&= e^{-w^2/4C} \int_{-\infty}^{\infty} e^{-C(t+jw/C)^2}dt \\
&= e^{-w^2/4C} \int_{-\infty}^{\infty} e^{-C(-1)^2(t+jw/C)^2}dt \\
&= e^{-w^2/4C} \int_{-\infty}^{\infty} e^{-C(t-jw/C)^2}dt \ \text{ because we integrate between -}\infty\text{ and -}\infty \\
&= \frac{e^{-w^2/4C}}{\sqrt{C}} \int_{-\infty}^{\infty} e^{-C(\tau-jw/\sqrt{C})^2}d\tau \ \text{ with } \tau = \sqrt{C}t \text{ and } d\tau = \sqrt{C}dt \\
&= e^{-w^2/4C}\sqrt{\frac{\pi}{C}} \ \text{ with } \int_{-\infty}^{\infty} e^{-z^2}dz = \sqrt{\pi} \quad\quad\quad (A.1)
\end{aligned}
$$

A.2/ FULL WIDTH AT HALF MAXIMUM OF A GAUSSIAN

The full width at half maximum of a Gaussian defined as $f(t) = e^{-Ct^2}$ is calculated as follows:

$$e^{-Ct_1^2} = \frac{1}{2}f(x_{max})$$

$$e^{-Ct_1^2} = \frac{1}{2}$$

$$-Ct_1^2 = -ln(2)$$

$$Ct_1^2 = ln(2)$$

$$t_1 = \pm\sqrt{\frac{ln(2)}{C}}$$

$$FWHM = 2\sqrt{\frac{ln(2)}{C}} \tag{A.2}$$

A.3/ RELATION BETWEEN Δk AND $\Delta\lambda$

The power spectral density of the source is written as a function of Δk:

$$S(k) = e^{-[\frac{(k-k_0)}{\Delta k}]^2} \tag{A.3}$$

In this case, Δk is the half width of the power spectral density at e^{-1}. It is related to $\Delta\lambda$, the FWHM of the power spectral density in λ as follows:

$$\Delta k_{FWHM} = 2\sqrt{ln(2)}\Delta k$$

$$k_{Max} - k_{Min} = 2\sqrt{ln(2)}\Delta k$$

$$2\pi(\frac{1}{\lambda_{Max}} - \frac{1}{\lambda_{Min}}) = 2\sqrt{ln(2)}\Delta k$$

$$\pi(\frac{\lambda_{Min} - \lambda_{Max}}{\lambda_{Max}\lambda_{Min}}) = \sqrt{ln(2)}\Delta k$$

$$\pi\frac{\Delta\lambda}{\lambda_0^2} = \sqrt{ln(2)}\Delta k$$

$$\Delta k = \frac{\pi}{\sqrt{ln(2)}}\frac{\Delta\lambda}{\lambda_0^2} \tag{A.4}$$

A.4/ SINUSOIDAL PHASE-MODULATING ALGORITHM

This annexe aims to describe in details the calculations involved in the sinusoidal phase-modulating algorithm [23].

The spectral interferogram can be written as:

$$I(k) = \frac{S(k)}{2}(R_r + R_{S_1} + R_{S_2} + ... + R_{S_n})$$

$$+ S(k) \sum_{n=1}^{N} \sqrt{R_R R_{S_n}} cos(\phi_{R-n} + Acos(w_a t + \theta))$$

$$= I_0(k)$$

$$+ \sum_{n=1}^{N} B_n cos(\phi_{R-n} + Acos(w_a t + \theta)) \tag{A.5}$$

Here the auto-correlation term has been removed for simplification. Applying the Fourier transform with respect to the time t, we obtain:

$$\mathfrak{F}(I(k,w)) = I_0\delta(w) + \mathfrak{F}\left[\sum_n B_n \left[cos(\phi_{R-n})cos(Acos(w_a t + \theta)) - sin(\phi_{R-n})sin(Acos(w_a t + \theta))\right]\right] \tag{A.6}$$

First, let's calculate the following term:

$$A = \mathfrak{F}\left[\sum_n B_n \left[cos(\phi_{R-n})cos(Acos(w_a t + \theta))\right]\right]$$

$$= \sum_n B_n cos(\phi_{R-n})\mathfrak{F}\left[cos(Acos(w_a t + \theta))\right] \tag{A.7}$$

Using the real part of the Jacobi Anger's expansion:

$$cos(ucos(\phi)) = J_0(u) + 2\sum_{q=1}^{\infty}(-1)^q J_{2q}(u)cos(2q\phi) \tag{A.8}$$

We obtain:

$$A = \sum_n B_n cos(\phi_{R-n})\mathfrak{F}\left[cos(Acos(w_a t + \theta))\right]$$

$$= \sum_n B_n cos(\phi_{R-n})\mathfrak{F}\left[J_0(A) + 2\sum_{q=1}^{\infty}(-1)^q J_{2q}(A)cos(2q(w_a t + \theta))\right] \tag{A.9}$$

Finally, we need to calculate:

$$B = \mathfrak{F}\left[\cos(2q(w_at + \theta))\right]$$

$$= \mathfrak{F}\left[\cos(2qw_at)\cos(2q\theta) + \sin(2qw_at)\sin(2q\theta)\right]$$

$$= \frac{\cos(2q\theta)}{2}\left(\delta(w - 2qw_a) + \delta(w + 2qw_a)\right) + \frac{-i \times \sin(2q\theta)}{2}\left(\delta(w - 2qw_a) - \delta(w + 2qw_a)\right)$$

$$= \frac{1}{2}\left(\delta(w - 2qw_a)e^{-i2q\theta} + \delta(w + 2qw_a)e^{i2q\theta}\right) \tag{A.10}$$

where δ is the delta function and J_q the qth order Bessel function.

By integrating B in A and A in Eq. A.6, we obtain:

$$A = \sum_n B_n \cos(\phi_{R-n})\mathfrak{F}\left[J_0(A) + 2\sum_{q=1}^{\infty}(-1)^q J_{2q}(A)\cos(2q(w_at + \theta))\right]$$

$$= \sum_n B_n \cos(\phi_{R-n}) \times \left[\mathfrak{F}(J_0(A)) + 2\sum_{q=1}^{\infty}(-1)^q J_{2q}(A) \times \frac{1}{2}\left(\delta(w - 2qw_a)e^{-i2q\theta} + \delta(w + 2qw_a)e^{i2q\theta}\right)\right]$$

$$= \sum_n B_n \cos(\phi_{R-n}) \times \left[\sum_{q=-\infty}^{\infty}(-1)^q J_{2q}(A) \times \left(\delta(w - 2qw_a)e^{i2q\theta}\right)\right] \tag{A.11}$$

Using the same method with the imaginary part of the Jacobi Anger's expansion:

$$\sin(u\cos(\phi)) = -2\sum_{q=1}^{\infty}(-1)^q J_{2n-1}(u)\cos((2n - 1)\phi) \tag{A.12}$$

We finally obtains:

$$\mathfrak{F}(I(k,w)) = I_0\delta(w)$$

$$+ \sum_n B_n \cos(\phi_{R-n}) \times \left[\sum_{q=-\infty}^{\infty}(-1)^q J_{2q}(A) \times \left(\delta(w - 2qw_a)e^{i2q\theta}\right)\right]$$

$$+ \sum_n B_n \sin(\phi_{R-n}) \times \left[\sum_{q=-\infty}^{\infty}(-1)^q J_{(2q-1)}(A) \times \left(\delta(w - (2q - 1)w_a)e^{i(2q-1)\theta}\right)\right] \tag{A.13}$$

It can be observed that:

$$\sum_n B_n \cos(\phi_{R-n}) = -Re\left\{\mathfrak{F}(I(k, w_a))\right\} / [J_1(A)\cos(\theta)]$$

$$\sum_n B_n \sin(\phi_{R-n}) = -Re\left\{\mathfrak{F}(I(k, 2w_a))\right\} / [J_2(A)\cos(2\theta)] \tag{A.14}$$

We define B(k) as:

$$B(k) = \left[\left(\sum_n B_n sin(\phi_{R-n}) \right)^2 + \left(\sum_n B_n cos(\phi_{R-n}) \right)^2 \right]^{1/2}$$

(A.15)

and

$$\Phi(k) = tan^{-1} \frac{\left(\sum_n B_n sin(\phi_{R-n}) \right)}{\left(\sum_n B_n cos(\phi_{R-n}) \right)}$$

(A.16)

The complex spectral interferogram is reconstructed as:

$$\hat{I}(k) = \sum_n B_n exp(-j\phi_n)$$

(A.17)

By applying the inverse Fourier transform, one obtains:

$$\hat{I}(z) = \mathfrak{F}^-1(\hat{I}(k))$$
$$= \sum_n \int_{-\infty}^{\infty} S(k) \sqrt{R_R R_{S_n}} exp(-2jk(z_R - z_n)) exp(j2\pi kz) dk$$
$$= \sum_n \sqrt{R_R R_{S_n}} \Gamma (z - (z_R - z_n))$$

(A.18)

where Γ is the auto-correlation function.

This method results in a spatial interferogram free of parasitic terms.

B

SILICON MATERIAL

B.1 / SILICON PROPERTIES

In microfabrication, silicon is purchased as wafers which are thin disks of monocrystal silicon. Depending on the fabrication process, silicon wafers have different properties such as the thickness, the diameter, the doping concentration impacting on the electric resistivity but also the crystallographic orientation, which affects the mechanical properties. These aspects are crucial for the design and should be taken into account. Here, a brief introduction to silicon and its properties is given.

The silicon is a chemical element, more precisely a metalloid, which symbol is Si and atomic number is 14. It is the eighth most common element in the universe by mass and is the second most abundant element of the Earth's crust after oxygen (27.7 % of the Earth's crust). However, it is rarely found as a pure element in nature. It is usually found as silicate minerals, containing mainly silicon and oxygen, and less often as silicon dioxide, also called silica, which is a major component in sand. Table B.1 summarizes silicon main properties.

Table B.1: Main properties of silicon. [168, 146, 169]

Properties	Value	Unit
Name, Symbol	Silicon, Si	
Atomic number	14	
Element category	Metalloid	
Melting point	1414	°C
Density	2.33	g/cm^3
Crystal structure	Diamond cubic	
Thermal expansion	2.6	$\mu m/(m.K)$ at 25 °C
Electrical resistivity	$2.3.10^3$ [†]	ohm.m at 25 °C
Young's Modulus	130-188 (depends on the direction)	GPa
Poisson's ratio	0.064-0.28	
Yield strength	7	GPa
Most stable isotopes (proportion of earth)	^{28}Si (92.23 %)	
	^{29}Si (4.67 %)	
	^{30}Si (3.1 %)	

[†] In industry, silicon is doped to increase its electrical resistivity

B.2/   FABRICATION

Starting material for silicon is relatively pure quartz based sand (silica). Sand is reduced in an arc furnace with coal, forming metallurgical grade silicon (MGS) with some impurities (metals).

$$SiO_2 + 2C \rightarrow Si\ (solid) + 2CO\ (gas) \text{ at 2000 °C for } \sim 8 \text{ days} \qquad \text{(B.1)}$$
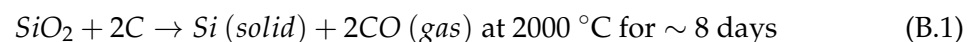
MGS is purified into trichlorosilane (TCS) by reaction with HCl.

$$Si\ (solid) + 3HCl\ (gas) \rightarrow HSiCl_3\ (gas) + H_2\ (gas) \text{ at 325 °C} \qquad \text{(B.2)}$$
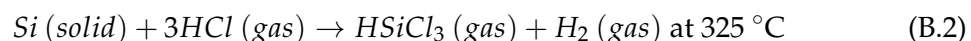
Purified TCS is finally reduced with H_2 to obtain electronic grade silicon. The chemical vapor deposition occurs in a cold room containing an heated Si rod which acts as crystalline seed. The result is an extremely pure polycrystalline silicon ingot that is transformed into a monocrystalline silicon ingot using the Czochralski (CZ) or the float-zone

(FZ) process.

$$HSiCl_3\ (gas) + H_2\ (gas) \rightarrow 3HCl\ (gas) + Si\ (solid) \text{ at } 325\,^{\circ}\text{C} \qquad \text{(B.3)}$$
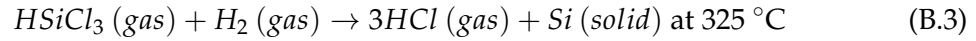
The Czochralski process uses the hyperpure polycrystalline silicon that is melted at high temperature (1500 °C) and a monocrystalline silicon seed. The seed is immersed in the melted silicon and vertically removed while rotating (Fig. B.1 (a)). This process results in a monocrystalline silicon ingot. For many applications, doped silicon is needed. The doping elements are added to the melted silicon to pull doped crystals. The dopants are added in the form of doped polysilicon for concentration control. The concentration of the dopant in crystal is not the same as in the melt. It is defined by the segregation coefficient k as:

$$k = \frac{C_s}{C_L} \qquad \text{(B.4)}$$

with C_s the concentration of dopant in solid and C_L the concentration of dopant in the liquid.

Since k is, in general less than 1, the dopant becomes increasingly more concentrated in the melt. This leads to a dopant concentration changes along the crystal ingot.
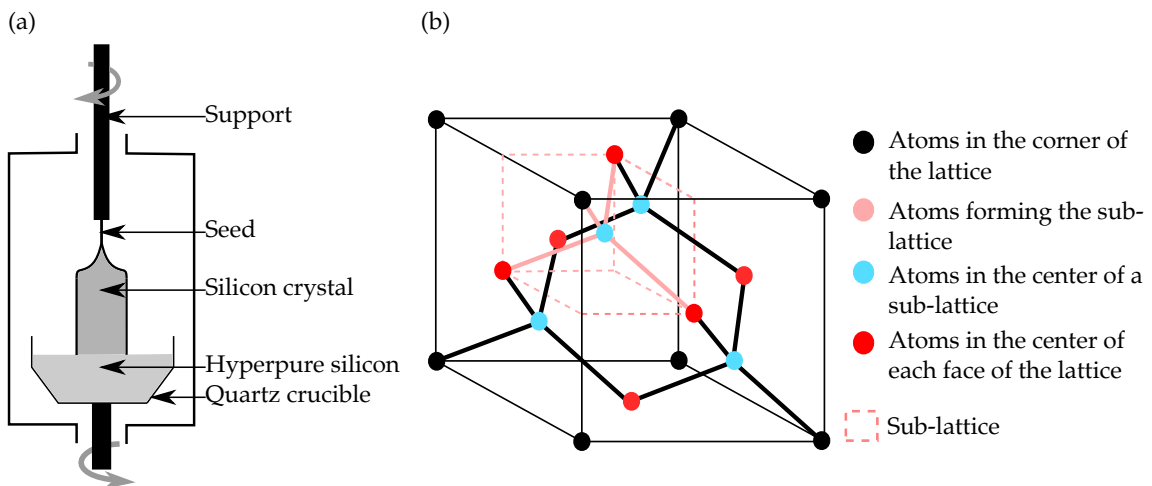
Figure B.1: (a) Czochralski fabrication process of silicon ingot, (b) diamond lattice of silicon.

The float-zone process is used when highly pure silicon is necessary, i.e. when oxygen ions present in the silicon crystal lattice after the CZ process is not tolerable. It represents only 2% of the wafer production market. It consists in fusing a monocrystalline seed to the polycrystalline silicon ingot and then a RF heating coil is used to heat locally the bar at the interface mono/polycristalline silicon. The heated zone is called the "float-zone". In the float-zone, the atoms align to the seed.

Once the monocrystalline silicon ingot is fabricated, it is usually diced into wafers with a diamond wire or saw.

B.3/ CRYSTALLOGRAPHY

In a crystal, the atoms are arranged on a regular grid called lattice. There exist 14 unique lattices, called the Bravais lattice[1]. The crystalline structure of silicon belongs to the family of cubic crystals and is called diamond (Fig. B.1 (b)).

To identify the orientation of the lattice, Miller indices are used. Each plane (hkl) is defined by its normal vector [hkl]. The hkl values are the reciprocals of the coordinates of the intersection of the (hkl) plane with the XYZ axis. If one of the value is negative, it is noted by adding a bar upon the index, like $\bar{h}$ for example. The different notations using Miller indices are given in Tab. B.2.

Table B.2: Miller indices notations

Notation	Description
[hkl]	The direction vector given by hkl
$\langle$ hkl $\rangle$	The family of direction vectors equivalent to [hkl]
(hkl)	The crystal plane normal to vector [hkl]
hkl	The family of planes equivalent to the plane (hkl)

Moreover, by convention, the directions [100], [010] and [001] corresponds to the cartesian XYZ direction, unless specified otherwise. The most commonly used wafer orientation is (100), which means that the top surface of the wafer is the (100) plane. Moreover, the orientation of the crystallographic direction in the plane of the wafer is given by a flat (one side of the wafer is cut) which is done during the wafer fabrication at the silicon ingot level. For typical wafers used in research, the primary flat is aligned with the [110] direction (Fig. B.2). The properties of silicon depends on its crystallographic orientation, therefore it is extremely important to take it into account for the design. When a (100) wafer is used, the X and Y directions, corresponding respectively to the [110] and the [$\bar{1}$10], have equivalent elastic properties [146]. However, all directions are not equivalent, i.e. silicon is an anisotropic material.

---

[1]A Bravais lattice is an infinite array of discrete points generated by a set of discrete translation operations
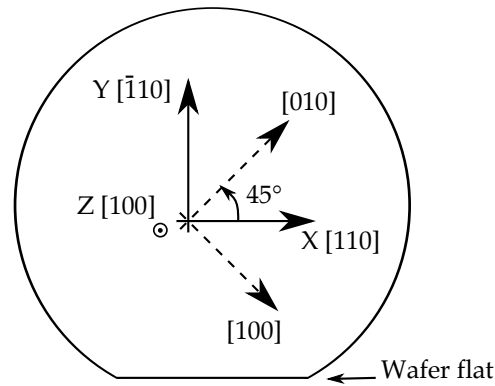
Figure B.2: Wafer (100) description with XYZ direction with respect to the wafer flat.

The Hooke's law describes the relationship between stress (σ) and strain (ϵ):

$$\sigma = C\epsilon \tag{B.5}$$

where C is the stiffness tensor and which can be also written as:

$$\sigma_{ij} = C_{ijkl}\epsilon kl \tag{B.6}$$

For an isotropic material, C can be replaced by a single value, noted E and called the Young's modulus. For an anisotropic material, axes of symmetry enables the simplification of the stiffness tensor. In the case of the crystallographic lattice of silicon, it reduces to the following tensor:

$$C = \begin{pmatrix} c_{11} & c_{12} & c_{12} & 0 & 0 & 0 \\ c_{12} & c_{11} & c_{12} & 0 & 0 & 0 \\ c_{12} & c_{12} & c_{11} & 0 & 0 & 0 \\ 0 & 0 & 0 & c_{44} & 0 & 0 \\ 0 & 0 & 0 & 0 & c_{44} & 0 \\ 0 & 0 & 0 & 0 & 0 & c_{44} \end{pmatrix} \tag{B.7}$$

The values of c_{11}, c_{12}, c_{44} have been reported [146]:

$$c_{11} = 165.6.10^9 \ Pa$$
$$c_{12} = 63.9.10^9 \ Pa$$
$$c_{12} = 79.5.10^9 \ Pa$$

These values are used to calculate the Young's modulus and the Poisson's ration in arbitrary direction.
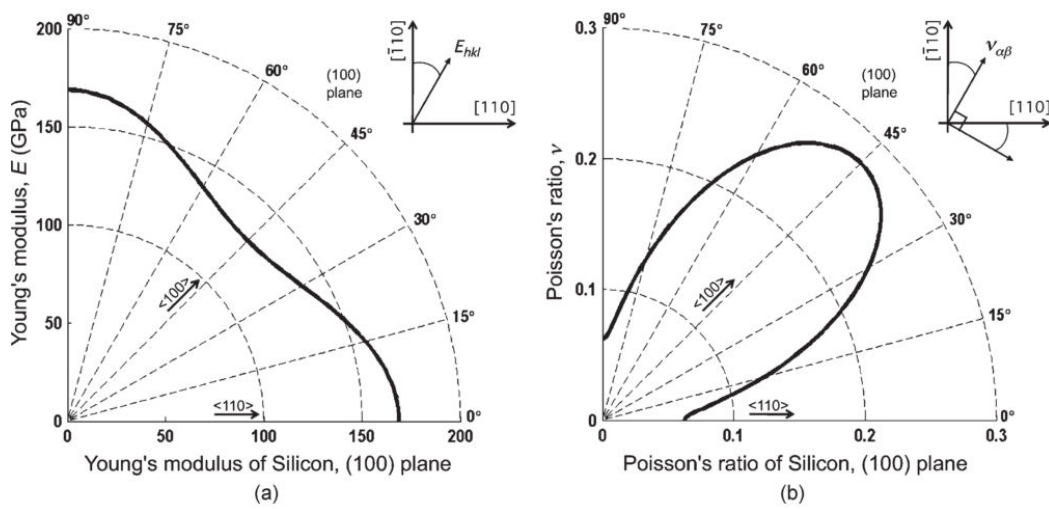
Figure B.3: Young's modulus and Poisson's ration of silicon in (100) plane [146].

C

SPRING CALCULATION CODE

The stiffness of the spring has been calculated using a code in Python. The code is the following one:

```python
from sympy import *
from sympy import sympify
import numpy as np


####################################################


###############Declaration of parameter

#Mo is the initail momentum
#To is the initail torsion
#a is the length of the first small beam
#b is th elength of the first long beam
#c is the legth of the second longer beam

M0=Symbol('M0')
T0=Symbol('T0')
epsilon=Symbol('epsilon')
a=Symbol('a')
b=Symbol('b')
c=Symbol('c')
Fx=Symbol('Fx')
Fy=Symbol('Fy')
Fz=Symbol('Fz')

# Declaration of Young's and shear Modulus
```

```
E=Symbol('E')
G=Symbol('G')

#Declaration of momentum of inertia of each beam
I=Symbol('I')

#Declaration of torsion constant of each beam
J=Symbol('J')

###################################################

###############Calculation of vertical stiffness

#Declaration of momentum and torsion of  each beam
M1=M0−Fz*epsilon
M2=−T0−Fz*epsilon
M3=M0−Fz*(epsilon+a)
M4=Fz*(b−epsilon)+T0
M5=M0−Fz*(epsilon+2*a)

T1=T0
T2=M0−Fz*a
T3=Fz*b+T0
T4=−M0+a*Fz+a*Fz
T5=T0

#Calculation of strain energy
U=integrate(1/(2*E*I)*M1**2,(epsilon,0,a))+integrate(1/(2*E*I)*M2
    **2,(epsilon,0,b))+integrate(1/(2*E*I)*M3**2,(epsilon,0,a))+
    integrate(1/(2*E*I)*M4**2,(epsilon,0,c))+integrate(1/(2*E*I)*
    M5**2,(epsilon,0,a))+integrate(1/(2*G*J)*T1**2,(epsilon,0,a))+
    integrate(1/(2*G*J)*T2**2,(epsilon,0,b))+integrate(1/(2*G*J)*
    T3**2,(epsilon,0,a))+integrate(1/(2*G*J)*T4**2,(epsilon,0,c))+
    integrate(1/(2*G*J)*T5**2,(epsilon,0,a))

#Solving differential equations
M0_sol=solve(diff(U,M0),M0)
T0_sol=solve(diff(U,T0),T0)
```

```
#Implementing solution of previous equation and simplification of
    the expression of the solution U
U1=U.subs(M0,M0_sol[0])
U2=U1.subs(T0,T0_sol[0])
U_simple=simplify(U2)

#Calculation of dz, the vertical displacement
dz=diff(U_simple,Fz)

#Calculation of kz, the stiffness
kz=factor(Fz/dz)

#Regrouping common powers of a E,I,G and J in the expression of
    kz
collect1=collect(kz,E*I*G*J)
collect2=collect(collect1,E*I)
collect3=collect(collect2,G*J)

#Simplifying kz
simple_kz=simplify(collect3)

print simple_kz

###Calculating kz for specific beam length and thickness
t=40e-6
w=50e-6
a_value=100e-6
b_value=2635e-6
c_value=2635e-6

##Calculating momentum of inertia, torsion constant and shear
    modulus
E_value=170e9

#Calculating I
I_value=w*t**3/12
print 'I='+str(I_value)
```

```
#Calculating J
sum_value=0

for i in range (0,10000):
    intermediar=1/(2*i+1)**5*np.tanh((2*i+1)*np.pi*t/(2*w))
    sum_value=sum_value+intermediar

J_value=w**3*t*(1-192/(np.pi**5)*w/t*sum_value)*1/3
print 'J='+str(J_value)

#Calculating G
poisson=0.28
G_value=E_value/(2*(1+poisson))
print 'G='+str(G_value)

##Calculating kz
kz_value=kz.subs([(E,E_value),(G,G_value),(J,J_value),(I,I_value)
    ,(a,a_value),(b,b_value),(c,c_value)],simultaneous=True)
print 'kz='+str(kz_value)

#####################################################

##############Calculation of lateral stiffness
#Declaration of momentum and torsion of each beam
M1=M0-Fx*epsilon
M2=M0-Fy*epsilon-Fx*a
M3=M0-Fx*a-Fx*epsilon-Fy*b
M4=M0-Fx*a-Fx*a-Fy*b+Fy*epsilon
M5=M0-Fx*(epsilon+2*a)

#Calculation of strain energy
U=integrate(1/(2*E*I)*M1**2,(epsilon,0,a))+integrate(1/(2*E*I)*M2
    **2,(epsilon,0,b))+integrate(1/(2*E*I)*M3**2,(epsilon,0,a))+
    integrate(1/(2*E*I)*M4**2,(epsilon,0,c))+integrate(1/(2*E*I)*
    M5**2,(epsilon,0,0))

#Solving differential equations
```

```
M0_sol=solve( diff (U,M0) ,M0)
U1=U. subs (M0, M0_sol [0])

#Solving differential equation in x and y
Fy_sol=solve( diff (U1,Fy) ,Fy)
Fx_sol=solve( diff (U1,Fx) ,Fx)

#Implementing solution of previous equation and simplification of
    the expression of the solution U
U2_x=U1. subs (Fy , Fy_sol [0])
U_x_simple=simplify (U2_x)

U2_y=U1. subs (Fx , Fx_sol [0])
U_y_simple=simplify (U2_y)


#Calculation of dx and dy, the lateral displacements
dx=diff (U_x_simple ,Fx)
dy=diff (U_y_simple ,Fy)

#Calculation of kx and ky, the stiffness
ky=Fy/dy
kx=Fx/dx


###Calculating kx for specific beam length and thickness
t=40e−6
w=50e−6
a_value=140e−6
b_value=2540e−6
c_value=2750e−6

##Calculating momentum of inertia , torsion constant and shear
    modulus
E_value=170e9

#Calculating I
I_value=t∗w∗∗3/12
```

```
print 'I='+str(I_value)

kx_value=kx.subs([(E,E_value),(I,I_value),(a,a_value),(b,b_value)
    ,(c,c_value)],simultaneous=True)
print 'kx='+str(kx_value)

ky_value=ky.subs([(E,E_value),(I,I_value),(a,a_value),(b,b_value)
    ,(c,c_value)],simultaneous=True)
print 'ky='+str(ky_value)
```

D

INTRODUCTION TO KEY
MICROFABRICATION PROCESSES AND
CORRESPONDING EQUIPMENTS AT
MIMENTO TECHNOLOGICAL
CENTER

Microfabrication technologies have first been developed by the semiconductor industry for the micro-electronics and more specifically for integrated circuit fabrication. The idea of microfabrication was the replication and the parallel, also called "collective" or "batch fabrication", fabrication of a large number of miniaturized micro-electronic components on the same substrate. The development of collective microfabrication techniques has lead to size and price reduction of electronic devices such as mobile phones and computers. Other scientific domains have then benefited from the developed techniques and micro-electro-mechanical system are now using the same techniques such as etching, thin film deposition and oxidation. Combining these capabilities with highly specialized micromachining processes, mechanical parts where fabricated leading to devices such as microgrippers, microtweezers [170, 171], electrostatic micromotors [172]. Multi-functional systems with microfluidic, biologically functionalized or optical parts were also investigated. For the micro-electronics, silicon was the most used substrate due to its interesting electronic properties such as the easy generation of insulation layers in silicon dioxide and the control of electronic properties by doping. Materials, such as insulators and metals, were under investigation to create multi layer connections. Then, processes to depose (or grow) structured layers such as silicon dioxide and metals, for example aluminium, have been developed. Later, processes to structure the silicon substrate were developed to create mechanical parts taking benefits from the interesting mechanical properties of

silicon. These techniques and the associated equipments are presented here.

D.0.1 / CLEANROOM FACILITIES

The environment of fabrication should limit contamination of the fabricate devices. In the macro-world contaminations are visible but in the micro-world any microparticles can be a contaminant. Then, a dust in microfabrication is as dangerous as a pebble in the macrofabrication; it can ruin the devices, damage the equipment or be a health risk for the employees. In the case of microfabrication, there are different types of contaminations: particulates, films and atomic contaminants. Particulates can be either organic mostly coming from humans such as hairs, dried skin,...) or inorganic like metals or silicon dusts. Films are essentially residues let after wafer processes (photoresist, oil,...). Finally atomic contaminations can occur when processing the wafer in contaminated chambers. Cleanrooms are environments where particulate concentration is minimized and kept under a certain level. Temperature and humidity are controlled as well. The cleanrooms are classified in terms of number of particles and size of particles. In 1966, the definition FD-STD-209 E states that a cleanroom is of class N if its distribution/dimension of particles is under a certain limit. In practice, for a cleanroom class 100, there must be less than 100 particles greater than 0.5 μm per cubic foot. This requires around 500 air changes per hour with specific air filters. The FD-STD 209 E classification was officially cancelled in 2001 in favour of the international convention ISO-14644-1 defined by the International Organization for Standardization (ISO). Still many people use the old definition. Table D.1 shows the ISO classification with the corresponding FD STD 209-E old classification.

Table D.1: Particle count levels for the ISO 14644-1 classification with the first column showing the corresponding FD-STD 209-E old classification.

Class		Number of particles per cubic meter by micrometer size					
FD-STD	ISO	0.1	0.2	0.3	0.5	1	5
	1	10	2				
	2	100	24	10	4		
1	3	1,000	237	102	35	8	
10	4	10,000	2,370	1,020	352	83	
100	5	100,000	23,700	10,200	3,520	832	29
1000	6	1,000,000	237,000	102,000	35,200	8,320	293
10,000	7				352,000	83,200	2,930
100,000	8				3,520,000	832,000	29,300
	9				35,200,000	8,320,000	293,000

To limit the contamination in the cleanroom, a specific procedure to enter the cleanroom is required. A first "grey" room is used for the employees to wear adapted clothing before entering the cleanroom. The basic clothing consists in a coverall suit, shoe cover and boots, a cap, a hood and gloves. In high quality rooms, facial mask is usually mandatory and gloves are usually compelled in chemical rooms. This equipment contributes to the protection of the device from the potential contaminations from the users as well as it protects the user from eventual health risks.

D.0.2/ PHOTOLITHOGRAPHY

In general, it is complicated to grow, deposit or etch material layers only in the areas where they are desired (selective deposition/etching). As a result, material layers are usually deposited across the entire surface and then removed from the area where they are not needed. The photolithography technique aims to transfer a desired pattern from a hard mask into a photoresist polymer layer on the wafer surface. Figure D.1 shows the different steps of the photolithography process. First, the photoresist is deposited on the wafer with different possible techniques. The standard way to deposit photoresist is spin coating. The photoresist is poured on the wafer and the wafer is spun during a specific time, with a specific acceleration and speed. These three parameters influences the quality and the thickness of the obtained photoresist layer. When the wafer surface is not flat, spinning of the resist is difficult and spray coating is an alternative to deposit uniformly the resist on the structured surface. After the photoresist coating, the photoresist is usu-

ally bake during a step called the soft bake that drive off the excess of solvent. Next, the wafer is aligned and put in contact with the hard mask and finally exposed to UV light. There are different types of contact between the wafer and the hard mask (vacuum contact, hard contact,...). Depending on the type of contact chosen, the resolution and the quality of the photolithography may vary. Only the area corresponding to the transparent area of the hard mask are exposed. In the case of positive photoresist, light induces a break in the polymer chain. On the contrary, for negative photoresist, light induces cross-linking in the polymer. The wafer is then immersed in a developing solution which removes the exposed photoresist for positive photoresists and the unexposed photoresist for the negative photoresists. Finally, the wafer is cleaned and dried. Some photoresist requires a post exposure bake (before the development) to stabilize the photo-generated chemicals or to suppress standing wave effect and also a hard bake (at the very end) to harden the photoresist and improve the adhesion to the substrate.
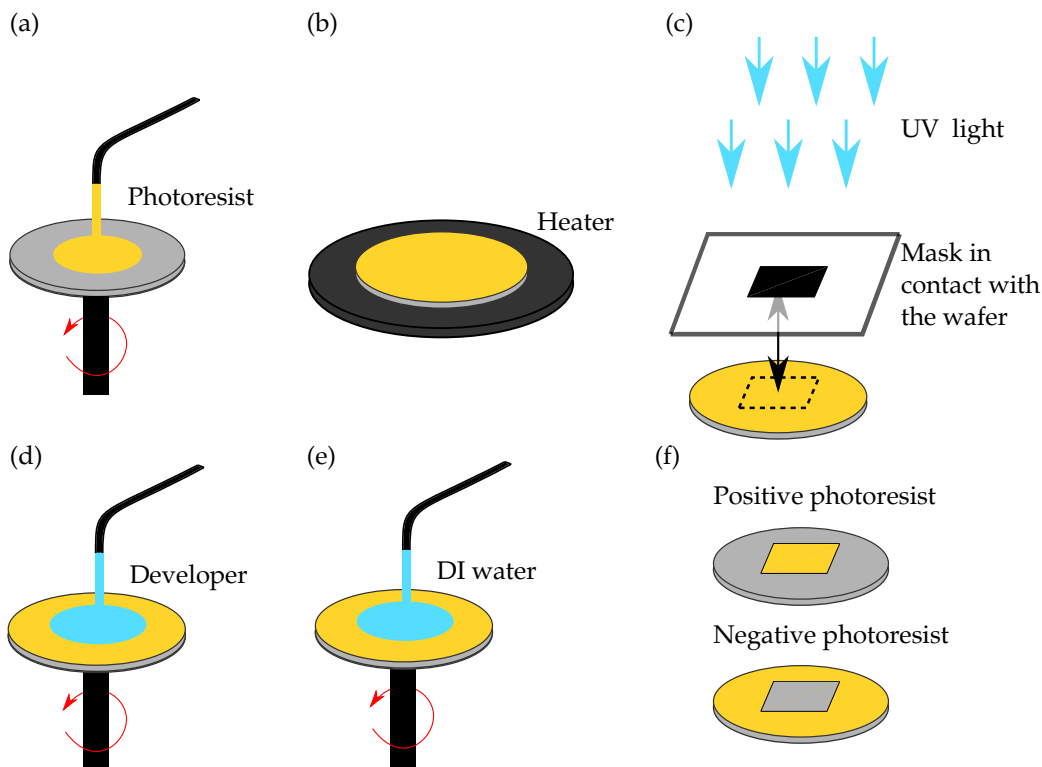
Figure D.1: Photolithography steps: (a) spin coating of photoresist on wafer, (b) soft bake, (c) UV exposure of the photoresist (in practice the mask is in contact with the wafer), (d) development of the photoresist, (e) Rinsing and cleaning of the wafer (DI water: deionized water), (f) developed photoresist in the case of positive and negative photoresist.

The resolution of the masks but also the alignment machine as well as the type of photoresist have an impact on the resolution of the pattern. Moreover, the quality of the photolithography is usually worst on the edge of the wafer. This is mainly linked to the inhomogeneity of resist thickness on the edge. The type of photolithography described

here corresponds to "mask contact" photolithography. This type of photolithography is a standard process, which has some limitations for more demanding structures. For example, the resolution is typically limited to 1 μm, the planarity of the wafer surface and the photoresist layer is critical, and the defect/contamination density due to the physical contact between the hard mask, and finally, the wafer is unacceptable for very small structures. To overcome these limitations, other photolithography techniques, such as projection photolithography and direct writing, but also other sources such as lasers, deep ultra-violet or electron-beam (e-beam), have been developed. Table D.2 presents different types of process with their corresponding properties, advantages and drawbacks.

In MIMENTO facilities, various photoresist are furnished on a regular basis such as S1813, S1828, SPR 220 3.0, LOR 7B, AZ9260, SU8 and Ti09. These resists can be spin coated (OPTIcoat 22, Karlsuss RC8) or spray coated (SUSS Microtec). There is one double side EVG620 aligner that is compatible with the wafer bonder support of the bonding machine EVG501. The non-standard exposition/alignment machines are shown in Tab. D.2. The EVG501 is a bonding machine used for anodic bonding and thermocompression bonding.

Table D.2: Non-standard photolithography processes.

Type of process Source	Resolution range	Advantages	Drawbacks	Equipment
Projection				
UV - Deep UV	$1 \mu m$ - 50 nm	Compatible with standard hard mask and photoresist No contamination (no contact) Non-flat surface can be correctly exposed If magnification is superior to 1 then a stepper is required (automatic alignment and focusing, step-and-repeat exposure, small masks)	Expensive systems	Perkin Elmer (SVG Micralign 740) Mag:1 (resolution=1 μm) Stepper Nikkon (deep-UV) Mag:6 (resolution=350 nm)
Direct writing				
Laser	50 nm	No hard mask Short exposure time compared to e-beam	Slow process (beam scanning) Very thin resist not compatible for etching Exposure of flat-surfaces only	Heidelberg DWL 200 (resolution=900 nm)
Electron-beam	10 nm	No hard mask Very precise process used to generate masks	Very slow process	Raith E_{line}(resolution=20 nm)

D.0.3/ PLASMA

A plasma is a state of matter as solid, liquid and gas. In this state, electrons wander around the nuclei of the atoms. A plasma consists of electrons, ionized molecules, neutral molecules, neutral and ionized fragments of broken-up molecules, excited molecules and free radicals. Free radicals are electrically neutral species that have incomplete bonding and are extremely reactive. The notion of plasma is introduced here because when energy is provided to the plasma, it can be used to remove material from a target which can be directly the processed wafer (etching) or, which etched material can be deposited on the processed wafer (deposition by sputtering). Hence, plasmas are really important in microfabrication. There are two ways to generate a plasma: by applying a DC voltage or a RF voltage between two electrodes between which a gas is introduced (Fig. D.2). When a DC voltage is applied between the anode and the cathode, free electrons are accelerated and elastically collides with atoms generating an ion and an additional electron. This cascading process creates a sustained reaction. In the same time, the excited gas atoms returning to ground state emit visible photons that can be seen as a glow in the chamber. When a RF voltage is applied to a pair of electrodes (typically 13.56 MHz), it accelerates electrons that collides with neutral gas molecules, forming ions and more electrons as with a DC voltage. The difference is that only the electrons are travelling between the two electrodes with an oscillitory path following the high frequency field whereas ions are too massive to respond to this field. In particular to sputter dielectric films, RF power enables to avoid the accumulation of electric load on the target. For RF generated plasma, the target electrode is smaller. Indeed, if both electrodes are symmetrical, the electric field is completely symmetrical and an identical sputtering rate occurs at both electrodes which prevent the film from growing. When the electrode areas are not equal, the field must be higher at the smaller electrode to maintain an overall current continuity. Therefore, making the target electrode smaller, the sputtering preferentially occurs on the target (Fig. D.2 (c)). In practice, for sputtering, the wafer is usually connected electrically to the chamber walls.
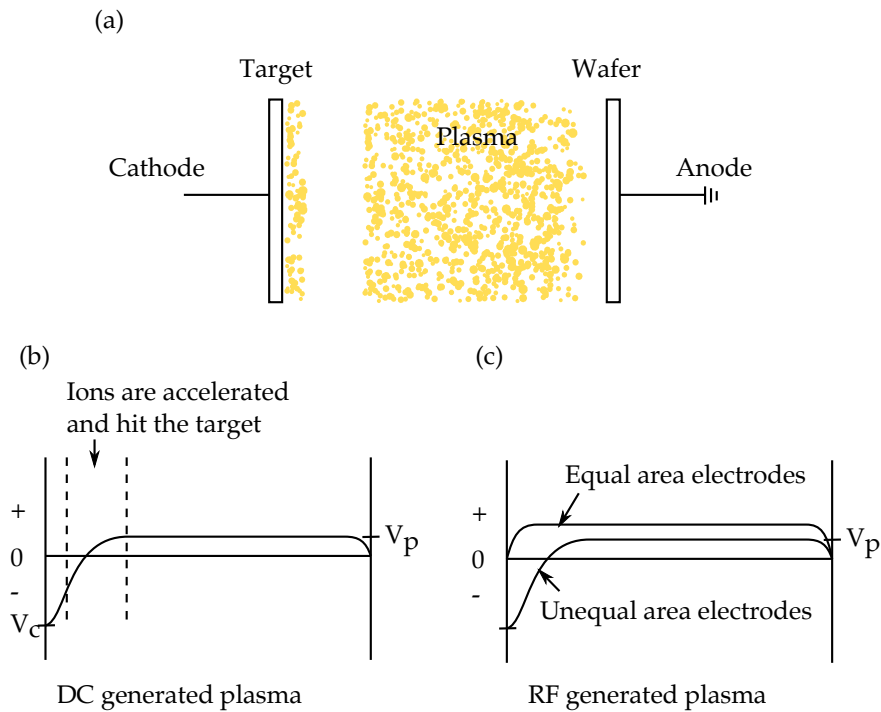
Figure D.2: Generation of a plasma by DC and RF voltage. (a) Illustration of the plasma, voltage graph between the two electrodes in the chamber in the case of (b) DC and (c) RF generation.

D.0.4 / THIN FILM DEPOSITION METHODS

The deposition of various material has been developed at the microscale. The most common deposition techniques can be classified in three main types of deposition: the epitaxy, the chemical vapour deposition and the physical vapour deposition. Epitaxy is a growth technique of monocrystalline layers on monocrystalline substrate. This technique consists to use the substrate as a crystal seed to grow the material by progressively adding atoms that are constituting the film. The film and the substrate can be different but should have similar crystalline and lattice parameters. When the substrate and the film are the same, it is called homoepitaxy whereas when they are different, it is called heteroepitaxy. Epitaxial techniques can be divided according to the type of phase transporting the atoms to be deposited. For example, when classified under the nature of the phase, three main techniques exist: the vapour phase epitaxy, the liquid phase epitaxy and the molecular beam epitaxy.

Chemical vapour deposition consists in a thin film formation from vapour phase reactants. The deposited films range from metals to semiconductors to insulators. All chemical vapour deposition processes involve using an energy source to break reactant gases into reactive species. Depending on the process conditions, different types of chemical vapour deposition (CVD) are identified: atmospheric pressure CVD (APCVD), low pres-

sure CVD (LPCVD), plasma enhanced CVD (PECVD) and metal organic CVD (MOCVD). Table D.3 gives the specificities, the advantages and the drawbacks of each techniques.

Table D.3: Comparison of CVD techniques in terms of advantages, drawbacks and deposited material.

CVD techniques	APCVD	LPCVD	PECVD
Advantages	High deposition rate	Good uniformity	Low temperature (225-450°C)
	Simple technique	Low stress	High deposition rate
		Good purity	
Drawbacks	Poor uniformity and conformality	Low deposition rate	Chemical contamination
			Hard to control deposition rate and stress
Material	Thick oxide	Polysilicon and dielectric	dielectric

Physical vapour deposition techniques (PVD) regroup the thermal and the e-beam evaporation and the sputtering. These techniques are mostly used for metal layers and alloys. For the thermal evaporation, the source material is hosted in a crucible that is heated with a current. The choice of the crucible material is important to avoid any contamination of the source material. For the e-beam evaporation, a filament is heated up to the electrons emission. The electrons are accelerated and deviated to hit the material in the crucible. There is no contamination from the crucible because it is kept cold. Possible contaminant from the heated filament are deviated by a magnetic field. With both techniques, once the material is heated enough, the material evaporates and is deposited everywhere in the chamber. Materials with a high melting point cannot be deposited easily by thermal evaporation that is why e-beam evaporation is now the most common. Sputtering is another technique based on ion bombardment to sputter a source material, called the target, and dislodge atoms of the target which are then deposited on the wafer. The ions used for the bombardment are usually argon ions (Ar^+). With this technique, the range of material that can be deposited is unlimited. Moreover, sputtering is usually performed at higher pressure than evaporation. To obtain argon ion bombardment, a plasma is generated.

In terms of deposition methods, evaporation and sputtering of a large range of metals are possible with respectively the Alliance EVA 450 and the Plassys MP500 available at MIMENTO technological center. However, during the period of this work, the evaporation

machine was unavailable. The sputtering machine allows the deposition of gold, titanium, chromium, copper and aluminium, which are metal layers widely used in MEMS for the creation of pads, mirrors but also bonding layers. A PECVD machine from Sentech (SI 500 D) is also available in the cleanroom, though it was operational at the end of this work. This machine is able to deposit silicon dioxide and nitride. Finally silicon dioxide can be thermally grown in a dedicated furnace.

D.0.5/   ETCHING TECHNIQUES

Etching techniques are used to remove a material layer from unwanted areas, the other areas being protected by a masking layer. As the deposition techniques, etching techniques are usually associated with a previous photolithography step, to etch the material only where it is not desired and thus create a specific pattern. The most commonly used etching methods can be grouped in two main types of etching: dry etching using ion bombardment to remove material from the wafer, i.e. a plasma, and wet etching using chemical solution that selectively etch the material. Classical masking layers are photoresist, silicon dioxide, silicon nitride and metals. The masking material is chosen in terms of its compatibility with the plasma or the etching solution, i.e. the etch selectivity. The etch selectivity is defined as the ratio between the etching speed of the material to be etched and the etching speed of the masking material. Dry etching is based on a gas-solid reaction, in which the etching material is gaseous and the etched material is solid. The higher the energy of the gas, the higher the physical etching and the higher the isotropy[1] of the etching. To give energy to the gas, a plasma is generated. The wafer is bombarded with ions which removes the material. Depending on the etched material, the gases used for the plasma and the masking layers are not the same. Table. D.4 summarizes the different type of etching.

---

[1]The isotropy of a process defines if it occurs identically, uniformly in all the directions. It is said anisotropic if a direction is preferred from the others.

Table D.4: Comparison of dry etching techniques depending on the excitation energy of the gas. The different etching techniques are also described in term of types of etching reaction (chemical or physical), their isotropy and their selectivity.

Etching techniques	Excitation energy	Pressure	Description
vapour etching	-	High	Chemical, isotropic, very selective
Plasma etching	10's to 100's of Watts	⟨100 Torr	Chemical, isotropic, selective
Reactive ion etching	100's of Watts	Low (10-100 mTorr)	Physical and chemical etching, adjustable (an)isotropy, quite selective
Sputter etching (Ion Mill)	100's to 1000's of Watts	10 mTorr	Physical, directional, low selectivity

Silicon is the most used material in microfabrication and specific techniques have been developed for this material. Wet etching can be either isotropic or anisotropic. These processes are generally sensitive to the temperature and composition of the etchants (concentration, additives) and quality of the silicon crystal (defects, impurities). Isotropic etchants such as HNA[2] give rounded profiles whereas anisotropic etchants such as KOH (potassium hydroxyde), TMAH (tretamethyl ammonium hydroxyde) and EDP[3] etch preferably ⟨100⟩ planes compared to the ⟨111⟩ planes. Figure D.3 shows the etching profile for (100) wafer in the case of isotropic and anisotropic etching.
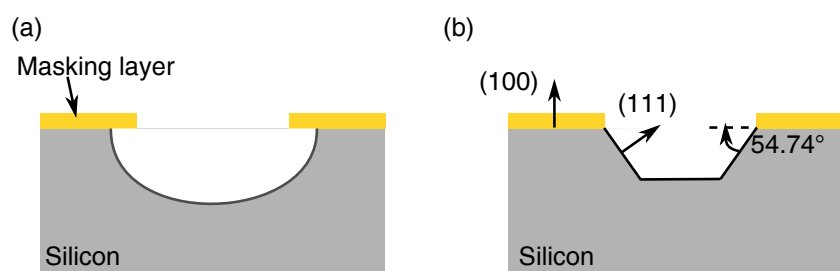
Figure D.3: Silicon etching profile for (100) wafer, which are the most common wafers and the ones used for this work: (a) Isotropic etching, (b) anisotropic etching.

---

[2]HNA is a mixture of nitric and hydrofluoric acids diluted in water or acetic acid. The diluent and the ratio of the etching acids have an impact on the etch rate [173].

[3]EDP is a mixture of ethylene diamine, pyrocatechol and water.

As a dry etching technique, reactive ion etching is classically used for the etching of silicon. Moreover, a time multiplexed deep etching technique, called DRIE for deep reactive ion etching, has been developed. The aim is to improve the anisotropy of the etching to obtain vertical walls by depositing a protective polymer. Side walls angles around $90° \pm 2°$ and etching depth up to 1.5 mm are obtained [174]. Figure D.4 illustrates the different steps used for the DRIE process. Firstly, the polymer passivation layer is deposited everywhere. Flurocarbon gases such as C_4F_8 are used to create a teflon-like polymer (polymerized CF_2). A first etching step removes the polymer from the horizontal surfaces. A second isotropic etching step attacks and removes the silicon. The etching gas is typically a mixture of SF_6 and argon.
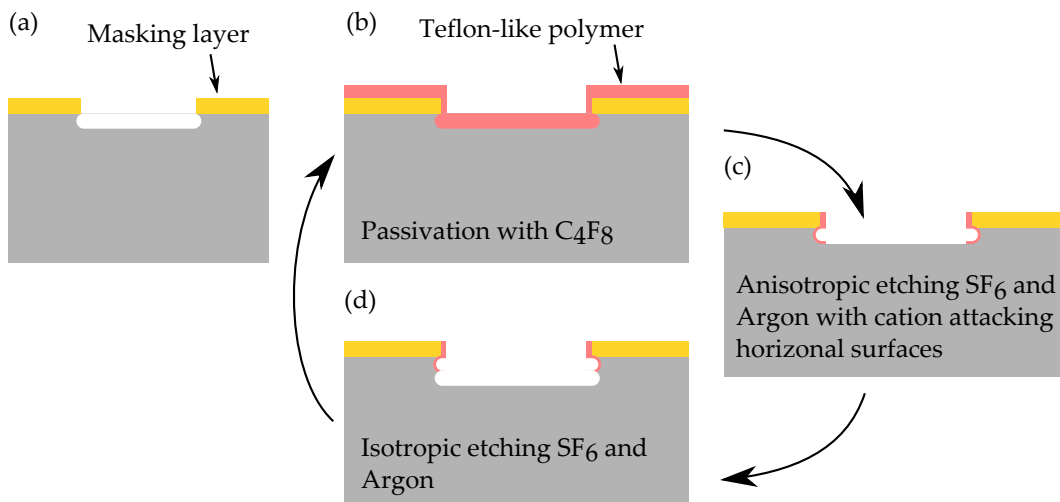
Figure D.4: DRIE etching steps: (a) silicon wafer with a masking layer, (b) deposition of teflon-like polymer, (c) etching of polymer on horizontal surfaces, (d) SF_6 silicon etching. The process loops from step (b) to step (d) until the targeted depth is reached.

There are two DRIE machines at MIMENTO technological center: a quite recent SPTS Pegasus Rapier and an older Alcatel A601E. In the SPTS machine, metal masks are forbidden in its chamber to prevent the contamination of the ceramic walls. The Alcatel machine has an aluminium chamber which can be easily cleaned by plasma and then metal masking layers are allowed. Another difference is the system of clamping, which is mechanical in the Alcatel and electrostatic in the SPTS. On the one hand, electrostatic clamping is more difficult for wafer which back side is highly structured. On the other hand, the mechanical clamping may lead to the wafer breakage for sensitive wafers due to deep structuration, small thickness or thermal stress. The properties of each DRIE machine are summarized in Tab. D.5. The cleanroom is also equipped with a RIE machine (Plassys) that can etch a wide range of materials (silicon, silicon nitride, silicon dioxide, titanium, nickel,...) but which can be also used to clean a wafer from organic residues. For this latter purpose, another machine is dedicated to oxygen plasma and wafer cleaning

in general (Nanoplas DSB6000).

Table D.5: Comparison of the DRIE equipment available at MIMENTO facilities.

Equipment	Alcatel	SPTS
Etched material	SiO_2 and Si	SiO_2 and Si
Clamping mechanism	Mechanical	Electrostatic
Detection of the end of etching	No	Yes
Notching limitation	Low frequency mode	Pulsed mode
Metal masks	Allowed	Forbidden
Availability	Partially available	Available

D.0.6/ CHARACTERIZATION METHODS

After each step of a fabrication process, the result must be characterized. Optical microscopes are used for optical observation of the surface quality of deposited or etched surfaces. It can also provide in plane as well as out-of plane measurements. The precision of the measurements highly depends on the objective used. To measure out-of-plane distances, a mechanical profilometer is used. The wafer is placed under a mechanical tip that goes down in contact with the wafer surface and scan the surface following a predefined line. The precision of the measurement highly depends on the tip diameter and on the chosen parameters (speed, frequency,...). This method requires that the layer, which thickness is to be measured, is structured. If it is not the case, then ellipsometry can be used to characterize dielectric films. Light is focused on the wafer, reflected by the wafer and detected. The change of polarization between emitted and reflected light is compared to a model. In particular, the change of polarization depends on the thickness and the refractive index of the dielectric. Finally, when higher resolution images are necessary scanning electron microscope (SEM) is used. SEM is based on the detection of electrons coming from the sample that is being hit by a beam of emitted electrons. The detected electrons are classically secondary electrons and back-scattered electrons. Secondary electrons results from the inelastic scattering interactions between electrons of the sample and the beam electrons. Back-scattering electrons are electrons from the emitted beam that are reflected back by the sample to the detector. The detected electrons carry an information on the topography of the surface hit by the electron beam. The resolution of a SEM is in the nanometer order.

In term of characterization, a recent optical microscope DM8000 from Leica, a mechanical profilometer Alpha-step from Tencor, a scanning electron microscope and an ellipsometer

Uvisel from Horiba are available in the cleanroom.

HARD MASKS DESIGN

Here, the masks used for the three strategies of fabrication of the vertical microscanner are shown (Fig E.2,E.3,E.4). For a better readability only one chip is shown. Each processed wafer is composed of 21 chips as shown in Fig. E.1

one
chip
area
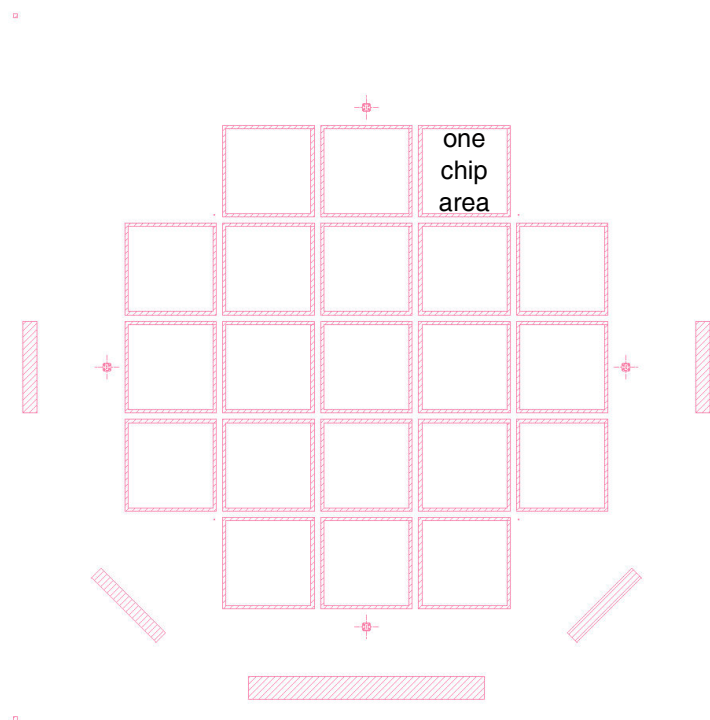
Figure E.1: Masks of the projection strategy flow chart. The masks numbers refer to the number given in the risk analysis table. This mask corresponds to a design for which chips can be manually separated by breaking small silicon bridges.

E.1/ PROJECTION STRATEGY

(a)

Silicon bride for manual separation of chips

Trenches in silicon to define chip size
(BS and FS)

Back side aperture

Isolation trenches between
microactuators and microsensors

(b)

(c)

Glass disks

Silicon cavities

Micromirror

First set of comb finger

Second set of comb finger

2 sets of comb finger

Mask 2 (silicon cavities)

Mask 3 (glass disks)

Mask 4 (glass disks)

Mask 5 (mechanical structure and first set of comb finger)

Mask 6 (second set of comb finger)

Mask 7 (back side aperture)

Figure E.2: Masks of the projection strategy flow chart: (a) design of one chip, (b) zoom on one glass support, (c) zoom on the comb drive structure. The masks numbers refer to the number given in the risk analysis table. This mask corresponds to a design for which chips can be manually separated by breaking small silicon bridges.

E.2/ THERMOCOMPRESSION STRATEGY

(a)

Silicon bride for manual separation of chips

Trenches in silicon to define chip size (BS and FS)

Back side aperture

Isolation trenches between microactuators and microsensors

(b)

Glass disks

Clear aperture on glass side

Micromirror

2 sets of comb finger

(c)

First set of comb finger

Second set of comb finger

Mask 2 (mechanical structure and first set of comb finger)

Mask 3 (second set of comb finger)

Mask 4 (clear aperture on glass wafer before thermocompression)

Mask 5 (glass disks)

Mask 6 (back side aperture)

Mask of shadow mask (contact pads and micromirrors)

Figure E.3: Masks of the thermocompression strategy flow chart: (a) design of one chip, (b) zoom on one glass support, (c) zoom on the comb drive structure. The masks numbers refer to the number given in the risk analysis table. This mask corresponds to a design for which chips can be manually separated by breaking small silicon bridges.

E.3/   SPIDER LEGS STRATEGY
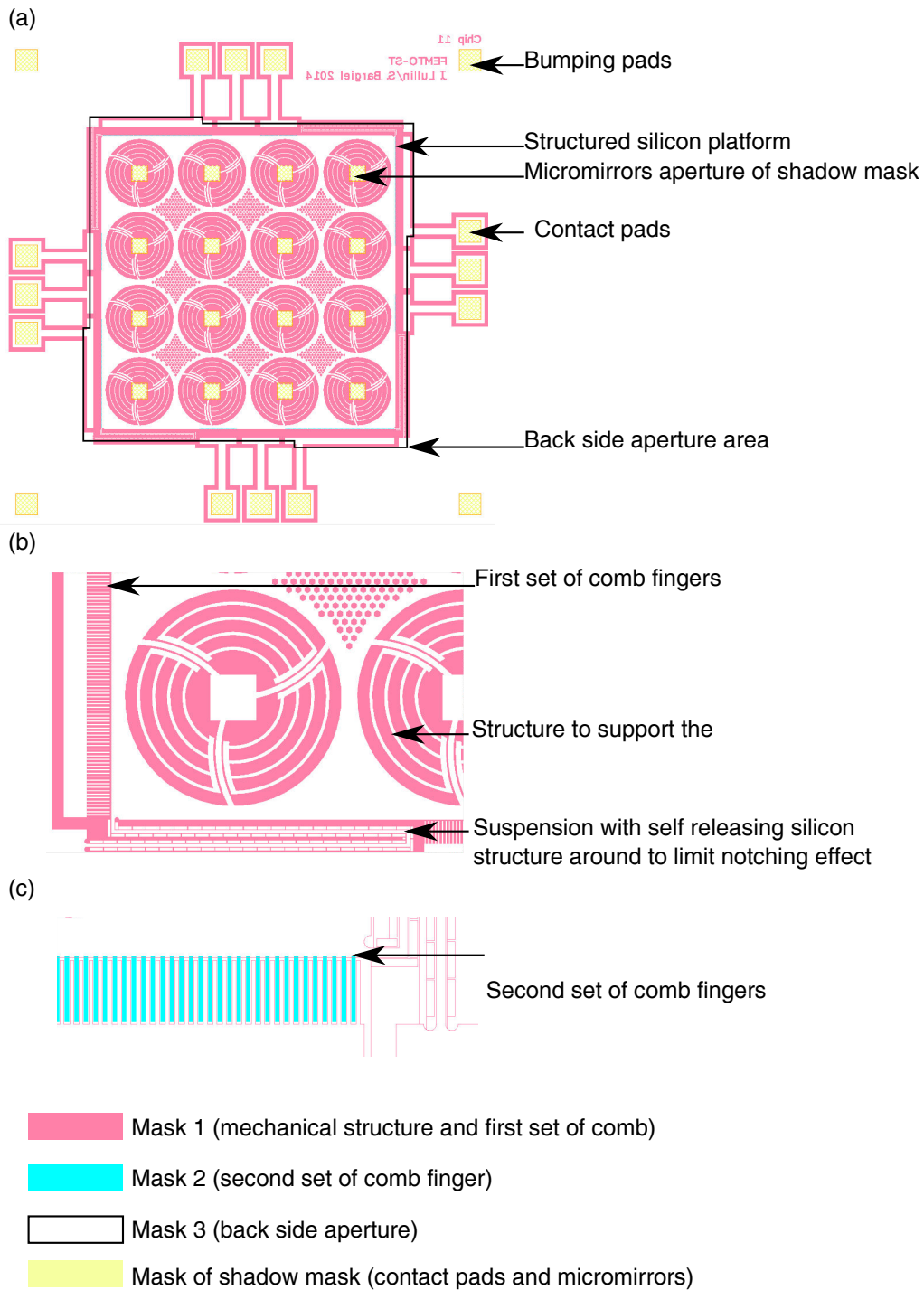
Figure E.4: Masks of the spider legs strategy flow chart: (a) design of one chip, (b) zoom on one suspended micromirror, (c) zoom on the comb drive structure. The masks numbers refer to the number given in the risk analysis table. This mask corresponds to a design for the wafer is integrated at wafer level with the other wafer constituting the Mirau interferometer.

Abstract:

This thesis describes the design, simulation and fabrication of a vertically actuated 4x4 array of micromirrors with embedded position sensing function. The vertical microscanner is meant to be integrated within an array-type Mirau microinterferometer realized with optical microcomponents fabricated using collective techniques. The microscanner, developed in this thesis, provides a reference signal that is used for the implementation of phase modulation interferometery in an optical coherence tomography (OCT) system. This thesis first introduces the need for adapted imaging systems for the early diagnosis of skin cancer and establishes the optical specifications required by this specific application. Based on these specifications, the design of the OCT system based on the Mirau microinterferometer is presented. In parallel, the state of the art of the microactuation technologies is discussed and comb drive electrostatic actuation is chosen, for its compatibility with the design of the Mirau microinterferometer, to actuate and sense the position of the array of micromirrors. Then, the core of the thesis deals with the development of the vertical microscanner, i.e. its design and simulations, its fabrication and its characterization.

Keywords: MOEMS, microscanner, Mirau micro-interferometer, full-field swept source OCT

Résumé :

Cette thèse décrit le design, la simulation et la fabrication d'une matrice 4x4 de micromiroirs actionnée verticalement et munie d'un capteur de position. Le microscanneur vertical a pour vocation à être intégré au sein d'un microinterféromètre de Mirau de type matriciel, réalisé à base de composants microoptiques fabriqués grâce à des méthodes collectives. Le mouvement du microscanneur, développé dans cette thèse, génère un signal de référence utilisé pour l'implémentation de l'interférométrie à modulation de phase dans un système de tomographie par cohérence optique (OCT). Dans un premier temps, la thèse introduit le besoin d'un système d'imagerie adapté pour la détection précoce des cancers de la peau et établit les spécifications optiques requises par cette application. À partir de ces spécifications, le design du système OCT basé sur le microinterféromètre de Mirau est présenté. En parallèle, l'état de l'art des technologies de microactionnement est décrit et un actionnement électrostatique à base de peignes interdigités est choisi pour actionner et lire la position de la matrice de micromiroirs. En effet ce type d'actionnement bénéficie d'une bonne compatibilité avec le design du microinterféromètre de Mirau. Dans un second temps, le cœur de la thèse expose le développement du microscanneur vertical, c.à.d le design et les simulations ainsi que la fabrication et la caractérisation.

Mots-clés :   MOEMS, microscanner, micro-interféromètre de Mirau, OCT à source à balayage plein champs

UFC
UNIVERSITÉ
DE FRANCHE-COMTÉ